Quantum sensing with integrated waveguides for ultra-fast spectroscopy in the mid infra-red

DISSERTATION

zur Erlangung des akademischen Grades

DOKTOR RER. NAT.

an der Fakultät für Naturwissenschaften

der Universität Paderborn

vorgelegt von

FRANZ HARTMUT ROEDER

am 20. Februar 2025

Erklärung der Selbstständigkeit

Hiermit versiche ich, die vorliegende Arbeit selbstständig verfasst und keine anderen als die angegebenen Quellen und Hilfsmittel benutzt sowie die Zitate deutlich kenntlich gemacht zu haben.

Paderborn, den 20. Februar 2025 Franz Roeder

Erstgutachter:	Prof. Dr. Christine Silberhorn
Zweitgutachter:	Prof. Dr. Thomas Zentgraf
Vertreter des Mittelbaus:	Dr. Frederik Thiele
Vorsitzender der Prüfungskommission:	Prof. Dr. Wolf Gero Schmidt

Contents

Summary

The development of practical quantum sensors for applications in ultra-fast spectroscopy necessitates their integration.

In this thesis, we use integrated waveguides as photon pair sources based on parametric down-conversion (PDC) to perform quantum spectroscopy with nonlinear interferometers. This requires the PDC sources to be broadband and highly non-degenerate. However, non-degenerate integrated sources are typically limited in bandwidth due to their long interaction length.

First, we overcome this limitation by dispersion-engineering and present two realisations of periodically poled, titanium in-diffused lithium niobate waveguides that generate spectrally broadband photon pairs at non-degenerate wavelengths in the near and mid infra-red.

Next, we employ the first PDC source as building block of a nonlinear interferometer. Based on our theoretical description of the system, we perform direct measurements of the bi-photon correlation time, an important metric that defines their simultaneity and the temporal resolution in a measurement.

In the following, we investigate the properties of two common geometries for nonlinear interferometers regarding their benefits, disadvantages, and optimal operation mode for quantum optical coherence tomography when working with integrated waveguide PDC sources.

Finally, we use the second PDC source in a nonlinear interferometer to perform absorption spectroscopy in the mid infra-red, while only detecting in the near infra-red.

Zusammenfassung

Die Entwicklung praktischer Quanten-Sensoren für Anwendungen auf dem Gebiet der ultra-schnellen Spektroskopie bedingt deren Integration.

In dieser Dissertation nutzen wir integrierte Wellenleiter als Photonenpaar-Quellen basierend auf parametrischer Fluoreszenz (PF) für ultra-schnelle Quanten-Spektroskopie in nichtlinearen Interferometern. Dazu müssen diese Quellen zugleich spektral breitbandige und weit separierte Photonen erzeugen. Integrierte Quellen sind jedoch oft aufgrund ihrer langen Interaktionslänge in der Bandbreite beschränkt.

Zuerst überwinden wir daher diese Beschränkung durch Dispersions-Anpassung und stellen zwei Realisierungen periodisch gepolter, Titan-ein-diffundierter Lithium-Niobat-Wellenleiter vor, welche breitbandige PF mit ungleichen Wellenlängen im nahen und mittleren Infrarot erzeugen.

Danach verwenden wir unsere erste Quelle in einem nichtlinearen Interferometer. Basierend auf der theoretischen Beschreibung des Systems, messen wir direkt die Korrelationszeit des Photonenpaares, ein wichtiges Maß für deren Gleichzeitigkeit und die zeitliche Auflösung in Experimenten.

Im Folgenden untersuchen wir zwei gebräuchliche Realisierungen nichtlinearer Interferometer auf deren Eignung für quanten-optische Kohärenztomographie mit integrierten Quellen.

Schließlich nutzen wir die zweite Quelle für Absorptionsmessungen im mittleren Infrarot, bei denen lediglich Photonen im nahen Infrarot detektiert werden.

List of publications

Throughout the course of this thesis, several of the presented results have been published in peer-reviewed journals, made available as a pre-print or in the proceedings of international conferences. These scientific contributions are listed below. We will link to the corresponding works in the main text.

First author publications

FR, R. Pollmann, M. Stefszky, M. Santandrea, K.-H. Luo, V. Quiring, R. Ricken, C. Eigner, B. Brecht and C. Silberhorn: *Measurement of Ultrashort Biphoton Correlation Times with an Integrated Two-Color Broadband SU(1,1)-Interferometer*, PRX Quantum **5**, 020350 (2024).

FR, A. Gnanavel, R. Pollmann, O. Brecht, M. Stefszky, L. Padberg, C. Eigner, C. Silberhorn and B. Brecht: *Ultra-broadband non-degenerate guided-wave bi-photon source in the near and mid-infrared*, New J. Phys. **26**, 123025 (2024).

FR, R. Pollmann, V. Quiring, R. Ricken, C. Eigner, B. Brecht and C. Silberhorn: *Towards integrated sensors for optimized OCT with undetected photons*, in preparation (2025).

Author contributions

R. Pollmann, **FR**, V. Quiring, R. Ricken, C. Eigner, B. Brecht and C. Silberhorn: *Integrated, bright broadband, two-colour parametric down-conversion source*, Opt. Express **32**, 23945 - 23955 (2024).

International conference proceedings

Frontiers in Optics + Laser Science 2022: *Bi-Photon Correlation Time Measurements with a Two-Colour Broadband SU(1,1) Interferometer*, paper FW1B.3.

Conference on Lasers and Electro-Optics/Europe (CLEO/Europe 2023) and European Quantum Electronics Conference (EQEC 2023): *An ultra-broadband, integrated mid-infrared photon-pair source*, paper ea_4_5.

Frontiers in Optics + Laser Science 2023: *Optical Coherence Tomography with Undetected Photons Based on an Integrated PDC Source*, paper JTu5A.55.

Quantum 2.0 Conference and Exhibition 2024: *Optimized OCT with Undetected Photons Based on an Integrated Waveguide PDC Source*, paper QTu4C.3.

List of abbreviations

FWHM	full width at half maximum
PDC	parametric down-conversion
JSA/JSI	joint spectral amplitude/intensity
JTA/JTI	joint temporal amplitude/intensity
NIR	near infra-red
MIR	mid infra-red
GV	group velocity
GVM	group velocity matching
GVD	group velocity disperison
TOD	third order dispersion
Ti:LiNbO$_3$	Titanium in-diffused lithium niobate
TE	transverse electric
TM	transverse magnetic
IC	induced coherence
OPD	optical path delay
OCT	optical coherence tomography
TD	time domain
FD	Fourier domain
FTIR spectroscopy	Fourier transform infra-red spectroscopy

1 Introduction

The application of quantum resources to classical measurement techniques has led to a massive advancement in today's technologies. Whereas the advent of lasers in the 1960s paved the way for the first quantum revolution, we are currently in the midst of the second quantum revolution, where quantum states are employed as resources for advanced measurement techniques and to construct new devices [1, 2]. Single photons, due to their inherent quantum properties, hold great potential as information carriers in the quantum regime. Thus, quantum states of light can be used in measurements that would typically be performed with classical light and provide benefits in precision or allow for completely new measurements. Some examples are gravitational wave detection, which nowadays employs squeezed states of light [3], or photonic quantum computing, which may use photons as a resource in Gaussian boson sampling [4, 5]. Thus, quantum light leads to the advent of new quantum measurements techniques and the development of real-world devices based on single photons [6].

An area of research in which classical measurement techniques are transferred to the quantum regime is the field of classical ultra-fast spectroscopy [6]. This kind of spectroscopy employs spectrally broadband light to probe the spectral and spatial features of an object under test with high precision. Typical systems rely on interferometric schemes where the light field is split into a probe and a reference path. After interaction with the sample, the probe light subsequently interacts with an unaffected copy of itself to obtain information about the object with a high precision. Experimentally, such methods are realised in interferometric schemes, which are based on passive, i.e. linear, optical elements to split and recombine the involved light fields. Therefore, probing and detection occur at the same wavelength in these systems, since only light fields at the same wavelength interact with each other in the absence of active optical elements. Moving towards low light levels, this limits high precision measurements to spectral regimes with sufficiently efficient and low-noise detectors. Thus, it hinders investigations in spectral regimes such as the mid infra-red, ranging from 2000 nm to 30 µm or THz spectral region, which ranges from wavelengths of 30 µm to 1000 µm. In these regions of the electromagnetic spectrum, efficient low-noise detectors are sparse in ambient conditions due to thermal radiation background. However, these are spectral regimes that are highly interesting in biophysics or environmental sciences due to the distinctive molecular rotational and vibrational absorption features that act like unique fingerprints [7, 8].

One way to circumvent this limitation is by using nonlinear interferometers. In these interferometers the passive beamsplitters are replaced by active, i.e. nonlinear, optical elements. Cascaded nonlinear processes have first been used with classical states of light to measure material properties of the nonlinear material itself [9] or a test object [10, 11], for example by observing changes in the generated light at the second harmonic of the pump light.

For us, nonlinear interferometers are interesting as they provide a means to overcome the limitation to the same wavelength for probing and detection. Furthermore, nonlinear interferometers have recently been used for quantum measurements, where nonlinear elements act as photon pair sources [12]. This allows to generate a quantum states of light within the interferometer itself and perform various new measurement techniques. One of them are so-called measurements with undetected photons. Here, a photon at a long wavelength probes the object under test, while the second photon at a shorter wavelength serves as a reference. The detection then happens at the short wavelength after the second nonlinear process. Such measurements with undetected photons help to overcome the challenge of sensing in the mid infra-red regime by only probing the sample at this wavelength while detecting in the near infra-red or even visible spectral range.

One of the first experiments using measurements with undetected photons was performed in 2014 by Lemos et al. [13]. In the experiment, two cascaded photon pair sources are aligned such that, at the output of the interferometer, the detected photon may have been generated either in the first or in the second source. This is achieved by aligning the long wavelength path from both processes on top of each other and super-imposing the short wavelength photons on a beamsplitter. Consequently, an interference in the rate of generated short-wavelength photons can be observed, as already proposed in 1991 [14]. Placing an absorptive object in one of the interferometer arms adds information about the source in which the photon has been generated and thus allows to retrieve the 'which source' information. As a consequence, the observed interference is diminished, even in the other arm where no object has been placed. The photon in the other arm can be at a different, non-degenerate, wavelength than the one probing the sample. Consequently, these setups allow to probe an object with photons in the mid infra-red while only detecting photons in the visible or near infra-red where good detectors are readily available.

In the following years, many experiments employed the method of sensing with undetected photons for imaging [13, 15–17]. Furthermore, measurement techniques from the field of ultra-fast spectroscopy, e.g. absorption spectroscopy, Fourier transform infra-red spectroscopy or optical coherence tomography, have been demonstrated [18–22]. However, most of those setups are based on bulk nonlinear crystals.

In order to allow for a large scale industrial fabrication and implementation of these methods in real-world devices, integration is key. Integrated optical sensors have proven to enable cheap, miniaturized, and accessible devices. Furthermore, they allow to bring the latest measurement techniques in spectroscopy to harsh environments [23, 24]. Another compelling argument is that the use of integrated quantum light sources allows for a higher brightness due to the strong confinement over a long interaction length and dispersion engineering of the generated spectra of each photon of the pair by adjusting the waveguide geometry. Therefore, waveguide-based sources are considered ideal candidates for applications in quantum spectroscopy which promises to open new paths for more precise or convenient measurement techniques [6].

In this thesis, we realise the implementation of integrated nonlinear interferometers with guided-wave photon pair source for ultra-fast spectroscopy with undetected photons. By this, we will overcome technical challenges and show how measurements in the mid infra-red can be performed while only detecting photons in the near infra-red. Simultaneously, we will harness the benefits of integrated optical waveguides as bi-photon sources with a high brightness and co-linear emission that can be further integrated into a practical device.

We will divide this thesis in four parts. The first part covers the fundamental concepts that are required for this work. Here, we discuss the basic building blocks of an integrated quantum sensor and present ways to transfer classical spectroscopy methods to the quantum regime. We start by introducing integrated waveguides, the guiding of light within them and dispersive effects on ultrashort pulses, which have special relevance for any ultra-fast spectroscopy technique. We will utilise the long interaction length of the light fields within these waveguides to realise efficient nonlinear optical processes, such as photon pair generation via parametric down-conversion (PDC). Finally, we introduce the concept of nonlinear interferometry based on waveguides as photon pair sources and discuss the specific properties of such interferometers which ultimately enable measurements with undetected photons.

The second part provides insight into the process of dispersion engineering, which is used to generate broadband non-degenerate photon pairs from our nonlinear waveguides. The two sources used in this thesis both operate with one photon around 850 nm while the other one lies either around 1400 nm in the telecommunication range or around 2800 nm in the mid infra-red. In particular, the development and characterisation of the latter source will be described in more detail as it was specifically designed for ultra-broadband spectroscopy with undetected photons in the mid infra-red within the scope of this thesis.

In the third part of the thesis, we present our realisation of a nonlinear interferometer based on an integrated PDC source in the near infra-red. We present different variations of the setup starting from a universal differential pumping scheme, which allows to adjust the pump power of the two processes, and evolve the setup towards pumping from only one direction. Both of these setups are realised in the so-called SU(1,1) geometry, where both photons from the first process are overlapped in the second one. Finally, the setup is altered such that one of the interferometer arms is combined at a linear element; an external beamsplitter. We label this setup the induced coherence scheme. In a first experiment, we present a method to measure the bi-photon correlation time of our source, an important benchmark in the field of ultra-fast spectroscopy. For this, we utilise the dependence of the observed interference from nonlinear interferometer on the spectral phase between the two processes. Furthermore, we study the optimisation of the parametric gain in the light of optimising optical coherence tomography measurements with undetected photons as an application. Here, we compare the SU(1,1) and the induced coherence setup geometry regarding their suitability for the implementation of optical coherence tomography measurements with undetected photons based on a guided-wave photon pair source.

The last part of this thesis is dedicated to realising a nonlinear interferometer using the ultra-broadband PDC source introduced in the second part. Here, we transfer concepts and findings from the interferometer in the near infra-red with the aim to construct a nonlinear interferometer in the mid infra-red. We demonstrate spectral and temporal interference and show measurements for absorption spectroscopy and Fourier transform infra-red spec-

troscopy in the mid infra-red while detecting in the near infra-red.
With that, we provide an understanding of nonlinear interferometers that contain waveguides as active elements and show applications that can be implemented in them. Thereby, we pave the way for future developments in the field of ultra-fast quantum spectroscopy with integrated waveguides and to make such a quantum sensor a real-world device.

2

Fundamentals

In this chapter, we discuss the fundamental principles on which we base our experiments and present the required knowledge for our goal of developing an integrated quantum sensor. We want to achieve this goal by implementing an integrated waveguide in a nonlinear interferometer, where the waveguide generates broadband, highly non-degenerate photon pairs. This will allow us to perform so-called measurements with undetected photons for applications in the field of ultra-fast spectroscopy.

In order to know which building blocks are required to achieve this goal, it is helpful to start by studying standard techniques and methods in classical ultra-fast spectroscopy, which can be translated to quantum spectroscopy with undetected photons.

2.1 Methods in ultra-fast (quantum) spectroscopy

Many of today's standard ultra-fast spectroscopy techniques are based on interferometric measurement schemes with broadband light which are performed, e.g., in a Mach-Zehnder interferometer. This setup is depicted in Fig. 2.1. Here, we show the functional components of the interferometer, which allow us to perform a) spectral interferometry, b) optical coherence tomography (OCT), and c) Fourier transform infra-red (FTIR) spectroscopy. Below the setup, we are comparing these techniques with respect to the sample used, the kind of temporal delay $\Delta\tau$, and the kind of detection. In the case of spectral interferometry, a spectral phase $\Phi(\omega)$ is measured at a fixed delay $\Delta\tau$ while detecting the output of the interferometer frequency-resolved on a spectrometer. OCT investigates layered objects to retrieve the layer separation and reflectivity. Those measurements can be performed with a fixed delay and frequency-resolved detection or by varying the delay and detecting in a time-resolved manner. Lastly, Fourier transform infra-red spectroscopy aims to measure the absorption profile $\alpha(\omega)$ of a sample in both arms by introducing a delay between two parts of the field and recording their time-resolved interference.

Before we can use this conceptual representation to describe the three techniques in detail, we will have to introduce ultra-short electromagnetic pulses.

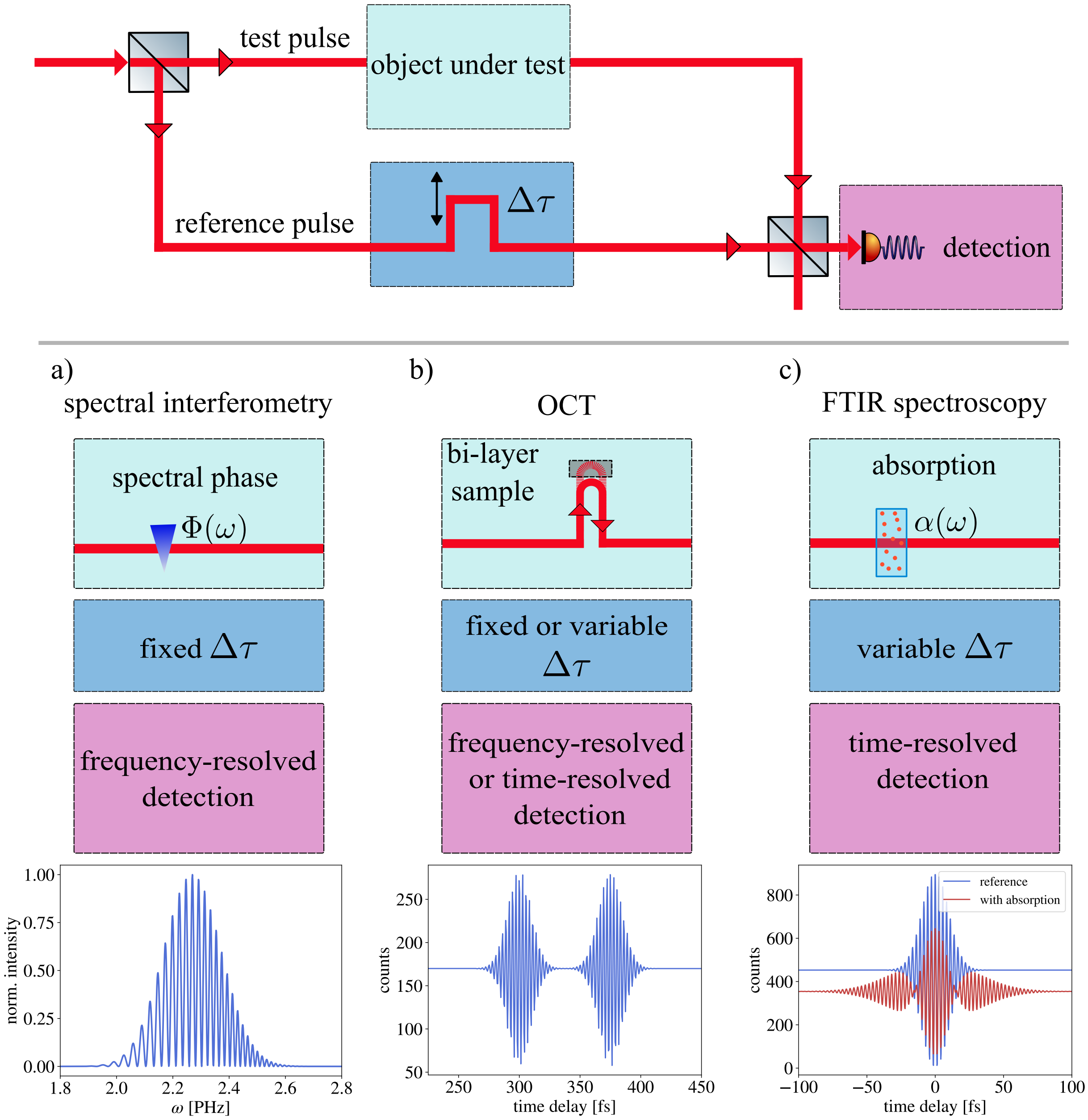

Figure 2.1: The concept of different spectroscopic measurement setups shows the underlying Mach-Zehnder interferometer with different functional elements for the inserted object under test, delay in the reference arm or detection method. The bottom line shows exemplary measurement outcomes for each method. a) In spectral interferometry a reference pulse is interfered with itself to characterise the unknown spectral phase $\Phi(\omega)$. b) Optical coherence tomography studies the separation and reflectivity of a system of partial reflective surfaces. c) The absorption $\alpha(\omega)$ of a sample is measured in Fourier transform infra-red spectroscopy.

Ultra-short electromagnetic pulses

Classical ultra-fast spectroscopy often relies, as one might expect from the name, on ultra-fast light pulses with durations of several hundred femtoseconds. Due to the Fourier relationship between time and frequency, these objects exhibit broad spectra, which enable the aforementioned spectroscopy techniques. In the following, we will formally introduce ultra-fast light pulses because the underlying concepts will later be required to understand quantum spectroscopy. We will utilise pulses to explain the phenomena in the classical ultra-fast spectroscopy setups although some of the presented methods do not strictly require light from a laser but, e.g., can also be realised with thermal light.
Many physical phenomena are described to their fullest by complex-valued functions, e.g., describing the amplitude and phase simultaneously. However, in an experiment, we can often only measure real quantities, such as the real or imaginary part of the quantity at hand. Therefore, we start by writing down the real-valued electric field $E(t)$ of an electromagnetic wave propagating with an amplitude E_0 and a frequency ω at a fixed position in space and without any spatial or polarisation dependence, as here we are merely interested in the description of a pulse in time and frequency. We can write this field as:

$$E(t) = E_0 \cos(\omega t). \tag{2.1}$$

In order to see the connection of this field to the complex representation, we can re-write it and utilise geometric identities to end up at:

$$\begin{aligned} E(t) &= \frac{1}{2}E_0(\cos(\omega t) + i\sin(\omega t) + \cos(\omega t) - i\sin(\omega t)) \\ &= \frac{1}{2}E_0(\cos(\omega t) + i\sin(\omega t) + \cos(-\omega t) + i\sin(\omega t)) \\ &= \frac{1}{2}E_0(e^{i\omega t} + e^{-i\omega t}). \end{aligned} \tag{2.2}$$

If we now assume $\omega > 0$, we can interpret the second term to cover the negative range of frequencies, and we can divide our real field into a positive and negative frequency part:

$$E(t) = E^+(t) + E^-(t) \tag{2.3}$$

with $E^+(t) = (E^-(t))^*$ being the positive and negative frequencies of the electric field. For the description of an ultra-short pulse, we employ the so-called slowly varying amplitude approximation (SVEA). This approximation holds as long as the spectral bandwidth of the pulse σ is much smaller than its central frequency ω_0, i.e., $\sigma \ll \omega_0$, which is the case for the pulses considered in this work where ω_0 is in the range of 1 PHz while the spectral bandwidths of the pulses do not exceed few tens of THz. This allows us to write the positive-frequency part of the electric field of the pulse as [25]:

$$E^+(t) = \frac{1}{2}\mathcal{E}(t)e^{i\omega_0 t} \tag{2.4}$$

where $\mathcal{E}(t)$ is the envelope function that describes the slow change in field amplitude over many optical cycles at the carrier frequency ω_0. This temporal expression can be translated to the spectral domain via Fourier transformation:

$$E^+(\omega) = \int \mathrm{d}t E^+(t) e^{-i\omega t}. \tag{2.5}$$

The resulting envelopes in the temporal and spectral domain, $\mathcal{E}(t)$ and $\mathcal{E}(\omega)$, consequently, are also connected via Fourier transform. Assuming a Gaussian shape for the envelope functions, and for clarity only considering the temporal and not the spatial degrees of freedom, we can write these functions as:

$$\mathcal{E}(t) = \mathcal{E}_0 e^{-\frac{(t-t_0)^2}{\tau^2}} \tag{2.6}$$

$$\mathcal{E}(\omega) = \mathcal{E}_0' e^{-\frac{(\omega-\omega_0)^2}{\sigma^2}} \tag{2.7}$$

with their respective amplitudes $\mathcal{E}_0$ and $\mathcal{E}_0'$ as well as their respective temporal and spectral widths τ and σ.

In many experimental settings, ultra-short pulses are exposed to spectral or temporal phases $\Phi(\omega)$ and $\Psi(t)$. Those can be captured by an additional phase factor of the form $e^{i\phi(\omega)}$ or $e^{i\Psi(t)}$ in the spectral and temporal envelope functions, respectively.

We show the spectral and temporal properties of an ultra-short pulse with a Gaussian spectral envelope in Fig. 2.2. In a), we depict the spectral envelope and flat spectral phase of the pulse, resulting in the smallest pulse width in the temporal domain in Fig. 2.2 b).

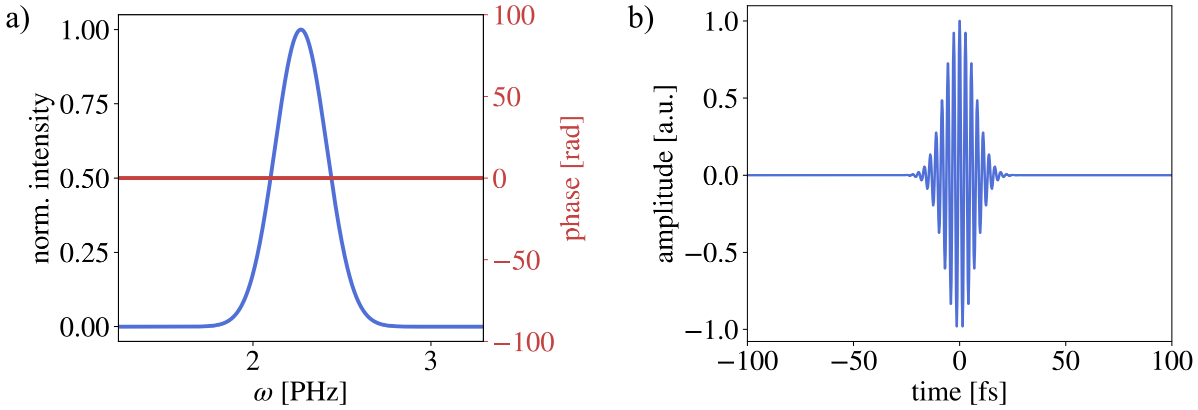

Figure 2.2: a) Normalised spectral intensity $|\mathcal{E}(\omega)|^2$ and phase $\Phi(\omega)$ of an ultra-short pulse. b) Corresponding real-valued electric field amplitude $E(t)$.

The case in which the pulse exhibits a flat spectral phase is referred to as the Fourier-limited case. An important property of ultrashort pulses, namely their time-bandwidth product (TBP), is calculated for this Fourier-limited situation and is given by TBP $= \ln 2 \cdot \sigma \cdot \tau =$

$\pi \cdot 0.441$ for a Gaussian envelope in the spectral and temporal domain with their respective $1/e$ widths σ and τ. However, in the presence of a spectral or temporal phase, this TBP exceeds this minimal bound. We discuss the TBP for different pulse shapes in more detail in App. A.1.

Another important property of ultra-short pulses is their coherence time $\tau_c = \frac{1}{\sigma}$, which describes the time over which a light pulse can interfere with itself. The link between coherence time and spectral bandwidth of the pulse is covered in the Wiener-Khinchin theorem [26]. The correlation time can be very long for a continuous-wave laser with a very small spectral bandwidth σ and rather short for an ultra-short laser pulse. The coherence time can be directly translated into a coherence length $l_c = c \cdot \tau_c$, which then describes a distance over which two copies of the same pulse interfere in space while propagating at the speed of light c. A short coherence time is used in measurement techniques like optical coherence tomography to achieve high temporal and thereby spatial resolution, as we will discuss below. There, a high spatial resolution is achieved for a short coherence length, which is given by

$$l_c = \frac{2\ln(2)}{\pi} \cdot \frac{\lambda_0^2}{\Delta\lambda_{FWHM}} \tag{2.8}$$

with λ_0 being the central wavelength and $\Delta\lambda_{FWHM}$ the spectral bandwidth of the used pulse [26].

With this description of ultra-short pulses in mind, let us look at three examples from the field of ultra-fast spectroscopy with which we can characterise different properties of objects under test.

Spectral interferometry

Spectral interferometry (SI) allows to measure both the spectral amplitude and phase of ultra-short pulses of light in a simple setup. This only requires a spectrometer to perform spectrally resolved measurements at the output and a way to delay a reference pulse with respect to the test pulse [27, 28], as listed in Fig. 2.1 a).

Here, we start with an ultra-short optical pulse at the input of the interferometer. This pulse is split into a test pulse $\mathcal{E}(\omega)$ and a reference pulse $\mathcal{E}_{ref}(\omega)$ at a beamsplitter. The amplitude and phase $\phi_{ref}(\omega)$ of the reference pulse need to be well known, as the method is in general not self-referencing [25]. The test pulse interacts with the object under test that imprints a phase term $e^{i\phi(\omega)}$, which appears as a factor on the spectral envelope in Eq. (2.7). In this example, we chose the phase to be quadratic, resembling a chirp, as it is induced by dispersive elements. Meanwhile, the reference pulse experiences a fixed delay $\Delta\tau$. Due to the shift theorem, going from t to $t + \Delta\tau$ in time leads to a linear phase term $e^{i\omega\tau}$ in the conjugated Fourier variable ω. Finally, the two pulses are superimposed on the second beamsplitter.

At the output of the interferometer, a spectrometer detects a spectral intensity given by

$$\begin{aligned} I(\omega) &= |\mathcal{E}(\omega)e^{i\phi(\omega)} + \mathcal{E}_{ref}(\omega)e^{i(\phi_{ref}(\omega)+\omega\Delta\tau)}|^2 \\ &= |\mathcal{E}(\omega)|^2 + |\mathcal{E}_{ref}(\omega)|^2 + 2\mathcal{E}(\omega)\mathcal{E}_{ref}(\omega)\cos(\phi(\omega) - \phi_{ref}(\omega) - \omega\Delta\tau) \\ &= I + I_{ref} + I_{int}. \end{aligned} \tag{2.9}$$

The first two terms contain only the individual spectral intensities of the test and reference pulse I and I_{ref}. They do not contain phase information. We are therefore interested in the interference term I_{int}. The modulation of the interference contains the phase of our test pulse with respect to the phase of the reference $\phi(\omega) - \phi_{ref}(\omega)$. Meanwhile, the phase $\omega \cdot \Delta\tau$ is the linear phase contribution from a fixed delay. The resulting spectral intensity on the spectrometer is shown in the first plot in Fig. 2.3 where we set $\phi_{ref} = 0$.

The spectral phase profile can now be extracted by applying a Fourier transform to the spectral interferogram. In a first step, the Fourier transform allows to retrieve $\tilde{I}(t)$. This temporal intensity features three peaks located at $-\tau, 0$ and τ, as shown in the central plot of Fig. 2.3. Next, we isolate one of those peaks with a filter $H(t-\tau)$ in the Fourier transform that is centred around the component at delay τ, such that:

$$\tilde{I}_{filtered}(t) = H(t-\tau)\tilde{I}(t). \tag{2.10}$$

We allow the component with delay τ to pass the filter and perform an inverse Fourier transform (IFT) of this filtered spectral component. We obtain a complex function containing the amplitude and phase of the interferometric component $I'(\omega) = \mathrm{IFT}(\tilde{I}_{filtered}(t))$. The argument then contains the phase difference between the reference and test pulse [25]:

$$\phi(\omega) - \phi(\omega)_{ref} - \omega\tau = \arg[\mathrm{IFT}(\tilde{I}_{filtered}(t))]. \tag{2.11}$$

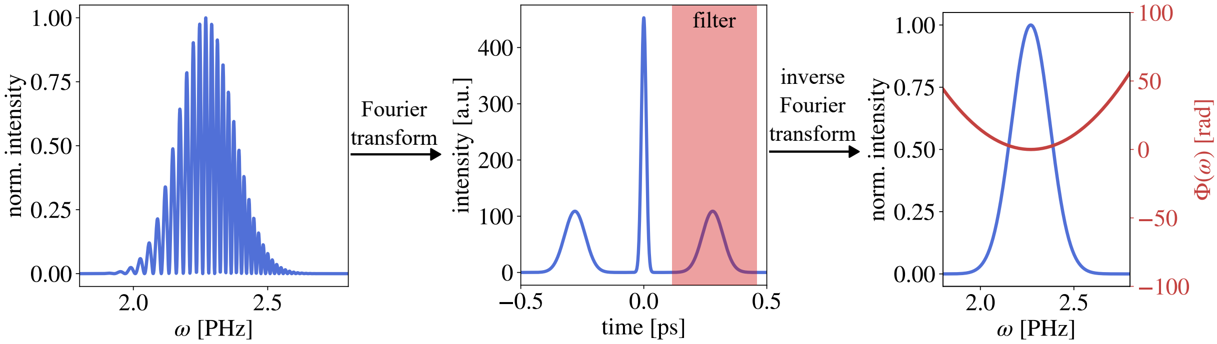

Figure 2.3: The process of phase characterisation via spectral interferometry starts with a spectral interferogram. The Fourier transform contains components at $-\Delta\tau, 0$ and $\Delta\tau$, of which the signal at $\Delta\tau$ is filtered out to be used in the following. Performing an inverse Fourier transform on this filtered signal allows to reconstruct the phase profile of the test pulse.

The phase difference between the reference, which has been introduced by the object under test, can then be extracted by subtracting a global linear phase, thus setting the phase to zero at one point in the pulse shape [27]. Since we assumed to know the phase of our reference pulse, we can now retrieve the phase of the object under test. The reconstructed pulse with its amplitude given by $|I'(\omega)|$ and the retrieved second order phase profile is shown in the right plot of Fig. 2.3.

Spectral interferometry thereby offers a means to characterise the phase of optical pulses. This allows us to extract information about phase changes acquired by the pulse while travelling through any dispersive or absorptive object under test. However, it requires the two pulses to be coherent and the reference pulse to be known, since only the relative phase to the reference pulse can be extracted. Furthermore, the temporal delay must be chosen sufficiently large to separate the Fourier components but at the same time small enough for the spectral fringes to be correctly sampled by the spectrometer.[1]

Due to the link between the spectral and temporal domain, ultra-short pulses are often given in their chronocyclic representation, which leads to a 2D representation of a pulse where one axis contains information about the pulses' properties in frequency and the other about the ones in time. This representation also facilitates the illustration of spectral phases and is used in more advanced phase retrieval methods. However, these phase retrieval methods go beyond the scope of this chapter; details can be found in the comprehensive review by Walmsley and Dorrer [25], which also covers pulse characterisation methods based on nonlinear interactions.

Optical coherence tomography

Optical coherence tomography (OCT) is a technique for measuring the distance and reflectivity of the layers within a multilayered object under test. In the experiment, light with a short coherence length l_c, for example, an ultra-short pulse, is used inside a Michelson interferometer as depicted in Fig. 2.1 b) and split into a reference and a probe pulse. As fractions of the probe light are reflected off multiple layers in the sample, the reference is delayed by a movable mirror, such that the delay $\Delta\tau$ between the probe and the reference can be adjusted.

Each fraction of the field, which is reflected off a single layer $\mathcal{E}_z$ leads to interference with the reference field $\mathcal{E}_{ref}$ at the detector, as we have seen previously. This spectral interference is integrated over the spectral bandwidth of the pulse $\Delta\omega$, when measuring a time-resolved interferogram with varying the delay $\Delta\tau$. This configuration is called time domain (TD) OCT [26]. The measured intensity can be calculated as:

$$\begin{aligned} I(\Delta\tau) &= \int_{\Delta\omega} \mathrm{d}\omega |\mathcal{E}_z + \mathcal{E}_{ref} e^{i\omega\Delta\tau}|^2 \\ &= \int_{\Delta\omega} \mathrm{d}\omega |\mathcal{E}_z|^2 + |\mathcal{E}_{ref}|^2 + 2\mathcal{E}_z\mathcal{E}_{ref}\mathfrak{R}(e^{i\omega\Delta\tau} + e^{-i\omega\Delta\tau}) \\ &= I_0[r_z + 1 + r_z e^{\frac{\Delta\tau}{\Delta\omega}} \cos(\omega_0\Delta\tau)]. \end{aligned} \tag{2.12}$$

---

[1] We note that the presented concept can analogously be applied in the spectral domain, which leads to a technique called 'spectral-shearing'. There, instead of a shift in time, a shift in frequency is applied between the two pulses and detection occurs in the temporal domain [25].

In the last step, we assumed that the integrated spectral intensity in both arms of the interferometer is I_0 such that a fraction of $r_z I_0$ is reflected by the sample. We therefore find the first two terms to only add a constant offset to the signal. Furthermore, we performed the integration and utilised the Wiener-Khinchin theorem [26] to find a coherence function $\tilde{\gamma} = e^{\frac{\Delta\tau}{\Delta\omega}}$ from the spectral envelope of the test and reference pulse. This function, which determines the width of the interference pattern in the time domain, is modulated with a carrier frequency ω_0. More details on this derivation and the connections between the involved properties can be found in [29].

Let us now assume a simple bi-layer system with layer reflectivities r_1, r_2 and an optical path difference (OPD) between the layers of ΔL and their positions z_1, z_2 with respect to the reference arm. We can re-write equation (2.12) to be expressed in space and only consider the part that contains interference to find [30]:

$$\begin{aligned} I(z) \propto I_0[&\gamma(z - z_1) r_1 \cos(2\omega_0(z - z_1)/c) \\ &+ \gamma(z - z_2) r_2 \cos(2\omega_0(z - z_2)/c)]. \end{aligned} \tag{2.13}$$

Again, the axial resolution is given by the coherence function, which we now express in terms of z to be

$$\gamma(z) = \exp\left(-\ln 2 \frac{2z}{l_c}\right). \tag{2.14}$$

This function drops to zero quickly as its argument increases and is strongly dependent on the coherence length l_c, which we introduced when discussing ultra-short pulses.

From the separation and visibility of the interference regions, the layer separation and reflectivity can be extracted. We depict the obtained signal on the left of figure 2.4

A more commonly used method is Fourier domain (FD) OCT. Here, the photo diode is replaced by a spectrometer and the reference arm remains fixed at position z [31] and can be directly described by Eq. (2.12) by not performing the integration in ω. This allows for the recording of interferograms that exhibit a beating between different frequencies. This beating is caused by the reflections from multiple layers in the sample and their different relative delays to the reference. The signal at the detector, which contains the interference, is given by:

$$\begin{aligned} I(\omega) \propto \tilde{I}_0(\omega)[&r_1 \cos(2\omega(z - z_1)/c) \\ &+ r_2 \cos(2\omega(z - z_2)/c) \\ &+ r_1 r_2 \cos(2\omega \Delta L/c)] \end{aligned} \tag{2.15}$$

with the source's spectral intensity $\tilde{I}_0(\omega)$. The layer separation can then be retrieved via Fourier-transform, which yields an amplitude in the temporal domain [30]. We can translate it to the spatial domain [2] and end up with an intensity profile that shows similar features as in the TD-OCT case:

---

[2] Here, we do not consider any dispersive material between the layers. In real-world applications, the frequency-dependent refractive index of the material between the layers changes the description.

$$\begin{aligned} I(z) \propto\, & r_1[\gamma(z-z_1)+\gamma(-z+z_1)] \\ & + r_2[\gamma(z-z_2)+\gamma(-z+z_2)] \\ & + r_1 r_2[\gamma(\Delta L)+\gamma(-\Delta L)]. \end{aligned} \tag{2.16}$$

This expression again shows an axial resolution that is governed by the coherence function $\gamma(z)$. Note that from this result, it is not possible to tell whether the optical path difference between the sample and reference arm is positive or negative. Furthermore, the last term shows self-interference terms at position ΔL that may hinder the unambiguous identification of layer separations. However, the $\Delta L/c$ is typically smaller than the delay between the arm $\Delta\tau$ difference and is therefore situated close to zero. Also, the peak height scales with $r_1 r_2$ and is therefore less than the actual reflections from the layers. The described procedure of retrieving the layer separation in our bi-layer system in FD-OCT is shown on the right side of Fig. 2.4, where we only plot the positive side of the resulting signal in the time domain.

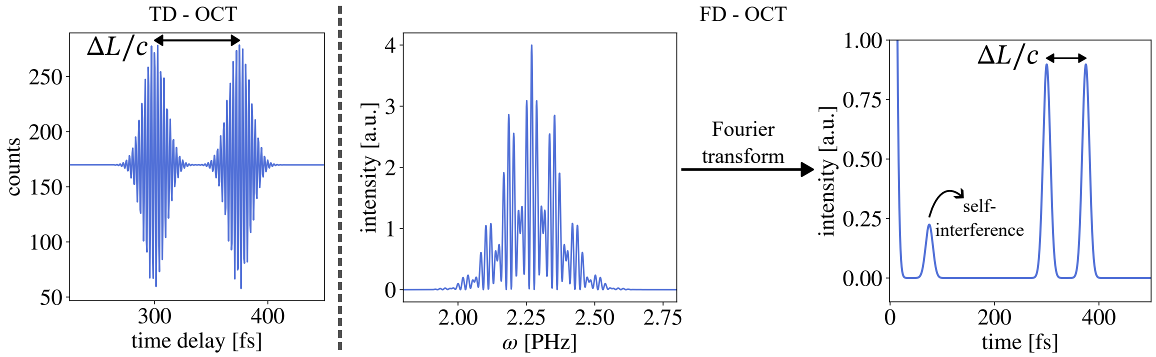

Figure 2.4: TD-OCT allows to extract the layer separation $\Delta L/c$ of a bi-layer system directly from the measured interferogram. In FD-OCT, a beating can be observed in the spectral interferogram. The Fourier transform of this spectral interferogram contains peaks that are separated by the layer separation, but also show self-interference terms.

Fourier-transform infra-red spectroscopy

Fourier-transform spectroscopy allows to measure the spectral intensity of a light field without the need for a spectrometer. Therefore, Fourier-transform infra-red spectroscopy is particularly popular, as spectrometers are sparse in the infra-red spectral region [27].
In FTIR, the interferogram is formed by superimposing the oscillations caused by all frequency components contained in the spectral intensity $I_0(\omega)$ of the involved field. Thus, the intensity at a photo diode for different temporal delays $\Delta\tau$ is given as [32]:

$$I(\Delta\tau) = \int \mathrm{d}\omega I_0(\omega)\cos(\omega\Delta\tau). \tag{2.17}$$

Thus, we see that the measured interferogram in the time domain $I(\Delta\tau)$ and the spectral intensity $I_0(\omega)$ are connected via Fourier transform [32]:

$$I_0(\omega) = \int \mathrm{d}\Delta\tau \, I(\Delta\tau) e^{i2\pi\omega\Delta\tau}. \tag{2.18}$$

The procedure of retrieval of the spectral distribution for an original pulse and a pulse with an absorption feature is depicted in Fig. 2.5, where we compare the measured interferogram from only the reference and with an absorber in the system. We note that in this description, we assume the absorptive sample to be placed in the common path of the interferometer for FTIR spectroscopy. In an alternative setup, called dispersive Fourier-transform spectroscopy [33], the sample is placed in one of the interferometer arms. This alters the equations above slightly but allows to retrieve the transmission spectrum as well as the dispersive properties in a single measurement.

In either configuration, the absorption feature can be identified in the spectrum after Fourier transform of the measured interferogram. To this end, the spectral transmission $T(\omega)$ is recovered by division of the spectrum with absorption $I_0(\omega)_{abs}$ by the reference spectrum $I_0(\omega)_{ref}$:

$$T(\omega) = \frac{I_0(\omega)_{abs}}{I_0(\omega)_{ref}}. \tag{2.19}$$

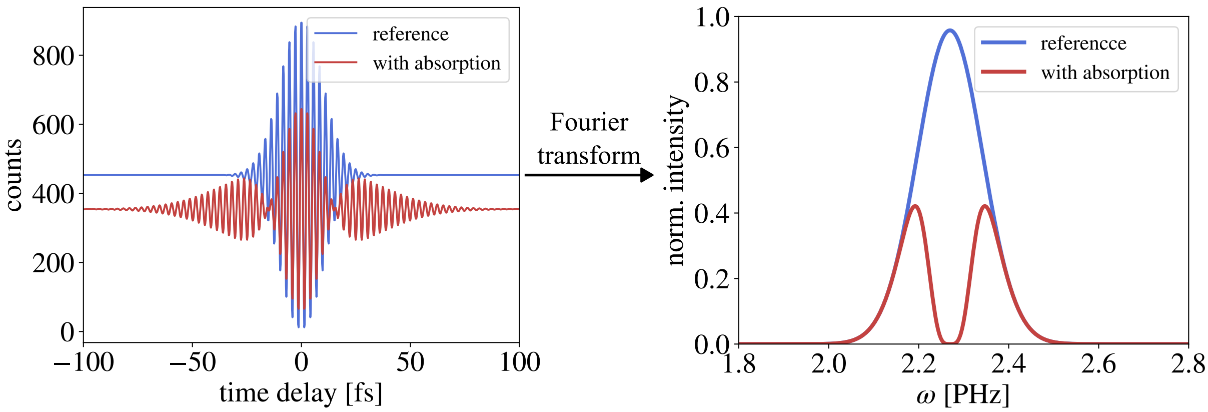

Figure 2.5: The process of pulse characterisation in FTIR is shown for the case of a reference measurement and with absorption in the system. The absorption leads to a change in the recorded temporal interferogram and can be identified in the spectrum after Fourier transform.

Throughout the measurements, a sufficiently small time step $\delta\tau$ which is smaller than the optical period $t_{opt} = 2\pi/\omega_0$ must be chosen in order to avoid aliasing effects. Moreover, since the spectral resolution in the Fourier transform is given by the number of sampled points N, this must be chosen according to the application in mind [28, 32]. FTIR offers advantages over spectroscopy techniques which are based on dispersive elements, namely that the signal-to-noise ratio is improved as all spectral components are recorded at the same time (Fellgett advantage) and as no input slit needs to be used, as opposed to grating spectrometers, and therefore more light can be collected (Jacquinot advantage) [32]. This makes the FTIR suitable for applications at low light levels or wavelength regimes where grating spectrometers are sparse.

Sensing with ’undetected’ photons

The presented measurement techniques from classical ultra-fast spectroscopy can be translated to the quantum regime by using nonlinear interferometers based on single photon sources [12, 34]. In these systems, the beamsplitters in the interferometric setups are replaced by active optical elements that generate single photons, e.g., photon pairs via parametric down-conversion (PDC). The corresponding schematic setup is depicted in Fig. 2.6 where we once again denote the functional blocks required for the measurements, which are now performed at two different colours for probing and detection in the so-called SU(1,1) configuration of a nonlinear interferometer.

As we will discuss in detail in section 2.6, nonlinear interferometers allow to observe interference in the number of generated photons after two cascaded bi-photon sources that each generate signal and idler photons with a certain probability amplitude. The interference occurs if the sources are aligned such that it cannot be distinguished whether a detected photon has been generated in the first or the second source. This leads to an interference in the probability amplitude of generating a photon pair, in contrast to classical interferometers, where the interference occurs in the field amplitudes. Here, we are depicting the SU(1,1) geometry where signal and idler from the PDC source 1 overlap in PDC source 2.
One advantage of nonlinear interferometers is that they allow generating and utilising single photons directly inside the interferometer and, therefore, have been used to perform measurements at low light levels and with increased phase sensitivity in comparison to the use of classical light [35]. More importantly, the generation of bi-photons at different wavelengths, e.g. the near-IR and mid-IR, allows to perform measurements commonly referred to as measurements with undetected photons. In those measurements, a coherent transfer of information occurs between both photons during the second nonlinear process. As a consequence, the information about a sample in one of the interferometer arms is imprinted on the interference patterns at both wavelengths at the output of the interferometer, as we will derive in section 2.6. This allows the photon at a long wavelength to interact with a sample and only detect the photon at the shorter wavelength, which might be in a technically more accessible spectral region. The foundation of this measurement scheme is the strong correlations in frequency and time between the photons generated at the short and long wavelengths. We will discuss the properties of such photon pair sources in detail in section 2.5.
Below, we present some of today’s realisations of methods in classical ultra-fast spectroscopy, utilising the method of measurements with undetected photons:

- **Spectral phase measurements** - Similar to the technique of SI, the spectral phase on a bi-photon can be measured within a nonlinear interferometer. In an experimental

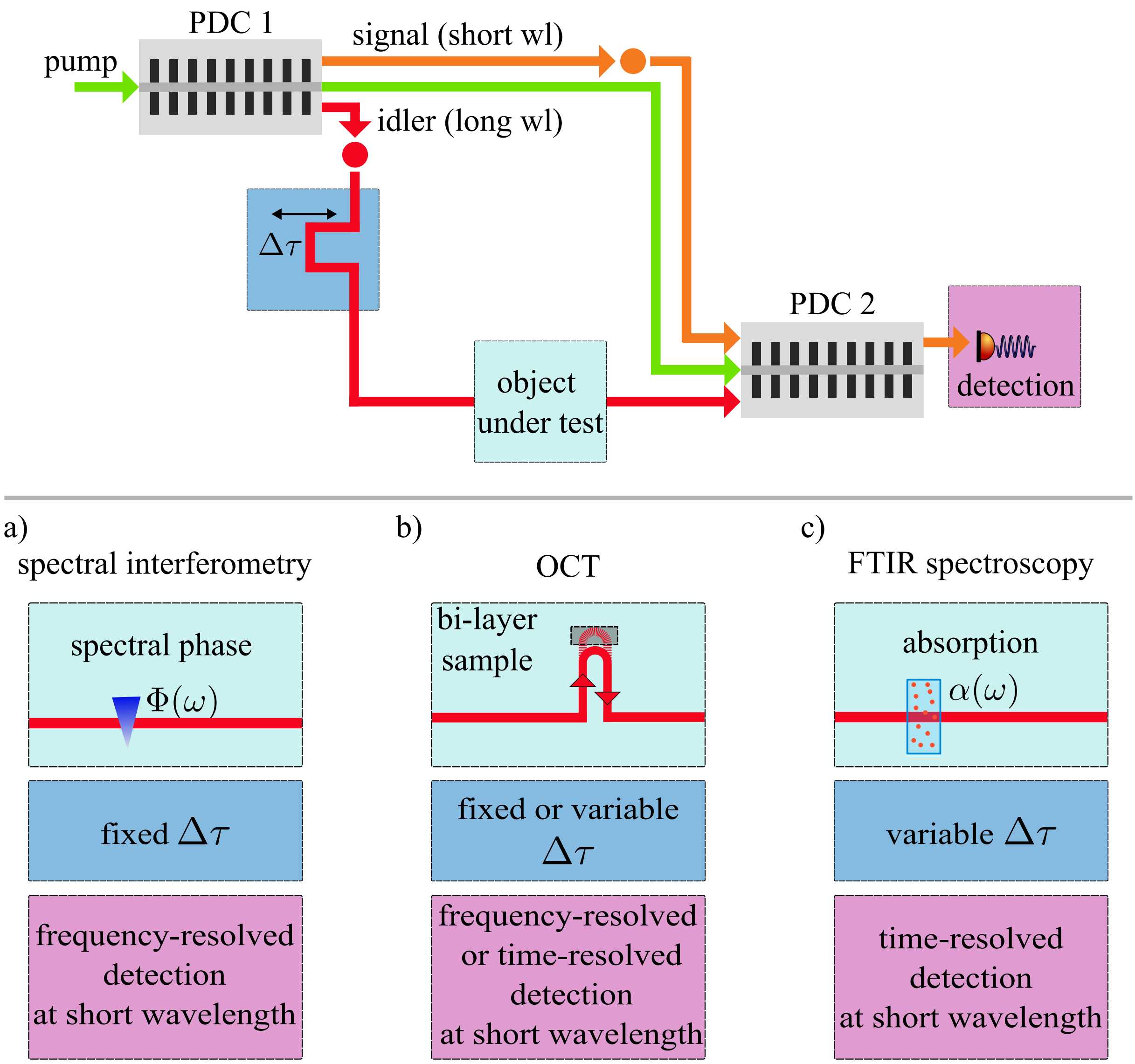

Figure 2.6: Applications of a nonlinear interferometer for measurements with undetected photons: a) Measurement of the spectral phase $\Phi(\omega)$. b) Optical coherence tomography to determine the separation and reflectivity of an object with partially reflective layers. c) Fourier transform spectroscopy or direct absorption spectroscopy to determine the absorption $\alpha(\omega)$ of the sample at the long wavelength. In all three methods, the samples are probed with the idler at a long wavelength while detection happens on the signal field at a short wavelength.

setup, a phase element is placed in the arm with the longer idler wavelength, while the spectral interferogram is observed in the signal output at a shorter wavelength with a spectrometer. The phase information of the object is imprinted on the bi-photon state from the first source and thus can be extracted from the interference of the probability amplitudes after the second process by measuring only the signal photons in a frequency-resolved detection [36]. A fixed relative delay between the two processes can be introduced either in the pump field or between the two photons of the biphoton from the first process as depicted in Fig. 2.6 and allows to shift the period of the spectral interferogram as in classical SI. This spectral interferogram can then be evaluated analogously to classical SI and yields the phase difference of the probability amplitudes from the first and second process. We will discuss the influence of phases in nonlinear interferometers in detail in section 2.6.2.

- **OCT** - In OCT with undetected photons the layered sample is placed in the idler arm while the FD-OCT or TD-OCT measurements are performed at the output of the signal wavelength. FD-OCT and TD-OCT measurements are realised with a fixed or variable delay $\Delta\tau$ between the signal and idler paths, respectively, and by performing either a frequency-resolved or time-resolved detection. In TD-OCT, an interference signal in the count rates of the detected signal photons can be observed if the path lengths of the signal arm is matched with the one of the idler photons that are reflected off the layers in the sample. Frequency-resolved detection allows to record a FD-OCT where the different frequencies in the spectral interference at the signal wavelength are given by path difference between the signal arm and the surfaces of the sample in the idler arm. Thus, information about this sample can be extracted in the same way as in the classical case. This allows to obtain information of layer thicknesses and reflectivities of a sample in the mid-IR while only detecting in the near-IR [21, 37]. Similar to the classical OCT, the axial resolution is now given by the marginal spectral width of one photon which defines the coherence length. Notably, in contrast to classical OCT, no self-interference can be observed in FD-OCT with nonlinear interferometers [22, 38]. This is due to the different interference process which does only lead to interference for delays between signal and idler photons from the first pass, but not for signal-signal delays which cause self-interference effects.

- **Absorption spectroscopy** - Absorption spectroscopy with undetected photons can be performed by placing the object under test in the long wavelength arm while detecting at the short wavelength. In order to observe absorption features directly, the visibility in the spectral interference pattern, a value similar to the contrast, can be evaluated after detection of the signal photons on a grating spectrometer. The visibility at each wavelength is directly proportional to the transmission of the object under test at this wavelength. Thus, the spectral transmission profile can retrieved [20]. The observed changes in visibility at the short wavelength are then translated to the absorption at the long wavelength due to strong frequency correlations.
  In a second approach, a temporal interferogram is recorded by scanning the delay $\Delta\tau$ between the signal and idler arm. This allows to perform an analysis similar to the one in Fourier transform spectroscopy on the measured signal counts at the short wavelength. We can thereby retrieve the underlying spectrum at the longer wavelength that, after dividing it by a reference, reveals the spectral transmission profile [19, 39]. In this measurement, information about absorption features at the long wavelength are contained in the temporal interferograms that are recorded at the signal wavelength without the need for frequency-resolving detectors.

Overall, we observe that the functional building blocks for measurements with undetected photons are almost identical to the classical applications of ultra-fast spectroscopy. However, there are some important differences. For one, multiple colours are now involved in the experimental setup. Furthermore, as the name suggests, detection happens at a different wavelength as the probing. Finally, a temporal delay between the two arms of the interferometer is most often introduced in the same arm as the sample for technical reasons. We will discuss the physics and properties of this measurement scheme in further detail in section 2.6.

Most of today's implementations of nonlinear interferometers for measurements with undetected photons rely on bulk crystals as bi-photon sources, which hinders integration and miniaturisation. Therefore, we want to construct a quantum sensor based on nonlinear waveguides. The presented overview shows that an integrated quantum sensor based on a nonlinear interferometer for measurements with undetected photons in the mid infra-red requires several conceptual building blocks.

Building blocks of an integrated quantum sensor

We want to base our quantum sensor on integrated waveguides. Therefore, we will start discussing the guiding of light in waveguides, as they provide a high confinement and allow for integration of the system. As we want to operate on spectrally broadband light, we are, furthermore, discussing the effects of the waveguide material dispersion on ultra-short pulses over a long interaction length.

Our waveguides should also operate as sources for broadband, non-degenerate photon pairs that will then be used inside the nonlinear interferometer. We are therefore introducing the concepts of nonlinear optics and discuss how to achieve phasematching in our structures. In order to generate the required strongly frequency-correlated quantum states, we employ the process of parametric down-conversion to generate correlated pairs of photons with a broad spectral distribution.

However, achieving the conditions of simultaneously bright and broadband photon pair generation is inherently challenging in integrated nonlinear waveguides due to normal dispersion. Therefore, the development of an integrated, dispersion engineered bi-photon source is crucial. We will present the design and characteristics of such sources in chapter 3.

We combine all this knowledge to theoretically describe the processes inside the nonlinear interferometer, consisting of two cascaded waveguide PDC sources. In this context, we are also discussing the influence of spectral phases and losses in such a setup.

Finally, this foundation will enable us to construct an integrated quantum sensor based on measurements with undetected photons. This will allow us to transfer concepts from the field of classical ultra-fast spectroscopy and measurements to be performed in this integrated quantum sensor.

2.2 Waveguides

Waveguide structures are widely used to guide light without significant losses and with a strong confinement. The latter allows for the concentration of high optical power densities over a long interaction length.
For gaining an intuitive understanding, let us start with a ray optics description of a waveguide. For this purpose, we start with a 1D planar waveguide structure that is depicted in Fig. 2.7 a). It consists of three layers that we refer to as cladding, film, and substrate with refractive indices n_c, n_f and n_s, respectively. These refractive indices are chosen such that $n_f > n_s \geq n_c$ as shown in Fig. 2.7 b).

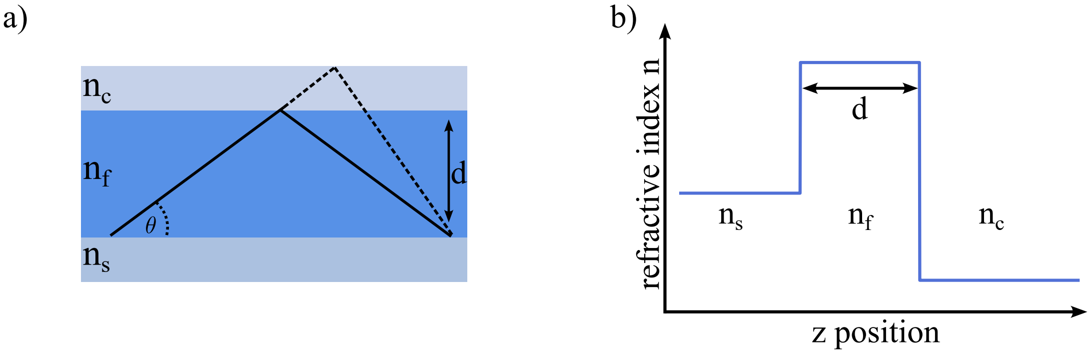

Figure 2.7: a) Illustration of a dielectric planar waveguide with layers of refractive indices n_c, n_f and n_s and thickness d. The dashed triangle can be used to derive the self-consistency condition for the input angle Θ as the phase of the wave needs to be equal modulo 2π upon reflection and free propagation. b) The refractive index profile of the depicted waveguide with $n_f > n_s \geq n_c$.

Depending on these refractive indices, total internal reflection inside the film occurs at incidence angles Θ that are smaller than the critical angles $\Theta_{c,s}$, which are dependent upon n_c and n_s [26]:

$$\Theta_{c,s} = \pi - \arcsin\left(\frac{n_{c,s}}{n_f}\right). \tag{2.20}$$

Inside this film, the guided wave travels at a phase velocity $c_f = c_0/n_f$ with a wave vector that can be split into a component along and orthogonal to the propagation direction. After being reflected by the cladding and substrate, the light field needs to constructively interfere with itself. Thus, it has to fulfill the so-called self-consistency condition

$$2k_0 n_f\, d \sin(\Theta) - 2\phi_r = 2\pi m, \tag{2.21}$$

where $m = 0, 1, 2, ...$ is a positive integer and ϕ_r is a phase shift acquired during reflection. Thus, the acquired phase during propagation with total internal reflections needs to be equal to the propagation of light that is not reflected and travels straight, modulo 2π. This condition leads to the formation of modes with specific reflection angles and their according propagation constants $\beta_m = n_f k_0 \cos(\Theta_m)$ [26]. This propagation constant describes the propagation speed of a specific mode in the waveguide and allows to calculate an effective refractive index $n_{eff} = \frac{\beta_m}{k_0}$ for each mode. Furthermore, it can be found that, depending on the width of the waveguide structure d either no, one, or multiple modes are supported at a given wavelength. This becomes especially interesting in the process of designing waveguides for nonlinear processes that involve multiple wavelengths.After discussing this intuitive, simpler model, we will now turn towards a more rigorous description of the guiding process in a waveguide.

The evolution of an electromagnetic field in a dielectric medium without a source term, which we will add to these equations later during the nonlinear optics section, can be described by Maxwell's equations. We can write them as [40]

$$\begin{aligned} &\nabla \times \vec{H} = \epsilon_0 n^2 \frac{\partial \vec{E}}{\partial t} \\ \text{and} \qquad &\nabla \times \vec{E} = -\mu_0 \frac{\partial \vec{H}}{\partial t}, \end{aligned} \tag{2.22}$$

where the electric field E and the magnetic field H are considered in a lossless medium with a scalar dielectric constant $\epsilon = \epsilon_0 n^2$, including the two-dimensional refractive index profile $n(x, y)$ of the waveguide and the scalar magnetic permeability μ_0. We can now define a guided mode with mode number ν and the corresponding propagation constant β_ν in the waveguide as a solution of Maxwell's equations of the form [40]:

$$\begin{aligned} \vec{E}(t, x, y, z) &= \vec{E}_\nu(x, y) \exp(i\omega t - i\beta_\nu z) \\ \vec{H}(t, x, y, z) &= \vec{H}_\nu(x, y) \exp(i\omega t - i\beta_\nu z). \end{aligned} \tag{2.23}$$

Furthermore, we consider electromagnetic waves with fixed angular frequency ω. Consequently, we can write Maxwell's equations as

$$\begin{aligned} \nabla \times \vec{H} &= i\omega\epsilon_0 n^2 \vec{E} \\ \nabla \times \vec{E} &= -i\omega\mu_0 \vec{H}. \end{aligned} \tag{2.24}$$

In many experiments, the light interacting in our waveguides has a defined polarisation. We therefore write the spatial components of the electric and magnetic fields as

$$\begin{aligned} \vec{E}(x, y, z) &= (E_x, E_y, E_z) \\ \vec{H}(x, y, z) &= (H_x, H_y, H_z). \end{aligned} \tag{2.25}$$

Next, we consider a propagation in z direction such that $E_z = 0$. Thus, we finally arrive at the wave equation in a scalar form for TE and TM polarisation, respectively:

$$\nabla^2 E_{x,y}(x,y) + (k_0^2 n(x,y)^2 - \beta^2) E_{x,y}(x,y) = 0. \tag{2.26}$$

Thus, we can solve Eq. (2.26) for different propagation constants β_ν for the respective modes ν. We can see that the refractive index profile $n(x,y)$ of the waveguide defines the number of guided modes and their propagation constants. In addition to the guided modes, possible solutions of the wave equation are the so-called substrate and radiation modes which lead to losses to the substrate and cladding layer, respectively, as the expression $k_0^2 n(x,y)^2 - \beta^2$ becomes negative.

As the refractive index changes depending on the waveguide geometry, we will receive different propagation constants β_ν and spatial modes. Thus, we need to tailor the refractive index and its derivatives for a broad range of frequencies to realise a specific waveguide geometry that fits the need of our experiment.

However, due to the capabilities of our fabrication, we are limiting ourselves to the use of weakly guiding channel waveguides based on $LiNbO_3$. The waveguides are formed by titanium strips being patterned on the surface and subsequently in-diffused to create the required refractive index profile. To model these waveguides, we are using a finite element method (FEM) to find solutions to Maxwell's equations for the waveguide geometry. In FEM, the partial differential equation is evaluated on a discretized grid made of geometrically simple sub-domains [41] and is thereby applicable to arbitrarily complex geometries. We have applied this technique for the modelling of our waveguide structures. We used a program called 'Focus2', which has been developed by Dr. Benjamin Brecht and Dr. Matteo Santandrea in our group. This program is frequently used to calculate effective refractive indices in the design process of a waveguide source. In this work, we used this program to extend the existing database by the newly designed waveguide geometries and implemented fine temperature steps to model the parametric down-conversion processes in them.

The numerical simulations allow to evaluate waveguide geometries with different widths and heights of the titanium strips, as well as to include fabrication parameters such as diffusion time and temperature, which result in the final, asymmetric index profile. The asymmetry in the index profile is due to the titanium in-diffusion on the surface of the $LiNbO_3$, leading to a refractive index jump at the interface between the waveguide structure and the air. More details on the fabrication and their limitation of our waveguides can be found in [42, 43].

In order to understand the dispersive properties we are looking for in our waveguides, we will next discuss the impact of dispersion on ultrashort pulses in a medium.

2.3 Dispersive effects on ultrashort pulses in waveguides

An ultrashort pulse, as it is used in many applications of ultra-fast spectroscopy, experiences various dispersive effects when propagating through a material. For waveguides, we need to consider material dispersion as well as modal dispersion, which are summarised in the frequency dependent propagation constant $\beta(\omega)$.

During the propagation through a waveguide of length L, the pulse will experience a spectral phase $\phi(\omega) = \beta(\omega)L$. As the refractive index of a material changes for different frequencies ω, different spectral components of the pulse acquire different phases. In order to describe these effects, we perform a Taylor expansion of the propagation constant β around the central frequency ω_0:

$$\beta(\omega) \approx \beta(\omega_0) + \underbrace{\left.\frac{\partial\beta}{\partial\omega}\right|_{\omega_0}(\omega-\omega_0)}_{GD} + \underbrace{\frac{1}{2}\left.\frac{\partial^2\beta}{\partial\omega^2}\right|_{\omega_0}(\omega-\omega_0)^2}_{GDD} + \underbrace{\frac{1}{6}\left.\frac{\partial^3\beta}{\partial\omega^3}\right|_{\omega_0}(\omega-\omega_0)^3}_{TOD} \tag{2.27}$$

where we can relate the derivatives of β with respect to ω to the group delay (GD), group velocity delay (GVD) and third order dispersion (TOD). More specifically, the group velocity of a pulse inside a waveguide is given by $v_g = 1/\beta'$ and the group velocity dispersion parameter $D = 2\pi\beta''$, which is commonly given as a material property in bulk systems [26]. In addition to material dispersion, we also need to consider the modal dispersion of our waveguide structures [44]. This contribution is included in the effective refractive index that we retrieve from the previously described numerical simulations and alters the effective refractive index and especially higher order dispersion depending on the waveguide parameters. This modal dispersion ultimately allows for dispersion-engineering by adjusting the waveguide geometry.

We show the effects of the different orders in the Taylor expansion, that is, no, linear, quadratic, and cubic spectral phases, on the shape of an ultra-short pulse in Fig. 2.8. We specifically introduce spectral phases as opposed to temporal ones, as they are imprinted either naturally by material dispersion or can be addressed conveniently in an experimental setup via pulse-shaping with setups based on dispersive optical elements such as gratings or prism [27].

We observe a temporal shift of the pulse for a linear spectral phase. A quadratic phase leads to a change in the instantaneous frequency and a broadening of the pulse. The formation of smaller pulses trailing the main pulse is observed in the temporal domain for a spectral phase of third order.

Let us have a closer look at the effect of second order dispersion on pulses with different temporal duration, as we will discuss this property later when measuring the bi-photon correlation time. For a pulse with a Gaussian envelope, the final duration τ of a transform-limited pulse τ_0 after propagation through a dispersive medium with length z and group velocity dispersion parameter D is given by

$$\tau(z) = \tau_0\sqrt{1 + (z/z_0)^2}, \tag{2.28}$$

with $z_0 = \frac{\pi\tau_0^2}{D}$ [26]. This effect of temporal broadening due to second order dispersion is illustrated in Fig. 2.9 for three pulses of different transform-limited durations. It can be observed that initially shorter pulses experience a stronger relative broadening compared to initially longer pulses, which is due to the difference in the spectral bandwidth that make up these pulses.

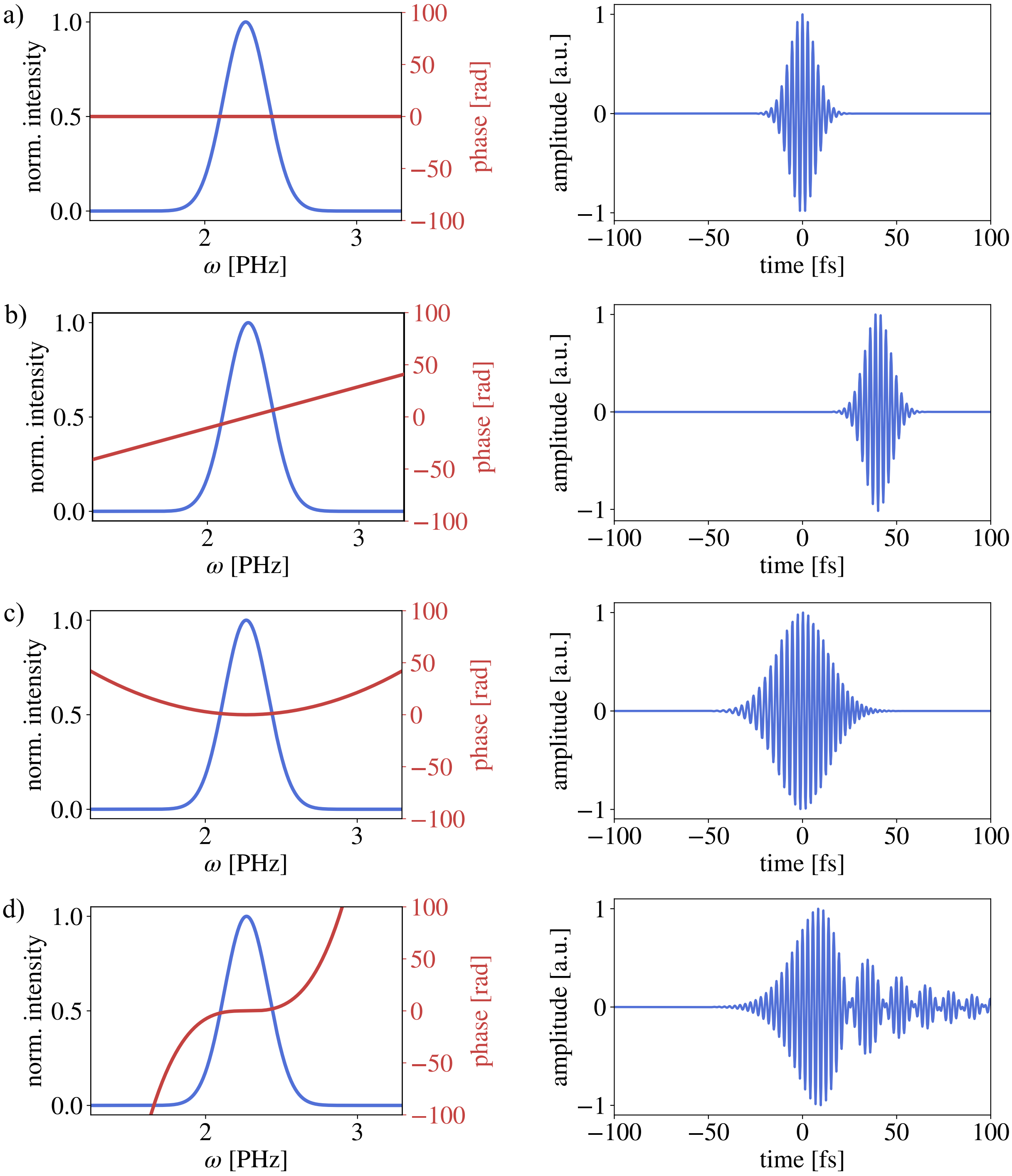

Figure 2.8: Spectral intensity and phase together with the corresponding temporal pulse shape for a) no, b) linear, c) quadratic and d) cubic spectral phases applied to an ultra-short pulse at a central wavelength of around 830 nm.

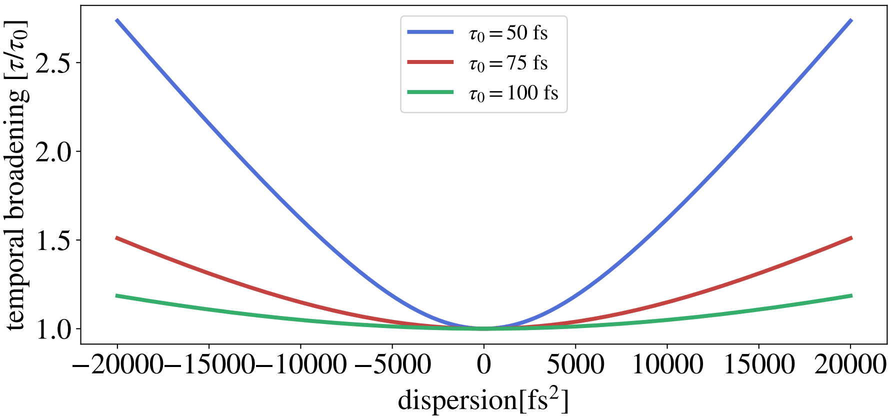

Figure 2.9: The effect of second order dispersion on the temporal duration τ of pulses with transform-limited durations of $\tau_0 = 50\,\mathrm{fs}$, $75\,\mathrm{fs}$ and $100\,\mathrm{fs}$.

2.4 Nonlinear optics

Many modern measurement techniques require to convert light from one wavelength to another. Such a conversion can be performed in the framework of nonlinear optics. A thorough description of the fundamentals can be found in [26, 45], on which we base the following discussion.

The interaction of light with a dielectric medium leads to a polarisation of the atoms because of the applied electric field.[3] As the electric field of an electromagnetic wave oscillates, so do the induced dipole moments. As the charges in the polarised atoms are accelerated in this oscillation, they emit electromagnetic radiation themselves. This radiation leads to a light field that interferes with the original one and, for low intensities, leads to effects such as dispersion and is represented by the refractive index of a material. In the low-intensity case, the polarisation density $P_{linear}(t) = \epsilon_0 \chi^{(1)} E(t)$ depends linearly on the electric field strength, while ϵ_0 is the permittivity of vacuum and $\chi^{(1)}$ is the linear susceptibility. In the case of higher applied electric field strength, this linear relation no longer holds and we need to add a nonlinear component to our polarisation density $P(t) = P_{linear}(t) + P_{NL}$. The nonlinear contribution is responsible for nonlinear effects such as frequency conversion. Formally, we expand $P(t)$ in a power series of $E(t)$ as

$$\vec{P}(t) \approx \epsilon_0[\chi^{(1)}\vec{E}(t) + \chi^{(2)}\vec{E}^2(t) + \chi^{(3)}\vec{E}^3(t)], \tag{2.29}$$

where we truncated the expansion after the third-order term. This truncation is reasonable since the second and third order susceptibilities for $\mathrm{LiNbO_3}$ as the material of choice in this work amount to [46]:

$$\chi^{(2)} \approx 3 \cdot 10^{-11}\,\mathrm{mV^{-1}}$$

---

[3] We will refer to this polarisation of atoms in a medium as polarisation density in the follow to avoid confusion with the polarisation that defines the direction of oscillation of an electromagnetic wave in space.

$$\chi^{(3)} \approx 2 \cdot 10^{-21}\,\mathrm{m^2V^{-2}}.$$

These orders of magnitude for these susceptibilities reduce further for higher orders of the susceptibility, since they are given by the linear susceptibility of the medium, which is then divided by the atomic electric field strength, which is of the order of $E_{at} = 5 \cdot 10^{11} V/m$. Therefore, the observable effects from higher order contributions are negligible for the field strengths that are typically realised in an experimental setup with a table-top laser system. Here, we only consider nonlinear effects of second order and write the nonlinear polarisation density with the second order nonlinear susceptibility $\chi^{(2)}$ as

$$\vec{P}_{NL}(t) = \epsilon_0 \chi^{(2)} \vec{E}(t)^2. \tag{2.30}$$

If we now consider an incident electric field $\vec{E}(t) = \vec{E}_1 e^{-i\omega_1 t} + \vec{E}_2 e^{-i\omega_2 t} + c.c.$ that has two frequency components ω_1 and ω_2, we find that the nonlinear polarisation density results in

$$\begin{aligned}\vec{P}_{NL}(t) = \epsilon_0 \chi^{(2)} [&\underbrace{\vec{E}_1^2 e^{-i2\omega_1 t} + \vec{E}_2^2 e^{-i2\omega_2 t}}_{SHG} \\ &+ \underbrace{2\vec{E}_1\vec{E}_2 e^{-i(\omega_1+\omega_2)t}}_{SFG} \\ &+ \underbrace{2\vec{E}_1\vec{E}_2 e^{-i(\omega_1-\omega_2)t}}_{DFG} + c.c] \\ &+ \underbrace{2\epsilon_0 \chi^{(2)} [\vec{E}_1\vec{E}_1^* + \vec{E}_2\vec{E}_2^*]}_{OR}.\end{aligned} \tag{2.31}$$

We can identify different second-order nonlinear processes in each line:

1. Second-harmonic generation (SHG) is a process in which light at double the frequency of one of the input frequency is generated.
2. Sum-frequency generation (SFG) is a process in which a light field with the sum of the input frequencies is generated.
3. Difference-frequency generation (DFG) induces a polarisation density at a frequency that is the difference between the two inputs.
4. Optical rectification (OR) is a process that leads to a static electric field in the medium.

They are also referred to as three wave mixing processes because they involve three frequency components. For now, we only considered the scalar equations. However, the involved fields and the resulting polarisation density can occur in all 3 different spatial polarisation degrees of freedom of the input field. In order to properly describe the material response to input fields of different polarisation, $\chi^{(2)}$ is generally a tensor of rank 3. However, we can reduce this to a matrix of dimension 3 x 6 using contracted notation and noting that there are only ten independent components when applying Kleinman's symmetry [45]. This then leads to the following expression:

$$\begin{pmatrix} P_x(\omega_3) \\ P_y(\omega_3) \\ P_z(\omega_3) \end{pmatrix} = \epsilon_0 \underbrace{\begin{pmatrix} d_{11} & d_{12} & d_{13} & d_{14} & d_{15} & d_{16} \\ d_{11} & d_{12} & d_{13} & d_{14} & d_{15} & d_{16} \\ d_{11} & d_{12} & d_{13} & d_{14} & d_{15} & d_{16} \end{pmatrix}}_{=\chi^{(2)}/2} \cdot \begin{pmatrix} E_x(\omega_1)E_x(\omega_2) \\ E_y(\omega_1)E_y(\omega_2) \\ E_z(\omega_1)E_z(\omega_2) \\ E_y(\omega_1)E_z(\omega_2) + E_z(\omega_1)E_y(\omega_2) \\ E_x(\omega_1)E_z(\omega_2) + E_z(\omega_1)E_x(\omega_2) \\ E_x(\omega_1)E_y(\omega_2) + E_y(\omega_1)E_x(\omega_2) \end{pmatrix}. \tag{2.32}$$

We can thereby classify nonlinear processes in three categories:

- Type 0 - All fields have the same polarisation.
- Type I - Both input fields have the same polarisation.
- Type II - Both input fields have orthogonal polarisation.

Due to the crystal structure of a specific material, not all entries in the matrix are present, and therefore only some processes are possible. For example, in the platform of $LiNbO_3$, the matrix containing the nonlinear coefficients takes the form [46]:

$$d_{LiNbO_3} = \begin{pmatrix} 0 & 0 & 0 & 0 & d_{15} & -2d_{22} \\ -d_{22} & d_{22} & 0 & d_{15} & 0 & 0 \\ d_{31} & d_{31} & d_{33} & 0 & 0 & 0 \end{pmatrix}. \tag{2.33}$$

Phasematching

Instead of inducing only a polarisation density at the desired frequency in a nonlinear material, we wish to generate a macroscopic output field. To this end, we require the contributions to the field across the material to be successfully added up in a constructive way, i.e. they need to add up with the correct phase. To find the condition for this coherent build-up, we will look at the exemplary process of difference-frequency generation.
Here, we now start from the three involved continuous-wave (cw) monochromatic fields at frequencies ω_p that propagate inside a waveguide along propagation direction z:

$$E_p(z,t) = E_p(z)e^{i(\beta_p z - \omega_p t)}, \tag{2.34}$$

where β_p is the propagation constant and $E_p(z)$ the field amplitude. If we now plug those fields into Eq. (2.30) we can write the nonlinear polarisation density for a DFG process as:

$$P_2 = \epsilon_0 d E_3 E_1 e^{i[(\beta_3 - \beta_1)z - (\omega_3 - \omega_1)t]}. \tag{2.35}$$

In this equation, d is the non-linear coefficient of the realised process where a strong field at frequency ω_3 interacts with a field at lower frequency ω_1 to generate the DFG field at $\omega_2 = \omega_3 - \omega_1$. We refer to the three fields as pump at ω_3, signal at ω_2 and idler at ω_1.

We can now substitute the electric field and polarisation into the wave equation [26]:

$$\nabla^2 E_2 - \frac{1}{c^2}\frac{\partial^2 E_2}{\partial t^2} = -\frac{1}{c^2}\frac{\partial^2 P_2}{\partial t^2}. \tag{2.36}$$

This equation is very similar to the one in equation (2.26). However, there, we already knew the form of the electric field and linear material response from the polarisation and included them on the left side of the equation. In this equation, we are explicitly stating the source term in the form of the non-linear polarisation on the right side of the equation.

By inserting equations (2.34) and (2.35) into equation (2.36), we arrive at the coupled mode equation for the generated field amplitude E_2

$$\frac{\mathrm{d}E_2(z)}{\mathrm{d}z} = \frac{8\pi i \omega_2 d E_3(z)}{n(\omega_2)c} E_1^*(z) e^{i\Delta\beta z}, \tag{2.37}$$

which contains the mismatch in the propagation constants $\Delta\beta = \beta_3 - \beta_1 - \beta_2$. The solution of this equation can be found together with the coupled wave equations for the other amplitudes, which can be derived analogously. There, the factor $\exp(-i\omega_2 t)$ cancels due to energy conservation, which we imposed before. This allows us to eliminate the fast oscillations and instead observe the change in the field amplitude $E_2(z)$ during the nonlinear process.

Under the assumption that the pump and idler field are constant and after integrating over an interaction region of the waveguide with length L, we arrive at the intensity for the DFG field from equation (2.37) to be

$$I_2(L) = L^2 |\gamma|^2 |E_1^*(0)|^2 \mathrm{sinc}^2\left(\frac{\Delta\beta}{2}L\right) \tag{2.38}$$

with $|\gamma|^2$ containing all constants. This intensity is plotted in Fig. 2.10 in units of $\Delta\beta L/2$.

From this equation, we can observe that the output intensity is increased by a longer interaction region L or a stronger input field intensity $E_1(0)$. Furthermore, the strongest signal output can be observed for $\Delta\beta = 0$. For values unequal to zero, a build-up happens over the so-called coherence length $L_{coh} = 2/\Delta\beta$. Due to material dispersion in common nonlinear media, phasematching cannot be obtained for arbitrary combinations of frequencies. One way to overcome this challenge is to use the material's birefringence to achieve phasematching. However, this also only grants phasematching for a specific set of wavelengths, especially when only considering co-linear phasematching processes in guided-wave systems. In contrast to co-linear phasematching, the vectorial character of $\Delta\beta$ can be used in bulk systems to fulfill phasematching by emitting the generated field into different angles in space [47]. This is not possible in guided-wave systems as a result of the confinement of

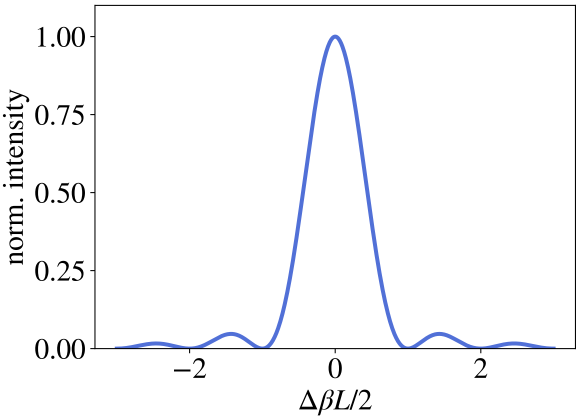

Figure 2.10: The normalised output intensity of a DFG process as a function of the phase-mismatch $\Delta\beta L/2$.

the fields.

To allow for flexible wavelength combinations, the method of quasi-phasematching (QPM) is used. In this method, an additional phase grating in the form of e^{-iGz} with $G = \Delta\beta$ is required. This can be achieved by periodic poling [48], which leads to a modulation of the nonlinear coefficient $d(z)$ in such a way that it can be expressed in a Fourier series as [26]:

$$d(z) = \sum_{m=-\infty}^{\infty} d_m e^{-i2\pi mz/\Lambda} \tag{2.39}$$

with the poling period Λ. This results in the condition that $\Delta\beta = m2\pi/\Lambda$, where m is the order of the phasematching that is often chosen to be 1 for the highest efficiency. With this applied periodic poling, the phasematching condition becomes $\Delta\beta \rightarrow \Delta\beta \pm \frac{2\pi}{\Lambda}$. We note here that imperfect fabrication may lead to a non-ideal ratio between the inverted domains with respect to the not inverted ones. This ratio is called the duty-cycle. However, as long as the periodicity of the poling is kept, this only reduces the efficiency of the process and does not shift the phase-matched wavelengths [49].

The periodic inversion of the crystal domains along an in-diffused waveguide is depicted in Fig. 2.11 a) together with the effect that the additional propagation constant from the periodic has on the phasematching condition. With periodic poling, we can thus fulfill phasematching $\Delta\beta = \beta_p - \beta_s - \beta_i - \frac{2\pi}{\Lambda} = 0$ for more combinations of signal and idler wavelengths.

In Fig. 2.11 b), we compare the output intensities of a process with birefringent phasematching, quasi-phasematching, and no phasematching for different interaction lengths L in units of the coherence length of the process L_{coh}. In the case of birefringent phasematching, a quadratic increase can be observed, while an oscillation of the output intensity just above zero can be witnessed in the case of no phasematching. For QPM, the crystal domains are inverted after one coherence length, which leads to a quadratic increase in the output intensity as well. However, the gradient and, thereby, the efficiency, is reduced by a factor of $(2/\pi)^2$ [45].

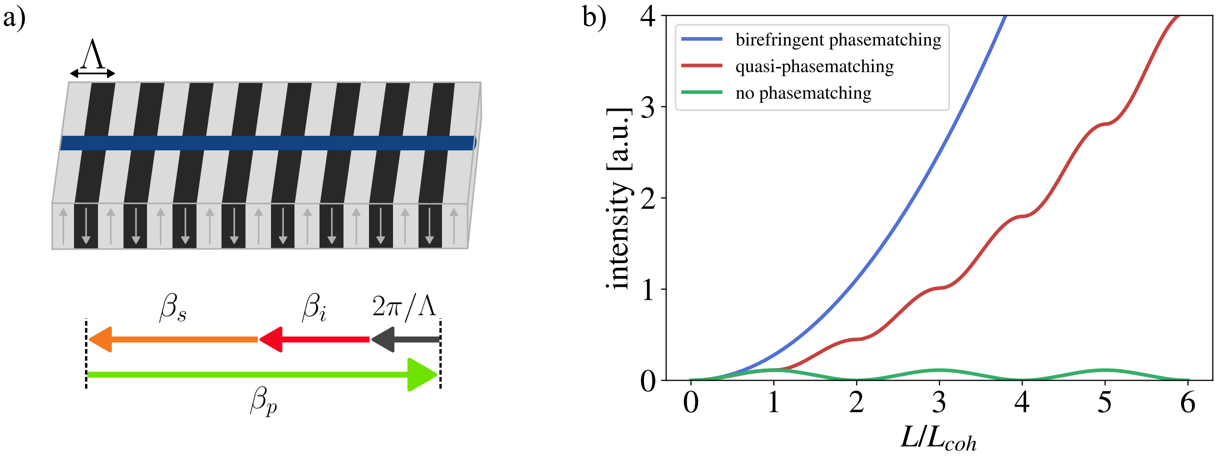

Figure 2.11: a) Periodic inversion of the crystal domains, visualized by opposing arrows, along an in-diffused waveguide is used to realise quasi-phasematching with a period Λ. The additional propagation constant $2\pi/\Lambda$ from the periodic poling allows to achieve phasematching at wavelengths of signal and idler that would normally not be phase-matched. Graphically, this is represented by the length of the arrows symbolizing β for signal, idler and QPM that now match the one of the pump. b) The output intensity for birefringent phasematching, quasi-phasematching and no phasematching is given for varying sample length L with respect to the coherence length L_{coh} of the process.

2.5 Parametric down-conversion

For quantum optics applications, single photons or photon pairs are essential. Here, we are choosing the process of parametric down-conversion to create photon pairs. We can think of this process as the inverse of sum-frequency generation in classical nonlinear optics. The principle is depicted in Fig. 2.12: A photon from a pump field spontaneously decays into two photons within a $\chi^{(2)}$ nonlinear medium, which is given by our periodically poled waveguide. The two generated photons are, for historical reasons, called signal and idler and can be non-degenerate in wavelength. In the following, we will refer to the photon with the shorter wavelength as the signal photon, while the idler will have the longer wavelength.

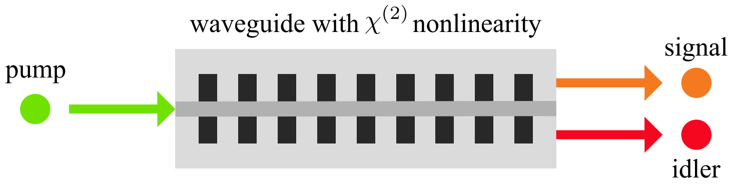

Figure 2.12: The process of PDC consists of a pump photon that spontaneously decays into a signal and idler photon within a waveguide with a $\chi^{(2)}$ nonlinearity.

To formally describe this process, we note that we can study the process of parametric down-conversion in the interaction picture with the evolution of the state vector in the low gain regime given by [50]

$$|\Psi(t)\rangle = \underbrace{\exp\left(\frac{1}{i\hbar}\int_{t_0}^{t} \mathrm{d}t' \hat{H}_{PDC}(t')\right)}_{=\hat{U}} |\Psi_0\rangle \tag{2.40}$$

where we assume $|\Psi_0\rangle$ to be the vacuum state $|0\rangle$ while $\hat{U}$ denotes the unitary operator in the interaction picture.
For the derivation of this unitary $\hat{U}$, we start with the quantisation of the electric field E that we have used in the previous section on nonlinear optical processes in order to describe the Hamiltonian of the PDC process. Using the correspondence principle, the quantised electric field $\hat{E}$ can be decomposed into its positive and negative frequency parts $\hat{E}^+(z,t) = (\hat{E}^-(z,t))^\dagger$ as we did in the description of ultra-short electromagnetic pulses in section 2.1:

$$\hat{E}(z,t) = \hat{E}^+(z,t) + \hat{E}^-(z,t). \tag{2.41}$$

In this equation, the electric field operator in one single polarisation and spatial mode is defined as [51]

$$\hat{E}^-(z,t) = C \int \mathrm{d}\omega \exp(-i[\beta(\omega)z + \omega t])\hat{a}^\dagger(\omega) \tag{2.42}$$

with the single mode ladder operator $\hat{a}(\omega)$ which fulfills $\hat{a}^\dagger(\omega)\hat{a}(\omega) = 1$ and C as an overall constant. Since the PDC process depends on the $\chi^{(2)}$ nonlinearity, it is very inefficient and a large number of pump photons are required to generate one photon pair. Therefore, we assume the pump to be a strong classical field and write it as

$$E_p^+(z,t) = \int \mathrm{d}\omega_p \alpha(\omega_p) \exp(i[\beta(\omega_p)z - \omega_p t]) \tag{2.43}$$

where $\alpha(\omega_p)$ is the pump function that is given by the spectral envelope of the laser in the experiment. With these ingredients, we can now construct the interaction Hamiltonian under the non-depleted pump approximation, which takes the form [50]

$$\hat{H}_{PDC}(t) = \int_{-L/2}^{L/2} \mathrm{d}z \chi^{(2)} E_p^+(z,t) \hat{E}_s^-(z,t) \hat{E}_i^-(z,t) + h.c. \tag{2.44}$$

Here, p, s, i denote the pump, signal, and idler fields while $\chi^{(2)}$ denotes the non-linearity of the medium and L its length. In this work, we assume the low-gain regime, where time ordering of the electric fields can be neglected. Time ordering effects arise from the fact that the electric field operators in the Hamiltonian do not commute in time [52]. However, for low gains, these effects are negligible and we can directly perform the integral over t' in Eq. (2.40) from $-\infty$ to ∞ which yields a Delta-function $2\pi\delta(\omega_s + \omega_i - \omega_p)$. This allows us to also evaluate the integral over ω_p. Plugging in the expressions for the electric fields, we can write the unitary operation in $\hat{U}$ in Eq. (2.40) as

$$\hat{U} = \exp\left[\frac{1}{i\hbar}\left(C' \int_{-L/2}^{L/2} \mathrm{d}z \int \mathrm{d}\omega_s \int \mathrm{d}\omega_i \alpha(\omega_s + \omega_i) \exp(i\Delta\beta z) \hat{a}_s^\dagger(\omega_s) \hat{a}_i^\dagger(\omega_i) + h.c.\right)\right] \tag{2.45}$$

with the overall constant C' and the phase-mismatch $\Delta\beta$ while $\hat{a}_s^\dagger(\omega_s)$ and $\hat{a}_i^\dagger(\omega_i)$ are the ladder operators for the signal and idler in their respective polarisation. Integration over the length yields the phasematching function $\Phi(\omega_s, \omega_i) = \mathrm{sinc}\left(\frac{\Delta\beta L}{2}\right)$ and leaves us with:

$$\hat{U} = \exp\left[\frac{1}{i\hbar}\left(C \int \mathrm{d}\omega_s \int \mathrm{d}\omega_i \alpha(\omega_s + \omega_i) \Phi(\omega_s, \omega_i) \hat{a}_s^\dagger(\omega_s) \hat{a}_i^\dagger(\omega_i) + h.c.\right)\right]. \tag{2.46}$$

As a final step, we can write the PDC state in the single-pair regime, where we restrict ourselves to the generation of no more than one photon per mode $\hat{a}(\omega)$ and therefore expand the exponential until the first order as [53]:

$$|\Psi\rangle \approx |0\rangle + B' \int\int \mathrm{d}\omega_s \mathrm{d}\omega_i f(\omega_s, \omega_i) \hat{a}_s^\dagger(\omega_s) \hat{a}_i^\dagger(\omega_i) |0\rangle. \tag{2.47}$$

We can see that the generated PDC state is described by the joint spectral amplitude (JSA) $f(\omega_s, \omega_i) = \Phi(\omega_s, \omega_i) \cdot \alpha(\omega_s + \omega_i)$. One part of the JSA is the phasematching function $\Phi = \kappa \cdot \mathrm{sinc}[\Delta\beta(\omega_s, \omega_i)\frac{L}{2}]$ with constant factors summarised in κ. The second part is the pump function $\alpha(\omega_s + \omega_i)$, which is defined by the used pump laser. Thus, parametric down-conversion needs to obey momentum (phasematching) and energy (pump) conservation as the other non-linear processes described above.
Although the JSA describes the two-dimensional population of the modes, we can calculate the number of photons per mode using the photon number operator $\hat{n}(\omega) = \hat{a}(\omega)^\dagger \hat{a}(\omega)$. For parametric down-conversion, the mean photon number is linked to the so-called parametric gain g, which we have so far included in the constant factor B' in equation (2.47), via [54]

$$\langle n \rangle = \sinh^2 g \approx g^2 \tag{2.48}$$

where the approximation is made for the case of low gain $g \ll 1$. This can be further linked to the experimental quantity of pump laser power P via $g \propto \sqrt{P}$ and will be further investigated when we are looking into losses and differential gains in nonlinear interferometers below.

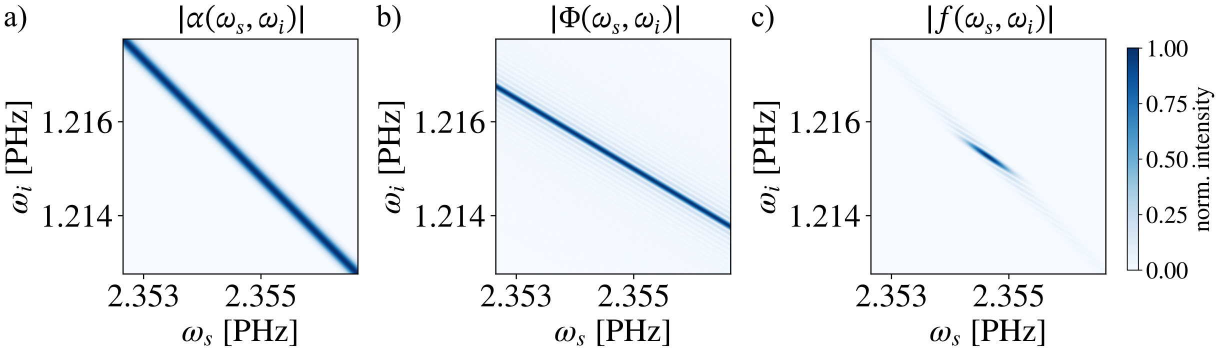

Figure 2.13: Formation of the JSA out of the a) pump function given by energy conservation and b) phase matching given by the material dispersion. Their overlap results in c) the JSA.

The decomposition of the JSA into a phasematching function and a pump function is depicted in Fig. 2.13. The shape of the phasematching function is determined by the dispersion, leading to a frequency-dependent mismatch in the propagation constant $\Delta\beta(\omega_s, \omega_i)$. Here, we choose a non-degenerate type II nonlinear process in a 40 mm long $LiNbO_3$ waveguide. The signal wavelength is centred at 800 nm and the idler at 1550 nm, which corresponds to the central frequencies of 2.355 PHz and 1.215 PHz, respectively. For illustration purposes, we use a pump field with 0.175 THz bandwidth. Due to the different angles of the pump function and phasematching, the resulting JSA only covers a narrow spectral region. We can tailor the shape of the phasematching function in order to achieve an overlap with the pump function over a larger range, and thereby achieve a more broadband JSA. We will see later that, e.g., the angle of the phasematching function is given by the group velocities of the signal and idler photons. The chosen JSA exhibits an anti-correlation between the generated signal and idler frequencies in the JSA. As a consequence, if the frequency of one photon from this JSA is detected, we can infer the corresponding frequency of the other photon. The same holds true for the case of a correlated JTA, from which we gain information about the arrival time of the second photon from the pair after detecting the first one. Therefore, although the frequency or time of a single photon of the pair covers a broad range, a joint measurement reveals a tight correlation. We refer to this property as energy-time entanglement.

The joint spectral intensity (JSI) $|f(\omega_s, \omega_i)|^2$ or its marginal distributions as a projection on the potentially non-degenerate signal and idler frequency axis can be measured rather easily. Measurements of the JSA and the contained phase information become much more difficult, such that the phase information from the JSA is typically lost.

Often, we are interested not only in the frequency domain but also in the temporal domain, in which we describe our photons in the so-called joint temporal amplitude (JTA) $\tilde{f}(\tau_s, \tau_i)$. The JTA can be obtained via a two-dimensional Fourier transform of the JSA. The ladder operators in the spectral domain in Eq. (2.47) transform via $\tilde{a}(t) = \int d\omega \hat{a}(\omega) e^{-i\omega t}$ such that $|\tau_s, \tau_i\rangle = \tilde{a}_s^\dagger(\tau_s)\tilde{a}_i^\dagger(\tau_i)|vac\rangle$. This leads to the PDC state in the temporal domain as:

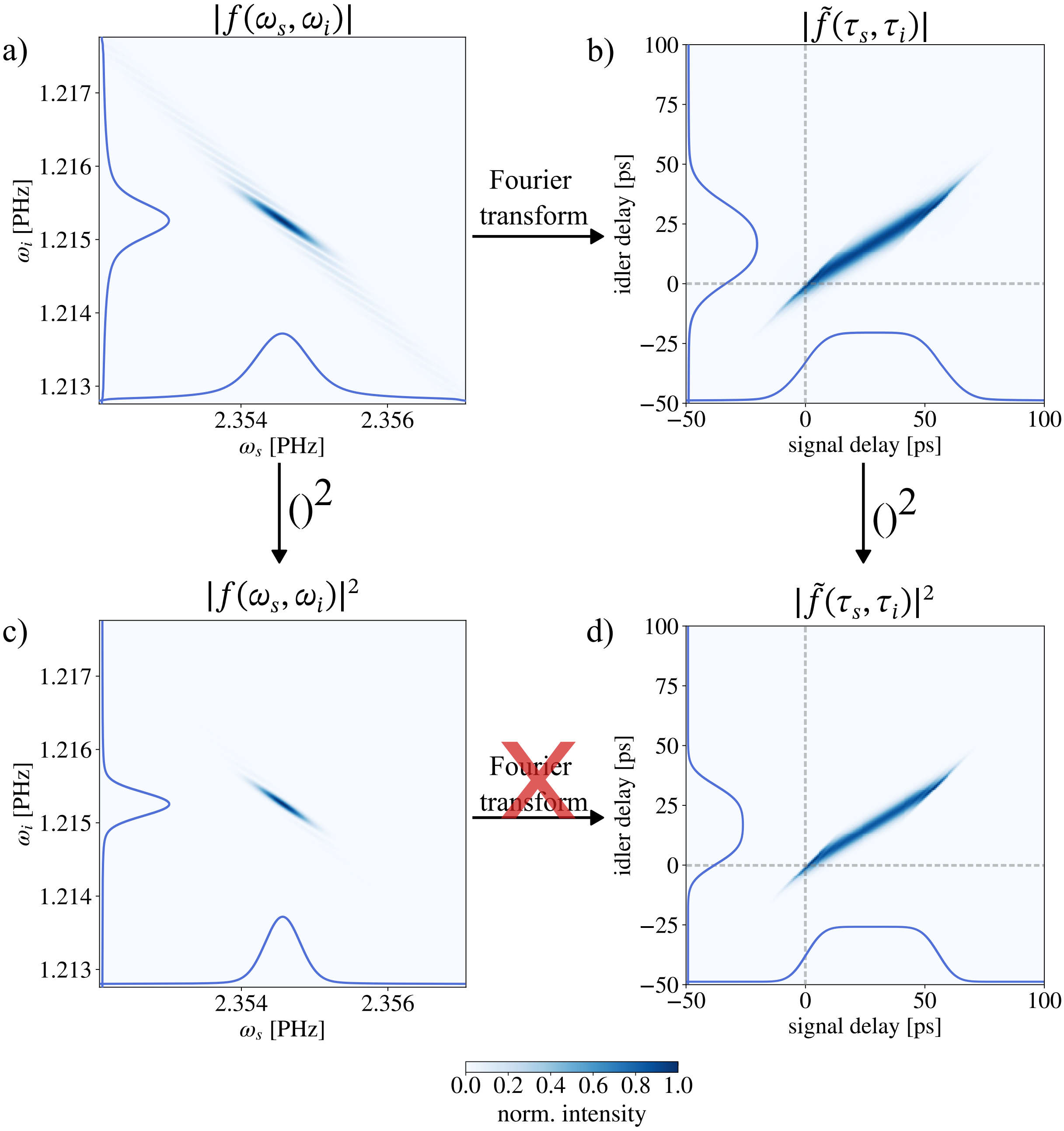

Figure 2.14: a) The JSA is obtained via the overlap of pump and phasematching function. b) Its Fourier transform yields the JTA. Their respective intensity squares result in c) the JSI and d) the JTI. The latter two are accessible in an experiment but not connected via Fourier-transform.

$$|\Psi\rangle = \int \mathrm{d}\tau_s \mathrm{d}\tau_i \tilde{f}(\tau_s,\tau_i)|\tau_s,\tau_i\rangle. \tag{2.49}$$

The JTI $|\tilde{f}(\tau_s,\tau_i)|^2$ is depicted as the modulus square of the Fourier transform of the JSA in Fig. 2.14. Due to the Fourier relation between the JSA and the JTA, a narrow frequency anti-correlation in the JSA leads to a large span of the JTA/JTI. Meanwhile, a large span of the JSA leads to a narrow temporal correlation of the JTA/JTI. In Fig. 2.13 b) and d), we can observe a shift of the JTA/JTI with respect to the point of zero time delay due to a spectral phase in the JSA. We highlight this behaviour by marking the point of zero time delay in Fig. 2.13 b) and d) with grey dotted lines and observe an asymmetry of the distribution to this point.

Experimentally, only the joint temporal intensity $|\tilde{f}(\tau_s,\tau_i)|^2$ can be accessed. However, such measurements are often limited by the detector's temporal resolution or jitter and fail to resolve ultra-short time scales associated with broadband PDC states [55]. Although the JTA is connected to the JSA via Fourier transform, this does not hold true for the intensities due to the lack of phase information.

The bi-photon correlation time is an important property that can be found as the uncertainty in the arrival time of one photon of the pair after the other one has been detected. In the JTI, it is given by the width of a cut through the distribution along one of the axes. Due to its importance, we will present a method to measure the correlation time for a broadband non-generate bi-photon state utilising a nonlinear interferometer in section 4.

In the beginning, we discussed spectroscopy methods based on classical light with broad spectral bandwidths. However, we would like to transfer these concepts to the single-photon regime and make use of the concept of measurements with undetected photons. To this end, we treat broadband PDC light in a way similar to classical pulses. This is possible because dispersive effects act on the quantised electric field $\hat{E}^{-}(z,t) = C\int \mathrm{d}\omega \exp(-i[\beta(\omega)z + \omega t])\hat{a}^{\dagger}(\omega)$ the same way as they do on classical electric fields. As the quantised electric field is given by the integral over the whole frequency range of signal and idler and therefore all spectral $\hat{a}(\omega)$ of the PDC process are affected by phase effects [50].

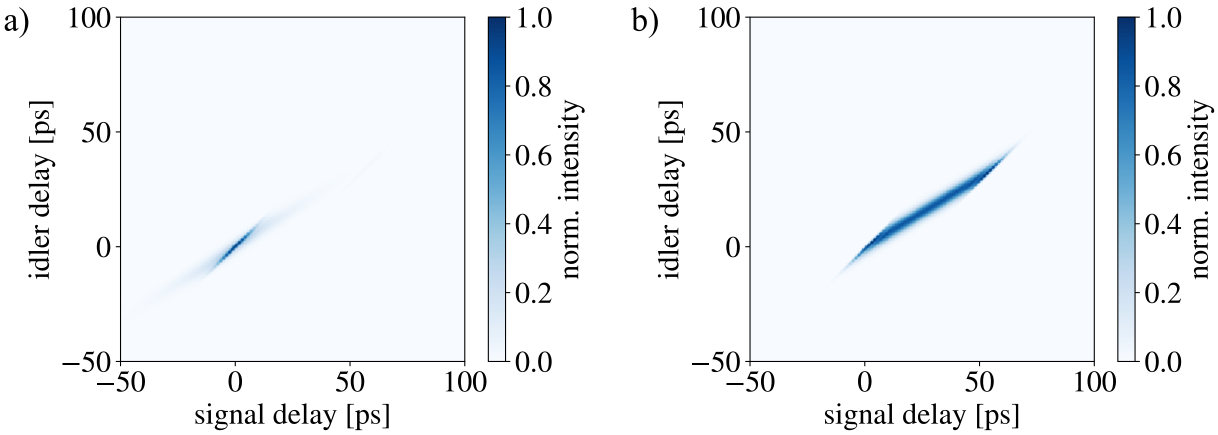

Figure 2.15: a) |JTA| from a process with no spectral phase in the JSA shows a narrow, correlated distribution. b) |JTA| from a process with a spectral phase on the JSA shows as broadened and shifted distribution. This behaviour is similar to the one experienced by a classical ultra-fast pulse and specifically applies to the marginal distributions, which are broadened for the process with a spectral phase.

An example of this behaviour is directly visible in Fig. 2.14, where the spectral phase on the JSA (not shown in the figure) is not zero, due to the different group velocities between pump, signal, and idler fields in the chosen process.

With no phase on the JSA, the JTA would exhibit a narrow feature centred around zero, as depicted in Fig. 2.15 a). However, due to the linear spectral phases between the three involved wavelengths, it takes a much more complex shape and this narrow feature is actually shifted along the diagonal direction, as we can see from Fig. 2.15 b). This is an effect that would be expected in the same way for a classical process where a linear spectral phase leads to a shift in time, as we saw in Fig. 2.8. For further illustration, we depict the absolute value of the JTA in this process without and with a spectral phase on the JSA in Fig. 2.15.

Thus, we can justify the description of broadband bi-photons in the same language as we would for classical pulses with the added feature of energy-time entanglement and strong (anti-) correlations between signal and idler [53, 56]. Therefore, we need to be careful in distinguishing joint properties of the whole bi-photon against properties of the single marginals, which are very different [50].

Specifically, the marginal distributions of signal and idler in Fig. 2.13 show a broad spectral coverage on their own, but simultaneously exhibit a strong frequency anti-correlation. On the other hand, a large spread can be observed in the marginals of the JTA in Fig. 2.14, relating to a large uncertainty in the arrival time of a single photon of the pair. However, the correlation time within which the other photon of the pair arrives after detection of the first one is rather small. In this work, we are therefore often referring to the broad marginal distribution in the JSA and the narrow correlation times in the JTA when we describe our bi-photons analogously to ultra-short pulses.

With this description, we are now able to describe a single bi-photon source. In a next step, we will first discuss the basic principles of nonlinear interferometers which are constructed by two cascaded non-degenerate PDC sources. Finally, we will discuss how to use such an interferometer for measurements with undetected photons.

2.6 Nonlinear interferometers

Nonlinear interferometers based on bi-photon sources are considered useful for various applications [12], such as improved phase sensing [54], metrology with squeezed light [57] or quantum state generation [58].
In this work, we want to perform measurements with undetected photons within an integrated nonlinear interferometer. Thus, we do not focus on employing the possible benefits in phase sensing but rather utilise the coherent transfer of information between signal and idler wavelengths that can be achieved with non-degenerate PDC sources with strong frequency anti-correlations. In contrast to previous work, which utilised nonlinear interferometers based on bulk nonlinear crystals as bi-photon sources, we use nonlinear integrated waveguides as photon pair sources. This allows us to achieve a higher brightness and to pave the way towards an integrated quantum sensor.
In the following, we will lay the theoretical foundations in order to understand the general concept of measurements with undetected photons. We will, furthermore, discuss the impact of spectral phases within the interferometer and varying pump gains.

2.6.1 Induced coherence without induced emission

In order to understand the general concept behind nonlinear interferometers based on PDC sources in the low-gain regime and how they can be used for measurements with undetected photons. We will start by discussing the scheme of induced coherence without induced emission [14]. The name of this concept is based on the assumption that at most one photon pair per mode is generated at the output of the interferometer; an assumption that is well justified for our sources, which we will present in chapter 3. The adapted original scheme of the setup in [13] is depicted in Fig. 2.16. In this figure, we are denoting the different modes of each process involved, as well as the total state after the second source.

We start by writing down the state $|\Psi\rangle$ from two superimposed PDC sources, PDC 1 and PDC 2. We do this in a simplified way by only considering the single photon pair contributions. Furthermore, we are only considering a single signal and idler mode $\hat{a}^\dagger$ and $\hat{b}^\dagger$ and omitting the JSA for now [14]

$$|\Psi\rangle = \eta(\hat{a}_1^\dagger \hat{b}_1^\dagger + \hat{a}_2^\dagger \hat{b}_2^\dagger)|0\rangle + (1-\eta)|0\rangle \tag{2.50}$$

with a process efficiency of η. The subscripts refer to the signal and idler modes generated in PDC processes 1 and 2. Next, we can introduce a phase ϕ between the two sources, as well as a transmission T of an object in the idler path. Thus, we are applying the beamsplitter model to describe the losses and add a reflectivity R (fulfilling $T^2 + R^2 = 1$), which couples in the vacuum mode $\hat{b}_0$, as shown in Fig. 2.16. By aligning the idler modes of both processes on top of each other, the mode $\hat{b}_1^\dagger$ from the first process becomes $\hat{b}_2^\dagger = T^* \cdot \hat{b}_1^\dagger + R^* \cdot \hat{b}_0^\dagger$. With this and by omitting the vacuum contribution, the new superposition state after the two sources takes the form

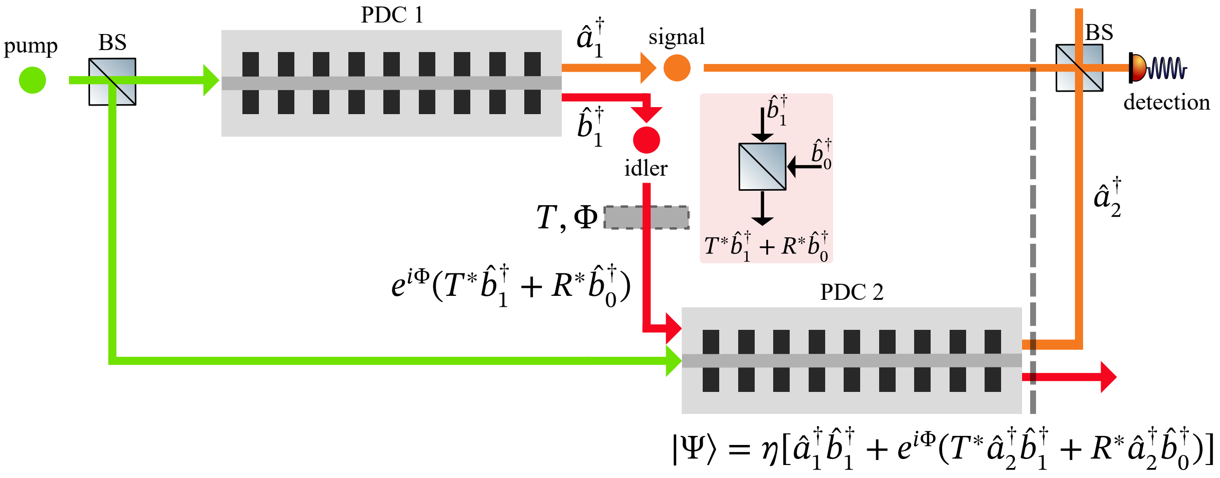

Figure 2.16: A schematic interferometer formed by two cascaded PDC sources to realise measurements with undetected photons of the transmission T in the idler arm utilising the effect of induced coherence without induced emission. Adapted from the experimental setup in [13]. We denoted the modes of each process as well as the total state after the second source. The object in the idler arm can be represented by a beamsplitter and couples the vacuum mode $\hat{b}_0$ to the system. The state at the output of the interferometer is stated next to the dashed line.

$$|\Psi\rangle = \eta[\hat{a}_1^\dagger\hat{b}_1^\dagger + e^{i\Phi}(T^* \cdot \hat{a}_2^\dagger\hat{b}_1^\dagger + R^* \cdot \hat{a}_2^\dagger\hat{b}_0^\dagger)]|0\rangle. \tag{2.51}$$

In a final step, the signal modes are overlapped on a 50:50 beamsplitter, while the idler is discarded. Throughout this treatment, we assume that any phases between the signal paths are zero since we can account for them via alignment or by introducing delays. We can calculate the count rates R_s from the mean photon number $\langle \hat{n}_s \rangle = \langle \hat{a}_3^\dagger \hat{a}_3 \rangle$ with $\hat{a}_3 = \frac{1}{\sqrt{2}}(\hat{a}_1 + \hat{a}_2)$ at one of the outputs of this beamsplitter to be

$$\begin{aligned} R_s &= \frac{1}{2}\eta^2[|1 + e^{i\Phi}T^*|^2 + R^2] \\ &= \frac{1}{2}\eta^2[R^2 + T^2 + 1 + (T^* e^{i\Phi} + Te^{-i\Phi})] \\ &= \eta^2[1 + T\cos(\Phi)]. \end{aligned} \tag{2.52}$$

From this simplified calculation, we can see that the transmission of the object in the idler arm, as well as the phase between the two processes, can be found in the interference pattern. The visibility of the interference is linearly connected to the idler transmission, while the phase between the processes determines the phase of the interference. It is now straightforward to expand on this model and include the spectral bandwidth of the PDC process, as well as additional phases in the calculation [14].

Going from the induced coherence setup to the so-called SU(1,1) interferometer means that the signal beam is aligned such that it now also travels through the nonlinear crystal. In this setup, the interference can be observed directly after the second PDC process without the need for an additional beamsplitter. This scheme is frequently used in practical applications, as it requires fewer optical components and can be easily implemented in a folded version of the setup. However, the same effects can be observed in this setup as in the induced coherence geometry. This is because we assume that no interaction between the signal and idler light from the first source occurs while they propagate through the second source. The main difference lies in additional phase terms that occur as a result of this propagation through the second source. This also leads to different degrees of freedom in the relative delays between the fields.

We note at this point that the operation of nonlinear interferometers in the high-gain regime, where induced emission is present, also leads to the transfer of information from one wavelength to the other while using classical light [59]. However, the demonstrated linear dependence of the visibility on the idler transmission in Eq. (2.52) is no longer given, and the signal intensity depends on that of the idler [38]. Furthermore, much higher light levels at the idler wavelength probe the sample, which might be a disadvantage for light-sensitive samples.

2.6.2 Sensing with undetected photons

After discussing the basic principle of a nonlinear interferometer, we will now include the joint spectral amplitude (JSA) and spectral phases in the description. A representation of a nonlinear interferometer, specifically the setup which we refer to as SU(1,1) interferometer, in Mach-Zehnder geometry is shown in Fig. 2.17.

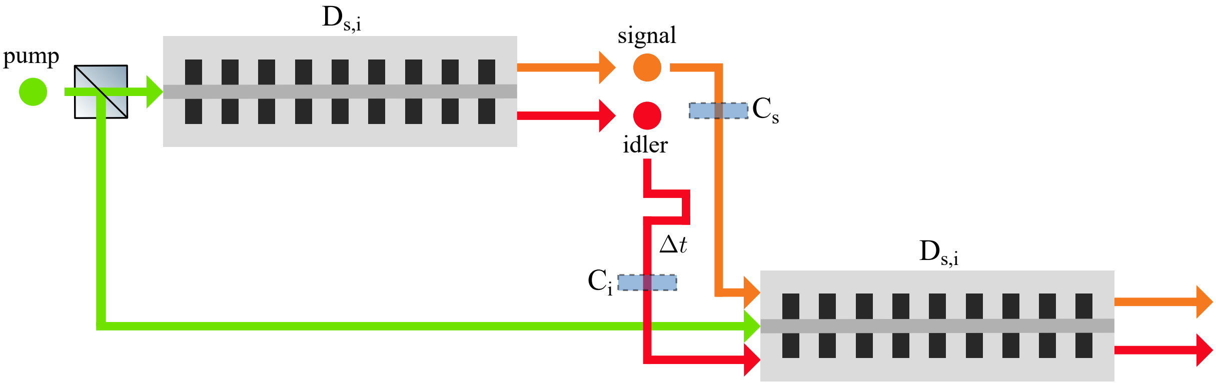

Figure 2.17: Two cascaded PDC sources forming an SU(1,1) interferometer with phases $D_{s,i}$ and $C_{s,i}$ applied to the signal and idler fields during the propagation through the nonlinear waveguide and from external sources. A linear phase is introduced between signal and idler by adding a time delay in the idler arm.

To capture the spectral properties of the interference, we express the actions inside the interferometer through the JSA $f(\omega_s, \omega_i)$, which governs the spectral distribution of signal and idler in a single PDC process as shown in Eq. (2.47). We can write down a JSA of the whole interferometer $f_{SU(1,1)}$ as a superposition of the ones of the two single sources with their relative phases. With this, the state at the output of the interferometer becomes

$$|\Psi\rangle_{int} = |\Psi\rangle_1 + |\Psi\rangle_2 = \int \mathrm{d}\omega_s \mathrm{d}\omega_i \underbrace{(f_1(\omega_s,\omega_i) + f_2(\omega_s,\omega_i))}_{=f_{SU(1,1)}(\omega_s,\omega_i)} \hat{a}^\dagger(\omega_s)\hat{b}^\dagger(\omega_i)|0\rangle \tag{2.53}$$

with $f_1(\omega_s,\omega_i)$ and $f_2(\omega_s,\omega_i)$ being the contributions from both PDC sources, including phases and absorption between them.
In the scheme considered in Fig. 2.17, the photons produced in the first pass of the pump field through the PDC source experience mainly second order dispersion $C_{s,i}$, introduced in either of the interferometer arms, as well as dispersion from the waveguide material itself $D_{s,i}$ when passing through the waveguide for the second time. Again, we assume that the generated photons from the first process only propagate through the waveguide but do not interact with the pump field. This goes in line with our previous assumption that at most one photon pair is generated either in the first or the second process. Furthermore, we will assume for now that the pumping strengths are equal and that there are no losses in between the interferometer arms. We will introduce the influence of these properties later.
In order to simplify the following calculations, we introduce a frequency detuning $\Delta\omega = (\omega_s - \Omega_s) = -(\omega_i - \Omega_i)$ with $\Omega_{s,i}$ as the central frequency of the signal and idler photons and furthermore consider a cw-laser as a pump light source. Thus, the JSA of a single PDC source is given by a one-dimensional function

$$f(\Delta\omega) = \mathrm{sinc}\left(\frac{\Delta\beta(\Delta\omega)L}{2}\right) e^{\frac{\Delta\beta(\Delta\omega)L}{2}}. \tag{2.54}$$

An external spectral phase, e.g. second order dispersion, on the joint spectral amplitude of a single PDC source can be described by [53]

$$f_{phase}(\Delta\omega) = f(\Delta\omega) \cdot P(\Delta\omega), \tag{2.55}$$

where $P(\Delta\omega) = \exp(i\Psi)$ is the total phase Ψ accumulated by photons generated in the first pass of the pump through the PDC source. For this phase, we assume an external second order dispersion $C_{s,i}$ on signal and idler, as well as second order dispersion that the bi-photon experiences on its second pass through the waveguide $D_{s,i}L$. In addition, we consider a time delay Δt_i in the idler arm. With this, we can write this JSA of the first process $f_1(\Delta\omega)$ at the end of the interferometer as

$$\begin{aligned} f_1(\Delta\omega) = f(\Delta\omega) &\cdot \exp[-i(D_sL + C_s)\Delta\omega^2 + \omega_s\Delta t_i] \\ &\cdot \exp[-i(D_iL + C_i)\Delta\omega^2]. \end{aligned} \tag{2.56}$$

The photons generated during the second pass of the pump field do not propagate through the interferometer arms, and thus only acquire the phase included in the JSA of a single PDC source $f_2(\Delta\omega) = f(\Delta\omega)$. This results in the total JSA given by

$$\begin{aligned} f_{SU(1,1)}(\Delta\omega) =& f_1(\Delta\omega) + f_2(\Delta\omega) \\ =& f(\Delta\omega)(1 + e^{-i(D_sL+D_iL+C_s+C_i)\Delta\omega^2 - i\cdot\omega_s\Delta t_i}). \end{aligned} \tag{2.57}$$

It can be seen directly from this expression that, due to the lack of cross-terms, the quadratic phase in either of the arms can be compensated by placing the corresponding amount of dispersion in either the same or the other arm of the interferometer [56]. The external part of the phase, which does not contain the waveguide dispersion, can be re-written as

$$\begin{aligned} \Phi_{ext}(\Delta\omega) &= \omega_s\Delta t_s + C_s\Delta\omega^2 + C_i\Delta\omega^2 \\ &= (\bar{\omega}_s + \Delta\omega)\Delta t_s + C_s\Delta\omega^2 + C_i\Delta\omega^2. \end{aligned} \tag{2.58}$$

This leads to an expression for the total phase of

$$\Psi = \frac{1}{2}\big([(D_s + D_i)L - C_s - C_i]\Delta\omega^2 - \Delta t_s\bar{\omega}_s - \Delta t_i\Delta\omega\big). \tag{2.59}$$

When expressing the real part of the exponential function in Eq. (2.57) as a cosine function, the total JSA becomes

$$f_{SU(1,1)}(\Delta\omega, C_s, C_i, \Delta t_i) = 2f(\Delta\omega)\cdot\cos(\Psi)\cdot\exp\left(i\frac{\Psi}{2}\right). \tag{2.60}$$

If we detect spectrally resolved interference in the signal arm, the spectral intensity is given by [36]:

$$S(\Delta\omega) \propto |f_{SU(1,1)}(\Delta\omega)|^2 \propto |f(\Delta\omega)|^2[1 + \cos(\Psi(\Delta\omega))]. \tag{2.61}$$

Thus, we can extract the spectral phase on the total JSA, which includes external phases in the signal and idler path, by measuring the spectral interferogram in the signal arm. The temporal interferogram is constructed by translating the idler stage while recording the single photon counts frequency-unresolved in the signal or idler arm. Consequently, the signal in the temporal interferogram is given by integrating the spectral interferogram over the frequency detuning $\Delta\omega$ for several stage positions with time delay Δt_i as

$$S(\Delta t_i, \Psi) = \int_{-\infty}^{\infty} \mathrm{d}\Delta\omega \left| f_{SU(1,1)}(\Delta\omega)\right|^2 = \int_{-\infty}^{\infty} \mathrm{d}\Delta\omega\, \mathrm{sinc}^2(\Delta\gamma\Delta\omega^2)\cdot\cos^2(\Psi(\Delta t_i)). \tag{2.62}$$

It can be seen that any phase Ψ that is introduced between the two PDC sources is present in the interference for both the signal and the idler. This enables measurements with undetected photons, thus retrieving information about a phase object in the idler arm while measuring at the signal output. Furthermore, we can observe that a phase in either of the interferometer arms leads to an altered temporal interference pattern.

2.6.3 Pump gain and losses inside the interferometer

The discussion above has been carried out assuming that there are no losses in between the two interferometer stages, as well as equal pump gains for both stages. However, we will see that adjusting the pump gain to account for unavoidable coupling losses can be used to optimise the interference visibility, which is often associated with a high signal-to-noise ratio and, therefore, essential for any application.

The effects of pump gain optimisation have been studied in several works aiming at ideal conditions for phase sensing with SU(1,1) interferometers [54, 60, 61]. In this work, we have performed experiments on gain optimisation in light of practical applications such as optical coherence tomography at the end of section 4.

Now, let us look at losses and unbalanced gains in an SU(1,1) setup. We are considering a system of two cascaded PDC sources similar to the one in Fig. 2.17 which now includes different transmissions $T_{s,i}$ and gains $g_{1,2}$ while detection can happen in the signal, idler, or coincidences. This setup is shown in Fig. 2.18 and is adapted from the concept in [54].

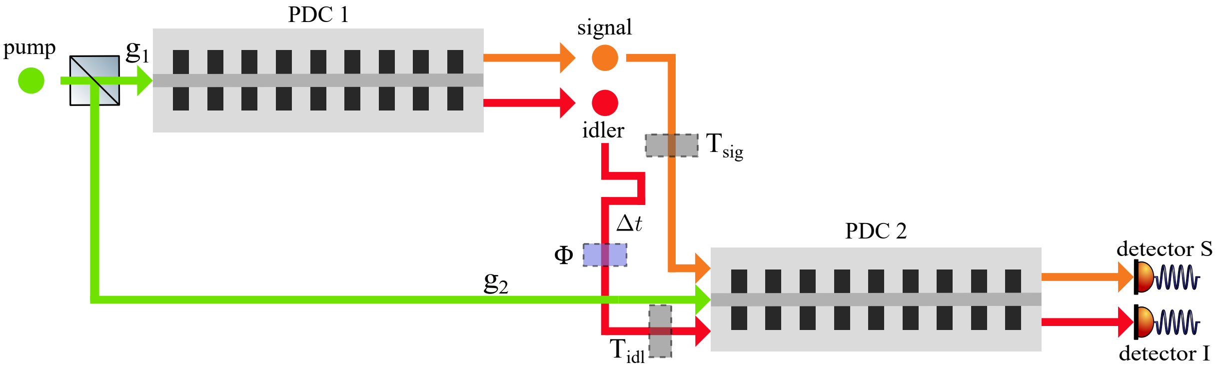

Figure 2.18: A schematic SU(1,1) interferometer depicting the pump gains g_1 and g_2 for PDC processes 1 and 2 as well as the transmissions T_{sig} and T_{idl} in the signal and idler arms within the interferometer with a phase object Φ.

In the following, we assume a single-mode theory. This means that we consider only one spectral mode for signal ($\hat{a}^\dagger(\omega_s)$) and idler ($\hat{b}^\dagger(\omega_i)$) instead of performing the integration over all frequencies as we did in Eq. (2.53). This single-mode description holds approximately true when recording spectrally resolved interference and evaluating the interference for a fixed frequency. The treatment of our system at such fixed frequencies is possible as the present anti-correlations in the JSA caused by the narrow-band pump laser allow to select a narrow spectral bandwidth at the signal wavelength that corresponds to the according idler wavelength range. Broadband effects such as dispersion are not observed over such a small spectral range and have to be included by integration over all frequencies.

In order to see the effect of losses, we investigate the probabilities to detect a photon for signal, idler, and coincidences $C_{s,i,coinc}$ after the interferometer. To this end, we recall from Eq. (2.48) that the mean number of photons per mode generated in each stage is given by

$$\langle n \rangle = \sinh^2 g \approx g^2 \tag{2.63}$$

and that we can link the parametric gain g to the experimentally accessible power of the pump laser as $g \propto \sqrt{P}$. Considering click detectors with unity detection efficiency for signal and idler leads to the following probabilities to detect a photon for signal, idler, and coincidences [54]

$$\begin{aligned} C_S &= T_{sig} g_1^2 + g_2^2 + 2\sqrt{T_{sig} T_{idl}} g_1 g_2 \cos(\Phi) \\ C_I &= T_{idl} g_1^2 + g_2^2 + 2\sqrt{T_{sig} T_{idl}} g_1 g_2 \cos(\Phi) \\ C_{coinc} &= T_{sig} T_{idl} g_1^2 + g_2^2 + 2\sqrt{T_{sig} T_{idl}} g_1 g_2 \cos(\Phi). \end{aligned} \tag{2.64}$$

The visibility of the interference is defined as $V = (C^{max} - C^{min})/(C^{max} + C^{min})$ with the maximal (C^{max}) and minimal (C^{min}) count rates. The respective visibilities are therefore given by

$$\begin{aligned} V_S &= \frac{2\sqrt{T_{sig} T_{idl}} g_1 g_2}{T_{sig} g_1^2 + g_2^2} \\ V_I &= \frac{2\sqrt{T_{sig} T_{idl}} g_1 g_2}{T_{idl} g_1^2 + g_2^2} \\ V_{coinc} &= \frac{2\sqrt{T_{sig} T_{sig}} g_1 g_2}{T_{sig} T_{idl} g_1^2 + g_2^2}. \end{aligned} \tag{2.65}$$

From this we can see that, for signal and idler, the maximum achievable visibility of the interference is limited by the coupling efficiencies to the waveguide, which are included in the transmission values in Fig. 2.18, at the wavelength that is not detected such that $V_S^{max} = \sqrt{T_{idl}}$ and $V_I^{max} = \sqrt{T_{sig}}$. Meanwhile, the gain ratio required to reach that visibility is given by the transmission at the same wavelength, namely $g_1^2/g_2^2 = 1/T_{sig,idl}$ for signal and idler, respectively. In the case of coincidences, the visibility can be maximised to 1 for the correct pump gain ratio of $g_1^2/g_2^2 = 1/(T_{sig} T_{idl})$. We depict the behaviour of the visibility for signal, idler, and coincidences at realistic transmissions of an SU(1,1) interferometer based on a waveguide PDC source of $T_{800} = 0.3$ and $T_{1400} = 0.5$ in Fig. 2.19. We observe different values for the maximal visibility for the interference in signal, idler, and coincidences. Furthermore, the optimal pump gain ratio shifts to higher values a lower transmission in the arm where interference is detected.

The interpretation of this result is that in order to achieve the maximum visibility for the signal or idler counts, the gains need to be adjusted such that each detection event of a signal or idler photon has equal probability of coming from the first or the second process.

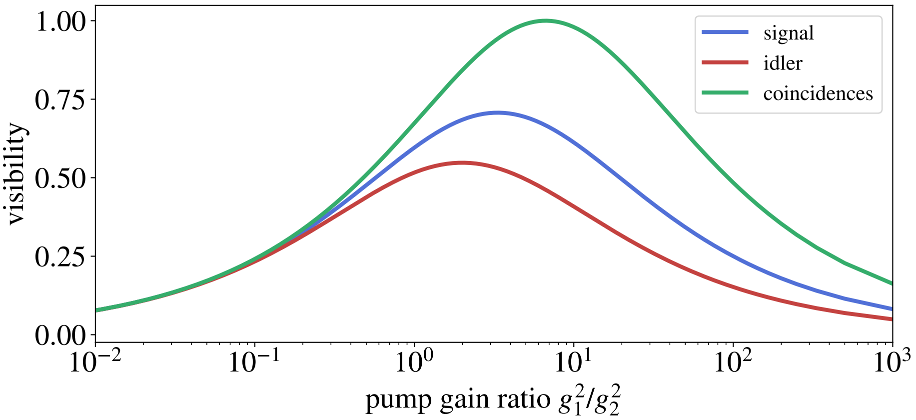

Figure 2.19: The visibility for signal, idler, and coincidence interference is shown for varying pump gain ratio. The transmission values are set to $T_{800} = 0.3$ and $T_{1400} = 0.5$.

However, the losses in the undetected arm lead to a distinguishability between the two processes, and thus ultimately limit the visibility of the interference as we discussed for the case of induced coherence in the beginning of this section. In the case of the coincidence counts, a different pump gain ratio is optimal as here both photons are detected, and therefore the gains need to be balanced so that they compensate for the losses in both channels. This then leads to visibility of unity as the same number of signal and idler photons are generated and contribute to the interference in coincidence counting. However, for measurements with undetected photons, maximising the visibility at the signal wavelength is most relevant.
We will use this knowledge to design the experimental setups for our nonlinear interferometers presented in chapter 4 and employ differential pumping with variable pump gain ratios to reach the optimal operation point for the application of optical coherence tomography with undetected photons.

Summary

In this chapter, we have laid the foundations needed for the following sections on source development and interferometry with undetected photons, first in the near-IR and ultimately in the mid-IR. We have discussed current measurement techniques in the realm of ultra-fast spectroscopy and how we can transfer them to the quantum regime. As we realise this transition with integrated waveguides, we discussed their essential properties as well as the effect of dispersion on ultra-fast pulses inside waveguides, as they are often not considered simultaneously. However, we will see that we can specifically engineer the waveguide's dispersion in order to realise the nonlinear optical effect of PDC with a large spectral bandwidth. This process will provide us with the photon pairs that are required in our nonlinear interferometer, which we described as a cascaded PDC process, which shows interference effects due to path indistinguishability between the photon pair sources. We demonstrated how such setups can be used for measurements with undetected photons and are influenced by losses inside the interferometer and the pump gain ratios.

3

Source engineering

In this work, we choose integrated waveguides as sources of photon pairs from PDC, since integration is key for the construction of a practical quantum sensor. Waveguide-based PDC sources, furthermore, provide a high brightness and co-linear emission of the bi-photons because of the strong confinement of the fields, guiding in a defined spatial mode, and the long interaction length. However, one major challenge when working with non-degenerate type II guided-wave PDC sources is that their phasematching bandwidth decreases with increasing interaction length L. This typically leads to a trade-off between brightness and spectral bandwidth.

This issue can be overcome using a technique called dispersion engineering. Flexible dispersion engineering has already been performed and is common in other platforms that utilise fibres that exhibit a $\chi^{(3)}$ non-linearity [62–64]. However, the use of $\chi^{(3)}$ materials implies lower nonlinear coefficients. Thus, for an integrated quantum sensor with a high brightness, we want to employ type II phasematching in our Ti:LiNbO$_3$ waveguides to make use of their $\chi^{(2)}$ non-linearity while still realising broadband PDC processes at two different wavelengths.

We will reach this goal in this chapter by first discussing the conditions that need to be fulfilled for a broadband PDC emission based on the waveguide's dispersion. In a next step, we simulate the dispersive properties for two waveguide geometries and find an operation point for so-called group velocity matching and group velocity dispersion cancellation. This allows us to design waveguide and poling patterns for two sources. The first one employs only group velocity matching and covers a spectral bandwidth of more than 7 THz at wavelengths of 830 nm and 1400 nm; therefore, we call it the near-IR (NIR) source. The second, further engineered source employs group velocity matching and group velocity dispersion cancellation in the mid-IR (MIR) and covers a spectral bandwidth of 25 THz of the generated photons at wavelengths of 850 nm and 2800 nm. Finally, we perform an in-depth characterisation of our MIR source and present its guiding properties at wavelengths in the mid infra-red, characterise the spectral emission of the PDC process depending on the waveguide temperature and pump wavelength and finally estimate a lower bound for the source's photon-pair rate.

3.1 Dispersion engineering

In chapter 2, we discussed that phasematching enables an efficient nonlinear optical process and the ways to achieve it. We discovered that the phasematching bandwidth for a three-wave mixing process over an interaction length L is given by

$$\Delta\omega = \frac{2}{\frac{\mathrm{d}\Delta\beta}{\mathrm{d}\omega}L} \tag{3.1}$$

with the bandwidths $\Delta\omega$ of the generated fields around their central frequencies. For a PDC process which is driven by a cw-laser, this bandwidth determines the width of the marginal signal and idler spectra, as we will discuss below. The phasematching bandwidth is dependent on the first derivative of the phase-mismatch $\Delta\beta$, thus, the phasematching bandwidth is linked to the group velocity mismatch between the interacting fields in most cases. However, this is only true as long as $\Delta\beta$ is mainly governed by first order terms in $\Delta\omega$. As soon as $\Delta\beta$ is dominated by higher orders in $\Delta\omega$, the phasematching function takes a different spectral shape. Additionally, a changed scaling of the phasematching bandwidth with the interaction length L can be observed.

We illustrate these changes for a process around 850 nm, a working point that will become relevant later, for a phase-mismatch $\Delta\beta$ with linear, quadratic and cubic terms to leading order, i.e.,

$$\begin{aligned} \Delta\beta_{linear} &= A\cdot(\omega-\omega_0) \\ \Delta\beta_{quadratic} &= B\cdot(\omega-\omega_0)^2 \\ \Delta\beta_{cubic} &= C\cdot(\omega-\omega_0)^3 \end{aligned} \tag{3.2}$$

with central frequency ω_0 and realistic values for dispersion coefficients of $A = 10000\,\frac{\mathrm{fs}}{2\pi\cdot\mathrm{mm}}$, $B = 10000\,\frac{\mathrm{fs}}{4\pi^2\cdot\mathrm{mm}}$ and $C = 10000\,\frac{\mathrm{fs}}{8\pi^3\cdot\mathrm{mm}}$.

In Fig. 3.1 a), we observe a change in the shape of the spectral intensity from a sinc^2-function to a rectangular shape, while the bandwidth increases for the fixed interaction length of $L = 40$ mm.

The resulting phasematching bandwidths of the generated fields are shown in Fig. 3.1 b). Here, we can not only observe an increase in bandwidth for higher orders, but also a different scaling with the interaction length, which can be read from the slopes of -1, $-1/2$ and $-1/3$ in the double-logarithmic plot for the respective orders in the phase-mismatch $\Delta\beta$. Therefore, using a longer waveguide for a process with a phase-mismatch $\Delta\beta$ which is dominated by a higher order term in $\Delta\omega$ does not lead to a reduction of the achievable bandwidth as quickly as it would happen in the case for a phase-mismatch that is linear in $\Delta\omega$.

This difference in the scaling behaviour allows us to lift the typical trade-off between a higher brightness and a smaller spectral bandwidth, that are typically associated with a longer interaction length. This is because $\Delta\beta$ stays close to zero for a larger range of frequencies around the central frequency of the process for higher leading orders.

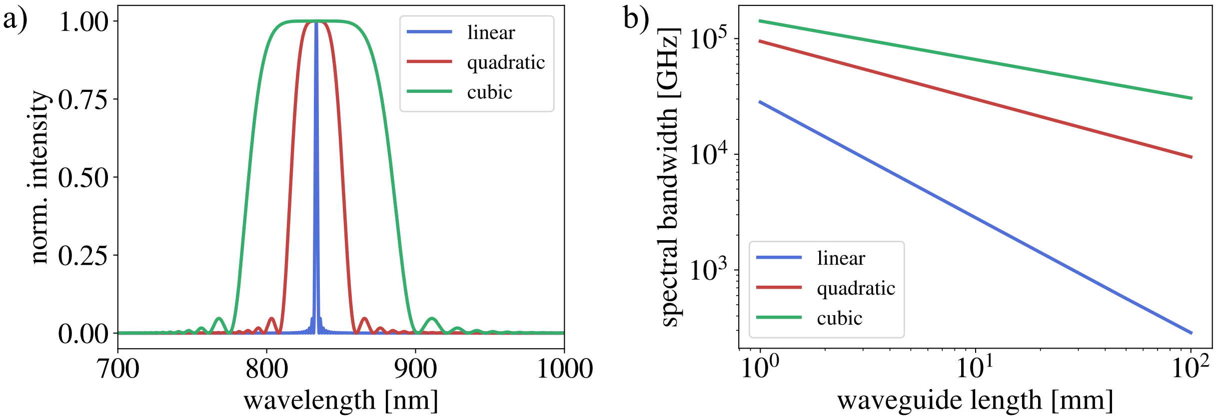

Figure 3.1: a) normalised intensity for a phase-mismatching $\Delta\beta$ that is linear, quadratic and cubic in $\Delta\omega$ to leading order as given in Eq. (3.2). The interaction length is fixed to $L = 40$ mm. b) Bandwidth of linear, quadratic and cubic phase-mismatch $\Delta\beta$ for different interaction lengths L.

We employ this property of broadband phasematching for a long interaction length when constructing the source for our quantum sensors, as this source should simultaneously cover a large spectral bandwidth and show a high brightness to enhance the signal-to-noise ratio in measurements.

Therefore, we look into the realisation of a phase-mismatch $\Delta\beta$ which is dominated by higher order terms in $\Delta\omega$ for a non-degenerate Type II PDC process. We derived in chapter 2 that the JSA $f(\Delta\omega)$ for a waveguide PDC source pumped by a cw-laser is given by

$$f(\Delta\omega) = \mathrm{sinc}\left(\frac{\Delta\beta(\Delta\omega)L}{2}\right) e^{i\frac{\Delta\beta(\Delta\omega)L}{2}} \tag{3.3}$$

with $\Delta\omega = \omega_s - \Omega_s = -(\omega_i - \Omega_i)$ being the detunings of the signal and idler frequency from their respective central frequencies Ω_s and Ω_i. We have seen that the phase-mismatch $\Delta\beta$ needs to be equal to zero for a large spectral range to achieve a broadband phasematching while keeping the interaction length long. We therefore perform a Taylor expansion of $\Delta\beta$ yielding

$$\Delta\beta(\omega_s, \omega_i) = \beta_p(\omega_s + \omega_i) - \beta_s(\omega_s) - \beta_i(\omega_i) - \frac{2\pi}{\Lambda} \tag{3.4}$$

$$\approx \Delta\beta^{(0)} + (\kappa_s - \kappa_i)\Delta\omega + \left[\frac{1}{2}(\eta_s + \eta_i) - \eta_p\right]\Delta\omega^2 + O(\Delta\omega^3). \tag{3.5}$$

We will show that we can eliminate the 0th, 1st and 2nd order of this Taylor expansion by periodic poling, group-velocity matching and group-velocity dispersion cancellation,

respectively. This allows to fulfill the phasematching condition $\Delta\beta = 0$ for a large range of frequencies and therefore increases the spectral bandwidth of the PDC process.
We visualise the process of gradually eliminating the lowest orders of the phase-mismatch $\Delta\beta$ in figure 3.2 with the leading order in the phase-mismatch being a) linear, b) quadratic and c) cubic in $\Delta\omega$. On the top, we depict the phases on the generated bi-photons due to the waveguide dispersion as discussed in section 2.3.
Below, we depict the shapes of the resulting JSA (red area) from the overlap of pump (blue) and phasematching (orange) together with the marginal spectral distributions (red curves). On the bottom of figure 3.2, we visualise the effect of different temperatures on the three PDC processes. We plot the normalised intensity of the marginal signal spectra with the corresponding idler wavelengths on the top x-axis for a cw pump laser. We choose pump wavelengths of 570 nm, 517 nm and 645 nm for a) to c). We simulate the output intensity at different waveguide temperatures, which are depicted on the y-axis. In the JSA picture, a change in temperature leads to a shift of the phasematching function against the pump function as a result of the temperature dependent refractive index. Thus, depicting these temperature tuning curves allows us to visualise the phasematching functions and observe changes in the spectral bandwidth of the processes where conditions such as group velocity matching and group velocity dispersion cancellation are only fulfilled at specific temperatures. We will come back to these representations when we discuss the operation point of our mid-IR PDC source.

Finally, let us have a closer look into the conditions that we need to fulfill to construct our broadband PDC sources by investigating the terms of different orders in the phase-mismatch. In a first step of our dispersion engineering routine, the 0-th order phase-mismatch $\Delta\beta^{(0)} = \beta_p(\Omega_s+\Omega_i)-\beta_s(\Omega_s)-\beta_i(\Omega_i)-\frac{2\pi}{\Lambda}$ is set to zero by an appropriate choice of the poling period Λ to ensure phasematching for the central frequencies. For our quantum sensor, we are aiming at a wavelength combination with the signal around 850 nm and the idler in the near infra-red or mid infra-red. The terms

$$\kappa_{s,i} = \left(\left.\frac{\partial \beta_p}{\partial \omega}\right|_{\Omega_s+\Omega_i} - \left.\frac{\partial \beta_{s,i}}{\partial \omega}\right|_{\Omega_{s,i}} \right) \tag{3.6}$$

are the inverse group velocities (GV) of the signal and idler photons, respectively, while the terms

$$\eta_{s,i} = \left(\left.\frac{\partial^2 \beta_p}{\partial \omega^2}\right|_{\Omega_s+\Omega_i} - \left.\frac{\partial^2 \beta_{s,i}}{\partial \omega^2}\right|_{\Omega_{s,i}} \right) \tag{3.7}$$

are their group velocity dispersion (GVD), in both cases relative to the pump field. For the pump, the expression for the GVD becomes

$$\eta_p = \left.\frac{\partial^2 \beta_p}{\partial \omega^2}\right|_{\Omega_p}. \tag{3.8}$$

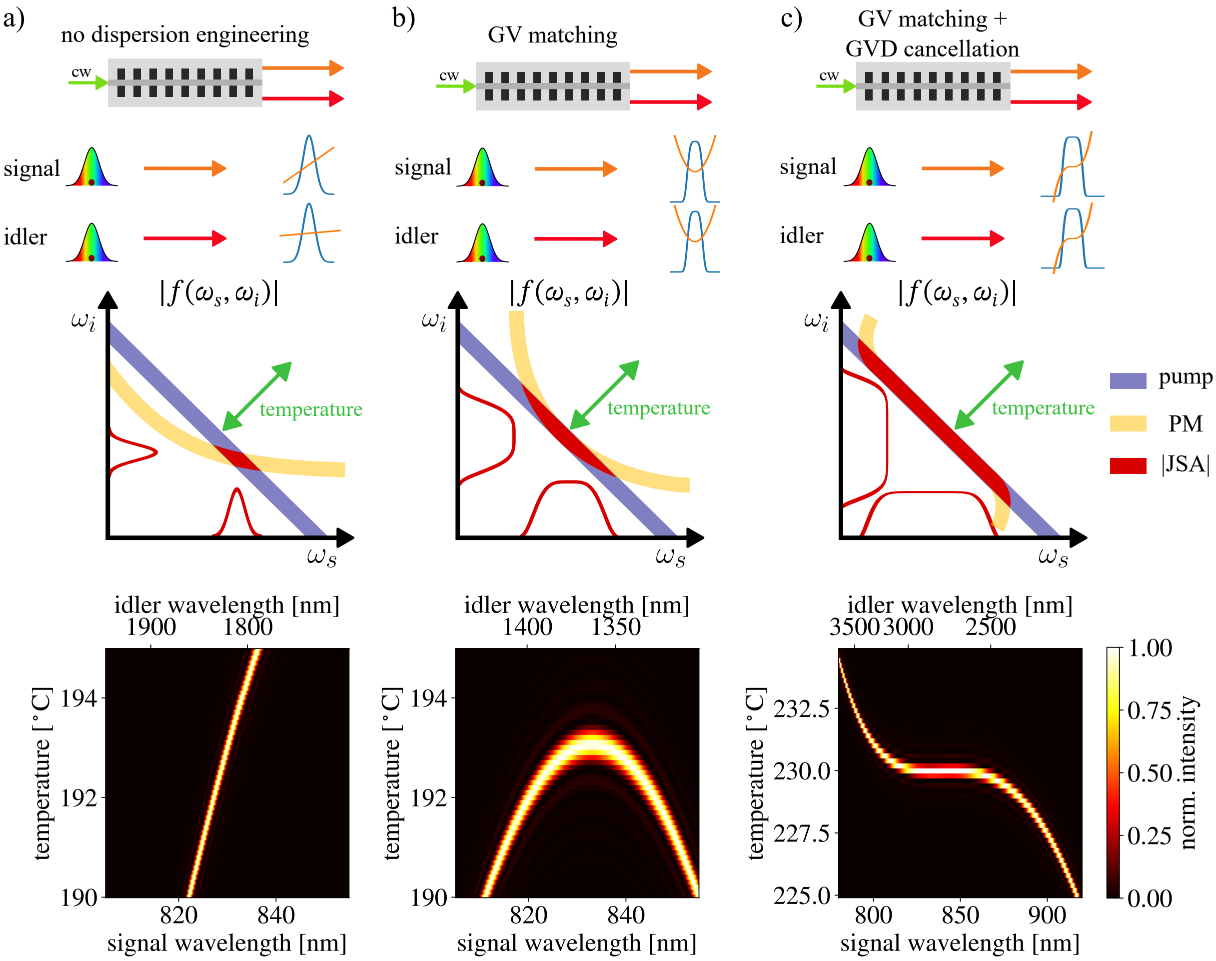

Figure 3.2: *Top:* The dispersive effects on the generated photons are shown for a) no dispersion engineering but 0th order phasematching by periodic poling, b) matched group velocities and c) additional group velocity dispersion cancellation. For each condition, the accumulated phases during the PDC processes on the signal and idler photons are shown in the spectral domain (orange line) together with the shape of the marginal spectra (blue line).
Middle: The joint spectral amplitude (JSA) is depicted as the overlap of pump function (blue) and phasematching (PM) function (yellow), resulting in different outputs for the signal and idler spectra (red). A change in the temperature shifts the phasematching function along the diagonal direction.
Bottom: The change in output spectrum during a temperature shift is shown. The normalised spectral intensity of the signal photon is simulated for the three different stages in dispersion engineering together with the corresponding idler wavelength on the top x-axis. The processes have been simulated for with pump wavelengths of a) 570 nm, b) 517 nm and c) 645 nm in a 40 mm long waveguide.

Due to the fact that a cw pump laser is assumed, $\Omega_p = \Omega_s + \Omega_i$. Therefore, contributions with derivatives containing β_p cancel each other in the subtraction of $\kappa_s - \kappa_i$ and $\frac{1}{2}(\eta_s + \eta_i) - \eta_p$, similar to the discussion in [65]. This becomes apparent when writing the terms for $\kappa_{s,i}$ and $\eta_{p,s,i}$ explicitly in equation (3.5).
We end up with a formula that only contains contributions in the first, second and higher orders

$$\Delta\beta(\Delta\omega) \approx \left(-\frac{\partial \beta_s}{\partial \omega}\bigg|_{\Omega_s} + \frac{\partial \beta_i}{\partial \omega}\bigg|_{\Omega_i} \right) \Delta\omega - \frac{1}{2} \left(\frac{\partial^2 \beta_s}{\partial \omega^2}\bigg|_{\Omega_s} + \frac{\partial^2 \beta_i}{\partial \omega^2}\bigg|_{\Omega_i} \right) \Delta\omega^2 + O(\Delta\omega^3). \tag{3.9}$$

We can see that the first order term of the phase-mismatch can be cancelled, if the signal and idler GVs are matched

$$-\frac{\partial \beta_s}{\partial \omega}\bigg|_{\Omega_s} + \frac{\partial \beta_i}{\partial \omega}\bigg|_{\Omega_i} = 0. \tag{3.10}$$

This condition is called GV matching. The PDC source based on this concept will be presented below. We use this source as the active element in our nonlinear interferometer in the near-IR, which we present and apply in section 4. In this setup, the source generates bi-photons that lie around 830 nm and 1360 nm while achieving a spectral bandwidth of up to 7 THz.
In a second step, by ensuring that the GVD of signal and idler has equal magnitude but opposite sign, the second order of the phase-mismatch can be cancelled

$$\underbrace{\frac{\partial^2 \beta_s}{\partial \omega^2}\bigg|_{\Omega_s} + \frac{\partial^2 \beta_i}{\partial \omega^2}\bigg|_{\Omega_i}}_{\Delta\beta^{(2)}} = 0. \tag{3.11}$$

We refer to this condition as GVD cancellation and define $\Delta\beta^{(2)}$ as the second order phase-mismatch. GVD cancellation is key to supporting the extreme bandwidths that are required for our source in the mid-IR. We employ this source in chapter 5 to construct a nonlinear interferometer with the signal photon at 860 nm and the idler photon at 2800 nm while achieving a bandwidth of 25 THz.
To fulfill these conditions in our home-built waveguides, we need to know the effective refractive indices of different waveguide geometries. We will discuss the underlying simulations and our findings that lead to the design of our waveguide and poling layouts in the next part of this chapter.

3.2 Simulations

To find the refractive indices for different geometries and fabrication parameters of our Ti:LiNbO$_3$ waveguides, we used an existing code called 'Focus2' which was written by Dr. Benjamin Brecht and Dr. Matteo Santandrea. This code is based on solving the mode equations inside a waveguide of defined dimensions and diffusion parameters via FEM, as we described in chapter 2.

We use the width and thickness of the titanium strip which is deposited and through in-diffusion defines the dimension of the waveguide as parameters in our design process. The diffusion temperature and diffusion time are chosen sufficiently large, such that all of the deposited titanium is in-diffused but still concentrated in a region below the original titanium strip to form the waveguide structure. More details on the fabrication process and the relevant parameters can be found in [43].

These simulations allow us to calculate the Sellmeier coefficients for TE and TM polarisation over a range of temperatures. In practice, we calculate the effective refractive index n_{eff} for the fundamental spatial mode at a range of wavelengths and fit the Sellmeier coefficients to it.

To investigate the sensitivity of our process to the waveguide temperature, we performed simulations for temperature steps as small as 0.02 K. Based on the resulting refractive indices, we calculated the derivatives of the phase-mismatch $\Delta\beta$ to achieve GVM or simultaneous GVM and GVD cancellation.

We note that the simulations are optimised to work in the visible and near infra-red regime. Therefore, we expect stronger deviations of the simulations from the actual refractive indices when going to wavelengths in the mid infra-red region. However, we will find that these deviations are mostly constant offsets in the refractive index at all wavelengths and therefore do not hinder our dispersion engineering in which we are interested in the wavelength dependent changes of the refractive index.

3.2.1 Group velocity matching

In our efforts to achieve group velocity matching (GVM), we start by inspecting the group velocity and group velocity dispersion for a 7 µm wide waveguide at a fixed temperature of 180 °C which are shown in Fig. 3.3. We choose 7 µm wide waveguides as they provide guiding at a single spatial mode for light at telecommunication wavelengths around 1550 nm. Using a type II process, we can find pairs of wavelengths with the same group velocities in Fig. 3.3 a). We can observe that the group velocity at TM polarisation is always larger than the one at TE. Meanwhile, the group velocities at both polarisations increase monotonically for longer wavelengths. Thus, in order to match group velocities, the signal photon would have to be polarised in TM and the idler in TE polarisation. [1] Turning to the next order in dispersion, we can see that both the signal and the idler experience positive GVD when propagating through the waveguide as depicted in Fig. 3.3 b). Furthermore,

---

[1] We are thereby following the historical convention of the signal photon being at the shorter and the idler photon being at the longer wavelength.

we can see that the GVD is stronger at shorter wavelengths, which is a typical property of dielectric media in the near-IR and telecommunication wavelength range due to normal dispersion [26]. Thus, we cannot find a point of GVD cancellation for this waveguide geometry and range of signal and idler wavelengths.

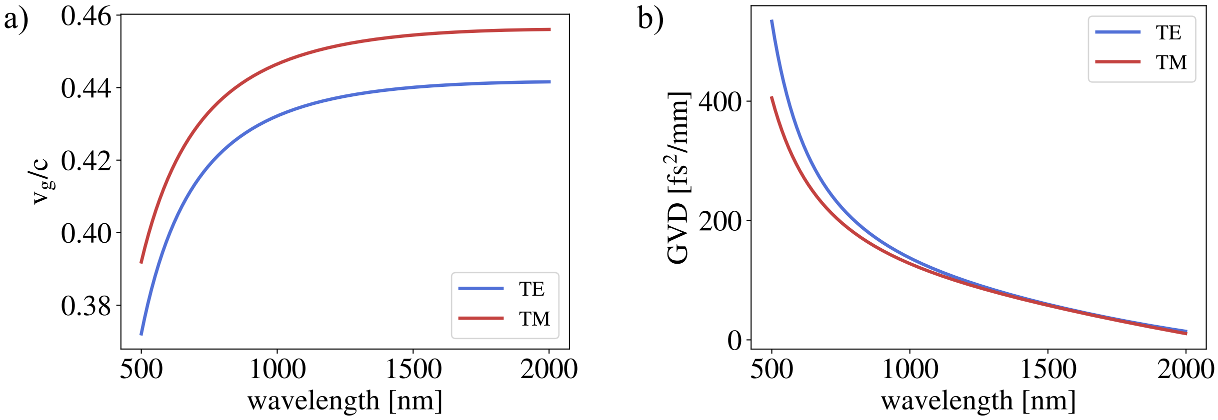

Figure 3.3: a) Group velocity of TE and TM polarised light in a 7 µm wide waveguide at a temperature of 180 °C. b) Group velocity dispersion for TE and TM polarisation for the same parameters.

To realise a PDC process with GVM for different wavelength-pairs of signal and idler for a fixed temperature, we adapt the pump wavelength and poling period as shown in Fig. 3.4 a). This allows to shift the working point to the desired position in signal and idler wavelengths or to adapt the poling period to existing pump laser infrastructure. At a fixed pump wavelength and poling period, the generated signal spectrum can be tuned with temperature as shown in Fig. 3.4 b). We can observe that fine-tuning in temperature is required to achieve the desired broadband emission. Furthermore, tuning the temperature provides a means to change the output spectrum of the source and thereby the spectral and temporal properties of the generated bi-photons. We will employ this fact in chapter 4 to generate bi-photons with different correlation times and observe their distinct properties in a nonlinear interferometer in the NIR.

3.2.2 GVM and GVD cancellation

Ultra-broadband emission that is linked to a simultaneous matching of the group velocities of signal and idler as well as opposite group velocity dispersion for these two fields can only be reached for a relatively fixed set of process parameters. We are therefore restricting ourselves to a range of output wavelengths. For our source in the mid-IR, we choose the wavelengths of the generated photons to lie around 850 nm and 2800 nm. Since the longest wavelength now lies in mid-IR, the used waveguides need to be wider in order to guide this field. This is because the longest guided wavelength, also called the cut-off wavelength, is defined by the size of the waveguide and the refractive index profile [40].

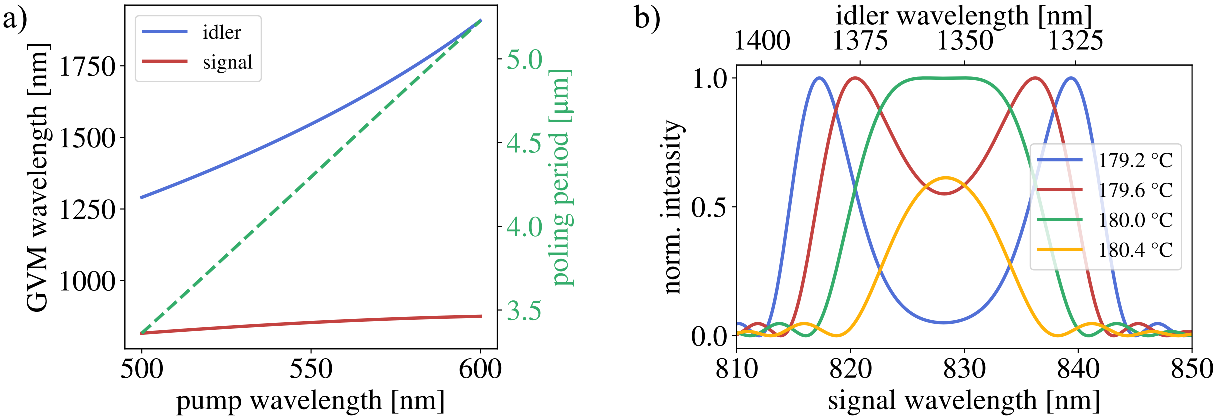

Figure 3.4: GVM for a waveguide of 7 μm width at a temperature of 180 °C. a) Wavelength pairs of signal and idler that fulfill group velocity matching for a fixed temperature with adapted pump wavelengths and poling periods. b) Signal spectrum for different waveguide temperatures at a fixed pump wavelength and poling period. The top x-axis shows the corresponding idler wavelengths.

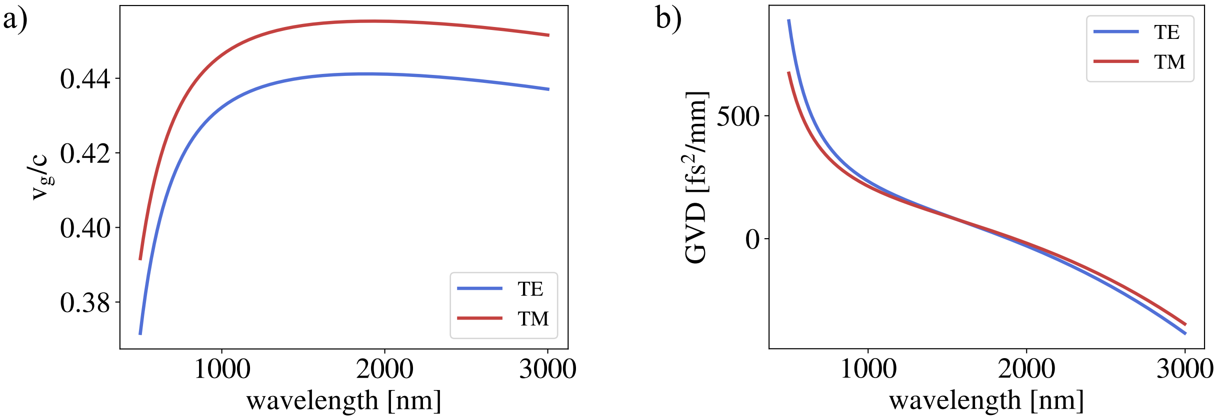

Figure 3.5: a) Group velocity of TE and TM polarised light in a 18 μm wide waveguide at a temperature of 180 °C. b) Group velocity dispersion for TE and TM polarisation for the same parameters.

Thus, we again depict the group velocity and group velocity dispersion of a 18 μm wide waveguide at a fixed temperature of 180 °C in Fig. 3.5. In part a) of the figure, we can see again that group velocity matching can be reached for the signal in TM polarisation and the idler in TE polarisation. Due to the different waveguide geometry, the figure differs from Fig. 3.3 and shows a drop in group velocity at longer wavelengths instead of a constant increase. As we extend our wavelength range into the mid-IR, we can also witness a different behaviour for the GVD. In Fig. 3.5 b), we observe a zero crossing around 1800 nm and negative GVD values for longer wavelengths. This region is called anomalous dispersion and is commonly observed in optical fibres. In these platforms, it is used for dispersion engineering [62, 66]. In our system, this behaviour allows us to find a pair of wavelengths at which the group velocities are matched and simultaneously exhibit opposite GVD.

We perform a series of steps to find a combination of temperature, poling period and pump wavelength that simultaneously fulfill the conditions of GVM and GVD cancellation. We fix the pump wavelength and vary the temperature of the waveguide to find the operation point for this specific pump wavelength.

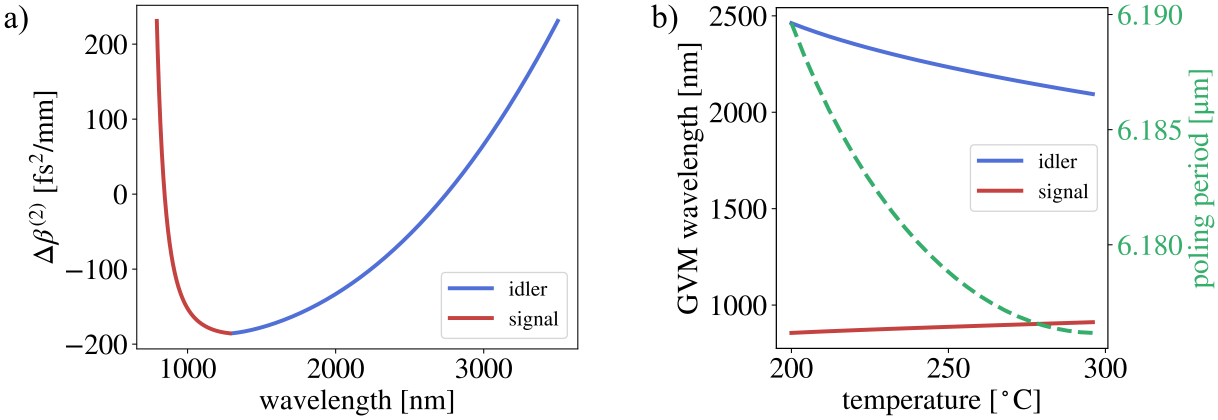

Figure 3.6: The process to achieve simultaneous GVM and GVD cancellation in a 18 µm wide waveguide at a fixed pump wavelength of 635 nm. a) The total second order dispersion $\Delta\beta^{(2)}$ in the JSA at a fixed temperature of 240 °C is calculated. The zero crossings determine the wavelengths at which the GVD of signal and idler cancel each other. b) The wavelengths where group velocity matching is fulfilled are calculated for a fixed pump wavelength with varying temperature. The temperature at which GVD cancellation and GVM are fulfilled simultaneously determines the wavelength combination, temperature and poling period of the operation point at this pump wavelength.

For each temperature, we first determine the poling period for a combination of signal and idler wavelengths that leads to no second order phase-mismatch $\Delta\beta^{(2)}$. GVD cancellation is reached at this combination of signal and idler wavelengths. Next, we calculate the total first order dispersion, i.e., the difference in group velocities between signal and idler at the previously found wavelength combination. We iterate this process for a range of temperatures until the point of simultaneous GVM and GVD cancellation is reached for a temperature at which the difference of group velocities is minimal. We illustrate the described procedure in Fig. 3.6, where we fix the pump wavelength to 635 nm and in a) calculate the second order of the phase-mismatch $\Delta\beta^{(2)}$ before finding the GVM wavelengths for different temperatures in b).

We note that the order of steps is crucial. optimisation for GVM in a first step would lead to an unambiguous combination of GVM wavelengths. As we have seen in Fig. 3.5 a), the group velocities reduce again at longer wavelengths. Hence this leads to two possible wavelength combinations of GVM and requires to fix a wavelength combination first by fulfilling GVD cancellation before reaching GVM.

Furthermore, we note that the GVM condition is more temperature dependent than the

GVD cancellation, since the wavelength combination that leads to GVD cancellation does not change more than a few nm for more than 100 K of temperature change. In turn, we observed that for GVM, the group velocity matched signal wavelength shifts by more than 50 nm from 855 nm to 911 nm for a temperature shift of 100 K.These studies of the parameter sets allow to deduce the design parameters for our source as well as the expected shift in the working point with temperature and poling period as the pump wavelength changes. The latter is depicted in Fig. 3.7. We can see that a specific waveguide temperature and poling period are required for any given pump wavelength in order to simultaneously fulfill GVM and GVD cancellation.

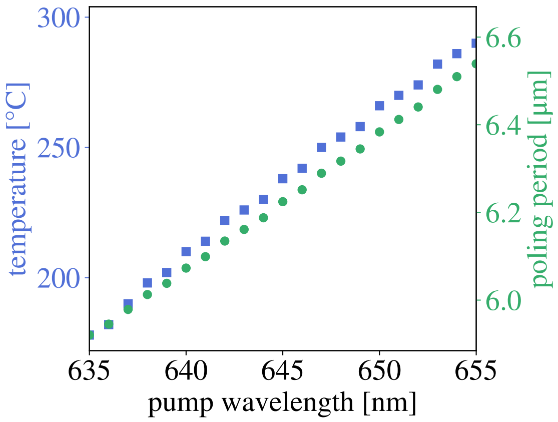

Figure 3.7: The waveguide temperature (blue) and poling period (green) that are required for a given pump wavelength to achieve simultaneous GVM and GVD cancellation in a 18 µm wide waveguide.

3.3 Waveguide and poling designs

We introduced the fabrication process of our periodically poled waveguides when discussing the parameters for our simulations which allow us to achieve GVM and GVD cancellation. Those parameters need to be given to our in-house cleanroom for sample fabrication. Therefore, we design photo-masks that will be used to define the areas of the titanium for in-diffusion in pattern that defines the waveguide geometry. Furthermore, we design poling masks that will be used for the deposition of gold electrodes in the following periodic poling process that leads to an inversion of the crystal domains [43].
In first iterations of the source's design, we observed a shift of the working point between the simulations and the experiment of 60 K for both sources. Therefore, the poling periods on the presented photo-masks are designed for temperatures around 120°C to end up at an actual operation around 180°C, which is required to mitigate photo-refractive effects. The resulting waveguide photo-masks with the annotated poling periods are depicted in the Appendix A.2.

3.3.1 NIR source design and characterisation

The NIR source has already been investigated in detail in [65]. Therefore, we will not characterise it in as much detail as the mid-IR source and perform this characterisation directly here together with the sources design parameters.
Historically, the source and its design are inspired by the quantum pulse gate [67], a device designed to perform a sum-frequency generation process which exhibits GVM of the pump and signal field at 860 nm and 1550 nm, respectively. Our PDC source has been adjusted to be pumped with a cw-laser around 514 nm and to generate broadband PDC light, thus inverting the original sum frequency generation process from the quantum pulse gate.

In our source design, we choose to fabricate waveguides with 40 mm length that are poled throughout the whole length. The poling periods range from 3.56 µm to 3.63 µm for waveguides with a width of 7 µm, to cover operation temperatures around 180 °C at the pump wavelength of 514 nm. Each waveguide chip contains 45 poled waveguides in groups of three waveguides each that have the same poling period. The layout of the photo-mask for the waveguides with annotated poling periods is shown in Fig. A.1 in Appendix sectionA.2.
The structure used to pattern the electrodes for poling is depicted in Fig. A.2 in Appendix section A.2. The poling structure is slightly broader than the actual waveguide onto which it will be patterned and exhibits a ratio of inversion over period of 0.45, which in fabrication results in a duty cycle of inverted and non-inverted crystal domains of 50/50 due to domain growth in the poling process.

Finally, we briefly present the temperature tuning behaviour in one of the first NIR sources. We note here that the poling period in this early sample has not been adjusted to the pump wavelength of the laser at 514 nm in these measurements yet. Therefore, GVM is observed at higher temperatures and longer signal wavelengths as in the ones used for the nonlinear interferometers in chapter 4 where an optimised source has been used. However, the qualitative behaviour of the sources is identical.The tuning of the signal spectrum has been measured on a single photon sensitive spectrometer while the temperature of the waveguide was varied in a home-built oven. The recorded signal spectra are presented in Fig. 3.8. We can qualitatively reproduce the expected behaviour in Fig. 3.4 b), namely, two peaks that are approaching each other for increasing temperature, ultimately forming a single, broadband spectrum. The spectra in the experiment exhibit a structure that deviates from the ideal sinc^2-shape. The additional peaks can be explained by inhomogeneities in the waveguide width and imperfections in the periodic poling [42].

We can see that these two parts of a peak merge at slightly different temperatures, such that the inner one, which is lower in height, merges at 516 K (top red curve) while the outer one merges later at 517 K (top green curve). As the inner maximum of the phasematching no longer overlaps with the pump function at this temperature, a cleaner broad spectrum can be achieved by heating to this specific temperature.

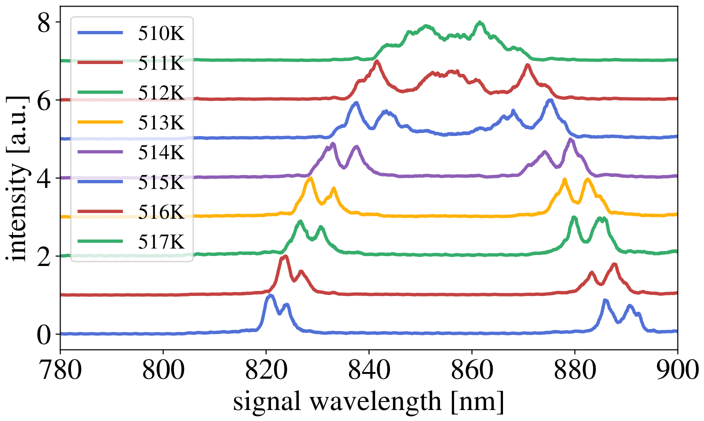

Figure 3.8: The signal spectrum for varying waveguide temperatures shows two peaks that eventually merge at the operation point where GVM is fulfilled.

This bespoke PDC source has been characterised in [65] to achieve a brightness of more than $1.5 \cdot 10^5 \frac{\text{pairs}}{\text{s}\cdot\text{mW}\cdot\text{GHz}}$, which is 3 order of magnitude beyond the brightness that has been achieved with comparable bulk nonlinear crystal sources. Furthermore, the source produces non-degenerate signal and idler photons with spectral bandwidths exceeding 7 THz. These properties match with the requirements for a non-degenerate photon-pair source in our nonlinear interferometer. Therefore, this source is implemented in our nonlinear interferometer in the NIR in chapter 4.

3.3.2 MIR source design

The MIR source is based on waveguides with titanium strips with widths of 18 μm, 20 μm, and 22 μm. To allow for maximum flexibility, the sample features poling periods ranging

from 5.8 µm to 6.3 µm. The waveguide chip has a length of 40 mm and comprises 15 groups of three periodically poled waveguides each. The mask layout is shown in Fig. A.3 in the Appendix A.2.
The poling patterns are designed analogously to the NIR case, whilst being adjusted for the varying waveguide widths and are shown in Fig. A.4.

Technical fabrication challenges

Although MIR waveguides have been produced by our clean-room in the past, there were no recent fabrications of waveguide chips with the required dimensions for the waveguides in this work. Since the production has not been optimised to our waveguide design, only a set of basic parameters existed for the fabrication of waveguides for the mid-IR. It therefore required intensive testing and optimisation of the process parameters to fabricate low loss, periodically poled waveguides for PDC in the mid-IR. Since many of the challenges have been overcome, we list them here briefly.
One challenge is connected to long diffusion times of 31 hours instead of 8.5 hours. Such long diffusion times are required as the thickness of the titanium strip has increased from 80 nm for our standard waveguides, which are designed for single spatial mode guiding at 1550 nm, to 140 nm. Furthermore, the titanium strips also increased in width from 7 µm to 18 - 22 µm to allow for guiding of light up to wavelengths of 4000 nm. The increased diffusion times lead to an increase in the fabrication time of these waveguides.
Moreover, the change in the waveguide width also leads to challenges for periodic poling. We realised that different widths of the poling windows on the same waveguide chip do not lead to satisfying results. This is because the applied current that is used to flip the domains can only be optimised for a specific poling area and, therefore, leads to under- or over-poling for the other ones. Thus, depending on the exact fabrication process of each waveguide chip, only one of the three waveguides in one group turned out to be poled correctly. Therefore, we visualised the domain walls with a second-harmonic microscope [68] for quality control. Studies of the poling quality over the entire length of a single waveguide showed strong variations in the poling quality. An image of three exemplary waveguide sections from these studies is shown in Fig. 3.9. The poling quality is linked to the widths of the three waveguides. Here, the waveguides, from top to bottom, exhibit widths of 20 µm, 22 µm and 18 µm and are from two neighbouring waveguide groups. While the waveguide with a width of 20 µm is properly poled, the one with 22 µm width is under-poled and the one with 18 µm width shows signs of over-poling. In the case of correct poling, the domain walls are separated and run through the whole waveguide. Under-poling leads to regions in the centre of the waveguide where no inversion and no domain walls are observed. Meanwhile, over-poling leads to merging regions that are larger than the intended poling period.

Furthermore, we require broadband dielectric anti-reflection coatings on the end-facets of the waveguides for our experiments. Those coatings are composed of thin layers of different dielectric materials. In our clean room, we use layer stacks made of SiO_2 and TiO_2. The combination of layers of different thickness and refractive index leads to constructive or destructive interference for incoming light in transmission or reflection, respectively.

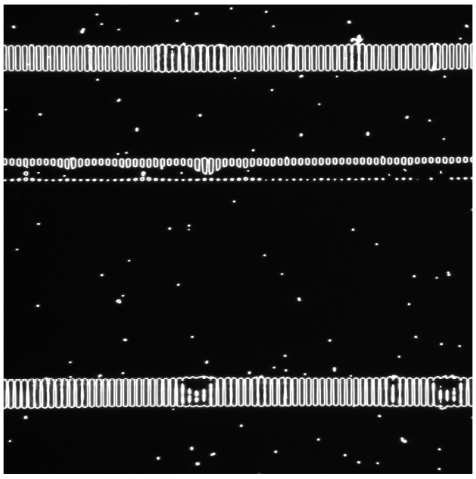

Figure 3.9: Second-harmonic image of the domain walls for three different waveguides on the mid-IR waveguide chip showing correct poling, under-poling and over-poling. Going from top to bottom, the waveguides have widths of 20 µm, 22 µm and 18 µm. We do not provide a scale here, since we are only interested in the overall poling quality.

The thickness of each layer scales with the wavelength and therefore increases for our field in the mid-IR. Additionally, many of those layers are required to achieve a uniform reflectivity over a wide range of wavelengths [69]. The fabrication of these thick layer stacks is time-consuming in production and prone to fabrication tolerances which limit their performance.

Additionally, we require dielectric mirrors to separate the pump, signal and idler light in order to guide and manipulate these fields separately in the interferometer. Such mirrors are not readily available and also had to be fabricated in-house. Fabrication of a dichroic mirror to split the signal and pump in the visible and NIR from the idler in the MIR was limited in performance due to the lack of absorption free substrate materials in the MIR and complex layer stacks [69]. Measurements of the transmission and reflectivity in the targeted wavelength bands of our in-house fabricated dichroic mirrors are shown in chapter 5, where we discuss our nonlinear interferometer in the MIR. We observe that the transmission of our dichroic mirrors at 3000 nm does not exceed 80%. This low transmission vastly limits the achievable visibility in later experiments with the MIR source as part of a nonlinear interferometer.

We were able to overcome some of the listed challenges by intense testing and optimisation. Thus, we are now equipped with sufficient knowledge to adapt the process parameter for the design and operation of a future generation of setups in this spectral regime. However, in some of the following experiments in chapter 5, we are still limited by the non-ideal elements in the setup.

3.4 MIR source characterisation

In this section, we characterise our newly designed PDC source for the generation of biphotons around 850 nm and 2800 nm from a cw pump laser at 650 nm. First, we show that the waveguides are actually guiding light at MIR wavelengths with low propagation losses and then discuss the properties of the PDC process. This process is based on the simultaneous matching of group velocities and the cancellation of the GVD of signal and idler.
This source and the PDC characterisation have been published in [70].

3.4.1 single-mode guiding and propagation losses

In a first step, we measure mode-images of the mid-IR field to ensure single-mode guiding at the required wavelengths for the three realised waveguide widths. We perform these measurements with a tunable cw-laser that emits light from 2 - 5 μm (Toptica DLC TOPO). The setup to record mode images and characterise linear propagation losses is presented in Fig. 3.10. In this setup, the polarisation of the laser is set by a half-wave plate before it is coupled into and out of the 40 mm long waveguide with CaF_2 lenses with focal lengths of 25 mm. Before detection, any light shorter than 1.9 μm is filtered out by a Germanium long-pass filter. This was necessary as the pump light of the TOPO system at 1064 nm leaks through the used port which emits the mid-IR light. We record the mode images on a mid-IR camera (ImageIR 5300) onto which we image the output of our waveguides. We use the built-in wavelength tuning capabilities of our laser to characterise the linear propagation losses of the mid-IR waveguide via a low-finesse Fabry-Pérot method [71]. To this end, the oscillations in the transmitted mid-IR power are recorded by a photoconductive mid-IR detector based on HgCdTe.

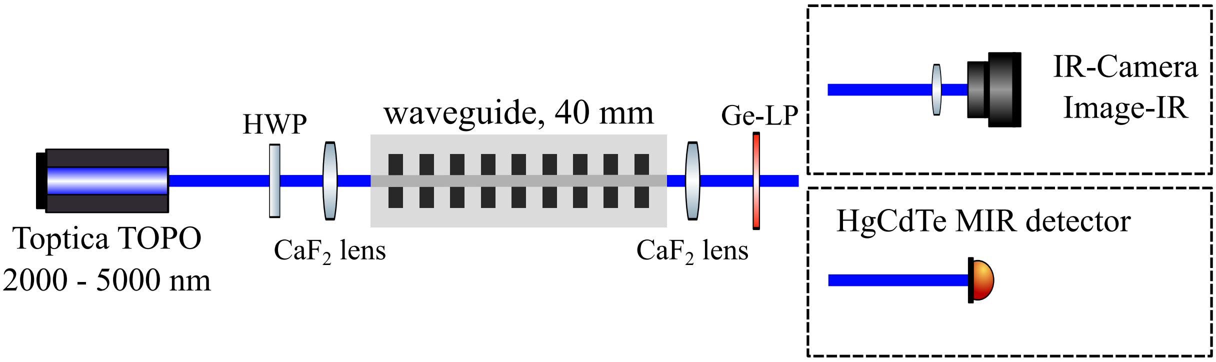

Figure 3.10: The experimental setup for measuring the MIR mode images and propagation losses of the waveguide at MIR wavelengths.

The images of the spatial mode within the waveguide are obtained by imaging the end-facet of the waveguide onto the camera. From the design of the waveguide widths, we expect the mid-IR light to be guided in the fundamental spatial mode. We observe this single spatial mode character in Fig. 3.11. Here, we recorded the modes for TE polarisation of the

MIR light at wavelengths of 2800 nm and 3800 nm. For each wavelength, waveguides with widths of 18, 20 and 22 µm have been investigated.
In all cases, single-mode guiding can be observed. We verified that guiding occurs only in the fundamental spatial mode by changing the in-coupling, which reduces the power in the waveguide but does not lead to a different guided spatial mode. For multi-mode guiding, we would expect that the input power would be distributed in higher order spatial modes upon coupling under an angle as the mode overlap for higher order spatial modes increases [72].

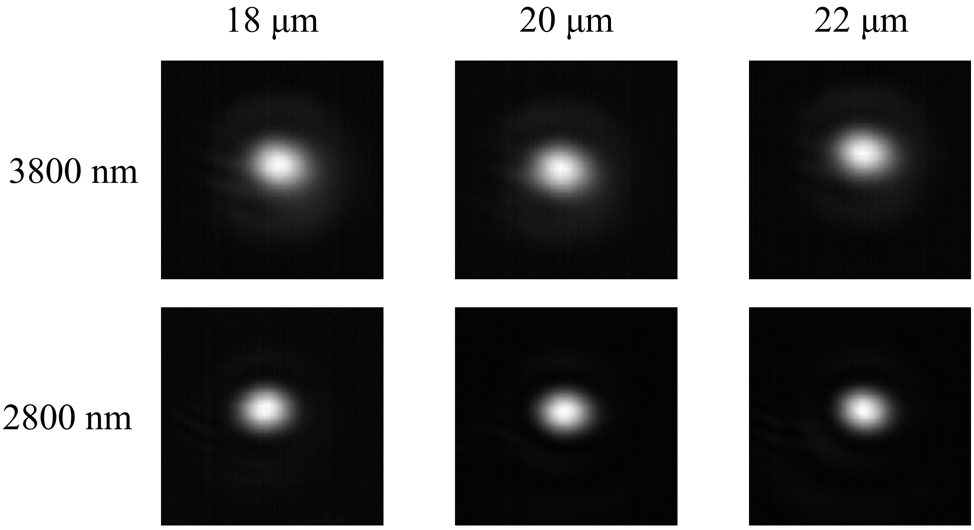

Figure 3.11: Images of the guided waveguide modes at 3800 nm and 2800 nm for waveguides with widths of 18, 20 and 22 µm. These images only serve as a qualitative comparison, as the magnification of the imaging setup was not extracted.

Subsequently, we characterise the propagation losses of the waveguide chips using a low-finesse Fabry-Pérot method [71]. An example of a typical measurement is depicted in Fig. 3.12 a), where we observe oscillations in the transmitted power at a mid-IR wavelength of 3000 nm as we slightly scan the wavelength. The propagation losses can be determined from the contrast of the oscillations.
In the analysis, we assume an end-facet reflectivity of 13.5% for TM and 12.5% for TE polarised light, which we obtained from the bulk refractive index of $LiNbO_3$, to calculate the propagation loss values. A typical measurement of the linear losses in TE and TM polarisation for a whole waveguide chip is presented in Fig. 3.12 b). In the measurement, we record only approximately 10 oscillations and observe visible differences in contrast of the recorded oscillations as the sample measurement in Fig. 3.12 a) shows. These are the sources for the error bars in Fig. 3.12 b), which depict the standard deviation of the extracted propagation losses. In most waveguides, we observe that the losses in TE polarisation are equal or lower to the ones in TM polarisation within the error bar. We expect to observe lower propagation losses for TE polarisation due to the titanium in-diffusion which leads to waveguides on the chip surface. Thus, TM polarised light is more prone to losses caused by defects on the surface. However, the error bars in the measurements are

too large to confirm this expectation. We measure typical propagation losses of less than 0.2 dB/cm for TE and TM polarised light for the majority of the waveguides. These low propagation losses make our waveguides suitable for loss-sensitive applications. For the experiment, we chose a waveguide with low linear optical losses for both polarisations and the matching poling period.

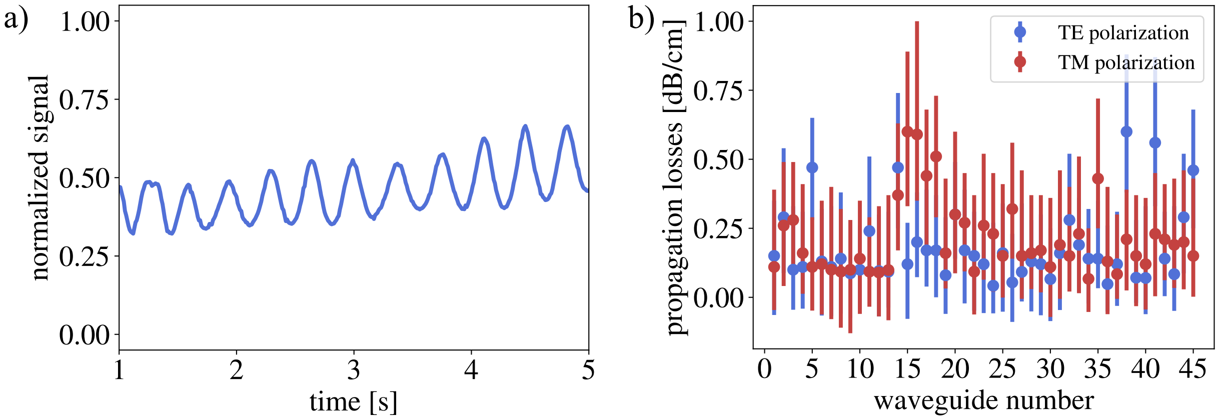

Figure 3.12: a) Example measurement with oscillations in the intensity of the mid-IR light at 3000 nm after the waveguide. The propagation losses can be determined from the contrast of the oscillations. b) Typical resulting propagation loss values across a full waveguide chip at 3000 nm for TE and TM polarisation.

3.4.2 PDC characterisation

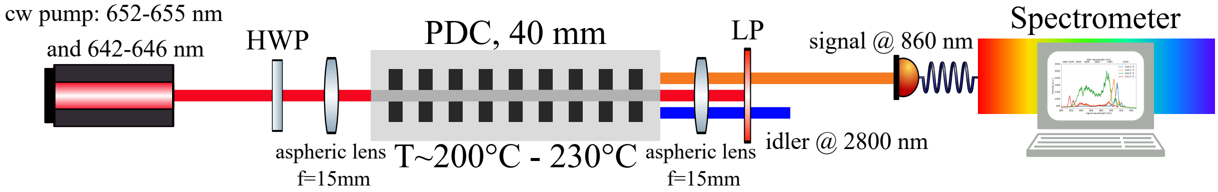

Figure 3.13: The experimental setup for measuring the signal spectrum from our ultra-broadband PDC source.

The setup to measure the generated signal spectrum is depicted in Fig. 3.13. We use one of two different external cavity diode lasers (TOPTICA DL pro) as pump lasers to address working points at different poling periods and waveguide temperatures across the sample. These lasers can be tuned from 652 nm to 655 nm and from 642 nm to 646 nm, respectively. We monitor the wavelength of the lasers with the same spectrometer that we use to measure the signal spectra from the PDC process. To generate PDC with the first laser as a pump, the waveguide sample is heated to about 230 °C while a temperature of around 200 °C is sufficient for the second laser. We designed the sample to operate at these temperatures to mitigate photo-refractive effects [73]. We set the sample temperature with a home-built copper oven via a resistive heating cartridge and PT100 temperature sensor which are driven by a temperature controller with integrated PID loop (Oxford Instruments MercuryiTC). The generated signal photons at a central wavelength of 860 nm are separated from the pump field by a 735 nm long-pass filter, coupled into a single-mode fibre and detected using a single-photon sensitive spectrometer (Andor Shamrock SR-500i spectrograph with Newton 970P EMCCD-camera).

We observe a shift between the measured spectra and the simulations that can be compensated by adjusting the pump wavelength by $-2,4$ nm and the waveguide temperature by -40 K when going from the experiment to the simulations. These shifts are applied in all the following results. These shifts are expected due to the previously discussed offsets in the used Sellmeier equations.

Results PDC characterisation

The general overview of the expected signal emission with varying waveguide temperature is depicted for pump wavelengths that are below, at and above the design wavelength in Fig. 3.14. This representation can be linked to the JSA where a shift in temperature leads to a shift of the phasematching function with respect to the pump and therefore changes their overlap as we already saw in Fig. 3.2. Here, we present the spectral emission at the signal and corresponding idler wavelengths, which are the marginal distributions in the JSA. A single signal spectrum is then given by a horizontal cut through the figure, which corresponds to one fixed temperature.

We observe a change in the curvature of the temperature dependent spectral emission when changing the pump wavelength, which leads to different spectral emissions while changing the temperature. One can see that only for the design wavelength of 646.5 nm, a broadband emission can be reached, which is observed as a plateau parallel to the x-axis in this figure. When a pump wavelength of 648.75 nm that is longer than the ideal working point is used, no such situation is reached and the emitted spectrum stays rather narrowband. Meanwhile, the signal wavelength shifts from higher to lower values when increasing temperature. In the case of a too short pump wavelength of 644.25 nm, the emitted signal spectrum exhibits up to three peaks while increasing the waveguide temperature. Still, no broadband emission is reached.

We note here that, in contrast to the NIR source, a change in the pump wavelength can not be compensated by the temperature to reach a similarly broadband emission. This is because, for this source, both GV matching and GVD cancellation have to be fulfilled simultaneously, which leads to a more strict set of requirements and thus only allows for single pump wavelength that matches a given poling period for ultra-broadband emission.

We support these simulations by investigating the signal spectra for the three cases. However, we used the two mentioned pump lasers for this study, such that the actual values of the pump wavelength differ from the ones in Fig. 3.14 except for the case of a too short pump wavelength.

We begin by investigating the case where the pump laser is set to the design wavelength.

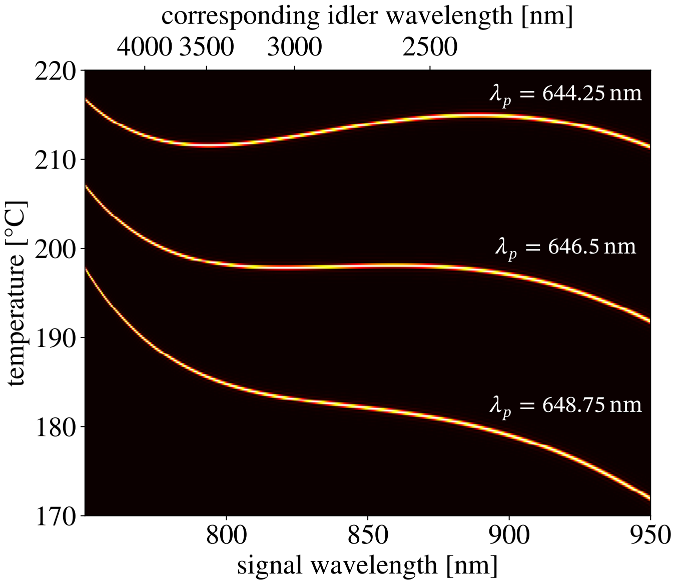

Figure 3.14: The resulting signal spectrum with varying temperature when the pump wavelength is set above (644.25 nm), at (646.5 nm) or below (648.75 nm) the design wavelength.

In Fig. 3.15 a) the temperature tuning curve is shown with horizontal cuts that represent the temperatures at which the signal spectra in figure 3.15 b) have been measured. These spectra are compared to the respective simulations and show good agreement in their position and bandwidth. Deviations in the shape of the recorded spectra can be attributed to imperfections in the phasematching, which lead to side lobes and deviations from the ideal sinc^2-shape, as well as to the coupling to single-mode fibres via lenses that are prone to chromatic aberrations. Overall, a bandwidth of 25 THz can be reached, spanning a corresponding idler range from 2400 nm to 3000 nm, as indicated on the top x-axis. In this spectrum, we can observe a dip in the spectral emission around 850 nm, which corresponds to an idler wavelength of 2850 nm. We can identify this feature as a signature of absorption at the mid-IR wavelength due to residual OH$^{(-)}$ groups. This absorption is known to occur in lithium niobate and depends on the concentration of the impurities [74]. We will revisit this effect again when incorporating our source into a nonlinear interferometer in chapter 5.

In a next step, we investigate the case of a too long pump wavelength, where we can no longer reach the same spectral bandwidth by temperature tuning. We tested this by setting the pump wavelength to different values while tuning the temperature. A comparison between simulations and the experiment is shown in Fig. 3.16. We extract the bandwidth of the signal spectra at 80 % of the maximum in order to reduce the impact of side lobes in the phasematching on the result. However in the experimental data in Fig. 3.16 b), oscillations in the output spectra caused by side lobes still influence the results, as can be seen from the oscillations in the bandwidth for the case of 653.1 nm. Overall, we observe that the maximum bandwidth increases as the pump wavelength gets closer to the design pump wavelength of 652.3 nm. The temperature at which the maximal bandwidth is reached shifts to

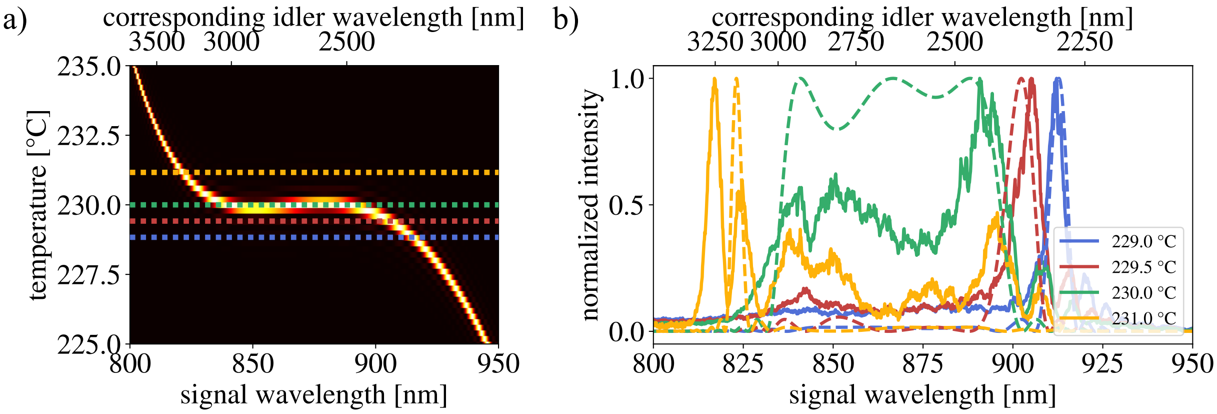

Figure 3.15: a) The simulated generated spectra at the design pump wavelength of 652.3 nm for different temperatures. The generated signal (idler) wavelengths are indicated on the bottom (top) x-axis. Coloured, dashed lines show the temperatures at which the spectra were measured experimentally. b) Measured signal spectra at different temperatures (solid, colour lines) and the corresponding simulated spectra (dashed, coloured lines).

higher temperatures for smaller pump wavelengths. Furthermore, the temperature range over which a broadband emission can be observed narrows down as the pump wavelength approaches the operation point at 652.3 nm. One implication from these measurements is that a high temperature stability is necessary to achieve the maximal bandwidth and that a less broad emission does not require this stability. This can be seen from the fact that the FWHM in temperature tuning of the simulated bandwidths amounts to less than 0.2 K at the operation point with a pump wavelength of 652.6 nm and increases to 2.5 K at the pump wavelength of 654.6 nm.

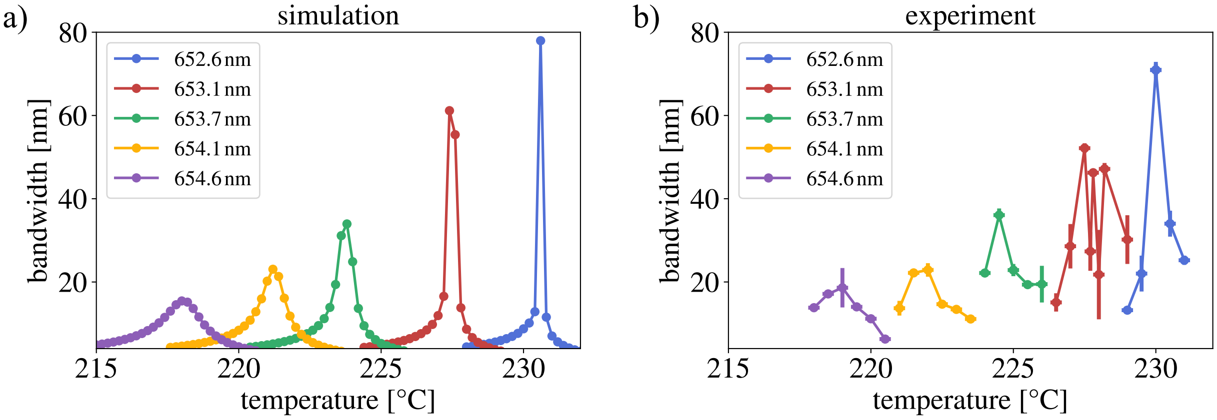

Figure 3.16: Change of the generated signal bandwidth for different pump wavelengths above the design wavelength while varying waveguide temperatures. a) Simulations for the bandwidth of the signal spectrum at different temperatures and pump wavelengths. b) The experimental spectra show the same increase in spectral bandwidth for decreasing pump wavelengths.

Finally, we investigate the situation of a pump wavelength that is shorter than the design pump wavelength. Here, the signal spectrum exhibits two regions that show a broad spectral emission during the temperature tuning. This is shown in comparison to simulations in Fig. 3.17. For low temperatures, a narrow peak at a long signal wavelength is present. However, as the temperature increases, a broad peak at a short signal wavelength forms, while the peak at the longer wavelength shifts towards shorter signal wavelengths. As the broad peak splits, three peaks emerge of which the middle one moves towards longer wavelengths for higher temperatures eventually leading to the formation of a second broadband peak. Finally, at high temperatures, only a single peak at a short wavelength is present. This behaviour can be captured in simulations as well as measurements. Low peak heights at the short wavelengths are caused by non-optimised coupling to the detector at these wavelengths due to chromatic aberrations. The presence of a signal in the measurements at wavelengths where no signal is predicted by the simulations is due to the side lobes in the phasematching which result in additional peaks.

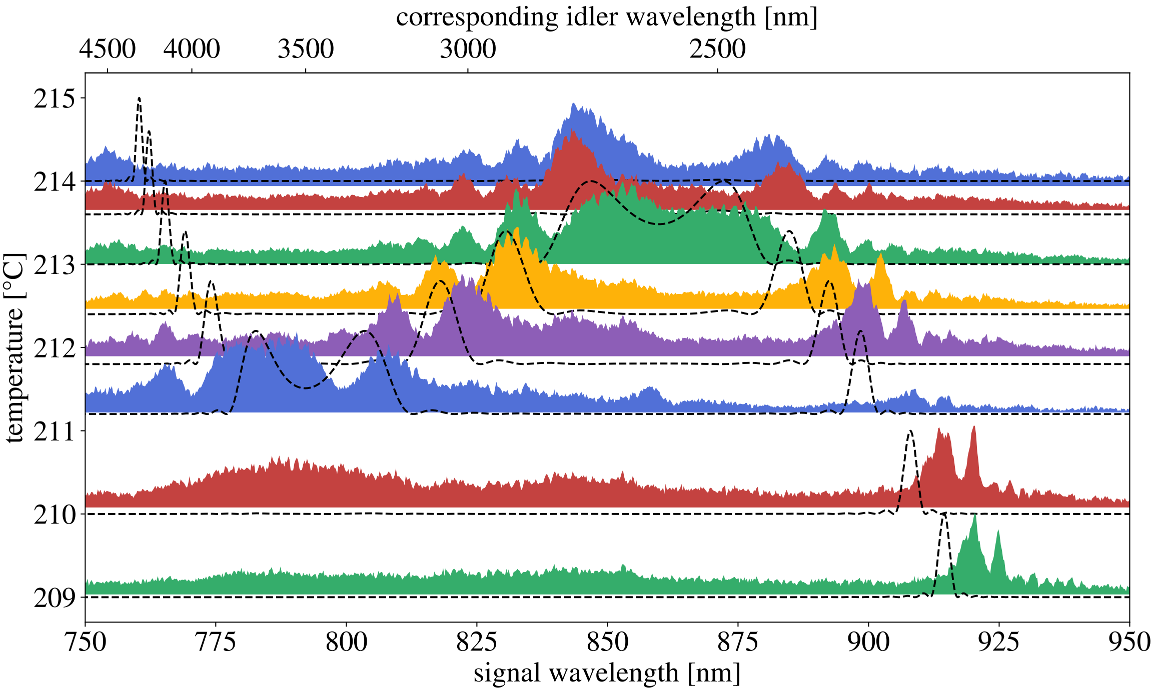

Figure 3.17: The change in the signal spectrum with temperature for a pump wavelength of 644.25 nm. Each spectrum is normalised to its maximum. This behaviour matches with the expected shape of the temperature tuning curve for a too short pump wavelength. The dotted curves represent the simulations at the corresponding temperatures.

3.4.3 Brightness estimation

The brightness of a source is an important metric for applications in metrology or sensing as it allows to use resources more efficiently and operate with a higher signal-to-noise ratio at a given pump power. Therefore, we would like to know the brightness of the MIR source. However, we are not able to measure coincidence count rates between the signal and idler photons, which would allow to differentiate counts which are caused by actual bi-photon events from the ones caused by background such as fluorescence and noise. To overcome this problem, we simultaneously measure the total signal photon counts on an avalanche photo-diode (APD) and the corresponding spectra on a spectrograph. This makes it possible to estimate a lower bound on the bi-photon rate, normalised to the pump power and spectral width of the signal marginal spectrum.

In a first step, we want to calibrate the counts on the spectrograph against the counts on the APD. We therefore integrate the counts on the spectrograph over the whole spectrum, which is depicted in Fig. 3.18 a). We measure the signal counts at the same pump powers with attenuation using a calibrated ND02 filter with a transmission of $T = 1.35\,\%$ on the APD. Furthermore, we assume a quantum efficiency of 45 % for the APD and an end-facet reflectivity of the waveguide of 14.78 % for PDC light at 850 nm. We will use these correction factors later to calculate the actual counts generated by the source. A deviation from these values will affect the inferred brightness of the source.

After recording the counts from the APD and the spectrograph, we retrieve a scaling factor between the two, which allows us to convert a part of the spectrally resolved counts to the equivalent number that would be detected on the APD. This scaling factor lies between 60 and 90 and depends on the pump power, as we can see in figure 3.18 b). Since both curves show a similar behaviour, we can use the information of the spectral measurements and apply them to the APD counts in order to retrieve the actual PDC count rates.

By detuning the waveguide temperature or pump wavelength, we can identify a background of fluorescence counts. These counts do contribute to the count rate on the APD, but are not part of the PDC process that we want to use in the experiment. They would be eliminated when using coincidence detection.Here, we assume these fluorescence counts to be constant over the whole spectrum as indicated in figure 3.18 a). We evaluate the ratio of fluorescence counts C_{fl} to the total counts in the spectrum C_{spec} and apply this ratio to the measured APD count rates C_{APD}. This allows us to calculate a lower bound for the pair rate from the PDC C_{PDC} from the remaining counts as

$$C_{PDC} = C_{APD} - \frac{C_{fl}}{C_{spec}} \cdot C_{APD}. \tag{3.12}$$

We end up with a lower bound for the brightness of around $0.6 \cdot 10^3 \, \frac{\text{pairs}}{\text{s·mW·GHz}}$. However, in Fig. 3.18 c) we can see that the brightness actually increases with increasing pump power up to a value of $1.2 \cdot 10^3 \, \frac{\text{pairs}}{\text{s·mW·GHz}}$. A possible cause for this behaviour is a difference in the scaling of the fluorescence rates, which we assumed to be linear. Furthermore, we note that the waveguide is supporting multiple spatial modes at the pump wavelength, such that a redistribution of the pump field among those modes at different pump powers might also influence the scaling of the PDC and fluorescence rates.

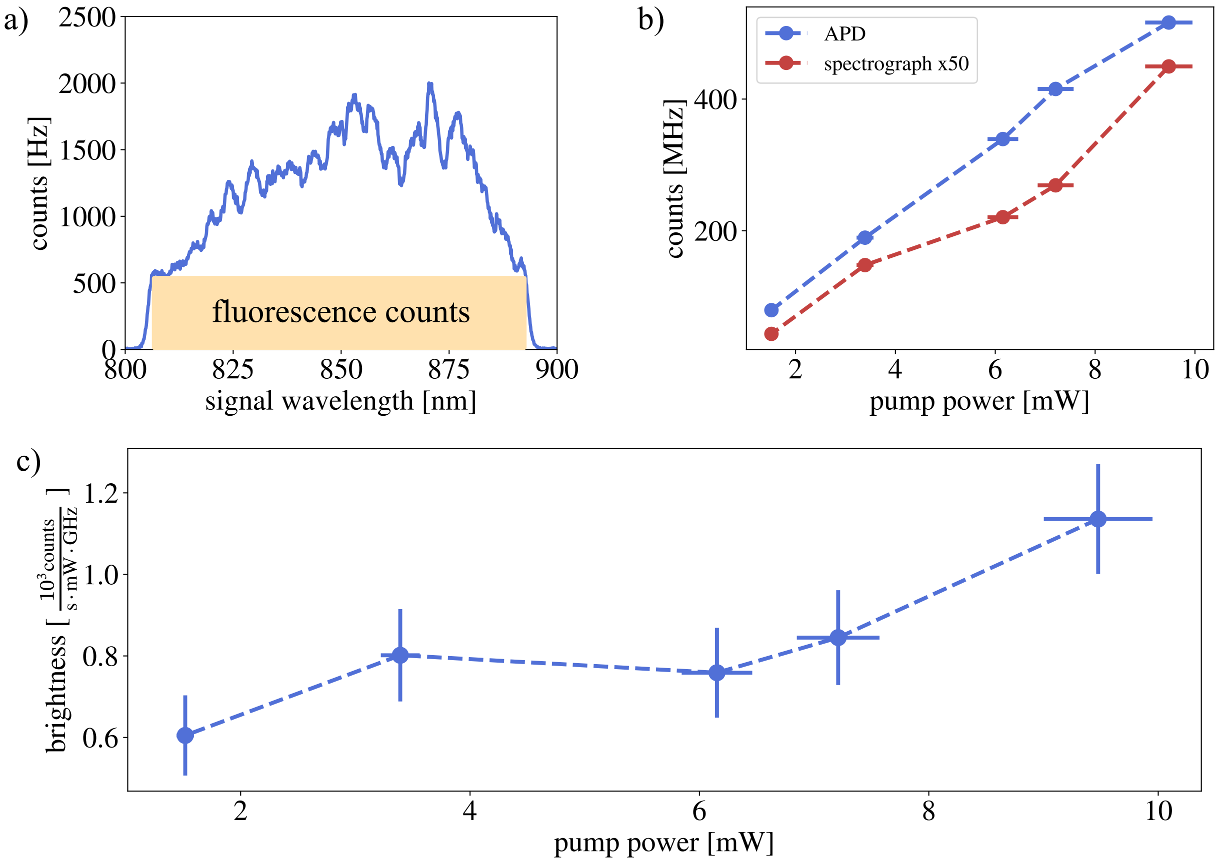

Figure 3.18: a) Spectrum of the mid-IR PDC source on the spectrograph, showing contributions fluorescence counts to the total amount of counts. b) Count rates recorded for the APD and the spectrograph at different pump powers. The counts of the spectrograph have been multiplied by a factor of 50 for better comparison. c) Estimated brightness for different pump power levels.

This estimation does not contain coupling efficiencies to the detection and, therefore, only provides a lower bound. We can take into account an estimated coupling efficiency of 20 %, which is reasonable for a not mode-matched fibre-coupling and has previously been measured with an alignment laser at 850 nm. With this we arrive at a pair rate on the order of $5 \cdot 10^3 \, \frac{\text{pairs}}{\text{s} \cdot \text{mW} \cdot \text{GHz}}$.

3.4.4 Comparison to state of the art bi-photon sources

We can put the two developed sources into perspective with other type 0 or type II sources in the literature, based on bulk or guided-wave PDC processes, and compare their brightness. To this end, we list typical examples in table 3.1 and thereby extend the comparison between broadband PDC sources made in [65].

We can observe that our sources are at least of the same brightness or even brighter than other sources in the literature based on bulk nonlinear crystals. Sources based on bulk crystal achieve similar or even larger spectral bandwidths, however, at the cost of a low brightness. Guided-wave PDC sources show a high brightness in general and are comparable to the ones reached by our sources. However, unless techniques such as GVM are employed, their spectral bandwidths are rather limited. Therefore, Type 0 sources are frequently used in order to obtain large spectral bandwidths with a high brightness due to the larger nonlinear coefficient in LN for the Type 0 process. However, this comes at the cost of indistinguishable signal and idler photons as they are generated in the same polarisation and often also the same wavelength.

To conclude, we can say that normalising the brightness of a source to its spectral bandwidth leads to a value which is ultimately limited by the nonlinear coefficients and the confinement of the light field. Thus, future platforms such as thin-film lithium niobate on insulator, which feature a high confinement, the possibility for dispersion engineering by adjusting the waveguide geometry and the high nonlinear coefficient of LN are promising candidates for very bright and broadband bi-photon sources for similar applications [75].

Table 3.1: Comparison of broadband Type II and Type 0 PDC sources in the literature in lithium niobate (LN) and KTP together with the developed sources based on GVM and GVD cancellation in this work. The presented sources are highlighted in bold font.

Source	Material	Phasematching	Bandwidth [THz]	Brightness $\left[\frac{\text{pairs}}{\text{s}\cdot\text{mW}\cdot\text{GHz}}\right]$
Type 0 [76]	WG LN	degenerate Type 0	5.2	$1.27 \cdot 10^6$
Type II [77]	WG KTP		0.3	$2.43 \cdot 10^5$
Type II [78]	WG LN		0.22	$1.13 \cdot 10^5$
Type 0 [79]	LN	degenerate Type 0	7	$2.45 \cdot 10^4$
Type 0 [80]	KTP	degenerate Type 0	8.2	$3.24 \cdot 10^4$
Type 0 [19]	LN	GVM	21	$< 7 \cdot 10^3$
Type II [81]	KTP	GVM	25	no information
Type II WG (NIR) [65]	WG LN	GVM	7	$1.5 \cdot 10^5$
Type II WG (MIR) [70]	WG LN	GVM + GVD cancellation	25	$> 10^3$

Summary

In this chapter, we presented our methods to model and design our integrated waveguides which serve as broadband, non-degenerate PDC sources as the main building block of the nonlinear interferometer. We introduced the PDC source in the NIR based on group velocity matching that allows for a tunable spectral emission, a bandwidth of up to 7 THz and a brightness of $10^6\,\frac{\text{pairs}}{\text{s}\cdot\text{mW}\cdot\text{GHz}}$. The newly developed MIR source was characterised in detail. The measured PDC spectra from this source showed good agreement with the simulations and allow for a broad spectral bandwidth of 25 THz. We estimated a lower bound of the source brightness to be $1.2 \cdot 10^3\,\frac{\text{pairs}}{\text{s}\cdot\text{mW}\cdot\text{GHz}}$. Both of these sources can now be applied in the following two chapters at the heart of the respective nonlinear interferometers.

4

Nonlinear interferometers in the near infra-red

The use of nonlinear optical elements for the generation of quantum states of light within interferometers has been proposed in the 1980s by the introduction of the SU(1,1) interferometer [34]. Since then, they have been used in experiments to increase phase sensitivity [54, 60, 82], to achieve quantum state manipulation [58, 83] and to realise measurements with undetected photons.

The first measurements with undetected photons were restricted to imaging [13, 15], where a setup based on the concept of induced coherence without induced emission has been employed after being first demonstrated in 1991 [14]. Shortly after, applications in the realm of spectroscopy, optical coherence tomography and more have evolved [12, 19, 20]. These systems mostly use a Michelson geometry for the interferometer design, which we will call the SU(1,1) geometry, and employ bulk nonlinear crystals as active elements in these interferometers. Meanwhile, hybrid approaches, which operate simultaneously in the SU(1,1) and induced coherence scheme, are used to switch between sensing modes [84].

In order to move towards an integrated quantum sensor, we want to find the best suited setup that accommodates the requirements posed by integrated waveguides since they exhibit fundamentally different properties as compared to the commonly explored bulk nonlinear crystals. Therefore, we will explore the capabilities of both the commonly used SU(1,1) scheme and the induced coherence scheme for the operation of a nonlinear interferometer based on integrated waveguides as sources for broadband, non-degenerate PDC.

We first present our developed setups in detail and discuss the performed experiments towards an integrated quantum sensor in the following. In this chapter, we realise nonlinear interferometers that are based on our NIR source with bi-photons at 830 nm and 1400 nm. We develop a technique to measure the bi-photon correlation time within an SU(1,1)-interferometer, as this correlation time is an important benchmark for applications in the realm of ultra-fast spectroscopy. Finally, we realise optical coherence tomography measurements in both interferometer geometries and compare their performance regarding the development of a future integrated sensor.

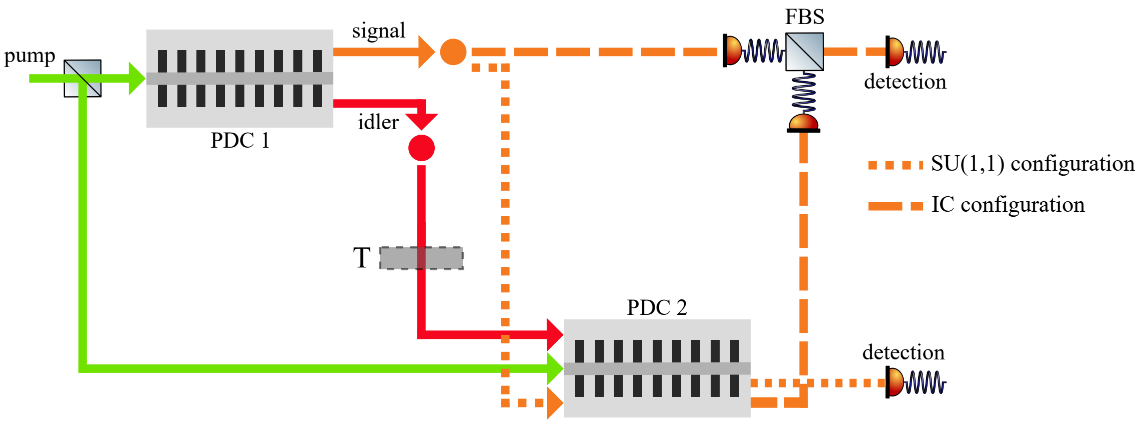

Figure 4.1: A nonlinear interferometer realised in the IC and SU(1,1) geometry. Both setups enable to measure the transmission T of an object in the idler arm by only detecting the signal photons.

4.1 Experimental setups

We start by presenting the different experimental realisations of nonlinear interferometers that we use for our experiments. At the heart of all setups in this chapter is a nonlinear waveguide, acting as a PDC source and generating group velocity matched signal and idler photons at 830 nm and 1400 nm. We presented the characteristics of that source in chapter 3 and discussed its flexibility in generating PDC spectra with different bandwidths by varying the waveguide's temperature.

In this work, we realise two different schemes, namely the induced coherence (IC) and the SU(1,1) geometry, which we introduced in chapter 2. These two geometries are depicted in Fig. 4.1. The conceptual difference between them lies in the place where the interference occurs. In the IC geometry, signal-signal interference is observed after an external beamsplitter, where the signal beams from the first and second pass are overlapped. Meanwhile, in the SU(1,1) scheme, interference can be observed directly in the signal beam after the second PDC source, as both beams are aligned through the second source. We will discuss the experimental differences between the two realisations below. In order to keep track of the currently used setup design in the following experiments, we will revisit these schematic sketches in the corresponding sections with an emphasis on the specific changes which are investigated in detail there.

4.1.1 SU(1,1) interferometer with differential pumping

The first setup is shown in Fig. 4.2 and resembles a classical interferometer in Michelson geometry, where the 40 mm long waveguide replaces the classical beamsplitters. This waveguide is equipped with anti-reflection coatings for all three fields, i.e., pump, signal and idler, on both facets. These and the following coatings have been designed and fabricated in-house.

We are utilising a differential pumping scheme to change the parametric gains g_1 and g_2 for the two PDC processes in the interferometer. This differential pumping is realised as the pump laser is split up into two different paths by a half-wave plate (HWP) and a polarising beam splitter (PBS). This allows to adjust the ratio of the pump power for the first and second process, while keeping the overall power constant. Each pump path exhibits an additional HWP to optimise the pump polarisation for the PDC process.

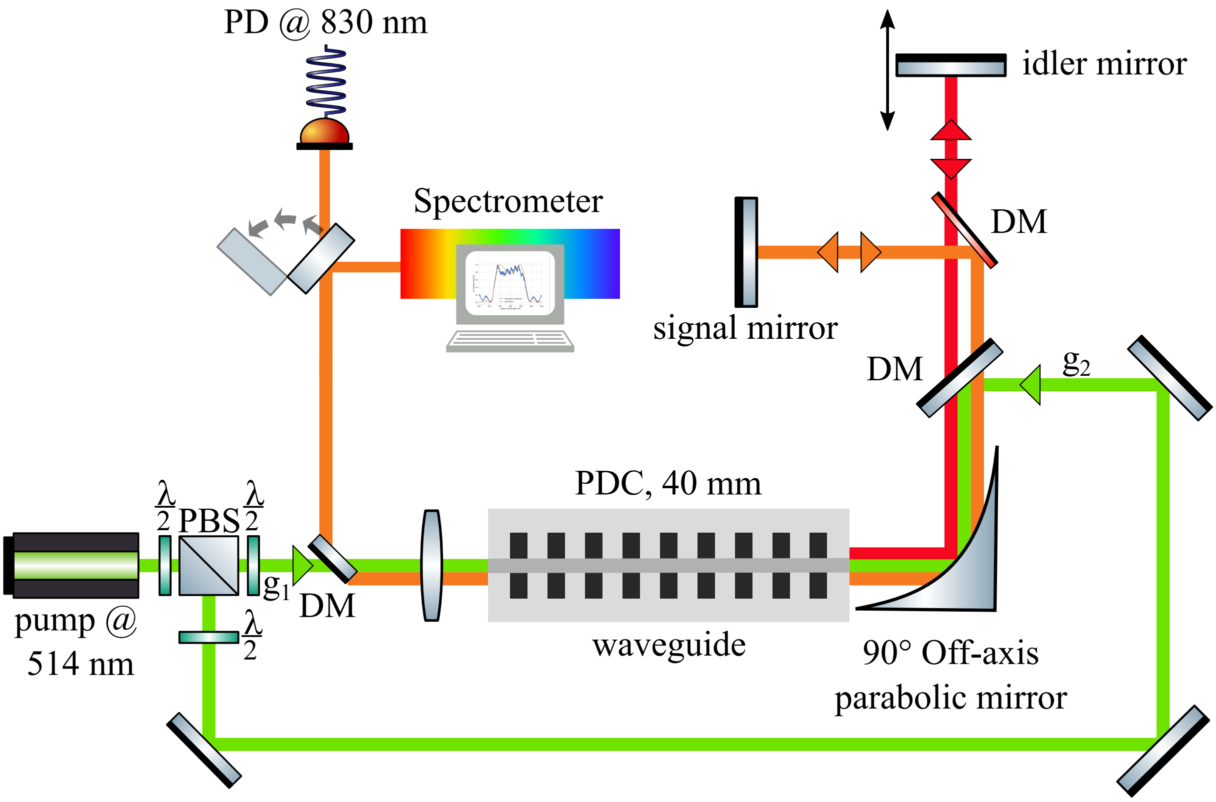

Figure 4.2: The experimental setup consisting of a 40 mm long waveguide as a source for PDC photons in a Michelson-geometry. A differential pumping scheme with parametric gains g_1 and g_2 for the first and second process is implemented. The end-mirror of the idler arm can be moved by a motorised stage. An off-axis parabolic mirror collimates the pump, signal and idler fields and focuses them back into the waveguide. After the second interaction, signal and idler photons are separated from the pump with a dichroic mirror (DM). Interference in the signal field is detected by a spectrograph or an avalanche photo-diode (PD) to record spectral or temporal interferograms, respectively.

In the setup, we use a cw-laser at 514 nm (Coherent Genesis CX-514) to generate signal and idler. After the first PDC process, the signal and idler fields are collimated by a 90° off-axis parabolic mirror, split up by dichroic mirrors and sent into separate arms. The end-mirror in the idler arm is placed on a motorised stage (PI M111.1DG), which enables to introduce a time delay between the signal and idler photons before they are both coupled back to the waveguide via the parabolic mirror. After coupling the pump light for the second pass to the waveguide, the second PDC process once again generates signal and idler. The signal and idler photons from the superimposed first and second process are collimated by the original in-coupling lens and separated with dichroic mirrors. Finally, interference can be observed by detecting the signal field with a spectrograph or an avalanche photodiode to retrieve spectral and temporal interferograms as a result of our standard measurement techniques, which we will discuss below.

4.1.2 SU(1,1) interferometer with single-sided pumping

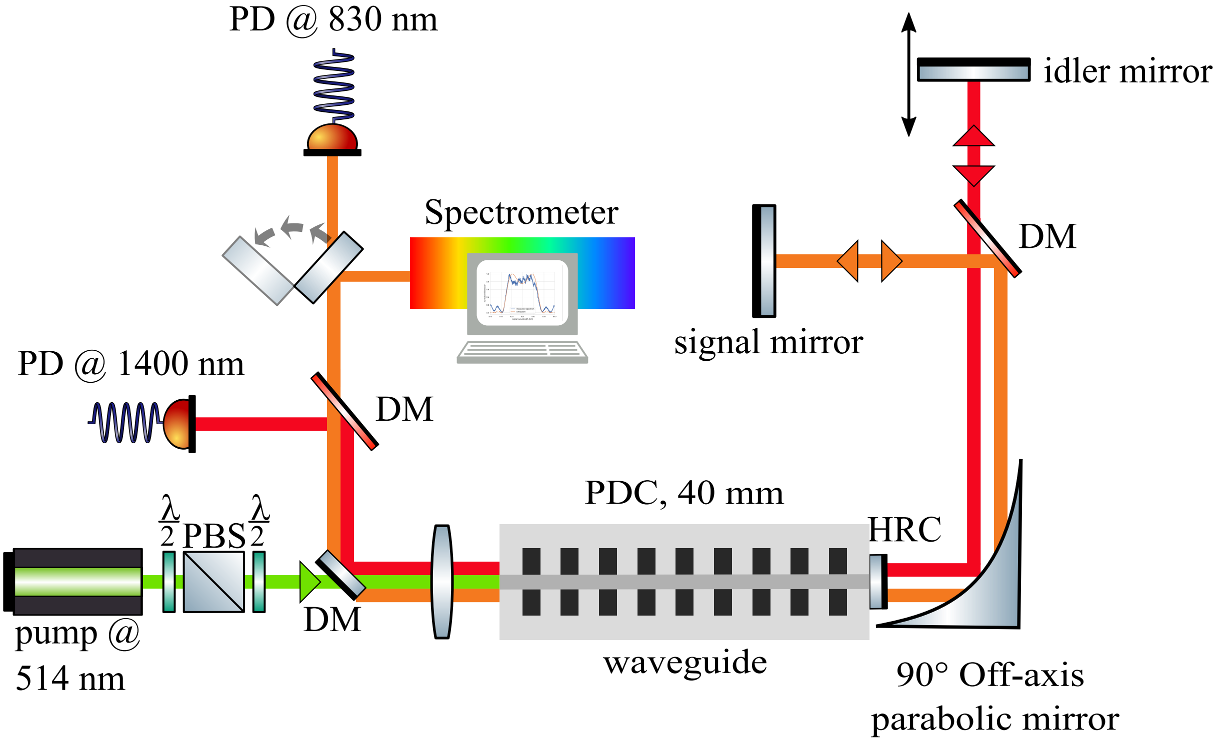

Figure 4.3: In the SU(1,1) interferometer with single-sided pumping, the pump light is reflected at one of the waveguide end facets by a high-reflectivity coating (HRC). This leads to almost equal parametric gains for both processes. The setup is identical to the one in Fig. 4.2 apart from an additional DM which is used to separate the idler light and detect it on an APD.

A further developed and simplified version of the setup in the SU(1,1) geometry only employs pumping of the waveguide from one side and is depicted in Fig. 4.3. Here, we use a waveguide with a high-reflectivity coating (HRC) for the pump wavelength at 514 nm to ensure the same pump mode in forward and backwards pumping. This is crucial since the waveguide supports multiple spatial modes at the pump wavelength, which all lead to slightly different generated PDC spectra as the light's propagation constant β inside the waveguide depends on the spatial mode. Therefore, phase-matching is fulfilled at different wavelength combinations for different spatial modes [85].

Furthermore, this design reduces the amount of optical elements in the setup and keeps a potential sample site in the idler arm free of any pump light as it does not exit the waveguide after the first pass. However, this setup does not allow for gain optimisation and leads to almost equal pump gains for the first and second stage of the interferometer under the assumption that the coating is ideal and the waveguide is lossless. This gain ratio is not optimal for the highest interference visibility in the presence of losses of the signal and idler due to unavoidable coupling losses when combining the fields in the waveguide for a second pass.

In many further aspects, this setup is similar to the general case with differential pumping. One difference between the setups is that we depicted the detection of the idler light after the waveguide with another avalanche photo-diode, as we will be using the temporal interferograms at the idler wavelength in the following correlation time measurements. At this point, we note that the setup has been designed such that we can switch between the differential and one-sided pumping setup by exchanging the used nonlinear waveguide sample which features either highly reflective or anti-reflective coatings for the pump light at one end-facet. The pump path can then be adjusted by rotating the HWP in the previous setup to full transmission of the pump laser power in the first process.

4.1.3 Induced coherence interferometer

In contrast to the previous two setups, the induced coherence scheme does not contain back-coupling of the signal photons into the waveguide after the first process. In this setup, the signal photons from both processes are rather interfered on a linear 50:50 beamsplitter. Although this scheme was the first to be used in demonstrations of the effect of induced coherence without induced emission in 1991 [14] and has been used in the earliest experiments that demonstrated imaging with undetected photons [13], it has since been replaced by the SU(1,1) scheme above. This is because the latter is often considered more practical when working with bulk nonlinear crystals, as it requires fewer optical components [19, 86].

However, we found that this scheme provides practical advantages when working with integrated waveguides. This is due to the guiding of multiple spatial modes in the waveguide at the signal wavelength of 830 nm. The presence of multiple spatial modes in the waveguide at the same time can lead to interference in the spectral intensity. This happens if the photons of the first PDC process are coupled back into a spatial mode different from the one in which the photons from the second process are generated. Additionally, the field at 830 nm experiences large amounts of second order dispersion due to the waveguide material, as we will see later when measuring the bi-photon correlation time. This additional dispersion can be avoided by interfering the signal fields at an external beamsplitter.

The corresponding setup is shown in Fig. 4.4 and largely resembles the previous ones. However, the signal field from the first process is not directed back through the waveguide but to a fibre-coupling. From there, the signal fields from both processes are interfered on a 50:50 fibre beamsplitter (Thorlabs TW805R5F2). One port of this beamsplitter is used to detect the spectral interferogram and the other port can be used to detect the temporal interferograms allowing us to simultaneously monitor interference effects in the spectral and temporal domain. In order to match the path lengths of signal and idler, an additional delay line has been incorporated in the signal path from the first process to the fibre-coupling, which is not shown in the figure. This delay can be used to align the setup for a coarse temporal matching between the signal and idler paths from the first process and the second process to simultaneously meet at the beamsplitter, as described in [13].

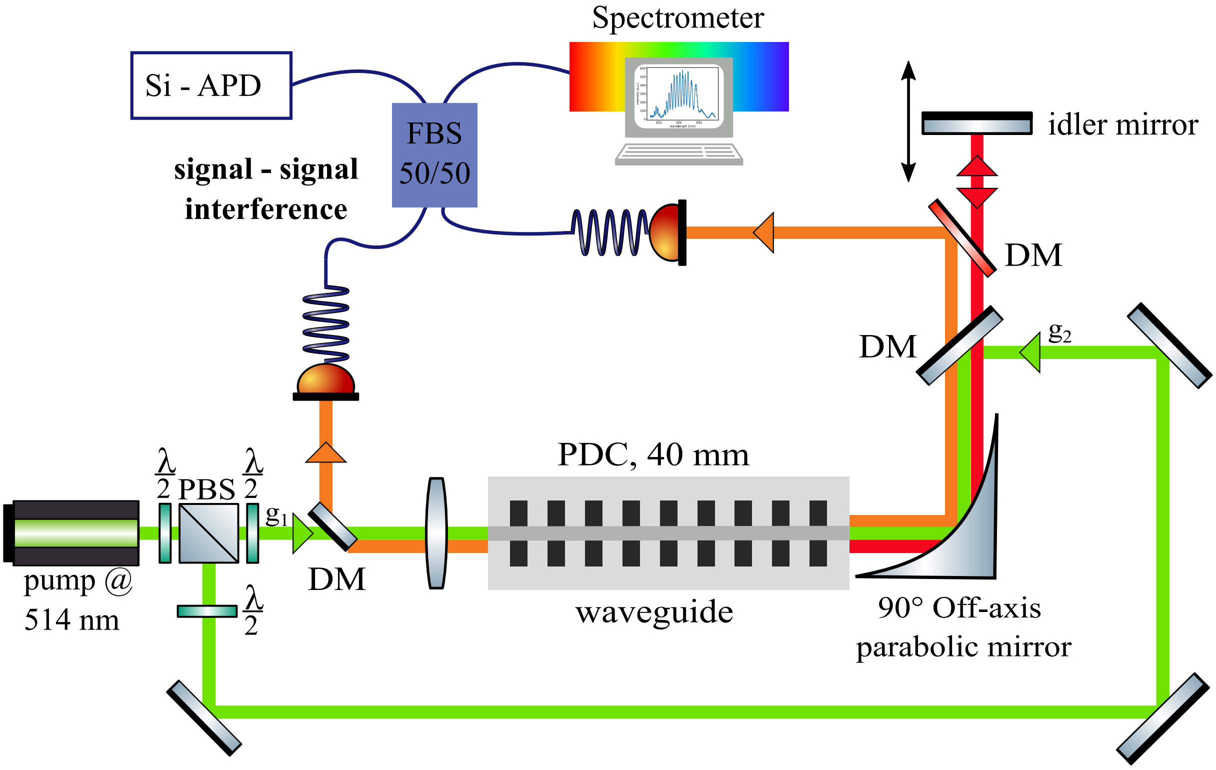

Figure 4.4: Setup with a differential pumping scheme and parametric gains g_1 and g_2 for the first and second PDC process respectively. In the induced coherence scheme, we couple the signal fields to single mode fibres individually and interfere them on an external 50:50 fibre beamsplitter.

4.1.4 Measurement techniques

In all three of the presented setups, we are employing similar techniques to record and process the collected data. Therefore, we present them here in a collected way. We distinguish between measurements that record spectral interferograms and those that record temporal interferograms.

Spectral interferogram

An interferogram in the spectral domain can be observed by recording the signal spectrum on a single-photon-sensitive spectrometer (Andor Shamrock SR-500i spectrograph with Newton 970P EMCCD-camera) for a fixed position of the translation stage in the idler arm. Fixing the stage position leads to a fixed offset of the signal and idler paths. Thus, a linear spectral phase is imprinted on the bi-photon which becomes apparent in the spectral interferogram in the form of equidistant fringes. Their period can be adjusted by changing the stage position. The effect of higher order dispersion can be observed as changes in this fringing period. We can record the signal spectrum from both PDC processes by blocking the back-reflection of the idler arm and thereby retrieve the underlying spectral intensity, which can be used as a reference.

We typically record spectra with an integration time of 1 s and a spectral resolution of 30 GHz. In order to achieve a sufficient signal-to-noise ratio in these measurements, we have to pump our waveguides with pump powers on the order of a few mW such that we generate a sufficient amount of PDC photons.

Temporal interferogram

Temporal interferograms are recorded by moving the translation stage while measuring the counts at the output of the interferometer. We are detecting photon counts with a silicon avalanche photodiode (Perkin Elmer Photon Counting Module SPCM-AQR-14FC) for the signal and an InGaAs APD (IDQ id200) for the idler. The detection events are recorded with a Swabian Instruments Time-Tagger 20. The counts are recorded with integration times ranging from 0.01 s to 0.3 s at each position, depending on the specific experiment at hand. The translation stage is moved with a step size of around $200 - 500$ nm and is positioned before each measurement to avoid vibrations in the system. The step size is chosen in that range to ensure a sufficient sampling of the interference fringes, which occur at a period equal to half the central idler wavelength of 1360 nm.

4.2 Correlation time measurements

The following results have been published in [87].

We introduced the bi-photon correlation time in chapter 2 as the uncertainty in the arrival time of one photon from a pair after the other one has been detected. Measuring the correlation time is important for applications in ultra-fast spectroscopy as it defines the achievable temporal resolution and is even crucial for estimating the absorption cross-section in entangled two-photon absorption experiments [6]. Knowledge about the correlation time becomes even more relevant for new, even more broadband bi-photon sources [75, 81, 88]. However, it is hard to measure the correlation time directly. This is due to insufficient detector timing resolution, jitter or gating pulse duration, which limits the resolution of direct measurements of the JTA to a few ps [55] while the bi-photon correlation times can be well below 100 fs. Meanwhile, methods based on nonlinear interactions, i.e. SPIDER or FROG [89, 90], are not compatible with single-photon signals and could potentially only observe dispersive effects on one of the marginal spectra and not joint features such as the bi-photon correlation time of a non-degenerate photon pair. At the same time, methods based on single-photon interferometry via the Hong-Ou-Mandel effect are not sensitive to capture dispersive effects [91].
For the case of our group velocity matched PDC source, the phase-free correlation time lies in the mentioned range below 100 fs. However, dispersive effects might increase the correlation time, which is detrimental for the application of such a source in the framework of ultrafast spectroscopy. Therefore, the measurement of the actual correlation time provides insight into the effects of dispersion on broadband bi-photons [92–97].
Therefore, we developed a technique to measure the bi-photon correlation time of our source by simultaneously measuring spectral and temporal interferograms while introducing controlled amounts of second order dispersion into the interferometer.

4.2.1 Underlying theory

We find that we can link the bi-photon correlation time to the width of the temporal interferogram recorded with an SU(1,1)-interferometer. We realise the correlation time measurements by introducing external second order dispersion in one or both arms of a SU(1,1)-interferometer, as schematically depicted on the right side in Fig. 4.5.
In a first step, we revisit equation (2.62), which is used as a foundation for our simulations to calculate the temporal interferogram for different amounts of second order dispersion between the two stages of the interferometer

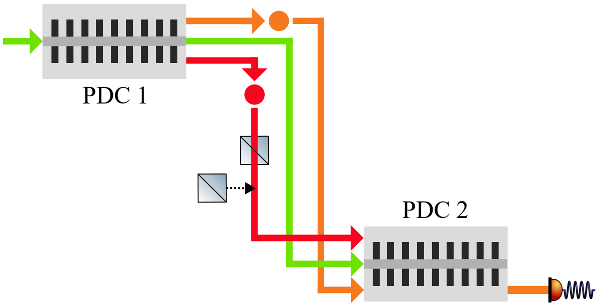

Figure 4.5: Schematic correlation time measurements for which dispersive elements are introduced between the two PDC processes.

$$S(\Delta t_i, \Psi) = \int_{-\infty}^{\infty} \mathrm{d}\Delta\omega \, \mathrm{sinc}^2(\Delta\gamma\Delta\omega^2) \cdot \cos^2(\Psi). \tag{4.1}$$

We can approximate this integral in order to gain an analytical solution and thereby an intuition for the effect of second order dispersion in the setup. We find an approximate analytical solution by splitting the cosine term in three terms

$$\cos^2(\Psi) = \frac{1}{2} + \frac{1}{4}\mathrm{e}^{2i\Psi} + \frac{1}{4}\mathrm{e}^{-2i\Psi}, \tag{4.2}$$

such that we can express $S(\Delta t_i, \Psi)$ as $S(\Delta t_s, \Psi) = I_1 + I_2 + I_3$. Explicitly written, this takes the form

$$\begin{aligned} S(\Delta t_s, \Psi) = & \int_{-\infty}^{\infty} \mathrm{d}\Delta\omega \, \frac{1}{2}\mathrm{sinc}^2(\Delta\gamma\Delta\omega^2) \\ & + \int_{-\infty}^{\infty} \mathrm{d}\Delta\omega \, \frac{1}{4}\mathrm{e}^{2i\Psi}\mathrm{sinc}^2(\Delta\gamma\Delta\omega^2) \\ & + \int_{-\infty}^{\infty} \mathrm{d}\Delta\omega \, \frac{1}{4}\mathrm{e}^{-2i\Psi}\mathrm{sinc}^2(\Delta\gamma\Delta\omega^2). \end{aligned} \tag{4.3}$$

In this formula, the sinc^2 term can be approximated by a Gaussian function

$$\mathrm{sinc}^2(\Delta\gamma\Delta\omega^2) \approx \exp\left(-\frac{\Delta\gamma}{\sigma}\Delta\omega^2\right) \tag{4.4}$$

with $\Delta\gamma = -\frac{(D_s+D_i)L}{2}$ and $\sigma = 2$ to match the FWHM of both functions. We note that this approximation is different from the one typically made, which is $\mathrm{sinc}(x) \approx \exp(-0.193x^2)$ [98]. Due to the quadratic argument $\Delta\omega$ in the sinc^2 term, we can not reproduce the same shape of the spectral envelope with this approximation. This makes the approximation less accurate as it is less applicable to the situation at hand. However, it is good enough to gain an intuitive understanding of the underlying processes.

When we apply this approximation, the first integral results in a constant offset of 0.5, as the result of a Gaussian integral. For the integration in $\Delta\omega$, I_2 becomes

$$I_2 = A \cdot \exp(-i\bar{\omega}_i\Delta t_i) \cdot \exp\left(\frac{\Delta t_i^2(i\Delta\gamma - 0.5i(C_s + C_i) + 0.5\Delta\gamma)}{\Delta\gamma + 2(\Delta\gamma - 0.5(C_s + C_i))^2}\right), \tag{4.5}$$

where $A = \frac{2}{3|\Delta\gamma|^{1/2}\sqrt{-\Delta\gamma+C_s+C_i}}$ and Δt_i is the temporal delay which we introduce in the idler arm between the two sources. I_3 yields the complex conjugate of I_2. We can identify $\zeta = \Delta\gamma - 0.5(C_s + C_i)$ as the total second order dispersion in the system. Put together, this results in a temporal interferogram given by

$$S(\Delta t_s, C_s, C_i) = \frac{1}{2} + A \cdot \exp\left(\frac{\Delta\gamma \Delta t_s^2}{2\zeta^2 + 0.5\Delta\gamma^2}\right) \cdot \cos\left(\frac{\zeta \Delta t_s^2}{4\zeta^2 + \Delta\gamma^2} - \bar{\omega}_s \Delta t_s\right). \tag{4.6}$$

We can see that the temporal interferogram is given by a constant offset, around which the signal oscillates with amplitude A. The interference is dependent on the spectral width of the underlying spectrum which is determined by the leading order in phase mismatch and thereby the intrinsic second order dispersion $\Delta\gamma$. Furthermore, the formula contains both the internal ($D_{s,i}$) and external ($C_{s,i}$) second order dispersion in the system. In any case, the amplitude $A = \frac{2}{3|\Delta\gamma|^{1/2}\sqrt{-\Delta\gamma + C_s + C_i}}$ of the interference is reduced by this second order dispersion.

The frequency of the interference fringes is mainly given by the central frequency of the light in the signal arm $\bar{\omega}_s$ and only slightly influenced by the second order phase in the interferometer, since $\bar{\omega}_s$ is much larger than realistic values for the second order dispersion. This minor contribution causes a relative time delay of the different frequencies. It becomes apparent that the width of the envelope of the temporal interferogram is given by the intrinsic second order dispersion of the nonlinear material, represented by the parameter $\Delta\gamma$, and can be altered by adding dispersive elements in the signal or idler arm introducing C_s and C_i. It is thereby irrelevant how the second order phase is distributed between the photons. This effect has found an application known as non-local dispersion cancellation [56].

We can further simplify the expression by introducing the width of the Gaussian envelope as σ_{env}^2, leading to

$$S(\Delta t_s, C_s, C_i) = \frac{1}{2} + A \cdot \exp\left(-\frac{\Delta t_s^2}{\sigma_{env}^2}\right) \cdot \cos\left(\frac{\zeta \Delta t_s^2}{4\zeta^2 + \Delta\gamma^2} - \bar{\omega}_s \Delta t_s\right). \tag{4.7}$$

Here, the width of the interferogram is now given by

$$\sigma_{env}^2 = \left|\frac{2\zeta}{\Delta\gamma} + 0.5\Delta\gamma\right|, \tag{4.8}$$

where $\zeta = \Delta\gamma - 0.5(C_s + C_i)$ is the total second order dispersion in the system. From this expression we can see that the minimal width of the temporal interferogram, i.e. without any second order dispersion, is given by $0.5\Delta\gamma$ and thereby dependent on the bandwidth of the JSA. This situation can be reached by cancellation of the intrinsic waveguide dispersion by anomalous external dispersion. For increasing amounts of external second order dispersion $C_{s,i}$, the width of the temporal interferogram increases faster for smaller $\Delta\gamma$. This is because external second order dispersion leads to a quicker broadening on shorter pulses, a known behaviour in classical ultra-fast optics. This leads to a distinctive behaviour for different spectral envelopes of the underlying JSA and thereby correlation times. This property has been exploited experiment to find the characteristic dependence between the temporal interference width and the second order dispersion. Here, we find that not only the spectral bandwidth, but also the spectral shape influences the temporal correlations.

We would like to highlight, that this scheme exploits the unique properties of SU(1,1)-interferometers, namely that the temporal interferogram is sensitive to second order dispersion and experiences a broadening as well as a reduction in its amplitude. Notably this effect does not arise in interferometers consisting of linear beamsplitters (e.g. Mach-Zehnder interferometers). A study of the sometimes-subtle differences between linear and nonlinear interferometers has been published in [99].

4.2.2 Simulations

A complete simulation of the experimental setup and the expected temporal interferograms for different amounts of second order dispersion must include our group-velocity matched PDC source which allows to tune the spectral bandwidth of the generated field via the waveguide temperature. We illustrate this tuning behaviour in Fig. 4.6. Here, we simulate the signal spectra for different waveguide temperatures ranging from 164.8 °C to 165.2 °C. This way, the presented spectra can serve as a reference to link the waveguide temperature to the spectral bandwidth and shape. We base our simulations on the bandwidth and spectral shape of the generated PDC light. This is necessary as not only the spectral bandwidth of the spectra reduces for higher temperatures, but also the spectral shape changes from a quasi top hat towards a sinc^2-like shape.

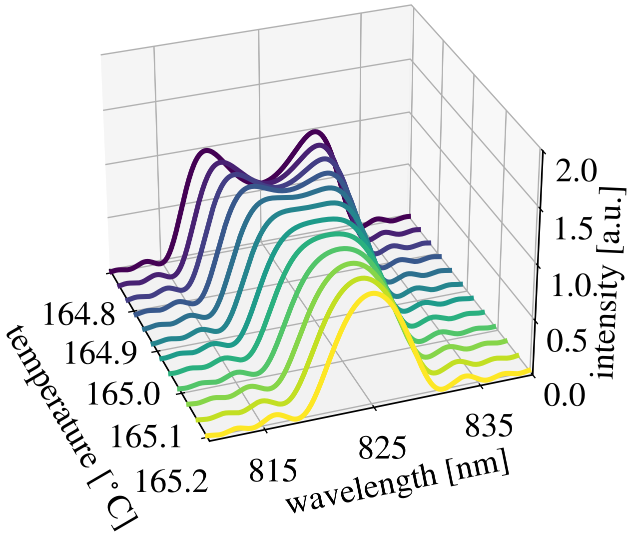

Figure 4.6: The signal output spectrum changes in terms of bandwidth and spectral shape when tuning the waveguide temperature from 164.8 °C to 165.2 °C.

We mentioned earlier, that we can express the JSI and JTI as one-dimensional functions due to the cw pumping. Thus, in Fig. 4.7, we simulate the JSI, JTI and resulting temporal

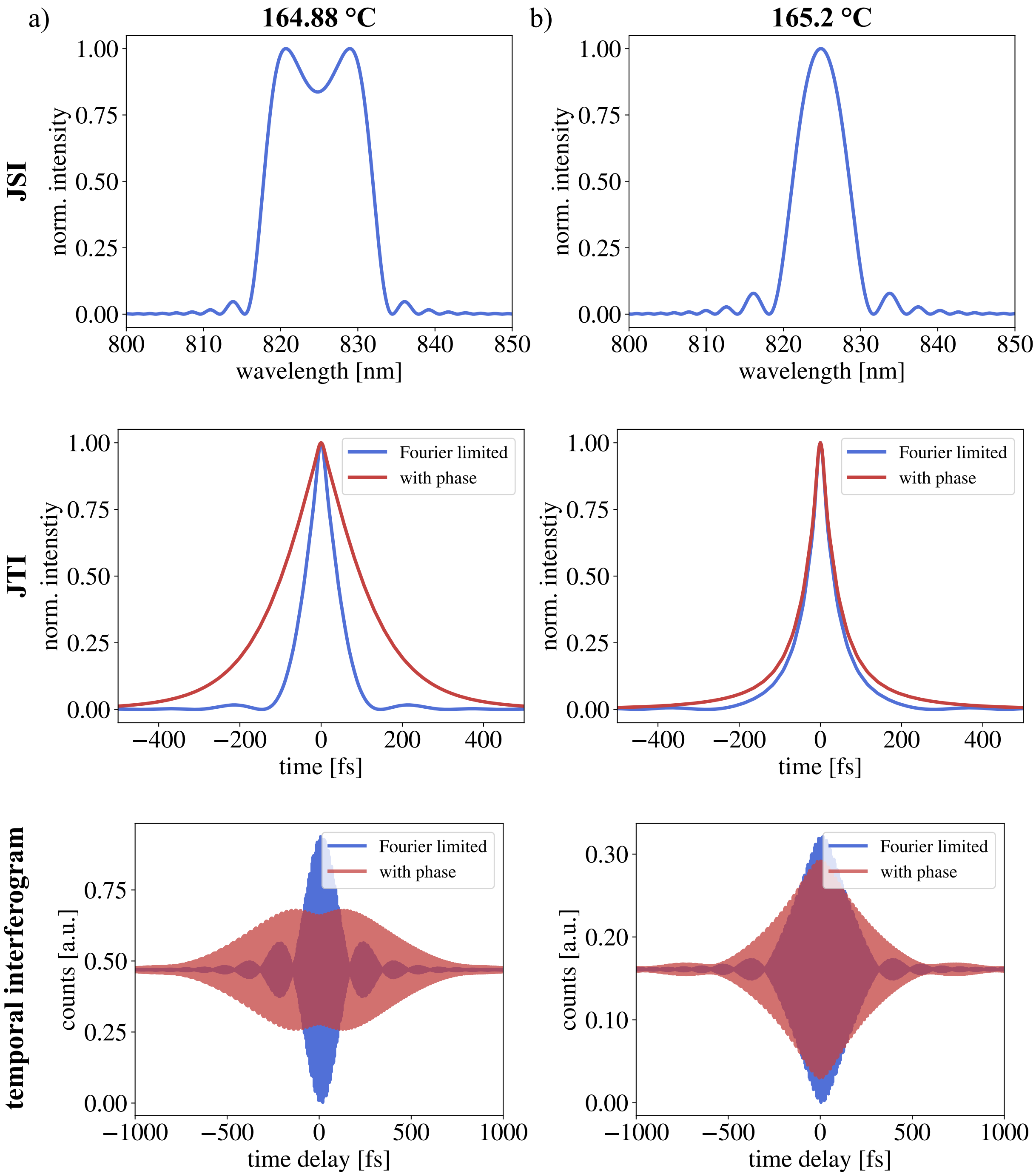

Figure 4.7: a) Simulation of JSI, JTI and temporal interferogram for the Fourier limited case and with the phase imprinted by the waveguide at a temperature of 164.88 °C. b) Simulations at a waveguide temperature of 165.2 °C.

interferograms for waveguide temperatures of 164.88 °C (a) and 165.2 °C (b). We can observe a broad spectrum with a rectangular shape and a narrower spectrum with a sinc^2-like shape. Consequently, the JTI, being the modulus squared of the Fourier transformed JSA, also exhibits different shapes. In both cases, we plot the JTI and temporal interferograms for the case of a Fourier-limited bi-photon and when taking into account the phases introduced by propagation through the waveguide. We can observe a broadening in the JTI for both spectra. The same is true for the temporal interferograms. However, we want to highlight here that the effect of the additional phase is less strong for the narrower spectrum; this can be linked to the temporal broadening of classical ultra-short pulses as illustrated in Fig. 2.9. Furthermore, the two different underlying spectral shapes also lead to different shapes of the temporal interferograms and not only to changes in their widths.

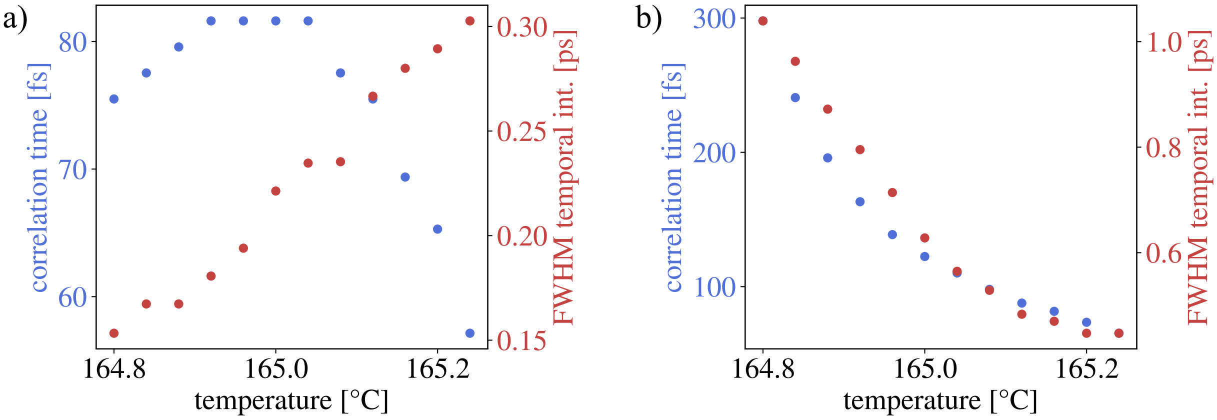

Figure 4.8: a) Simulation of the correlation time and the FWHM of the temporal interferogram for different waveguide temperatures for the Fourier limited case and b) with the phase imprinted by the waveguide.

The transition of the PDC spectra from the top hat to the sinc^2 shape while simultaneously changing their bandwidth results in a counter-intuitive relation between the correlation time and the FWHM of the temporal interferogram in the Fourier-limited case, which is shown in Fig. 4.8 a). Here, the correlation time reaches a maximum with increasing temperature and drops again for narrower bandwidths, while the FWHM of the temporal interferogram increases further. This can be explained by the change in the time-bandwidth-product (TBP), when transitioning between the spectral envelopes if we compare them in Fig. 4.6. Namely, the TBP is dependent on the shape of the spectral intensity and, thereby, the product of the FWHM of the spectrum and temporal intensity change. Thus, the same spectral bandwidth can lead to a different temporal bandwidth. One peculiarity that arises from this is that, for low temperatures, a small FWHM of the temporal interferogram and simultaneously long correlation time can be observed while a short correlation time corresponds to a larger FWHM of the temporal interferogram at high temperatures.
This situation can no longer be observed in the presence of phases in the setup, as showcased in Fig. 4.8 b). Due to the dispersive broadening, the broad spectra at low temperatures lead to a long correlation time and a large FWHM of the temporal interferogram and vice versa for the narrow spectrum. The peculiarity observed for the Fourier-limited case can also be attributed to the criteria used to determine the correlation times. We used the FWHM of the JTI to define this quantity, as it is common in the existing literature. However, using a criterion like the $1/e^2$ leads to a correlation time that is larger for the narrower spectrum at higher waveguide temperatures as shown in Fig. 4.9 a). As before,

the choice of criteria does not impact the changes in the correlation times in the case of a phase in the setup as presented in Fig. 4.9 b).

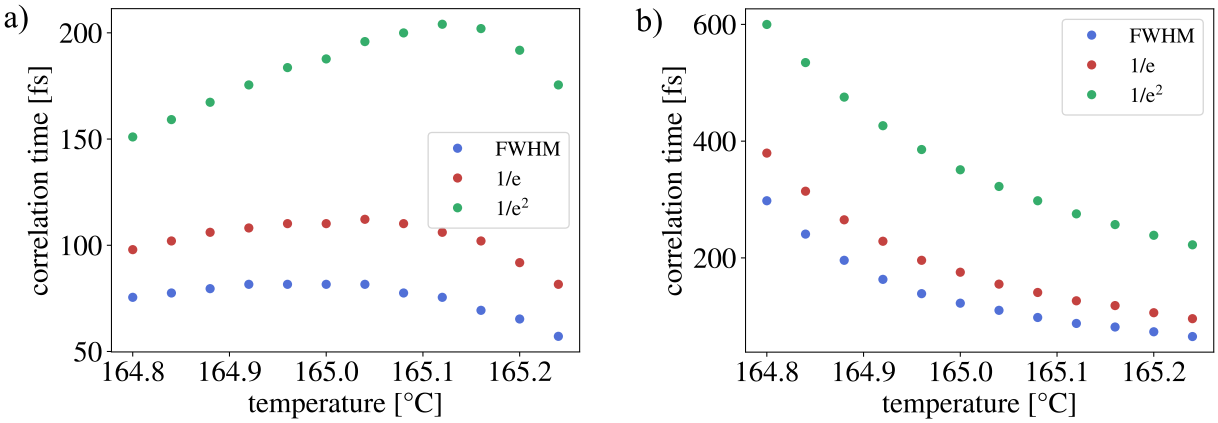

Figure 4.9: a) Correlation times calculated from the JTI with different criteria for the width estimation at varying temperature for the Fourier-limited case. b) Correlation times for varying temperatures calculated with phase from the waveguide present in the JTI.

4.2.3 Results

In order to distinguish different correlation times in our measurements, we employ two different PDC spectra with different spectral bandwidth and time-bandwidth products by tuning the waveguide temperature. These spectra are shown in Fig. 4.10. At the nominal operation point of the source at 164.9 °C, we reach a bandwidth of 6.46 THz and as we increase the temperature to 165.2 °C, the bandwidth reduces to 2.82 THz. The transition from a quasi top hat to a sinc^2-shape in the spectra leads to different time bandwidth products of around 0.88 and 0.44, respectively.

In the experiment, we first measure the spectral interferogram for a fixed idler mirror position and then record the temporal interferogram while moving the idler mirror. This procedure is repeated for three different amounts of dispersive material in the interferometer arms and for both underlying PDC spectra. The dispersion has been realised by placing polarising beamsplitters of lengths 10 mm to 20 mm in both signal and idler arm in order to realise additional second order dispersion of up to 5000 fs^2. The specific combinations are: no material, 20 mm + 20 mm idler, 20 mm + 20 mm idler and 15 mm signal, 20 mm + 20 mm idler and 15 mm + 10 mm signal. The typical raw-data measurements of the temporal and spectral interferograms can be seen in Fig. 4.11. The visibility of the temporal interference is limited by the back-coupling at the respective opposite wavelength, as discussed in section 2. This back-coupling is lower for the light at 800 nm due to the multi-mode guiding of the waveguide at this wavelength. Furthermore, the second order dispersion present in the system reduces the amplitude of the interference further as discussed above. The counts at the idler wavelength around 1400 nm are lower than the ones of the signal due to a lower detection efficiency of 15% with the InGaAs-APD as opposed to 45% with the Si-APD. Finally,

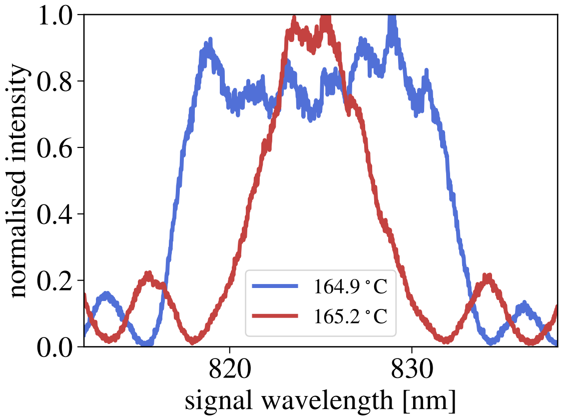

Figure 4.10: The recorded signal spectra from a single pass through the waveguide without interference at temperatures of 164.9 °C and 165.2 °C with spectral bandwidths of 6.46 THz and 2.82 THz and different shapes of the spectral envelopes leading to TBPs of 0.88 and 0.44, respectively.

uneven fibre-coupling efficiencies to the detection have to be taken into account. However, since we are only interested in the envelope of the temporal interference patterns, the obtained visibilities of up to 30 % in the signal arm and 15 % in the idler arm are sufficient. These visibilities are reasonable in comparison with the transmissions of signal and idler in the setup. Due to losses during coupling out of and back into the waveguide, the transmissions are estimated to be around 0.4 for the idler and 0.3 for the signal.

For the used configuration, the pump gain ratios are almost equal as the pump power in the forward pass is the same as the one in the backwards pass due to the high-reflectivity coating on the waveguide end-fact. This does not yield the ideal visibilities, which are bound by the transmissions in the signal and idler arm, as we discussed in section 2.6.3. Therefore, the theoretically achievable visibilities lie around 50 % for the signal and 30 % for the idler. The actually measured visibilities are reduced compared to these values as they calculated for the case of a single-mode theory. However, the correct description of the temporal interferogram requires a broadband theory that takes the second order dispersion into account. We can therefore conclude that less visibility is observed for the idler in comparison to the signal and that both values are below the achievable maximum due to second order dispersion in the setup.

The spectral interferogram at the signal wavelength in Fig. 4.11 shows a higher visibility of above 30 %, as the spectrally resolved interferogram can be more adequately described by the single mode theory which we used to estimate the expected visibilities. Thus, the visibility at every single frequency is less affected by second order dispersion in comparison to the temporal interferogram in which all frequencies contribute to the interference signal simultaneously. Here, the effects of second order dispersion can be seen in a linear change in the frequency of the interference along the spectrum to which we would refer as chirp in classical ultra-fast optics.

The recorded spectral and temporal interferograms have been further processed to extract the second-order dispersion in the system and the width of the temporal interferogram. This processed data is presented in Fig. 4.13. To retrieve the normalised spectral inter-

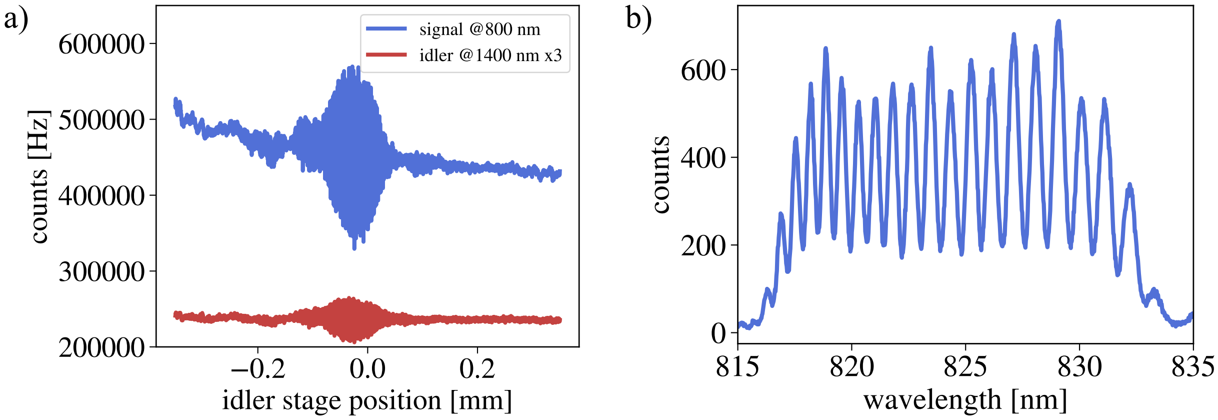

Figure 4.11: Sample raw data of a) the temporal interference in signal and idler photon counts and b) the spectral interference in the signal arm.

ferogram in Fig. 4.13 b), a reference spectrum with a blocked idler-path, leading to no interference, has been subtracted and the signal has been normalised to its maximum.
The raw data from the temporal interferogram in Fig. 4.11 a) shows slow drifts and fluctuations due to misalignment and temperature as well as air current fluctuations during the measurements. These drifts are removed from the signal by Fourier-transforming the time trace and applying a window function with a width of roughly half of the Fourier-space that cuts out the low and high frequency noise, leaving only the contributions to the actual interference. This interference has an oscillation period equal to half the wavelength of the moved arm, in this case the idler at a central wavelength of 1400 nm, corresponding to a frequency of the oscillations of 430 THz. The effect of filtering the signal in the Fourier-domain for a set of sample data is depicted in Fig. 4.12. Here, the red shaded area is multiplied with a mask function that eliminates values which do not contribute to the interference.

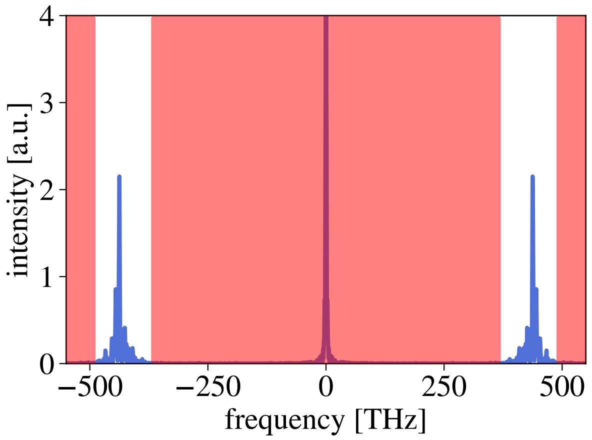

Figure 4.12: The raw data of the temporal interferogram is filtered in the Fourier-domain, by applying a mask function with value 0 in the red shaded area and value 1 for the rest.

Performing an inverse Fourier transform on the remaining parts of the signal leads to the interferogram presented in Fig. 4.13 a). This plot also shows the upper and lower envelope that are fitted to the interference pattern by applying a Savitzky-Golay averaging filter to the data. The FWHM of the temporal interferogram is extracted from these two envelopes. The error bar on the FWHM of the temporal interferogram was obtained by measuring 20 subsequent interferograms without any additional dispersive material in the interferometer arms. These measurements resulted in a relative error of 11.8 % for the standard deviation of the interferograms FWHM, which are most likely caused by instabilities in the setup from the waveguide temperature, stage position and couplings. The same relative uncertainty has therefore been applied to the other measurements.

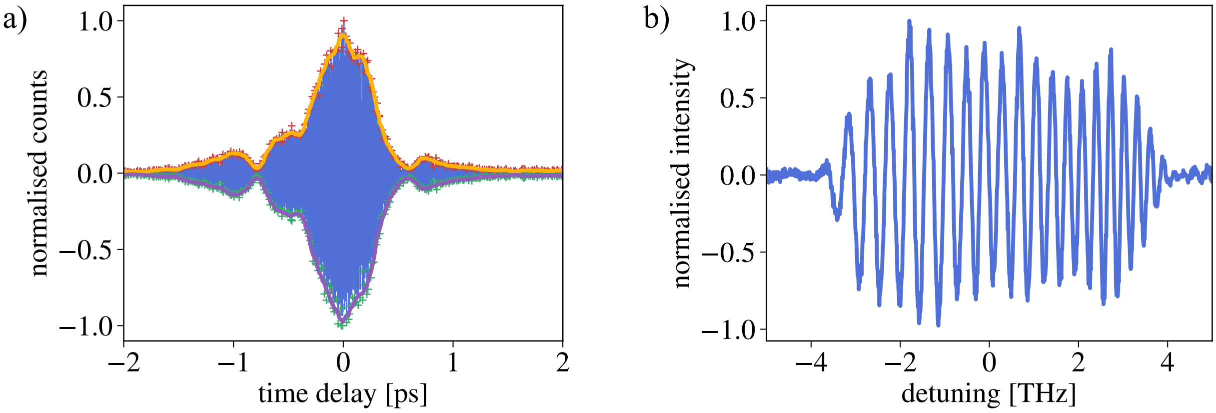

Figure 4.13: a) The temporal interferogram that was used to calculate the temporal interference width from the indicated upper and lower envelopes of the interference pattern and b) the normalised spectral interferogram that was used to retrieve the chirp in the system.

From the spectral interferogram, we aim to extract the chirp. Therefore, we evaluate the oscillations in the spectral domain with a two-step fitting routine. The fitting function is given by [36]

$$S(\Delta\nu) \propto |f(\Delta\nu)|^2 \, (1 + \cos[\Psi(\Delta\nu)]) \, . \tag{4.9}$$

In this formula, the spectral intensity $S(\Delta\nu)$ is given in terms of the frequency detuning $\Delta\nu$ around a central frequency. We fit the obtained data to this formula by isolating the maxima and minima in the spectral interferogram and evaluating their instantaneous period to obtain the starting parameters for the fit of the cosine function. Afterwards, multiple iterations of the fitting routine are performed and the lowest deviation of the resulting curve in a range of 4 THz around the central frequency is used to calculate the polynomial fit parameters in $\Psi(\nu)$. The frequency range has been chosen such that both, the narrow and broad PDC spectrum, are contained as well as to ensure a sufficiently strong interference signal over the background in the measurement. The described two-step fitting process is illustrated on a sample data set in Fig. 4.14.

The fit parameters allow us to extract the linear and quadratic phase. In the presented example, we can quantify the quality of the fit by $R^2 = 0.975$, which is in line with the

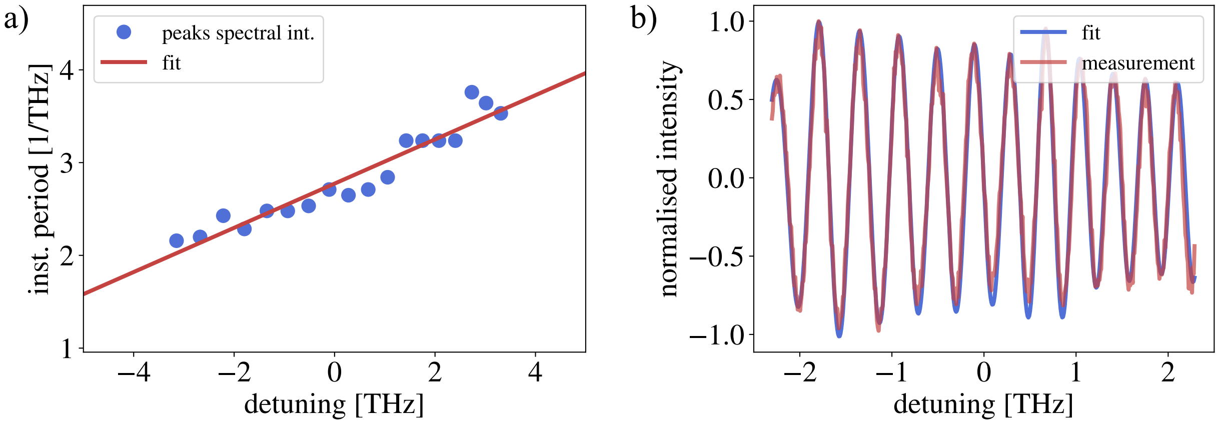

Figure 4.14: a) Fitting a linear slope to the instantaneous period of the interference to obtain the starting parameters for the cosine-fit. b) Cosine-fit together with measured data for a region of 4 THz in frequency detuning.

other fit results. We retrieve an intrinsic second order dispersion of the waveguide itself of $|\Delta\gamma| = 14800 \pm 240\,\mathrm{fs}^2$, where the error bar includes the error of the performed fit. The value of the second order dispersion agrees with the theoretical prediction of $10893\,\mathrm{fs}^2$ which is calculated from the dispersion data of the waveguide. The observed difference can arise from the dielectric end-facet coatings on the waveguide and other elements in the setup like dichroic mirrors which contribute to second order dispersion in the system. The obtained value for the second order dispersion from the waveguide might also be impacted by imprecision in the Sellmeier equations that we used for the refractive index calculation, that is based on an ideal waveguide geometry.

The presented method for the retrieval of spectral phases in the system can be further advanced by measuring many spectral interferograms while simultaneously moving the stage in the idler arm This changes the linear phase between signal and idler by introducing the delay Δt_i. In this type of hybrid spectral-temporal measurement, the spectrograph records a spectrum at each stage position which is also recorded. The spectral interferogram at each stage position is again given by Eq. (4.9). We can generalize this equation to write down the full 2D-distribution including the introduced temporal delay Δt_i and the idler angular frequency ω_i. This then leads to

$$S(\Delta\nu, \omega_i, \Delta t_i) \propto |f(\Delta\nu)|^2 \left(1 + \cos[\Psi(\Delta\nu) + \omega_i \Delta t_i]\right). \tag{4.10}$$

Thus, the contribution of higher order phases which stem from second order dispersion is contained in $\Psi(\Delta\nu)$ while the linear spectral phase $\omega_i \Delta t_i$ is introduced by translating the stage in the idler arm. We refer to this measurement scheme as a spectral-temporal interferogram.

The results from this simultaneous measurement scheme are presented in Fig. 4.15 a) where we show the two-dimensional data and a cut along a fixed stage position, yielding a single spectral interferogram. We can observe a linear chirp in the spectral interferogram resulting from the combination of linear and quadratic phases. Taking into account the appropriate starting parameters and the step size of the stage, we can perform a two-dimensional fit to the data, which is presented in Fig 4.15 b).

We find a good qualitative agreement between the measured data and the simulations presented in Fig. 4.15 a) and b), respectively. Thus, we can use the fit parameters to retrieve the second order dispersion in the system. In the presented data set, a second order dispersion of 17300 fs^2 has been extracted, which agrees with the one-dimensional data set with the corresponding additional second order dispersion that has been introduced for this exemplary data set. The additional optical path is found to be 1.5 mm. However, the linear and quadratic phase are not fully independent. Thus, a reference for the stage position would be needed to fix one of the two parameters. Therefore, we do not provide values of the error for the obtained values, as we only found a qualitative agreement of the measurements with the simulation.

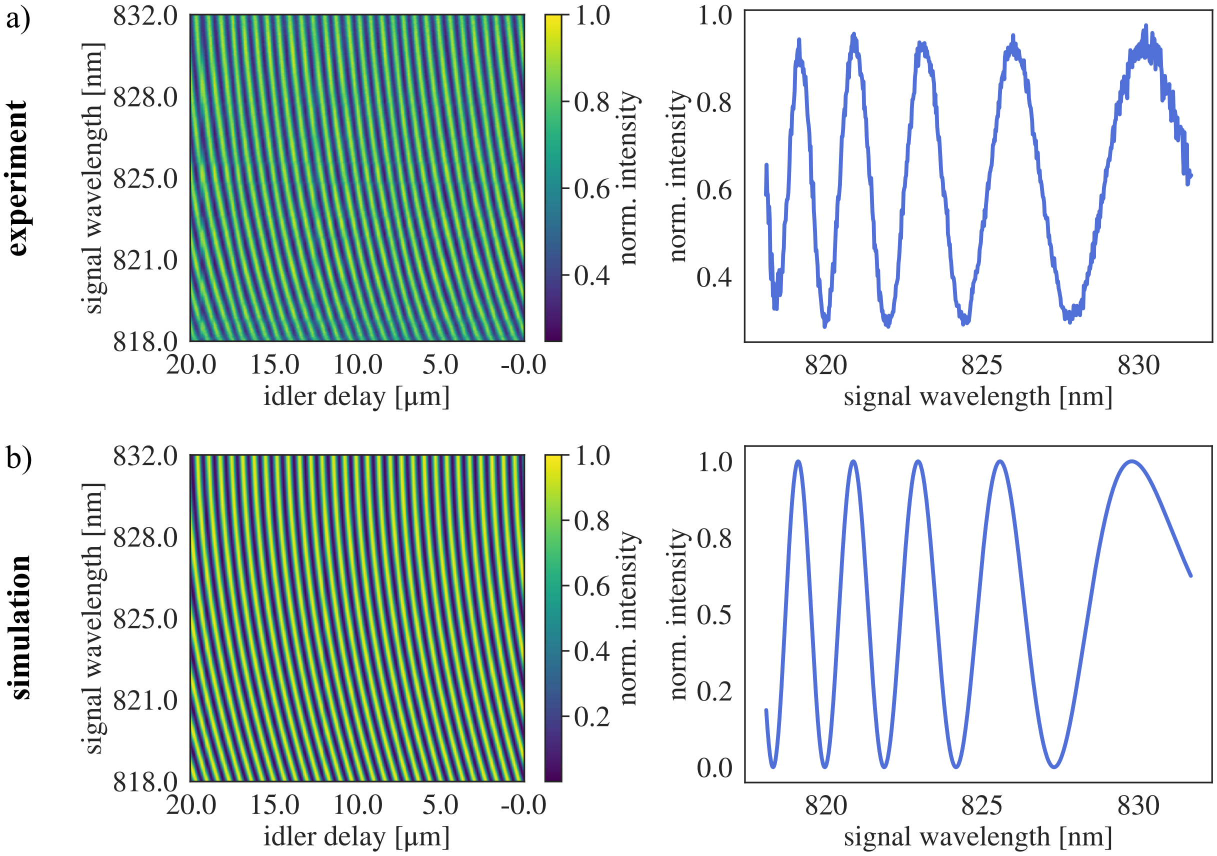

Figure 4.15: a) Experimental data of a spectral-temporal interferogram and one single spectral interferogram obtained as a vertical cut at a fixed idler delay. b) Simulation based on the fitted parameters of linear and quadratic phases in the interferometer and one single spectral interferogram obtained as a vertical cut at a fixed idler delay showing the same behaviour as the experimental data.

One major challenge with in the fitting routine to the spectral-temporal measurement, that hinders a quantitative matching between the experiment and the simulations, is that the phases can not be fitted reliably, due to the periodicity of the signal. This periodicity leads to convergence of the fit for linear phases that are far off from the actually present one as the optimisation algorithm finds a minimum in the difference between the simulation and the data set before converging to the correct value. We can observe this difference between the experimental data and the simulation in Fig. 4.15 b), where the 1D cut of the simulation shows a slightly different period and phase than the experimental data. Thus, multiple iterations of the fitting routine with different starting parameters are needed to find the actual parameters for the phase.

The presented method in principle allows to perform even more accurate measurements of the second order dispersion and extract additional parameters of phases, e.g., due to absorption in the system. However, it has not been used routinely as instabilities in the setup and non-uniformity in the step sizes of the stage hinder the convergence of the 2D fitting. An improved experimental setup and retrieval algorithm may provide means to employ this method as a standard measurement as the spectral phase in the interferometer become more complex.

For the final results of our correlation time measurements, we combine the obtained width of the temporal interferogram with the retrieved second order dispersion in the system. We show this combined data in Fig. 4.16. It reveals the characteristic dependence of the temporal interference width on the total second order dispersion. Additionally to the data points for the two different underlying PDC spectra, we plotted the corresponding simulations of the temporal interference width for different chirp value.

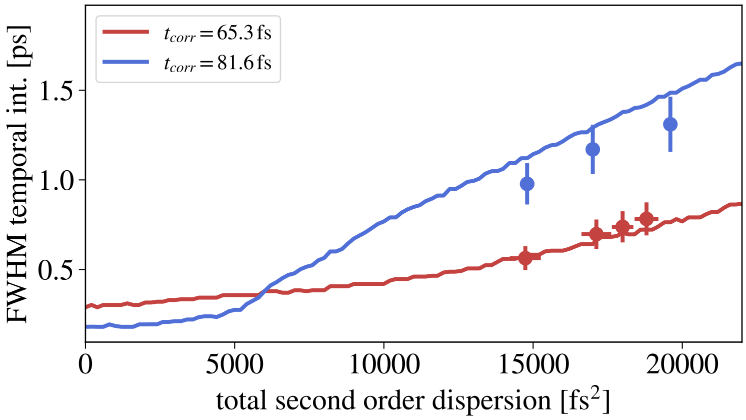

Figure 4.16: Correlation time measurement for two different spectra linking the temporal interference width and the second order dispersion extracted from the spectral interferogram.

We observe the described dependence between the temporal interference width and the second order dispersion that is different for both spectra. Deviations of the measured data points from the simulations can be attributed to the assumption of perfect phasematching and to the fact that our simulations do not account for effects from the multi-modedness of the waveguide for the pump and signal fields. Those effects lead to artefacts and additional spectral features that lead to a deviation of the spectral envelope from the ideal one.

With this confirmation of our simulations and the information about the intrinsic second order dispersion of the waveguide, we can now calculate the actual correlation time of the generated bi-photons, which we find by including this phase in the Fourier transform of the JSA.

The actual correlation times, given as the FWHM of the JTI, amount to 73.5 fs and 177.5 fs for the narrow and broad spectrum respectively. They are larger than the Fourier-limited ones due to the second order dispersion of the waveguide material. Assuming a flat phase profile, the minimum correlation times of 65.3 fs and 81.6 fs can be calculated for the narrow and broad spectrum. These can be reached by introducing the correct amount of anomalous second order dispersion in the setup and thereby account for the existing dispersion.

We can observe that the calculated correlation times vary in a counter-intuitive way, with the short correlation time being attributed to the narrower spectrum. This can be linked to the different spectral shapes and the corresponding TBPs of 0.44 and 0.88, cf. Appendix A.1, respectively. Furthermore, the temporal shape of the bi-photon varies for different spectra, hence the criterion for defining the correlation time may yield different results.

The obtained correlation times are relevant for further experiments involving entangled two-photon absorption or applications in the realm of ultra-fast spectroscopy. In those applications, one might want to alter the PDC spectra to optimise the bi-photon's spectral and temporal shape for the application at hand. In the following section, we turn to such an application, namely optical coherence tomography (OCT) with undetected photons. There, we will see that the correlation time ultimately limits the achievable temporal and thereby depth resolution by defining the width of the temporal interferogram.

4.3 Optimising optical coherence tomography

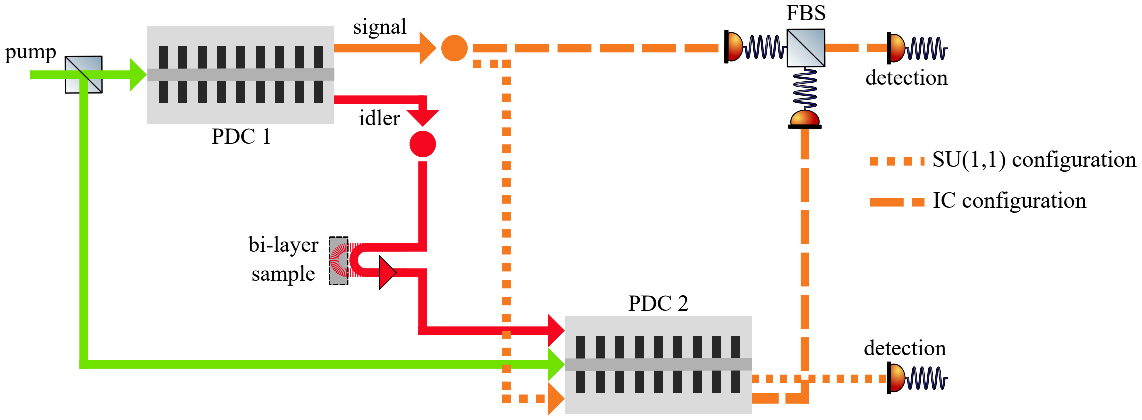

Figure 4.17: Concept for OCT measurements with undetected photons. We are examining the IC and the SU(1,1) scheme regarding their capabilities of performing OCT with undetected photons on a bi-layer sample in an integrated interferometer.

In section 2.1, we introduced optical coherence tomography as one of the techniques from the toolbox of ultra-fast spectroscopy. Here, we want to transfer this classical measurement scheme for high resolution depth imaging to the quantum regime. Thus, we realise OCT measurements in our nonlinear interferometer, which then allows us to perform measurements with undetected photons. OCT with undetected photons has been studied in various contexts before. Most of these realisations employ bulk nonlinear crystals. In order to move towards a practical sensor for OCT with undetected photons, integration is key. However, the use of integrated optical elements comes with its own challenges. Therefore, we investigate how to construct an optimal OCT scheme for measurements with undetected photons using integrated optical elements. An optimised version of a quantum sensor should satisfy the following conditions:

- high axial resolution
- high signal-to-noise ratio (SNR)
- easily implemented in fully integrated design
- affordable

In a next step, we check which of our realisations of nonlinear interferometers based on integrated waveguide PDC sources fulfills those criteria the most. We are therefore comparing two different schemes in which we can perform OCT measurements with undetected photons, namely the SU(1,1) and IC geometry, as depicted in Fig. 4.17 where we now added a layer sample in the idler path. We have introduced the experimental realisations of these geometries in section 4.1 and found that the main difference between the two designs lies in the place where the interference occurs. In the SU(1,1) geometry, signal and idler from PDC 1 are both coupled back to PDC 2. Interference can be observed directly after this stage. In the IC geometry, the interference happens externally as the signal fields from PDC

1 and PDC 2 are interfered on an external fibre-beamsplitter, after which the interference in either of the outputs can be detected.
Thus, in the following, we will discuss the benchmarks of the SU(1,1) and IC geometry for OCT with undetected photons.

To this end, let us start with the benchmarks of a classical OCT system and revise the basic concepts in the context of our experimental setups. We discussed in chapter 2 that there are two operation modes of OCT: time domain (TD) OCT and Fourier domain (FD) OCT. In both of them, the maximally achievable axial resolution Δz is given by the coherence length of the source l_c via

$$\Delta z = l_c = \frac{fc}{\Delta \nu}. \tag{4.11}$$

In this formula, c is the speed of light in vacuum and f a factor that changes for different shapes of the spectral envelope of the source and can be derived via the Wiener-Khinchin theorem[1]. For our source, which exhibits a rectangular spectrum, this factor is close to $f = 1.2$. With a spectral bandwidth in the experiment of 5.2 THz, this formula predicts an axial resolution of $\Delta z = 69\,\mu\text{m}$.
Since TD-OCT requires the scanning of the reference mirror, which is fixed in FD-OCT, it is often not the preferred method due to potentially longer acquisition times which comes with sampling at many stage positions in comparison to the acquisition of a single spectrum and the requirement to move parts in the setup [31]. Additionally, TD-OCT is prone to second order dispersion in the setup which leads to a broadening of the signal and thus a reduced axial resolution Δz that requires correction in post processing. However, FD-OCT comes with its own limitations as a spectrometer is required in contrast to a simple photodiode in TD-OCT case. This spectrograph needs to cover a large enough spectral range to capture the whole source spectrum and simultaneously provide a high resolution. The resolution limits the maximal axial measurement range ΔL_z which is given by [100]

$$\Delta L_z = \frac{\Delta z}{2}\frac{N}{2}, \tag{4.12}$$

with N being the number of detection pixels. In our experimental setups, we illuminate $N = 670$ pixels of the spectrograph. We estimated the ideal axial resolution of our system to be $\Delta z = 69\,\mu\text{m}$ and thereby arrive at a maximal axial measurement range in FD-OCT to be $\Delta L_z = 11.5\,\text{mm}$.
We see that FD-OCT shows a limited axial scanning range and that TD-OCT holds potential benefits by using a photo-diode instead of a single-photon sensitive spectrograph for detection in the low light regime. Therefore, we will investigate both TD-OCT and FD-OCT and compare the resources needed for OCT measurements with undetected photons in our setup. However, in order to understand how these OCT interferograms form, let us

---

[1] The effect of different factors between spectral and temporal properties reminds on the TBP discussed in section A.1 in the appendix. However, in this derivation the FWHM of a sinc-function instead of its square is considered as the shape of the auto-correlation function, which leads to a different factor.

have a closer look into the theory for OCT with undetected photons in the SU(1,1) and IC geometry.

4.3.1 Description of OCT with undetected photons

We start by describing the state which contains the two photon component of a PDC process at signal and idler frequencies ω_s and ω_i as [53]

$$|\Psi\rangle = C \int \mathrm{d}\Delta\omega f_{PDC}(\Delta\omega) |\bar{\omega}_s - \Delta\omega\rangle \otimes |\bar{\omega}_i + \Delta\omega\rangle, \tag{4.13}$$

where C is a constant related to the conversion efficiency, including the pump gain parameter g. Furthermore, we again use the frequency detuning $\Delta\omega = \omega_s - \bar{\omega}_s = -(\omega_i - \bar{\omega}_i)$ around the central frequencies of signal $\bar{\omega}_s$ and idler $\bar{\omega}_i$ and assume pumping with a cw-laser.

The JSA f_{PDC} of the process is once more given by

$$f_{PDC}(\Delta\omega) = \mathrm{sinc}\left(\frac{\Delta\beta(\Delta\omega)L}{2}\right) \exp\left(i \cdot \frac{\Delta\beta(\Delta\omega)L}{2}\right). \tag{4.14}$$

Now, we want to introduce a bi-layer sample consisting of two surfaces at which one of the fields, here the idler, from the first PDC process can be reflected back. This reflection leads to a splitting with the layer reflectivities $r_{1,2}$ which fulfill $r_1^2 + r_2^2 = 1$. Together with the sample thickness d, the bi-layer system imprints an amplitude and phase that can be described as

$$r(\Delta\omega) = r_1 + r_2 \exp\left(i \cdot \frac{2n_g d\Delta\omega}{c}\right), \tag{4.15}$$

assuming a constant group refractive index n_g over the spectral range of the incident PDC light. Thus, only a part of the idler photons probability amplitude is directly reflected back to the nonlinear crystal while the rest is reflected back with an additional linear spectral phase from the second layer of the bi-layer sample. Upon interaction with this bi-layer, our two photon state changes to

$$|\Psi\rangle_{OCT} = C \int \mathrm{d}\Delta\omega f_{PDC}(\Delta\omega) |\omega_s\rangle \otimes \left(r_1|\omega_i\rangle + r_2 \exp\left(i \cdot \frac{2n_g d\Delta\omega}{c}\right)|\omega_i\rangle\right). \tag{4.16}$$

Under the assumption that at most one photon pair is present at the output of the interferometer, we can write this expression as

$$\begin{aligned}|\Psi\rangle_{OCT} &= C\int \mathrm{d}\Delta\omega\left(\cdot f_{PDC}(\Delta\omega)r_1|\omega_s\rangle|\omega_i\rangle + f_{PDC}(\Delta\omega)r_2\exp\left(i\cdot\frac{2n_g d\Delta\omega}{c}\right)|\omega_s\rangle|\omega_i\rangle\right)\\ &= C\int \mathrm{d}\Delta\omega\left(\cdot f_{PDC}(\Delta)r_1 + f_{PDC}(\Delta)r_2\exp\left(i\cdot\frac{2n_g d\Delta\omega}{c}\right)\right)|\omega_s\rangle|\omega_i\rangle.\end{aligned} \tag{4.17}$$

Finally, the second PDC source contributes a state $|\Psi\rangle_{PDC,2}$, which is equivalent to a single PDC source, to the output state of the whole interferometer $|\Psi\rangle_{int}$ with no additional phases such that we can write this state as $|\Psi\rangle_{int} = |\Psi\rangle_{OCT} + |\Psi\rangle_{PDC,2}$. Thus, when we now investigate the two-photon component of that final state, we can identify a new JSA of the interferometer that is, together with an additional adjustable time delay on the idler arm of τ, given by

$$\begin{aligned}f_{int}(\Delta\omega) =& f_{PDC}(\Delta\omega)\\ &+ r_1 f_{PDC}(\Delta\omega)\exp(i\tau\Delta\omega + \Phi_{int}(\Delta\omega))\\ &+ r_2 f_{PDC}(\Delta\omega)\exp(i\tau\Delta\omega + \Phi_{int}(\Delta\omega) + 2n_g d/c\Delta\omega).\end{aligned} \tag{4.18}$$

Here, the phase terms includes internal phases Φ_{int} from the interferometer itself, e.g., dispersion from the waveguide material, c.f. [70] for more details on the influence of phases in the same setup. The spectral interferogram is given by $S(\Delta\omega) \propto |f_{int}|^2$. Thus, we end up with

$$\begin{aligned}S(\Delta\omega) \propto |f_{PDC}(\Delta\omega)|^2(1 + r_1^2 &\cdot \cos(\Phi_{int}(\Delta\omega) + \tau\Delta\omega)\\ &+ r_2^2 \cdot \cos(\Phi_{int}(\Delta\omega) + \tau\Delta\omega + 2n_g d/c\Delta\omega)).\end{aligned} \tag{4.19}$$

We can observe a spectral interference pattern exhibiting a beating between two frequencies, which can be adjusted by the reference delay τ. Upon Fourier transformation, these lead to two distinct peaks with a width that is determined by the correlation time of the involved bi-photons. By adjusting the reference delay τ these peaks can be shifted in order to lie separated from the low-frequency noise from the detection device as ultimately, their distance determines the layer separation $2 \cdot n_g d$. The TD-OCT signal can then be obtained by integration over all frequencies and varying the reference time delay τ_{ref} such that the detected signal counts $C_s(\tau_{ref})$ become

$$C_s(\tau_{ref}) = \int_{-\infty}^{\infty} \mathrm{d}\Delta\omega |f_{int}(\Delta\omega, \tau_{ref})|^2. \tag{4.20}$$

In the frequency-unresolved case, a variance in the signal counts can only be observed if the argument in the cosine terms in Eq. (4.19) are close to zero. Thus, while scanning the reference delay, interference around the position of the surfaces can be observed, which is again separated by $2n_g d$. Also here, the bandwidth of the PDC, but also internal phases from second order dispersion limit the axial resolution. The extraction of information about

layered objects under tests in nonlinear interferometers in IC or SU(1,1) schemes have been described in earlier works in a more general framework [21, 22, 38].
We have seen that the constant C in the previous discussion is related to the pump gain g, which we discussed in detail in section 2.6.3. Adjusting this pump gain allows us to maximise the visibility of the interference, which is typically associated to a higher signal-to-noise ratio - one of our requirements on a quantum sensor.

4.3.2 Gain optimisation in SU(1,1) and induced Coherence

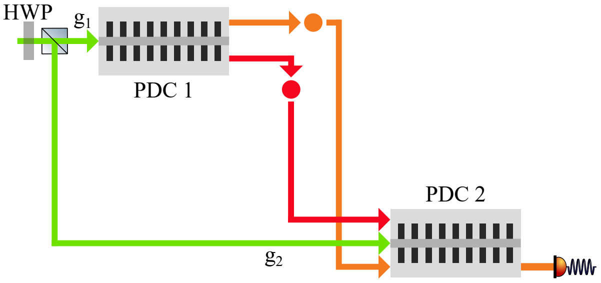

Figure 4.18: Schematic SU(1,1)-interferometer setup for gain optimisation.

Differential pumping allows to mitigate waveguide coupling losses and restore a high visibility in lossy interferometers. Here, we first investigate the spectral visibility for both setups in order to find the optimal operation point for our OCT measurements. For completeness, we investigate the visibilities at 800 nm, 1400 nm and for coincidence counts (CC), although for OCT measurements with undetected photons, only the visibility at the signal wavelength is relevant. The corresponding setup for differential pumping in a SU(1,1) geometry is depicted schematically in Fig. 4.18 for reference. As we have seen in section 2.6.3, the visibilities for the SU(1,1)-geometry are given by

$$V_{800} = \frac{2\sqrt{T_{800}T_{1400}}g_1g_2}{T_{800}g_1^2 + g_2^2} \tag{4.21}$$

$$V_{1400} = \frac{2\sqrt{T_{800}T_{1400}}g_1g_2}{T_{1400}g_1^2 + g_2^2} \tag{4.22}$$

$$V_{CC} = \frac{2\sqrt{T_{800}T_{1400}}g_1g_2}{T_{800}T_{1400}g_1^2 + g_2^2} \tag{4.23}$$

The formulas from the SU(1,1) geometry change slightly for the case of induced coherence, since now two loss parameters that represent the fibre-couplings $T_{800,1}, T_{800,2}$ for the signal fields from the first and the second pass have to be considered, as indicated in the schematic sketch in Fig. 4.19, that serves as a reference. We derive them analogously to the ones in the SU(1,1)-geometry in Appendix A.3 and only give the results here:

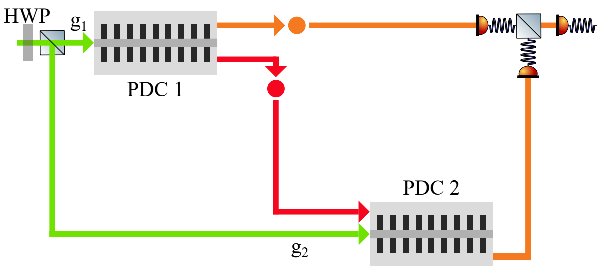

Figure 4.19: Schematic IC-interferometer setup for gain optimisation.

$$V_{800,IC} = \frac{2\sqrt{T_{800,1}T_{800,1}T_{1400}}g_1g_2}{T_{800,1}g_1^2 + T_{800,2}g_2^2} \tag{4.24}$$

$$V_{1400} = \frac{2\sqrt{T_{800,1}T_{800,2}T_{1400}}g_1g_2}{T_{1400}g_1^2 + g_2^2} \tag{4.25}$$

$$V_{CC} = \frac{2\sqrt{T_{800,1}T_{800,2}T_{1400}}g_1g_2}{T_{800,1}T_{1400}g_1^2 + T_{800,2}g_2^2} \tag{4.26}$$

In both setup geometries, a high visibility is achieved by balancing the losses in the interferometer arms such that the probability to detect a photon from either of the two PDC processes at the signal detector is the same. This means that we can mitigate losses from the first pass, which lead to a lower number of photons present at the point of interference, by pumping the second process less strong, thus generating less photons in this second process. This intuitive explanation allows us to assess and design setups according to the expected losses in the respective interferometer arms.

It can be seen that the visibility in the idler arm is now bounded by the product of $T_{800,1}$ and $T_{800,2}$. Therefore, the achieved visibility in the idler temporal interference pattern is very low in the induced coherence case, as both of the fibre-coupling efficiencies lie around 30%. However, for our OCT measurements with undetected photons, we are only interested in a high visibility of the spectral interferogram at the signal wavelength of 800 nm,

The visibility in the spectral interferogram at 800 nm for different pump gain ratios is shown in Fig. 4.21. As we are interested in OCT as an application, we measured the visibilities for a plain mirror (red curve) and a partially reflective neutral density filter that reflects about 50 % (blue curve) as the end-mirror of the idler stage.

In order to evaluate the visibility of the spectral interferograms, multiple interferograms were recorded for a fixed detuned idler stage position while the gain in both stages was varied by the HWP in the setup. Two of those spectral interferograms at different pump gain ratios g_1^2/g_2^2 of 0.15 and 3 are shown in Fig. 4.20 showcasing vastly different visibilities of (27.4 ± 3.6) % and (59.2 ± 4.9) %. These visibilities have been extracted by calculating the difference between neighbouring maxima and minima in the spectral interferogram, assuming a constant visibility, resulting from a constant coupling efficiency and absence of losses, across the full spectrum. We use the mean value of the visibilities from all evaluated pairs of maxima and minima as the data point for the visibility while their standard deviation is used for the error bar.

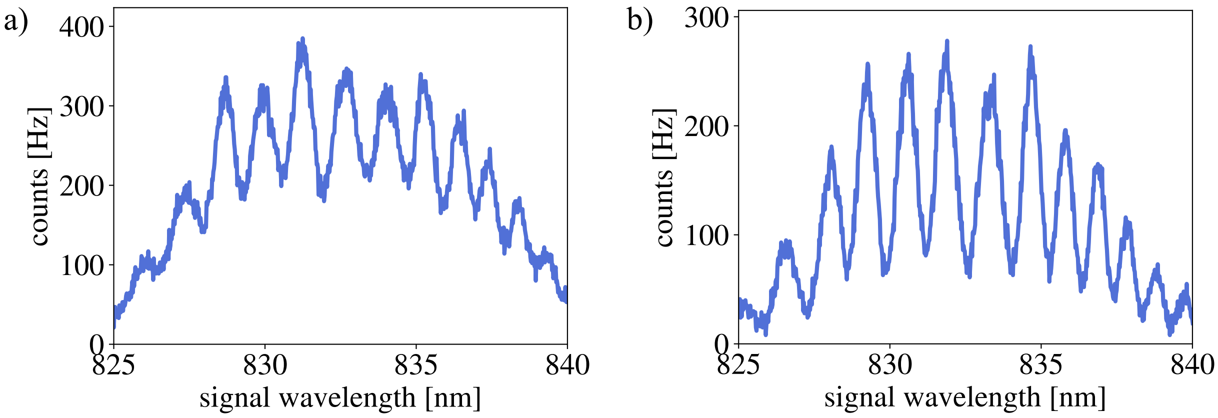

Figure 4.20: Spectral interferograms in the SU(1,1) geometry with pump gain ratios and visibilities of a) $g_1^2/g_2^2 = 0.15$, $V = (27.4 \pm 3.6)\,\%$ and b) $g_1^2/g_2^2 = 4$, $V = (59.2 \pm 4.9)\,\%$.

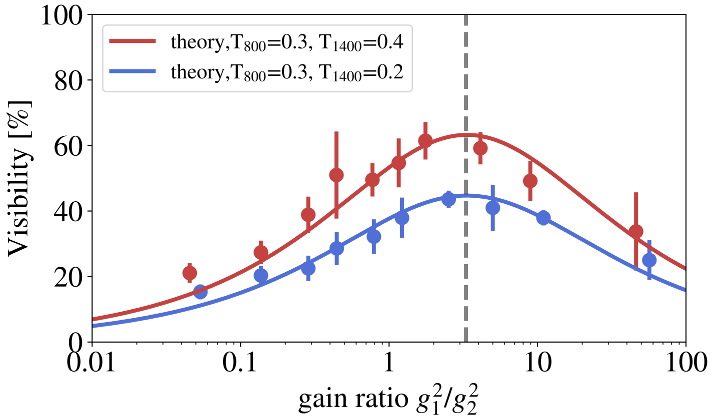

Figure 4.21: Pump gain optimisation in the SU(1,1)-setup with a plain silver mirror (red curve) and a partially reflective (50 %) neutral density filter (blue curve) as the idler end-mirror.

In Fig. 4.21, the measured data points agree well with the theory, which only takes into account the back-coupling efficiencies for signal and idler of $T_{800} = 0.3$ and $T_{1400} = 0.4$. The signal transmission stays constant, since this path is not altered while the idler transmission drops to $T_{1400} = 0.2$ for the second data set, as the filter is introduced. Thus, the visibility is reduced and ultimately limited to $\sqrt{T_{1400}}$. This can be attributed to the fact that we can adjust the gain ratio for T_{800}, which leaves us with the dependence on T_{1400} in Eq. (4.21). It can be seen that, for both cases, the visibility exhibits a maximum at the same gain ratio. At this pump gain ratio, the highest SNR can be expected in measurements and

the highest sensitivity to changes in the transmission, e.g. at layer interfaces of an object under test, is expected. The fact that the maximum stays at the same gain ratio is useful for practical applications, as this allows the gain in the interferometer to be adjusted before introducing a sample.
The same behaviour of gain optimisation can be observed for the case of induced coherence. The measurements of the visibility in the signal at different pump gains in this is presented in Fig. 4.22. As it was also the case for the SU(1,1) setup, the maximal visibility is given by the back-coupling efficiency T_{1400} and can be reached for a pump gain ratio of $g_1^2/g_2^2 = \frac{T_{800,2}}{T_{800,1}}$. Thus, we observe a more balanced pump gain ratio close to 1 to be optimal in the experiment since the fibre-coupling efficiencies are almost equal. In the presented data, the measured values for the fibre-coupling efficiencies in the experiment were used to calculate the curve for the theoretically expected visibility.

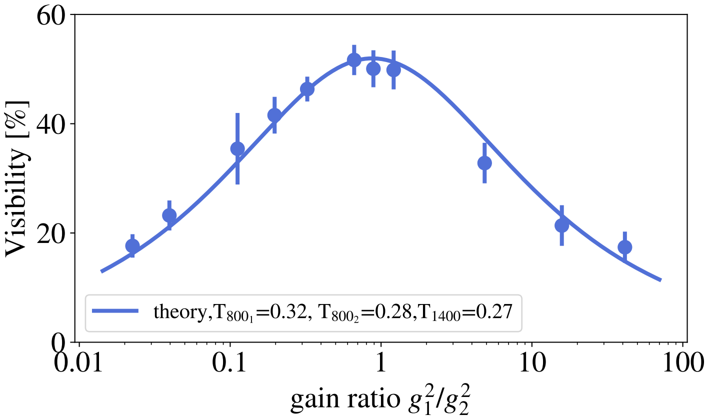

Figure 4.22: Pump gain optimisation in the IC-setup. The theory includes the measured fibre-coupling efficiencies.

Thus, we can say that in both setups, SU(1,1) and IC, we can maximise the visibility by adjusting the pump gain ratio. This optimisation can be performed before introducing an object under test, and therefore allows for calibration of the respective setup for a wide range of samples in our OCT measurements with undetected photons.
In the next step, we will look at the influence of losses in the signal arm and the minimal detectable layer reflectivity in the current setup.

Influence of losses

In a practical application, the presented OCT setups could be exposed to ambient losses due to scattering or loss mechanisms. We therefore studied the effect of losses in the signal arm by introducing ND filters of different strength in the SU(1,1) setup and recording the resulting visibilities. The measurements are in good agreement with the calculations and show that for an increased loss in the signal arm, the pump gain ratio needs to be increased, cf. Fig. 4.23. However, the maximum visibility remains the same for all measurements.

The results can be translated directly to the IC case, where losses in only one of the signal

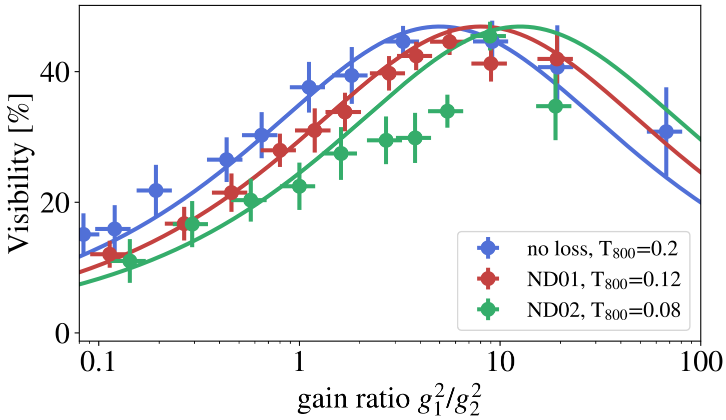

Figure 4.23: Shift of the optimal pump gain ratio for the maximum of the visibility in the signal interferogram for different values of additional losses in the signal arm.

paths would lead to a shift in the pump gain ratio, while a common loss in both arms would leave it unaffected.

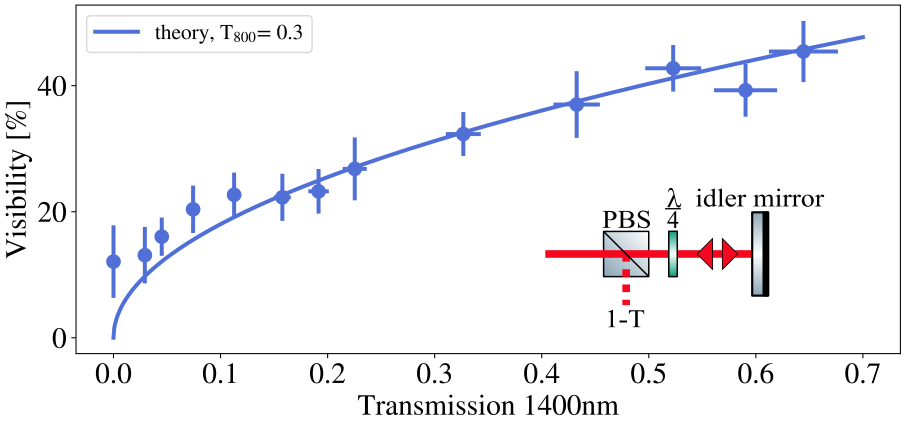

Figure 4.24: The retrieved spectral visibility at the signal output with varying transmission in the idler arm. The expected behaviour as determined by Eq. (4.21) is shown as the solid blue line. The inset shows the added variable losses in the idler arm, which we realised with a PBS and quarter wave plate in a double pass configuration.

In a next step, we test the minimal detectable layer reflectivity in our setup. To this end, we introduce a combination of a polarising beamsplitter (PBS) and quarter wave plate (QWP) in the idler arm. Turning the QWP leads to a gradually increasing portion of the light being directed to the rejection port of the PBS. We measure this rejected fraction for different QWP angles in order to calibrate the transmission in the arm. In figure 4.24, the obtained data for the spectral visibility is compared to the theoretical prediction and shows a good agreement. We can see that the theoretically expected visibility is extracted from the interferograms down to a transmission in the idler arm of 5 %. We note that these measurements were taken with a single acquisition detection and exposure times of the spectrograph of 1 s. One could

more accurately measure low transmissions by taking longer or averaging measurements. For comparison, we will present the influence of averaging to OCT measurements at the end of this section.
After investigating the influence of losses and the conditions for maximal visibilities, we will next preform actual time domain and Fourier domain OCT measurements on an object under test at the optimal pump gain ratios that were previously determined.

4.3.3 Performing OCT measurements with undetected photons

In this section, we compare FD-OCT and TD-OCT with undetected photons performed with the SU(1,1) and the IC setups, which we presented in figures 4.2 and 4.4. The details of the experimental setups were discussed in section 4.1. For reference, the combined figure 4.25 highlights the differences between these two setups. For all measurements, the same sample was used: a ND03 filter fixed to the end-mirror of the idler path. This object allows to realise a bi-layer system composed of two separated surfaces where the light is split up roughly equally, as half of the light is reflected back from the first surface and the other half is left to be reflected by the mirror after passing the ND-filter. The optical path difference (OPD) between the two surfaces amounts to 3.0 ± 0.3 mm and has been calculated from the product details given by the vendor.

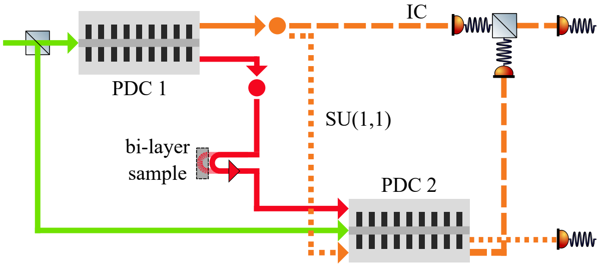

Figure 4.25: Schematic SU(1,1) and IC geometry for OCT.

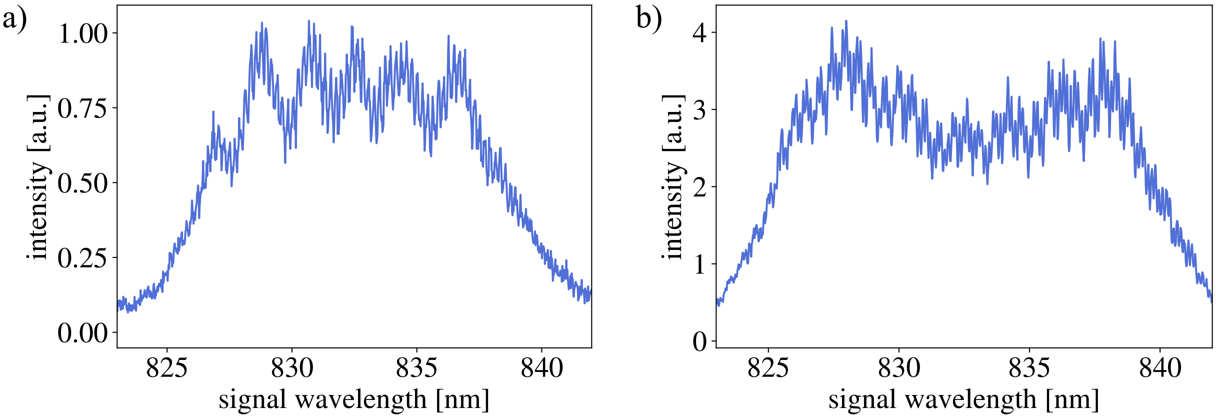

Figure 4.26: Data from the Fourier domain OCT measurements revealing a beating in the spectral interferogram for a) the SU(1,1) geometry and b) the IC geometry.

The FD-OCT signal is recorded for a fixed arm length imbalance that is chosen such that a beating in the spectral interferogram can be observed. This beating corresponds to different temporal offsets which translate to linear spectral phases. The data for the SU(1,1) and IC case is presented in Fig. 4.26. This data is Fourier transformed and results in peaks in the temporal domain corresponding to the reflections from the different layers. The amplitude of the positive part can then be used to determine the layer separation, as their relative spectral linear phase leads to a separation in this temporal picture. The offset from zero can be chosen freely by adjusting the idler arm length. The results for SU(1,1) and IC schemes are shown in Fig. 4.27. Here, we transfer the x-axis from the temporal domain to the spatial domain and show the peaks with the indicated OPD ΔL between the two layers of the sample for both setups in a) and a close-up of two peaks in b). We determine the FWHM of the peaks and receive the axial resolution Δz of our FD-OCT measurement in both schemes.

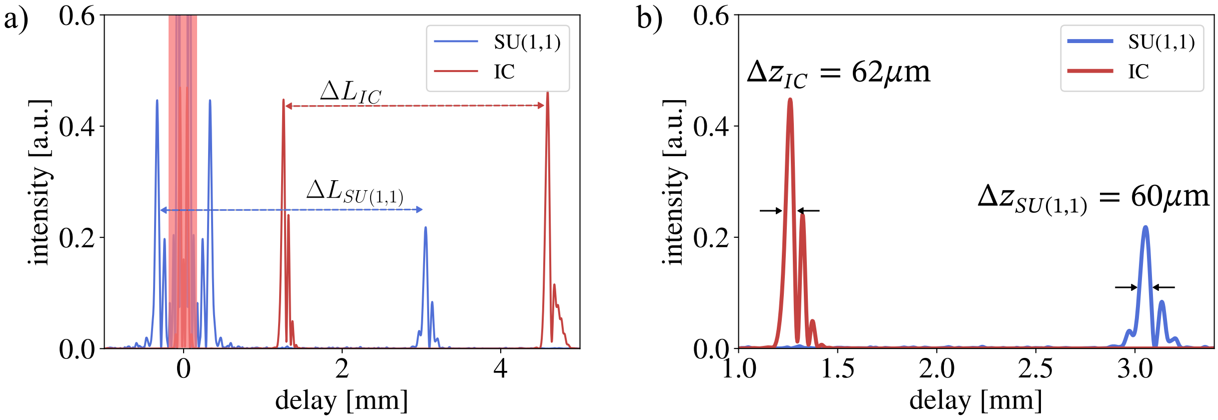

Figure 4.27: a) Retrieved Fourier intensities from a FD-OCT measurements of a bilayer object under test that allow to extract the optical path difference between the layers in the SU(1,1) and IC geometry of $\Delta L_{SU(1,1)} = 3.41$ mm and $\Delta L_{IC} = 3.33$ mm. b) Close up to the peaks in the FD-OCT for SU(1,1) and IC showing similar resolutions Δz of 60 µm and 62 µm (FWHM).

In the case of SU(1,1), we obtain an OPD of $\Delta L_{SU(1,1)} = (3.41 \pm 0.06)$ mm. However, in order to achieve this result, one peak in the negative part and one peak in the positive part of the Fourier transform have to be considered. This is due to the fact that the delay between the signal and idler arm has been set such that for the first surface, the signal arrives before the idler, while for the second surface, the signal arrives after the idler. We can successfully distinguish the two peaks that belong together as the side lobe in the spectrum is flipped for the peak which is located close to zero on the positive side. Therefore, we can assign this peak to the negative half of the Fourier-transform, which we are not interested in. We note that placing the point of zero OPD between the two surfaces in the measurement might allow to increase the axial scanning range of the FD-OCT method.
For the IC case, a layer separation of $\Delta L_{IC} = (3.33 \pm 0.06)$ mm can be extracted. These results are close to the expected OPD given by the ND03 filter of 3.0 ± 0.3 mm within the error margins given by the axial resolution of our OCT measurement and the fabrication tolerances for the object under test. Both FD-OCT results may deviate slightly from the expected value as a result of calibration inaccuracies of the spectrograph as well as to imperfect alignment.

In both setups we reach a similar depth resolution of 60 µm (FWHM), as can be seen from the close-up of both two peaks in Fig. 4.27 b). These peaks are broadened due to second order dispersion in the setup, which can be compensated in post-processing. However, the obtained value is still smaller but close to the previously calculated ideal axial resolution of 69 µm. The deviation between the measured and calculated axial resolution is likely caused by the assumptions made for the spectral envelope and bandwidth of our bi-photon spectra. Since the axial resolution value is closely connected to the bandwidth of the bi-photon source and thereby its correlation time, we can calculate the width of the temporal interferogram for a Fourier-limited correlation time and thereby obtain a limit for the axial resolution. We have seen before that the Fourier-limited correlation times lies in the order of 80 fs and leads to a temporal interferogram with a width of 0.2 ps. This corresponds to a resolvable optical path delay of $\Delta z = 60$ µm. This shows that our measurement is consistent with the estimation of the resolution based on the coherence length associated to one spectrum.

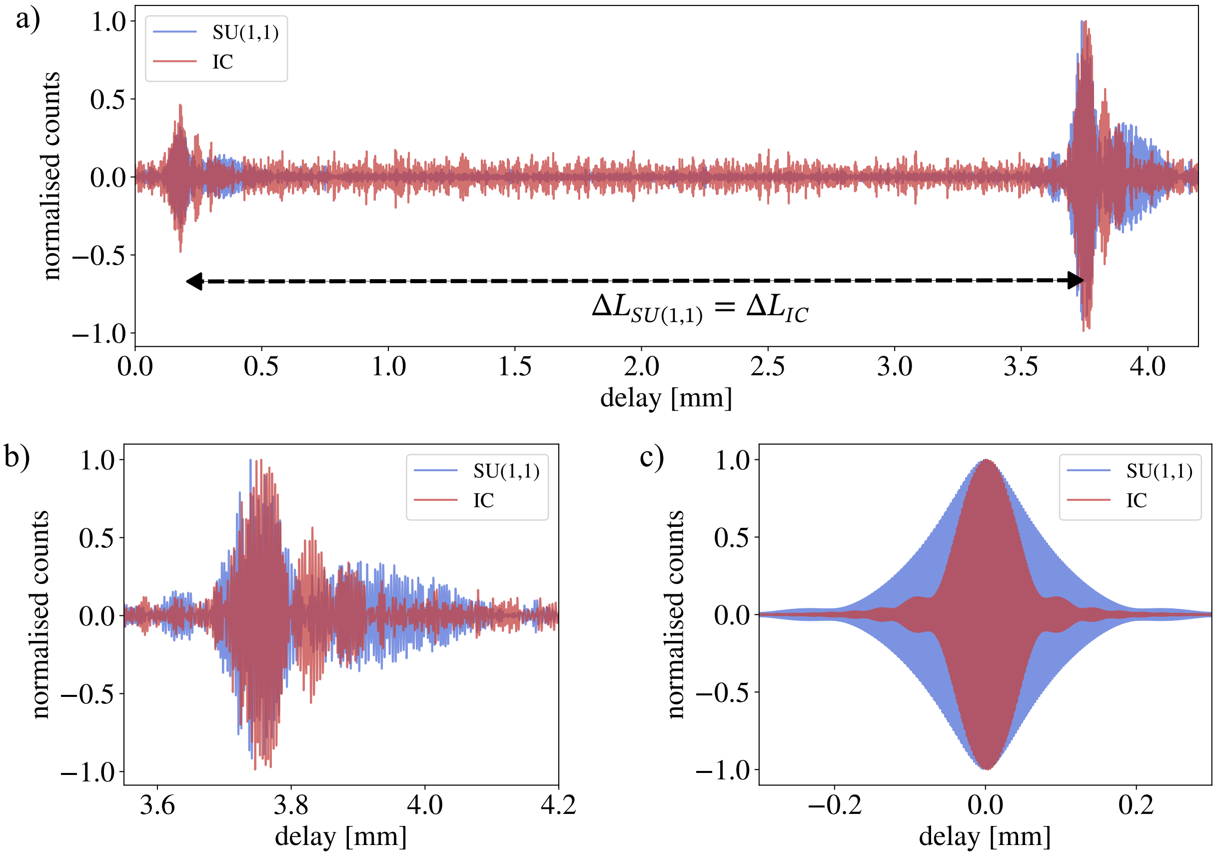

Figure 4.28: a) TD-OCT trace for the same object with the SU(1,1) and IC geometry from which a layer separation of . b) A close-up to one of the peaks reveals a higher resolution Δz for the IC geometry of 96 µm in comparison to 140 µm for the SU(1,1) geometry. c) A simulated comparison of SU(1,1) and IC in the close-up. In the SU(1,1) scheme, a second order dispersion of 11000 fs^2 is present and only 3000 fs^2 in the IC scheme.

After studying the two setups for the case of FD-OCT measurements, we will now turn to TD-OCT. This method records temporal interferograms and therefore does not require frequency-resolved detection. Additionally, we have seen in the beginning of the section that FD-OCT can only record a limited maximal layer separation given by the resolution of the spectrograph. This limit no longer applies for TD-OCT. Meanwhile, the main drawbacks of this method are longer measurement times and the susceptibility to spectral phases within the interferometer that broaden the temporal interferogram. A measurement of TD-OCT is presented in Fig. 4.28 a) from which a layer separation of $\Delta L_{SU(1,1)/IC} = 3.56 \pm 0.14(0.10)$ mm is extracted in both setups. Here, the error refers to the axial resolution of the SU(1,1) and the IC scheme. The close-up on one of the peaks in Fig. 4.28 b) reveals a higher resolution for the IC scheme, since the FWHM of the main peak of the temporal interference pattern reduces from 140 μm in the SU(1,1) scheme to 96 μm in the IC scheme. This agrees well with simulations of the temporal interferogram for different amounts of second order dispersion in Fig. 4.28 c) where 11000 fs^2 are present in the SU(1,1) scheme and only 3000 fs^2 in the IC scheme, thus reproducing the same widths of the temporal interferogram as we observed experimentally. The additional peaks observed in the experiment can be attributed to the non-ideal phase-matching shape, spatially multi-mode contributions to the interference and contributions to third or higher order dispersion from the setup.

Through this study, we find that due to the smaller amount of second order dispersion, the actual correlation time in the IC geometry is lower compared to the SU(1,1) geometry, which allows us to perform measurements with a higher temporal or spatial resolution as the temporal interferogram exhibits a narrower width.

Finally, we compare the required pump powers, integration times, number of acquisitions and the resulting total measurement time, as well as the achieved axial resolution for TD-OCT and FD-OCT in the IC and SU(1,1) scheme in Tab. 4.1.

Table 4.1: Comparison of the experimental parameters for performing TD-OCT and FD-OCT in the SU(1,1) and IC scheme.

method	pump power [mW]	int. time [s]	acquisitions	meas. time [s]	resolution [μm]
TD-OCT	0.05	0.02	48000	960	SU(1,1): 140 μm IC: 96 μm
FD-OCT	5	1	1	1	SU(1,1): 60 μm IC: 62 μm

Although FD-OCT appears to be superior to TD-OCT, it should be noted that the experiments have been carried out at different pump power levels. From the comparison in Tab. 4.1, we can see that TD-OCT and FD-OCT use a similar amount of resources in our current setup. For the FD-OCT, pump powers on the order of a few mW were required to record interferograms with integration times of $0.2 - 1$ s. In the TD-OCT case, the pump power was as low as 50 μW and the integration times per point were 0.02 s. Additionally, those measurements were acquired by a comparably cheap Si-APD. If we assume that the needed acquisition time is inversely proportional to the signal on the spectrograph, the measurement time for FD-OCT will increase by a factor of 100 at the same pump power level

as the TD-OCT measurements.
Currently, a major draw-back in our realisation of TD-OCT are the long measurement times on the order of 30 minutes. Those are mainly caused by the step-wise scanning of the stage in the idler arm. We can improve our measurement procedure by using a stage in scanning mode. Together with a coarser sampling, this brings TD-OCT and FD-OCT measurements to the same time scale. Furthermore, TD-OCT does not require an expensive single-photon sensitive spectrometer. Thus, we find that TD-OCT in the IC scheme is the choice for the implementation of an integrated sensor for OCT measurements with undetected photons.
Comparing the results of our OCT measurements with undetected photons to the literature, we see that setups based on bulk nonlinear crystals achieve a higher axial resolution down to 20 μm due to broader spectra [37] [2]. However, this comes at the cost of a lower normalised brightness as these setups typically operate at pump power levels around hundreds of mW. Current experiments for OCT with undetected photons based on bulk nonlinear crystals often operate in interesting mid infra-red spectral range. However, extending our work into this regime is well in reach by translating our findings a version of the nonlinear interferometer that operates with our mid-IR PDC source- We will present first measurements in such a setup in chapter 5. Due to its larger spectral coverage, we expect to achieve a higher axial resolution down to 14 μm in the future.
Furthermore, we can conclude that IC geometry is beneficial when performing OCT measurements with undetected photons based on an integrated PDC source, as it does not require back-coupling of the signal field and allows for a higher resolution in TD-OCT. This finding is unique to integrated implementations as for nonlinear interferometers based on bulk crystals the SU(1,1) geometry is preferred due to a presumably easier setup [18, 37].
realisations of OCT with undetected photons which go beyond the demonstrated proof-of-principle experiments have achieved significantly higher signal-to-noise ratios and shorter acquisition times [37]. Thus, we will provide an outlook towards future improvements in our system by making use of averaging effects.
The presented results and considerations in this section are currently being prepared in a manuscript [101].

4.3.4 Outlook: averaging effects

For a practical quantum sensor, we need to employ more advanced techniques of data acquisition and make use of averaging to increase the SNR. As the IC geometry turned out to be the preferred realisation for an integrated quantum sensor, we performed FD-OCT and TD-OCT measurements using this scheme and investigate the changes in the SNR as we average for longer times with the spectrograph or average multiple temporal interferograms.

In these measurements, we define the signal-to-noise ratio as

$$SNR = \frac{|S_{max}|^2}{|S_{mean}|^2}. \tag{4.27}$$

---

[2] We note that we converted the resolution in the publication according to our definition.

Here, S_{max} denotes the maximum of the measured signal while S_{mean} is the mean value of the noise amplitude.

The effect of longer integration times of the spectrograph on the SNR in the FD-OCT measurement is shown in Fig. 4.29, showcasing a repeatable FD-OCT measurement for different integration times of the spectrograph ranging from $0.2 - 5$ s. In this measurement, a significant increase in the signal-to-noise ratio can be observed, which is depicted as an inset in the figure. Thus, increasing the integration time enables practical OCT applications with undetected photons. The same effect can be observed by increasing the brightness of the source or the pump power. We note here that a better SNR with longer integration times is only possible due to the good phase stability of the setup. Phase fluctuation would otherwise lead to a saturation of the SNR for longer integration times as soon as the acquired interference fringes shift against each other. For a good stability, these phase fluctuations should be less than $\Delta\Phi = \pi$ at the central frequency of our spectrum. This relates to a required stability of the arm length difference between signal and idler of around 415 nm, since the period of our interference is given by half of the wavelength in the moving arm. Thus, the requirements on the mechanical stability of the signal and idler arm are different and more care needs to be taken to fix the signal mirror.

For our FD-OCT measurements, we observe a linear increase of the SNR and reach a maximum value at 1 s integration time of 31 dB. This is value is not yet comparable to the one of 66 dB at 1 s integration time in [37]. Meanwhile, we did not optimise our system to achieve the highest possible SNR, such that we believe that the reported value can be further improved.

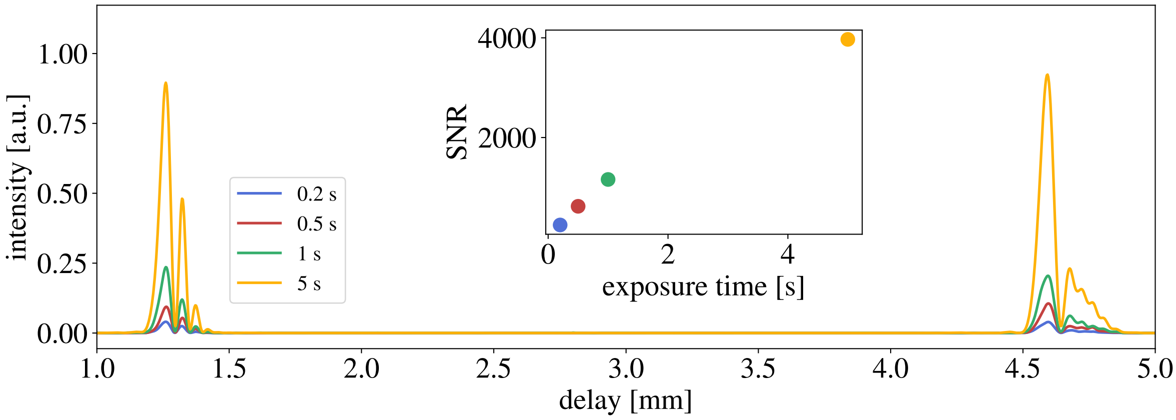

Figure 4.29: FD-OCT measurements for different integration times of the spectrograph ranging from $0.2 - 5$ s. The resulting SNR is given in the inset of the figure.

The positive effects of averaging can also be observed in the case of TD-OCT. In Fig. 4.30, a single interferogram is presented together with the average of four subsequently recorded interferograms. It can be seen, that the noise outside the interference peaks is strongly suppressed even for this small amount of averages. The SNR increases from around 300 to over 4000, corresponding to an increase from 24 dB to 36 dB. It can further be observed that the temporal shape of the interferograms is identical for the single and averaged signal.

As the delay stage has a limited repeatability, we need to shift the recorded interferograms against each other. We do so by changing the indices in the x-axis for each of the four recorded interferograms and choosing the first interferogram as a reference. With this, we can overlap the shifted interferograms correctly to form an average by constructing a similarity function

$$C(d) = \sum_{k=0}^{n} p_{meas}(k+d) \cdot p_{ref}(k). \tag{4.28}$$

In this expression, k is the index in the acquired data array with a total length of n, while d is the shift that is introduced between the current measurement and the reference data set. The value of d can vary from negative to positive values. The maximum of the similarity function allows to extract the required shift to properly overlap the two measurements and perform an average. In the presented measurements, this shift amounts to roughly 4 µm, which gives an indication of the drift in the relative optical path length between signal and idler in our setup over a duration of roughly 20 minutes. This drift can be caused either by the alignment or due to the non-perfect bi-directional repeatability of the translation stage. The procedure of averaging of temporal interferograms can be continued with any data set and the same reference, eventually leading to different required shifts on the data.

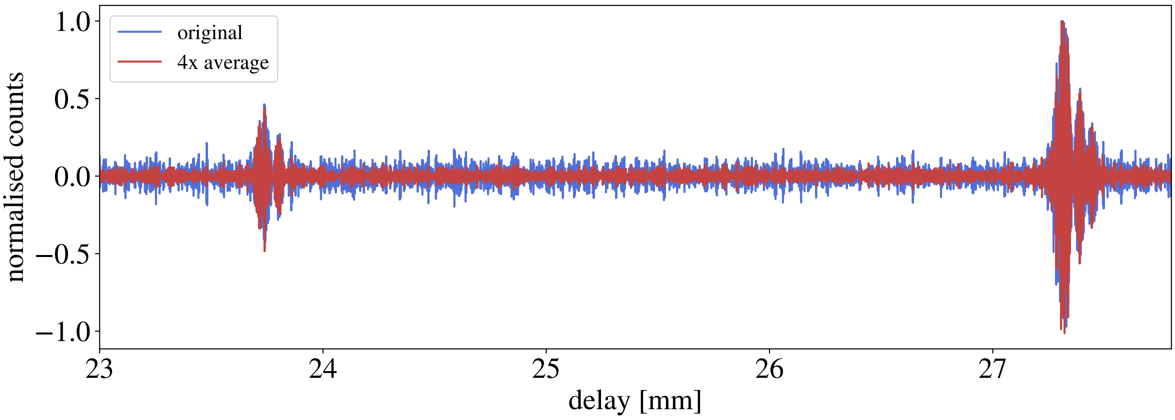

Figure 4.30: TD-OCT measurements showing a single acquisition and the average of 4 sequential acquisitions that have been shifted for the highest similarity. This averaging procedure leads to a visibly increased SNR.

A stage in scanning mode would allow to acquire many interferograms in a short amount of measurement time. Together with the presented shifting procedure, this would allow for a quick acquisition of TD-OCT measurements with high SNR. Realistic scanning times for one interferogram are then in the range of a few seconds [19, 102] with a stage of scanning speeds of several mm/s and scanning ranges of more than 10 mm.

These findings on the beneficial effects of averaging on temporal and spectral interferograms can be directly translated to the operation of a nonlinear interferometer in the mid-IR.

Summary

In this chapter, we presented experiments on nonlinear interferometry with undetected photons in three different experimental setups utilising our integrated, group velocity matched PDC source for the generation of signal and idler at 830 nm and 1400 nm with a spectral bandwidth of up to 7 THz. First, we used the source in an SU(1,1)-interferometer, where we demonstrated a technique to measure the bi-photon correlation time of any source. Using this technique, we determined the correlation time of our source to be below 100 fs. We furthermore found that the bi-photon correlation time varies with the spectral bandwidth and shape of the generated PDC spectra. From our measurements, we were able to extract the second order dispersion introduced into the setup by our waveguide and potential objects under test, which increase the actual correlation time. Control over spectral phases in the setup allowed us to carry out phase measurements with undetected photons that achieve a precision of 250 fs^2.

Next, we investigated the optimal conditions for OCT measurements with undetected photons. To this end, we realised a nonlinear interferometer in the commonly used SU(1,1) geometry and the induced coherence geometry. During this investigation, we found that the IC geometry allows to circumvent back-coupling to a spatially multi-mode waveguide and is therefore practical when using integrated waveguide PDC sources. In both setups, we optimised the pump gain ratio between the two PDC processes and found that the optimal ratio is independent of the reflectivity of an object under test in the idler arm in both schemes. In this optimal setting, we performed FD-OCT and TD-OCT and found an axial resolution of 60 μm in FD-OCT in both setups. However, in the case of TD-OCT, we found an increase in resolution of 96 μm for the IC scheme instead of 140 μm for the SU(1,1) scheme. Considering the required resources, we concluded that TD-OCT in the IC scheme is the best choice for the implementation of OCT with undetected photons. Finally, we presented an outlook towards increases SNR by utilising averaging effects in the measurements.

5

Nonlinear interferometer in the mid infra-red

As the final step in our efforts towards the development of an integrated quantum sensor in the mid-IR, we now want to make full use of the potential of measurements with undetected photons by utilising our newly developed mid-IR photon pair source in a nonlinear interferometer.

After presenting and characterising the setups with our PDC source in the near-IR in chapter 4, we now transfer our knowledge from the previous section to an interferometer that utilises a PDC source with photons at 860 nm and 2800 nm as the active element.

The mid-IR spectral region is widely known as the 'fingerprint region' for organic materials due to their characteristic absorption features [8]. Thus, we first realise absorption measurements with undetected photons by detecting the spectrally resolved interferogram on an NIR spectrometer at the signal wavelength around 860 nm. Furthermore, we perform first measurements of Fourier-transform spectroscopy with undetected photons, still only detecting the signal photons with a Si-APD. This measurement is performed spectrally unresolved by measuring the temporal interferogram analogously to the classical technique of FTIR spectroscopy.

First, we look at the experimental setup of our nonlinear interferometer in the mid-IR. Although we saw in chapter 4 that the induced coherence scheme yields benefits when working with integrated waveguides, we employ the SU(1,1) scheme here. We decided to use this scheme for our first setup as it has been investigated in more detail at the time of the experiment and allows to find the point of zero path delay between signal and idler more easily.

5.1 Experimental setup

In the experimental setup, depicted in Fig. 5.1, we employ our new ultra-broadband mid-IR PDC source, which has been characterised in detail in chapter 3. We pump the 40 mm long Ti:LiNbO$_3$ waveguide with a cw-laser which is tunable from $644 - 649$ nm (Toptica DL pro). We use a combination of an HWP and PBS for power control, together with another HWP, to set the polarisation of the pump light in order to address the Type II phasematching of the PDC process. Due to the elliptical beam shape from the pump laser and a limited choice in aspheric lenses for coupling to the waveguide, a telescope and a cylindrical lens have been used in the pump path to match the pump field to the waveguide mode. The position of these elements has been calculated and adjusted such that the pump field is coupled to and guided in the fundamental spatial mode. The waveguide is heated to a temperature around 200 °C to achieve phasematching as well as to reduce the impact of photo-refraction, as discussed previously. The current waveguide is not equipped with anti-reflection coatings, due to their complexity in fabrication. The transmitted pump light, as well as the generated signal and idler fields, is collimated by a 90° off-axis parabolic mirror before the different colours are separated by dichroic mirrors. The first dichroic mirror that separates the pump and signal fields from the idler field has been fabricated in-house, as such mirrors are not readily available commercially. A standard dichroic mirror (Thorlabs LP735) is used to separate the pump and signal field. All fields are reflected back by their respective end-mirrors. The end-mirror in the idler arm can be translated by a motorised linear stage (PI M-112-1DG). This allows to vary the optical path difference between the signal and idler arm, which introduces a linear spectral phase. After recombination on the dichroic mirrors, all three fields are coupled back to the waveguide via the parabolic mirror.

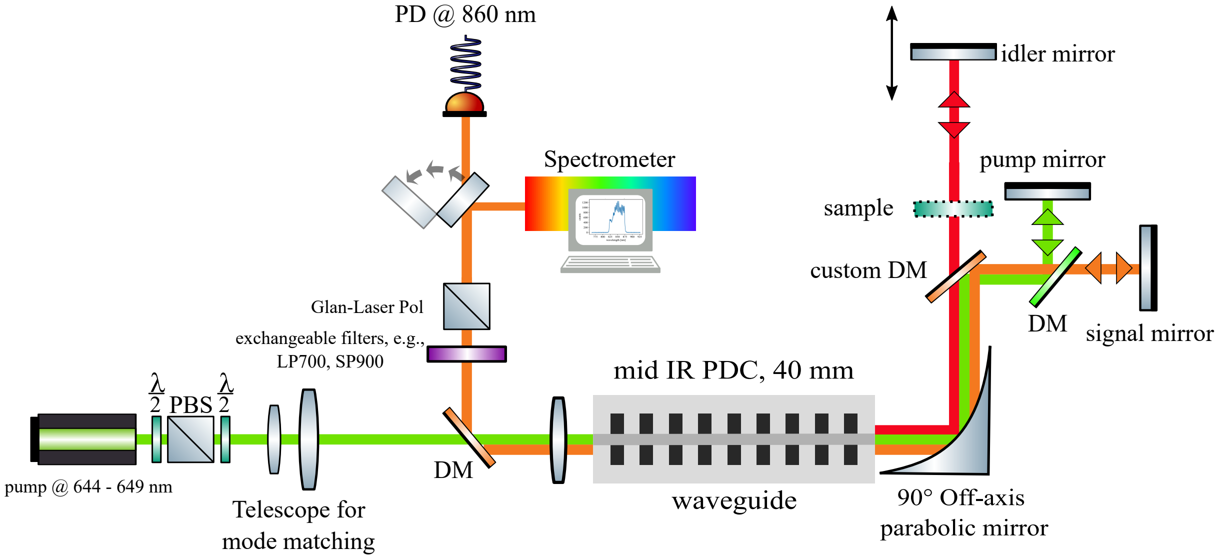

Figure 5.1: The setup of the nonlinear interferometer in the SU(1,1) geometry in the mid-IR is based on our new mid-IR PDC source. The pump, signal and idler generated in the first process are collimated by an 90 ° off-axis parabolic mirror, separated with custom and standard dichroic mirrors (DM) and reflected back by the end-mirrors in the respective interferometer arms. All fields are coupled back to the waveguide via the off-axis parabolic mirror. In the waveguide, the pump field drives a second PDC process that can generate signal and idler photons. After the second pass, the signal field is isolated with a dichroic mirror, filtered and detected either frequency-resolved on a spectrometer or time-resolved via photon-counting with an avalanche photo-diode (PD) and while scanning the stage in the idler arm.

We note here that the pump gain ratio is assumed to be close to optimal without the need for adjusted pump powers, as the pump field experiences similar coupling losses as the signal field. We saw in section 2.6.3 that the optimal gain ratio is given by the inverse transmission of the signal field. The main factor for different coupling losses comes from the multi-mode guiding of the pump field, such that not all of the pump power can be coupled back to the waveguide. However, we tried to minimise this issue via alignment.

After the second PDC process, the signal light is once again separated from the pump via a dichroic mirror and spectrally filtered. Furthermore, we introduce a Glan-Laser polariser in the detection path to detect only the TM polarisation of the generated signal photons and suppress unpolarised fluorescence from the waveguide or competing higher order PDC processes. After coupling to a single-mode fibre, spectral or temporal interference can be observed. The measurements are performed on the same single-photon sensitive spectrometer and avalanche photo-diode that we used in chapter 4 and are carried out with the same integration times and step sizes of the linear stage.

Special components in the MIR

In the presented setup, the large difference between the wavelengths of the involved fields, the large bandwidth of the signal and idler fields, as well as idler wavelengths in the mid-IR spectral region require a careful design of the experiment and pose challenges in the experimental realisation and day-to-day alignment. Here, we list some of those challenges and considerations we encountered during the first assembly of the nonlinear interferometer based on an integrated waveguide in the mid-IR.

Due to the large spread of wavelengths, a parabolic mirror is used to collimate the fields after the first PDC process as well as to couple back all three fields into the waveguide without the need for compensation of chromatic aberrations. The non-trivial alignment of such a parabolic mirror can lead to coupling into one of the higher-order spatial modes of the waveguide at the pump and signal wavelengths for the second pass through the waveguide. As we discussed in the previous chapter, this problem can be diminished by careful alignment and mode matching or by employing the induced coherence geometry, which eliminates the need to couple the signal field back into the waveguide.

We discovered that optical components such as dichroic mirrors for all three wavelengths, with the longest one laying in the mid-IR, are not readily available from commercial vendors and often require custom coating designs. We contacted our in-house cleanroom for the design and fabrication of the needed dichroic mirror that would separate the idler from the pump and signal field. In this mirror, we experience losses in the substrate and observe that imperfections in the design and fabrication of the layer stack, which forms the coating, limit its performance. The coating design tends to be susceptible to fabrication imperfections because of the high number of dielectric layers such that small changes of the thickness in single layers lead to a large impact on the overall performance. All together, this leads to transmission values at the mid-IR wavelengths below 80 %. As the idler field passes this element twice, such a reduced transmission vastly limits the achievable visibility of the spectral interference to below 80 %, which does not yet include losses on the end facets of the waveguide or during coupling. For the experiment, multiple dichroic mirrors have been fabricated to mitigate fabrication tolerances. Two of them had a substrate of congruent $LiNbO_3$ while one has been fabricated on Mg:$LiNbO_3$ with adjusted parameters for the layer stacks. The characterisation of the dichroic mirrors with their reflectivity at the near-IR wavelengths around 850 nm and transmissivity in the mid-IR around 2800 nm is shown in Fig. 5.2.

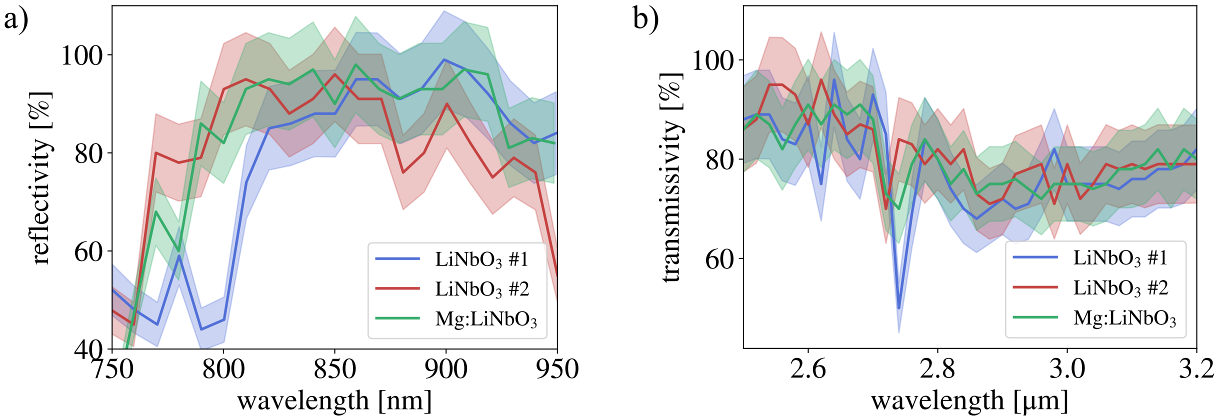

Figure 5.2: a) Reflectivity at the near-IR wavelengths and b) transmissivity at the mid-IR wavelengths for three different dichroic mirrors.

In both measurements, tunable cw-lasers at the respective wavelengths are used, and the reflected or transmitted power is detected with a power metre. The error bars in Fig. 5.2 are given by the 5% error in the detected power on the power metre. The measurements are performed with the dichroic mirror at an angle of incidence of 45°. In all three cases, the near-IR and pump light is reflected while the mid-IR light is transmitted. We chose this design in order to minimise the number of necessary layers. However, this comes at the cost of increased transmission losses due to absorption in the substrate material. We can observe that for the near-IR wavelengths, only the dichroic mirror on Mg:$LiNbO_3$ provides a high reflectivity over the full target range from 800 nm to 900 nm. At mid-IR wavelengths, the transmissivity is similar for all three mirrors. They show absorption characteristics around 2750 nm with different strengths, which are caused by $OH^{(-)}$ groups in the $LiNbO_3$ material, whose concentration is known to vary in different batches of the material. We observed a similar absorption during the PDC generation process in chapter 3. Due to the best performance among the three, we choose to work with the dichroic mirror based on the Mg:$LiNbO_3$.

We note here that the waveguide has not been equipped with anti-reflection coatings for the involved wavelengths. This leads to higher losses at the end-facets of around 13.5 % at the idler wavelength, which limits the achievable spectral interference visibility further to 69 %, ultimately resulting in a final achievable visibility of 49 % after considering coupling losses to the waveguide of around 50 % as a typical value when working with a parabolic mirror. Furthermore, the lack of anti-reflection coatings means that the setup is more sensitive to mechanical instabilities due to the use of a cw pump laser. We therefore observe strong variations in the generated PDC rates when both processes are driven simultaneously, as shown in the next section. This implies an increased need for post-processing of the recorded temporal interferograms.

5.2 Temporal and spectral interferograms

In our experiments, we first record temporal and spectral interferograms without an object under test to study the behaviour of the interferometer itself with the new source and compare the results to our simulations.
Let us start by looking at the recording of a temporal interferogram. The signal has been recorded with a Si-APD and a TimeTagger for an integration time of 0.05 s per step, while varying the idler arm lengths in steps of 350 nm. A sample of the raw data for a temporal interferogram is shown in Fig. 5.3. The data exhibits strong variations in the signal counts, which are not caused by the interference but rather by the mentioned instabilities from the lack of anti-reflection coatings in the setup. The actual interference occurs around a value of 14.35 mm for the stage position and shows a different periodicity than the slower random drifts in the count rate.

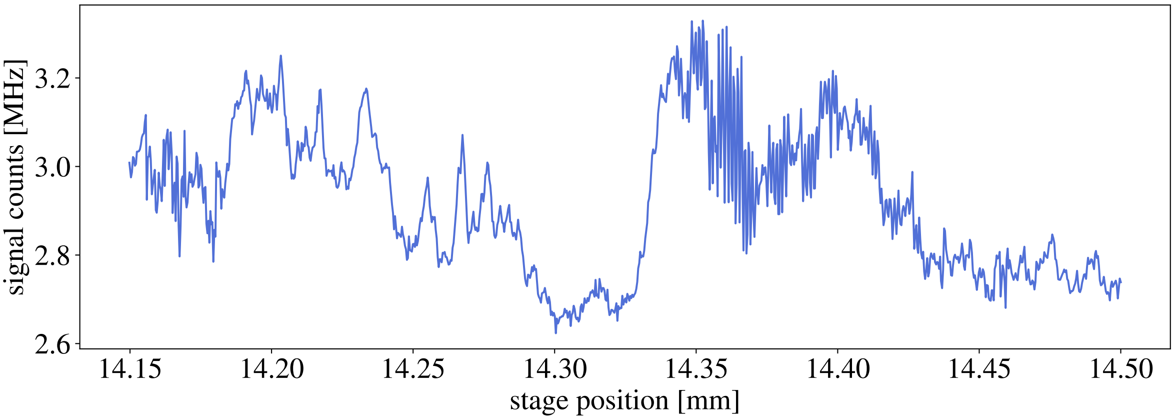

Figure 5.3: Raw data of the signal counts forming the temporal interferogram. The counts are recorded with a Si-APD while the idler end-mirror position is scanned with a linear translation stage.

In order to retrieve the desired interference pattern, we perform a Fourier transformation of the signal and apply a filter to eliminate the noise contributions. The applied Fourier-filter and the processed temporal interferogram, which we retrieve via inverse Fourier transform, are shown in Fig. 5.4. The filter is set to a value of 1 around the period of the oscillations in the interferogram, which is given by the idler wavelength since the end-mirror in the idler arm is translated to introduce a relative time delay. All other frequency components, especially the ones at low frequencies that are caused by power fluctuations, will be suppressed by setting the filter to a value of 0. We mark the suppressed regions in red in figure 5.4 a). We retrieve a cleaned temporal interferogram via inverse Fourier transform of the manipulated spectrum. We can now use this temporal interferogram for further investigations.

Spectral interference can be observed in the signal spectrum in Fig. 5.5 a). Here, we depict the case with a blocked idler path in red, which should lead to no interference, and plot the signal in the case of an unblocked idler path in blue. The steep edges on the spectrum are caused by the spectral filters in the detection path. These have been placed there to suppress fluctuations in the measurement of the temporal interferograms. As the idler arm

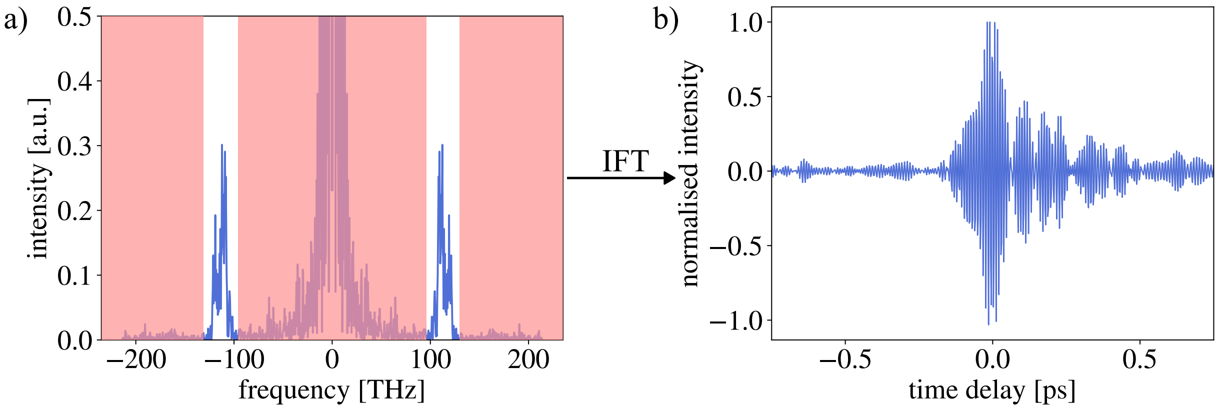

Figure 5.4: a) Applied filter in the Fourier transformed raw data of the temporal interferogram. The filter suppresses components outside a band around the frequency of the interference given by the idler wavelength. b) Temporal interferogram retrieved from the inverse Fourier-transform.

is unblocked, interference can be observed. The period of the interference can be adjusted with the path delay between signal and idler and is chosen such that enough oscillations are visible to optimise the coupling for a homogeneous and high visibility across the whole spectrum. Dividing this interferogram by the reference without interference, i.e., with the idler arm blocked, allows to observe the interference in detail in Fig. 5.5 b). This normalised spectral interferogram exhibits a varying period of the oscillations, which is mainly caused by the third order phase on the bi-photon and other phase contributions. Furthermore, we can observe that the retrieved spectral interferogram in Fig. 5.5 b) is not centred around a normalised intensity of 1. Additionally, the red reference spectrum in Fig.5.5 a) shows some residual fluctuations although the idler arm is blocked. Both of these effects are likely due to reflections of the signal and idler light on the end-facet of the waveguide, leading to interference although the idler path is blocked. The aforementioned fluctuations in the signal count rate can be another source for the offset in intensity between the signal and the reference spectrum.

Next, we check whether our modelling of the interference process matches the observed interference patterns. With this, we can confirm the expected operation of the interferometer and gain insights into the effect of phases between the interferometer arms.
We start in the temporal domain where we employ the same theory as in chapter 4 to simulate the temporal interferogram. We determine the bandwidth of a single PDC process to be 50 nm and apply the relative phases between the two processes, especially the linear phase introduced by the translation stage. A comparison between the measured and simulated temporal interferogram is shown in Fig. 5.6 a). We added a spectral phase of $-8000\,\mathrm{fs}^3$ of third order dispersion to the simulation to match them to the measurements. This additional phase can be caused by operating the PDC source at a slightly detuned point away from the assumed operating point underlying the simulations. We obtain a temporal interference width of 80 fs (FWHM) the measurements and simulations. Both interferograms show oscillations trailing the main peak at delays between 0.1 and 0.3 ps, which are a result of the third order dispersion on the bi-photon. Deviations between the

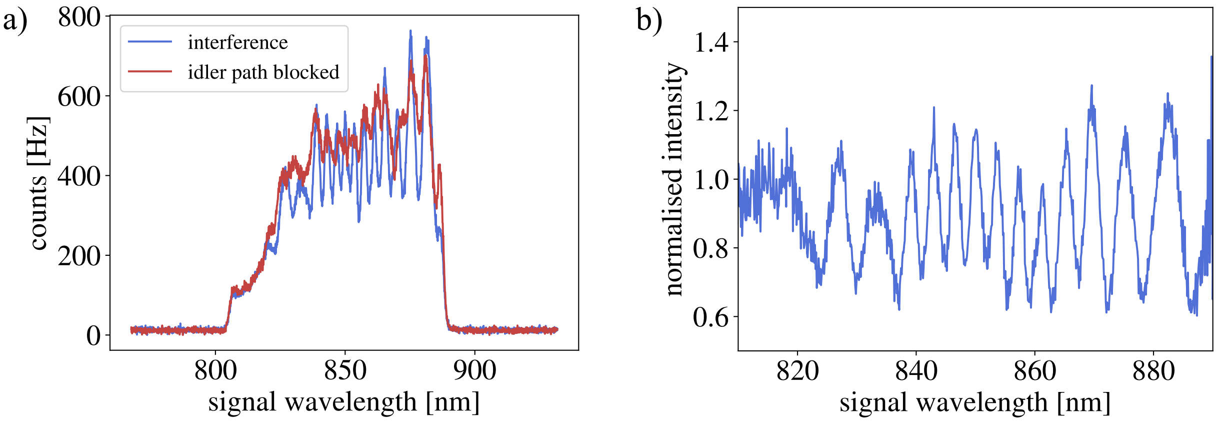

Figure 5.5: a) Raw data of the spectrally resolved signal counts forming the spectral interferogram together with the background measurement recorded with the idler path blocked. b) Normalised spectral interference retrieved by dividing the full interference signal by the measurement with a blocked idler path.

simulation and experiment are likely caused by additional higher order phase contributions and the back-coupling of the signal field into higher order spatial modes of the waveguide. In the simulations, we can remove all dispersive effects, such that we arrive at the temporal interferogram for a phase-free JSA. This then exhibits a temporal width of only 50 fs, which is related to a bi-photon correlation time of 25 fs. The simulation for the phase-free interferogram is presented in Fig 5.6 b). One would require to compensate for phases of $-600\,\mathrm{fs}^2$ of second order dispersion and $13000\,\mathrm{fs}^3$ of third order dispersion in the current experimental setup to achieve this phase-free case.

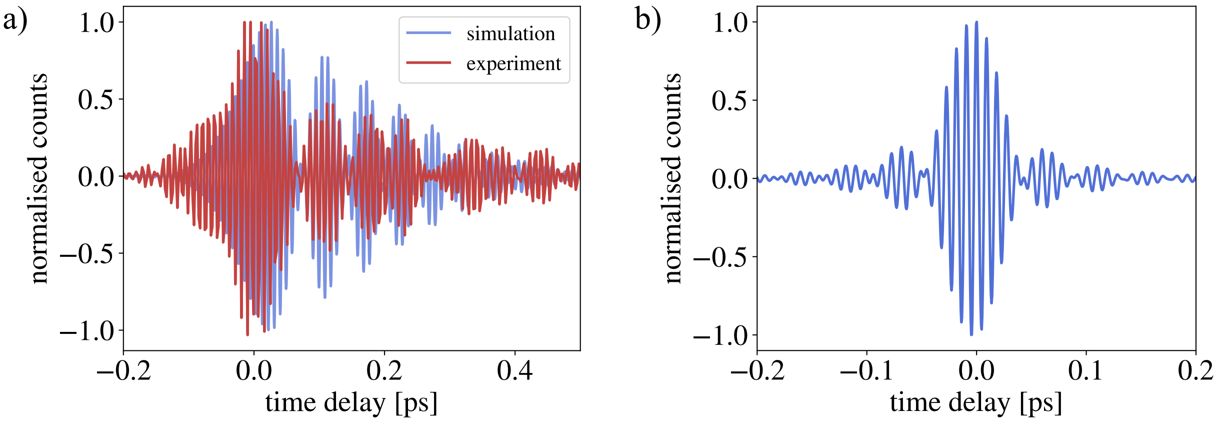

Figure 5.6: a) Measured temporal interferogram compared to the simulated interferogram based on the underlying PDC spectrum. b) Simulated temporal interferogram with no spectral phase on the JSA.

In the next step, we turn to the investigation of the spectral interference. The recording of subsequent spectral interferograms while scanning the linear phase between signal and idler close to zero OPD allows us to observe more fundamental properties of the interference, which are related to the unique feature of third order dispersion as the leading order spectral phase contribution in the setup. We display such a spectral-temporal scan alongside with vertical cuts corresponding to the spectral interferograms at fixed linear phases in Fig. 5.7 a) and b) as well as simulations that reproduce the observations qualitatively in Fig. 5.7 c) and d).

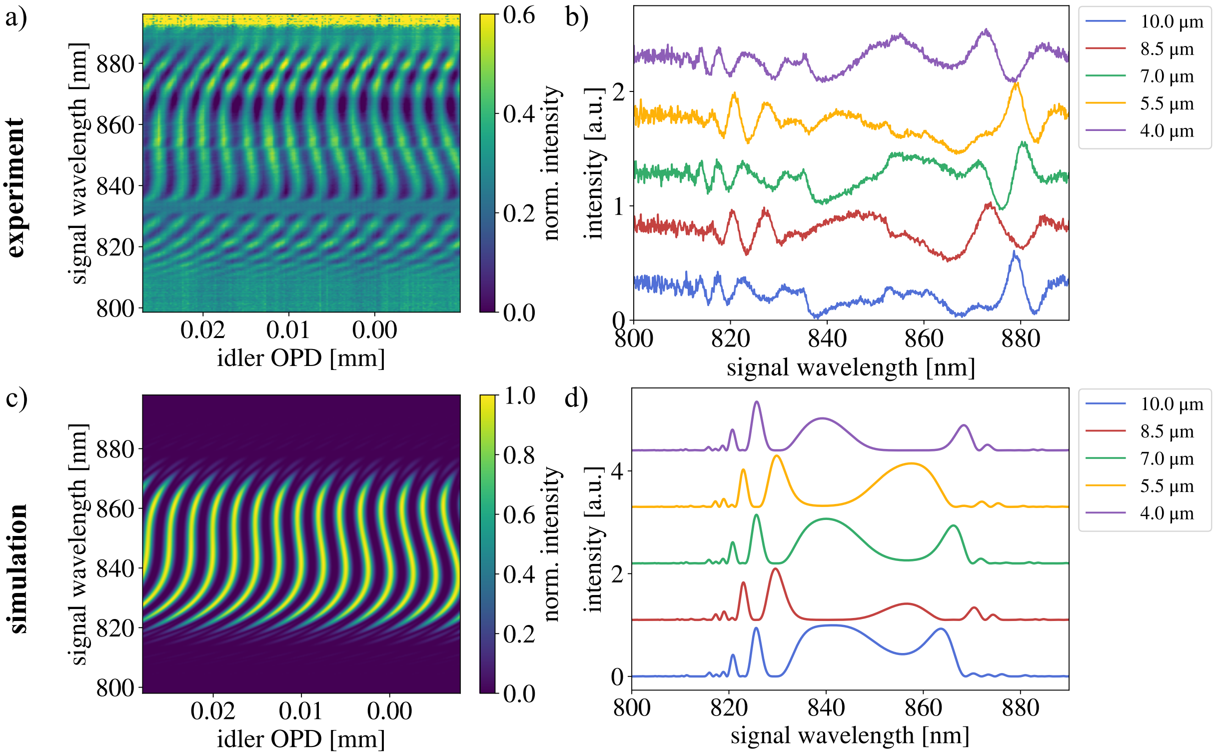

Figure 5.7: a) Experimentally recorded spectral-temporal map for different introduced optical path differences close to the balanced condition in the idler arm. b) Spectral interferograms for a fixed OPD. c) Simulated spectral-temporal map around zero OPD. d) Simulated spectral interferograms for a fixed OPD.

To match the simulation with the experiment, a residual second order dispersion of 2500 fs^2 and third order phase of 30000 fs^3 have been added to the linear phase introduced by the delay. Those values are realistic given the optical elements and waveguide dispersion in the current setup, although we do not aim to reproduce the system quantitatively at this point. We note that they deviate from the values in the temporal scan, which is because we used two different operation points in the PDC spectrum for these measurements.

In Fig. 5.7, the stage position in the experimental data set has been adjusted to an OPD that matches the simulation, as the point of zero OPD cannot be determined with sufficient precision in the experiment. We can observe a cubic shape of the interference maxima across the frequencies, both in the experiment and the simulations. The position of the interference maxima allows us to gain insight into the phase profile on the JSA for the whole system in the same way as we discussed in section 4.2.3. Again, this phase can be attributed to the third order phase, which the bi-photons from the first PDC process encounter when propagating through the waveguide for a second time.

Furthermore, in the spectral-temporal maps in Fig. 5.7 a), we can observe a region at a signal wavelength of 830 nm that does not show any interference. We attribute this to absorption of the idler photon from the first process in the waveguide material during the second pass due to the aforementioned absorption line of O-H groups around 2800 nm. This absorption makes the two PDC processes distinguishable in this wavelength range and thus imprints itself on the measurements of the signal interference, leading to a reduced visibility. This is the first time that we can observe absorption spectroscopy with undetected photons, although unintended. Interestingly, the expected phase jump due to a nearby absorption feature can be observed as a bending in the interference maxima around wavelengths of 840 nm in Fig. 5.7 a).

Finally, we can compare the evolution of spectral interferograms at different but fixed OPDs with the simulations in Fig. 5.7 b) and d). In the experiment, we can observe multiple fringes at short wavelengths, a central region with a single fringe and a broader interference fringe at the longer wavelengths. This behaviour can be reproduced in the simulations and is yet another manifestation of the cubic phase on the bi-photon. Similarly to the description in chapter 4, these interferograms or the whole spectral-temporal map could be used to retrieve the bi-photon phases within the interferometer while only measuring the signal photon.

5.3 Application: MIR absorption spectroscopy with undetected photons

In the beginning, we set the goal to perform spectroscopic measurements with undetected photons in the mid-IR. Thus, we now present two methods to detect absorption features around 2750 nm while only detecting single photons at 850 nm. We measure the same absorption feature once by detecting the spectrally resolved interference pattern and once by performing a time-resolved measurement, which is equivalent to Fourier-transform spectroscopy.

MIR absorption spectroscopy with an NIR spectrometer

We will start with the spectrally resolved absorption measurements. Here, we can use the previously discussed spectral-temporal maps in combination with absorptive samples in the idler arm. This technique then enables absorption spectroscopy by comparing the recorded visibility at each wavelength with the visibility at the same wavelength during a reference measurement. This intuitive technique has already been used previously in setups with bulk nonlinear crystals [20]. In Fig. 5.8 a), we first show the spectral-temporal map of a reference measurement without external absorption, as well as two cuts with different visibilities in and outside the region of absorption in Fig. 5.8 b). The retrieved visibility from these cuts along each wavelength is depicted in Fig. 5.8 c). The shaded region around the curves represents the error that originates from the variation in the visibility at each wavelength cut when varying the stage position. Note here, that we use the reading for the stage position from the experiment, which results in an OPD close to zero.

In order to determine the spectral transmission $T_{sample}(\omega_p-\omega_s)$ of an object under test in the idler arm, we revisit Eq. (4.9) from chapter 4, which gives us an expression for the spectral interferogram as we record it on the spectrograph. However, we are now also considering potential unequal gains for the two PDC processes γ_1 and γ_2. This leads to a modified equation of the form

$$S(\omega_s) \propto |f(\omega_s)|^2 \left(\gamma_1 + \gamma_2 \sqrt{T(\omega_p - \omega_s)} \cos[\Psi(\omega_s)]\right) \tag{5.1}$$

where the measured spectral intensity $S(\omega_s)$ is given by the underlying JSA $f(\omega_s)$. The relative spectral phase $\Psi(\omega_s)$ between the involved fields can vary for every frequency component, for example, by introducing a linear delay. For each spectral bin, the interference visibility given by $V = \frac{S_{max}-S_{min}}{S_{max}+S_{min}}$ can be evaluated and yields $V = \frac{\gamma_2}{\gamma_1}\sqrt{T(\omega_p - \omega_s)}$. Thus, the visibility is governed by the gains of the two PDC processes and the transmission $T(\omega_p - \omega_s) = T_{setup}(\omega_p - \omega_s) \cdot T_{sample}(\omega_p - \omega_s)$ with contributions from the experimental setup and the introduced sample.

In order to determine the transmission of the sample and eliminate the influences of the experimental setup, we record a reference scan without the sample and perform a subsequent

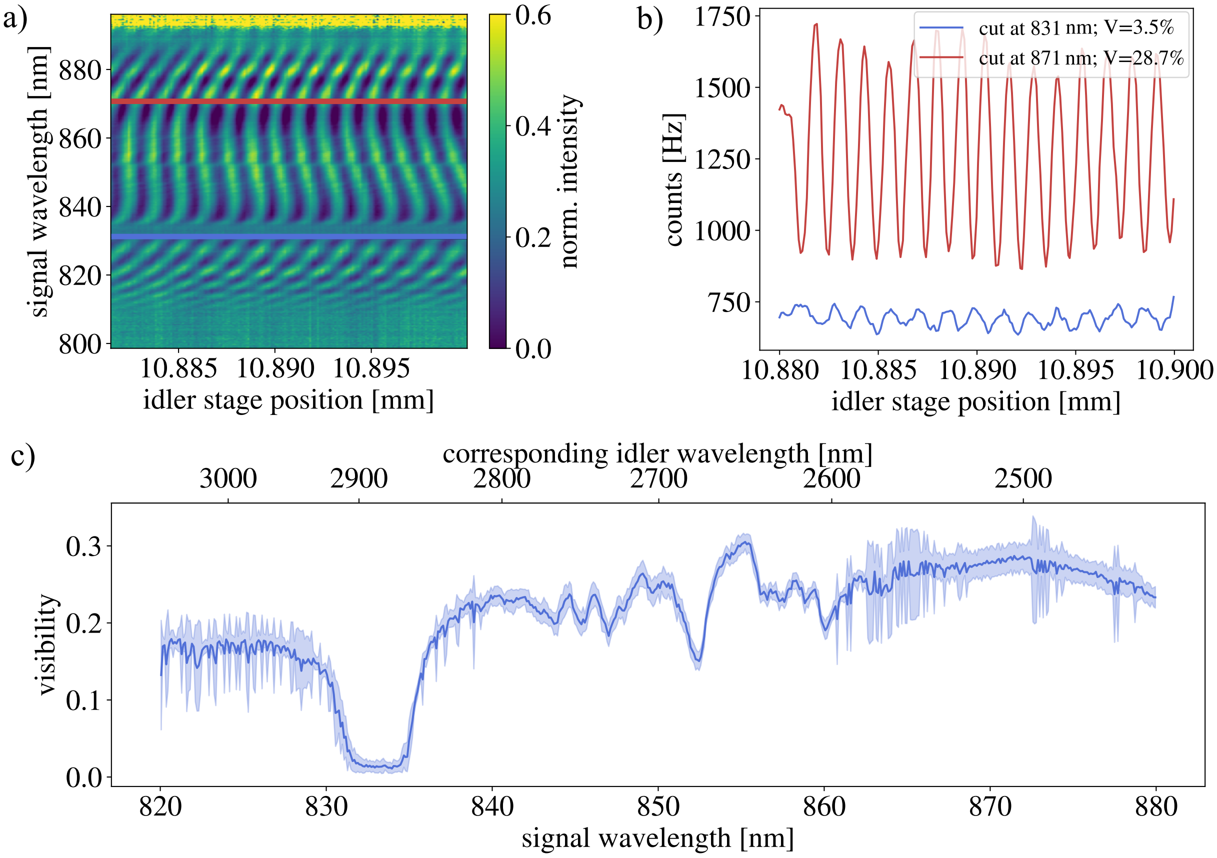

Figure 5.8: a) Spectral-temporal map for stage positions around zero OPD. b) Counts at two selected wavelengths with a high and low visibility due to absorption. c) Resulting visibility for the whole spectrum, showing an absorption feature at 832 nm and a maximal visibility around 30 %.

measurement with the sample in the idler path under the same conditions. This allows to divide the obtained visibilities with the sample (V_{sample}) by the ones without it ($V_{reference}$) and to finally end up with the samples transmission as

$$\frac{V_{sample}}{V_{reference}} = \frac{\frac{\gamma_2}{\gamma_1}\sqrt{T_{setup} \cdot T_{sample}}}{\frac{\gamma_2}{\gamma_1}\sqrt{T_{setup}}} = \sqrt{T_{sample}}. \tag{5.2}$$

The results of this evaluation are shown in Fig. 5.9. We present the measured spectral-temporal maps of spectral interferograms for different stage positions for the case of a 1 mm and 5 mm UV fused silica (UVFS) glass sample in the idler arm in Fig. 5.9 a) and b). In Fig. 5.9 c), we first plot the visibilities for three different measurements, namely a reference measurement without a sample and measurements for 1 mm and 5 mm of UVFS glass in the idler arm. A transmission spectrum of UVFS glass at mid-IR wavelengths is given in the Appendix Fig. A.6. Note that we recorded two reference measurements, one for each sample. As they are very similar, we show only the reference before the measurement with 1 mm of UVFS glass in Fig. 5.9 c).

We can observe a clear reduction in the interference visibility for the measurements with the sample in comparison to the reference. This reduction in visibility is equivalent to a sample absorption at signal wavelengths around 845 nm, which corresponds to idler wavelengths in the range of 2750 nm.

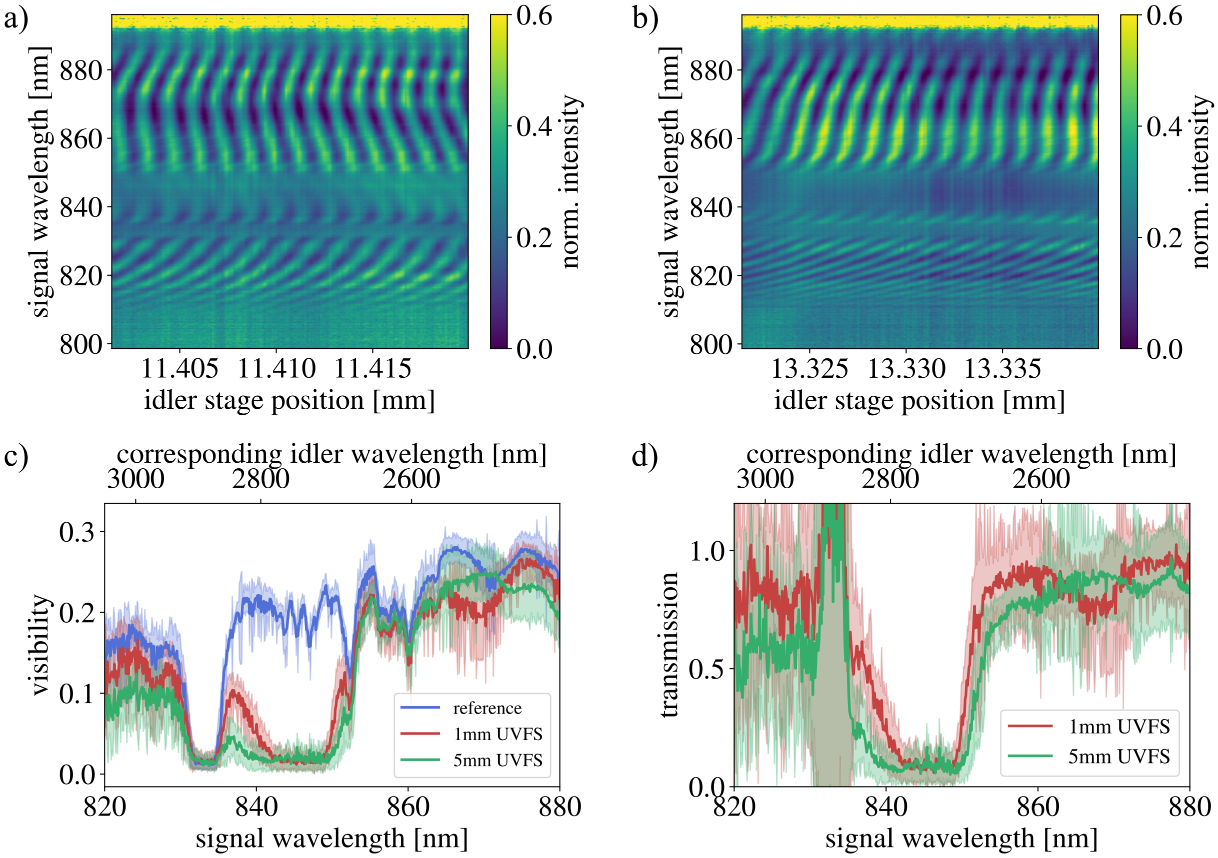

Figure 5.9: a) Spectral-temporal map of spectral interferograms at different stage positions with 1 mm UVFS sample in the idler arm. b) Spectral-temporal map of spectral interferograms at different stage positions with 5 mm UVFS sample in the idler arm. c) Visibility over the covered spectrum for the reference measurement, with 1 mm, and with 5 mm UVFS in the idler arm. d) Extracted transmission of the 1 mm and 5 mm sample retrieved by division of the visibilities by the reference.

Finally, we use the corresponding reference measurements to obtain the transmission spectra for both samples in Fig. 5.9 d). Due to the inherent absorption in the wavelength region around 832 nm, the division of the visibilities leads to unphysical values and error bars at these wavelengths. The absorption due to the introduced UVFS glass sample around 845 nm can be observed for both samples. Furthermore, the absorption gets stronger for the thicker sample as expected. Since we hit the noise floor in the centre of the absorption line, we can witness this increase in absorption by the broadening of the absorption region for the thicker sample. The large error bars on the retrieved transmission in the regions without absorption can be reduced by increased stability in the setup, as they are likely caused by

power-fluctuations which influence the extracted interference visibility.
Apart from determining the spectrally resolved transmission of our object under test, the measurement of these spectral-temporal interferograms allows to extract the phase information of the object and thereby reconstruct the full complex refractive index. This can be done by tracing the position of the interference maxima that show clear shifts around the interference regions in Fig. 5.9 a) and b). However, such an analysis would require a better SNR in the measurement and a high spectral resolution. Nevertheless, this would allow to use the full potential of this method for future applications.

Fourier-transform absorption measurements

Single-photon sensitive grating spectrometers can be expensive and the previously presented method for absorption spectroscopy with undetected photons is limited in resolution to the one of the spectrograph. Furthermore, comparably high photon pair rates are needed for the measurement of a spectral interferogram with a sufficiently high SNR, as we discussed for our OCT application in chapter 4. We therefore also demonstrate Fourier transform spectroscopy with undetected photons, which we introduced in 2. In this measurement, we detect the spectrally unresolved count rates in the signal field with an APD while translating the idler mirror. The resulting temporal interferogram then contains information about the spectral intensity of the idler light, which can be retrieved via Fourier transformation.
We perform Fourier-transform spectroscopy measurements with undetected photons by recording temporal interferograms with and without the absorptive sample in the idler arm. In Fig. 5.10 a) these temporal interferograms are shown. One can observe that the temporal interferogram's shape changes upon the placement of a 1 mm thick UVFS sample in the idler arm. Additionally, we observe a lower SNR in the normalised interferogram with the sample due to the absorption and potential scattering at all wavelengths from the object, which leads to an increased noise floor outside the interference region.

The Fourier transform of the two temporal interferograms is depicted in Fig. 5.10 b). The obtained spectra are given by the spectral content of the light in the arm in which we introduced the delay to record the temporal interferogram, here the idler. Thus, we can observe an absorption that leads to a narrowing of the peak centred around 2650 nm when the sample is introduced in the idler arm. To retrieve the presented spectra, the Fourier transform of the measurement with the sample in the idler arm has been shifted to match the rising edge of the reference spectrum without absorption. This is necessary because the used translation stage does not provide equally sized steps, but rather shows a variation in the step size, which leads to noise and shifts in the Fourier-components. The oscillations in the spectra and an increased noise floor outside of them are caused by the fluctuations in the count rates and can be mitigated by averaging, as discussed in the last section of chapter 4. In the presented measurements, the SNR is rather low which impairs the quality of the results in comparison to the ones obtained with the spectrometer.
The influence of the low SNR also becomes apparent when extracting the transmission profile of the sample as shown in Fig. 5.10 c). This transmission was calculated by dividing the

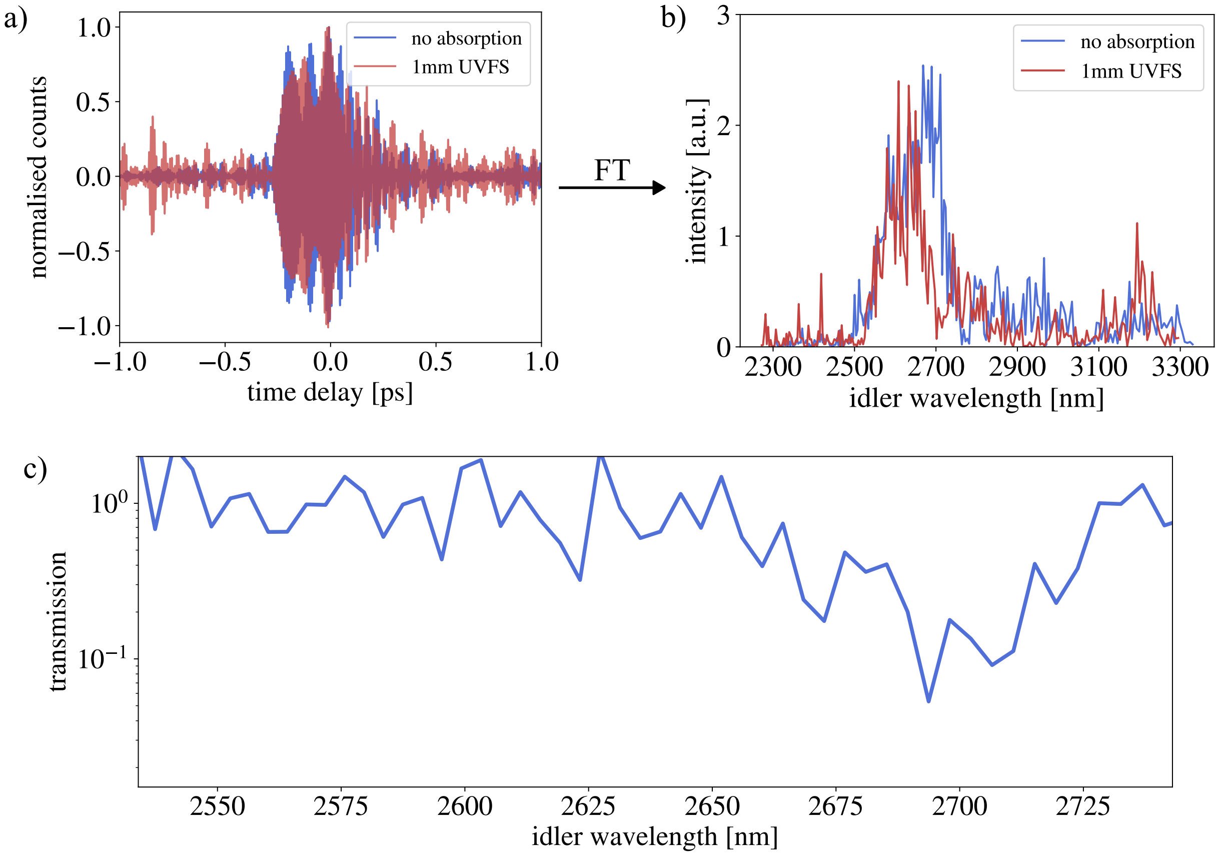

Figure 5.10: a) Temporal interferograms with and without 1 mm UVFS glass absorber the idler arm. b) Fourier transform of the temporal interferograms resulting in spectra with a reduced width in the case of a sample due to absorption around 2700 nm. c) Extracted transmission of the UVFS sample showing a broad absorption dip around 2700 nm.

spectrum of the measurement with the sample by the reference. Although we can still extract the same absorption feature around 2700 nm as in the spectrally resolved absorption measurement, strong fluctuations in the transmission outside as well as across the absorption region can be observed.

Nonetheless, we are able to perform Fourier transform absorption measurements in the mid-IR within our nonlinear interferometer and measure an absorption feature that qualitatively matches the result of the absorption measurement with the spectrograph. Remarkably, the pair rates incident on the detector have been about 2 orders of magnitude lower in the Fourier transform measurements. This ability to measure with a lower photon flux and the possibility to use a cheaper, not frequency-resolving detector makes this method favourable despite the low SNR of this first proof-of-principle measurement.

In order to improve the presented measurements, a scanning stage approach could be employed. This would allow to sample the temporal interferogram multiple times and receive an averaged temporal interferogram with less fluctuations in the photon counts similar to the discussions at the end of chapter 4. The setup will greatly benefit from anti-reflection coatings on the waveguide end-facets and an improved design of the dichroic mirror to separate pump, signal and idler light. This would further enhance the SNR and the stability of the measurement. However, these improvements are well within reach and have the potential to bring the demonstrated techniques to real-world applications.

Summary

In this chapter, we demonstrated how our newly developed ultra-broadband, waveguide PDC source can be used as the active element in a nonlinear interferometer. We discussed the technical challenges in the design and operation of such an interferometer which operates at wavelengths of 850 nm and 2800 nm. Especially the requirement of special, broadband optical coatings and a low transmission of substrate materials at the mid-IR wavelength lead to challenges that have been overcome and finally allowed for a successful implementation of measurements with undetected photons with a waveguide PDC source in the mid-IR.

To characterise the interferometer, we presented and analysed the retrieved spectral and temporal interferograms. Those interferograms showed a good agreement with our theory and predict ultrashort correlation times on the order of 25 fs. Additionally, we witness the effects of third order dispersion in the setup as the leading order term in the spectral phase and potentially allows for precise second order phase measurements with undetected photons.

Furthermore, we employed the setup to demonstrate first experiments on absorption spectroscopy with undetected photons utilising integrated waveguides. We performed these measurements by utilising two methods: once by using an NIR grating spectrometer and once by performing Fourier transform spectroscopy. We demonstrated measurements of the absorption feature in UVFS glass around 2750 nm on samples with different thicknesses.

With this, we showcased the implementation of two more methods from the toolbox of ultra-fast spectroscopy that can be performed as measurements with undetected photons in the mid-IR, all based on an integrated waveguide PDC source. The use of a waveguide in these measurements implies an increased brightness which is connected to a higher SNR and paves the way towards a fully integrated quantum sensor.

6

Conclusion and Outlook

6.1 Conclusion

In this thesis, we have explored the first realisation of measurements with undetected photons in the mid-IR in nonlinear interferometers while utilising integrated nonlinear waveguides as sources for photon pairs from PDC. We performed measurements from the field of ultra-fast spectroscopy for which we designed, fabricated, characterised and employed broadband, highly non-degenerate PDC sources in integrated waveguides.

We first discussed the design requirements for broadband, non-degenerate integrated PDC sources. Those have been realised by studying the dispersive effects of our waveguides in detail and further developing the dispersion engineering technique of group-velocity matching to reach simultaneous group-velocity dispersion cancellation between the generated signal and idler photons. With this, we constructed two PDC sources that achieve bandwidths of 7 THz and 25 THz, respectively, at vastly non-degenerate wavelengths. Both PDC sources allow to generate broadband, non-degenerate photons and at the same time achieve a high brightness, which is similar or larger than the one of comparable bulk crystal sources. The NIR source based on group-velocity matching generates photons around 830 nm and 1400 nm. The newly developed MIR PDC source with one photon generated around 830 nm and the other in the mid-IR around 2800 nm has been studied in detail. In this study, we investigated the change of the emission spectrum for a variation in the waveguide temperature while having the pump wavelength set at, below or above the design pump wavelength. The obtained results match the simulations, underline our understanding of the processes in dispersion engineering and enable us to realise the desired PDC output spectra.

In the remainder of the work, both PDC sources have been employed in nonlinear interferometers. The first measurements have been carried out in an interferometer based on the NIR source, as this source was developed first and relied on our standard fabrication procedure. After the development and testing of the MIR source, we were able to transfer concepts and knowledge gained from the nonlinear interferometer in the NIR to the setup of a nonlinear interferometer that comprises the MIR source.
The interferometer in the NIR was implemented in two different geometries of the nonlinear interferometer: the commonly used SU(1,1) scheme and the induced coherence scheme.

Here, we found that the induced coherence scheme provides practical benefits when working with integrated waveguides, as the signal field of both processes is interfered on a classical beamsplitter. This eliminates the need to couple the signal field from the first process back to the waveguide, which supports multiple spatial modes at the signal wavelength.
In a first experiment, we used the nonlinear interferometer to demonstrate a technique for measurements of the actual and Fourier-limited bi-photon correlation time of our source. This was accomplished by developing a model for the system including spectral phases and simultaneously measuring the width of the temporal interferogram and the second order dispersion from the spectral interferogram. Combining these two measurements reveals a characteristic dependence between them, which allowed us to extract the bi-photon correlation time of less than 100 fs for two different PDC spectra.
In a next step, we turned towards applications by developing an optimised measurement scheme for optical coherence tomography with undetected photons. We performed pump gain optimisation in the SU(1,1) and induced coherence geometry and found in both cases that the losses experienced by the detected signal field can be mitigated by pump gain optimisation. Meanwhile the optimal gain ratio is not affected by losses introduced by the sample in the idler arm. Subsequently, we performed TD-OCT and FD-OCT in both geometries of the setup and found that TD-OCT in the IC geometry is beneficial when performing OCT measurements with undetected photons based on an integrated PDC source. This is due to the lower second order dispersion experienced by the signal field and thus a higher axial resolution in TD-OCT in the IC geometry. Finally, we presented ways to further optimise the measurements by utilising averaging effects for an increased SNR.

Ultimately, we used the mid-IR PDC source as the core of a nonlinear interferometer. We characterised the interferometer and observed spectral and temporal interference that agrees with our theory. We found that this ultra-broadband PDC source enables short correlation times on the order of 25 fs, which could be used to increase the temporal resolution of ultra-fast spectroscopy measurements. In this interferometer, we demonstrated absorption spectroscopy with undetected photons with a NIR spectrograph and by performing Fourier transform spectroscopy. With both methods, we were able to detect absorption features in the mid-IR while only measuring photons in the near-IR. Although such measurements had already been performed with bulk nonlinear crystals, the use of an integrated waveguide in these experiments promises a higher brightness and therefore more effective measurement in comparison to those realisations.

6.2 Outlook

This work lays the foundation for future experiments combining ultra-fast spectroscopy and nonlinear waveguides for metrology applications. The use of waveguides enables us to construct an integrated quantum sensor with competitive benchmarks in comparison to current classical systems while allowing for measurements with undetected photons. Meanwhile, the high brightness and simultaneously large spectral coverage make the presented PDC sources promising candidates for real-world applications.

Future experiments towards the goal of a fully integrated sensor would feature more dedicated measurement routines like averaging and show an improved stability of the setups, e.g., via optical coatings. Those improvements would boost the existing experiments in the mid-IR beyond the stage of proof-of-principle measurements. Further integration of the currently free space elements, such as delays and dichroic mirrors, is possible. However, this poses challenges on the integrated optical building blocks due to the large spectral bandwidths of the signal and idler fields that are required for ultra-fast spectroscopy [103]. The advent of new material platforms such as thin-film lithium niobate (TFLN) would allow for highly efficient and cost effective integrated sensors. One main advantage of this platform lies in strong mode confinement, which allows for interferometers with small footprints [104, 105]. In this material platform, even higher flexibility in the PDC generation process via dispersion engineering is feasible [75]. Therefore, it seems realistic that a nonlinear interferometer could be fully integrated on a chip in TFLN. However, as a platform, TFLN needs to mature further. Currently, only limited control over the design parameters and the fabrication are achieved. However, this poses problems when aiming at the construction of a full quantum sensor on chip.

There are also more exotic changes that could be made to the presented devices in order to tailor the properties of the used interferometers. For example, the use of pulsed pump lasers in the presented nonlinear interferometers would be a way to realise pump-probe spectroscopy applications with undetected photons. Such experiments with pulsed light can be carried out by measuring temporal interference which does not require as strict frequency correlations as the spectral domain for measurements with undetected photons, as has recently been shown [106, 107].

Additionally, spectral shaping of the bi-photon state between the two stages of the interferometer by manipulation of the spectral components of one photon in the Fourier-plane of a grating could allow us to find the ideal state for sensing applications and allow to compensate for dispersion from the waveguide material by introducing the opposite spectral phase in one of the interferometer arms.

We discussed the two possible geometries of the nonlinear interferometer, the SU(1,1) or IC design. However, a hybrid approach between them might open up new sensing paths. This can be realised by constructing a setup where a change in the polarisation of one field from the first PDC process determines whether it follows a SU(1,1), IC or both paths [84].

Finally, there are several tasks for measurements with undetected photons in the mid-IR interferometer which are worth pursuing. Among them are OCT measurements in the mid-IR with an even higher axial resolution down to 14 μm. Samples of interest in the mid-IR region are biological tissue, paints or even ceramics [20]. The combination of OCT with Fourier transform spectroscopy can be realised by performing TD-OCT and evaluating the spectrum of each temporal interferogram. This would allow to extract the transmission properties of the materials between the reflective layers in an object under test. Ultimately, free space gas sensing in the MIR and the determination of concentrations for environmental gases is another path towards a useful application of the developed sensor [39].

In conclusion, we gained a deep understanding of waveguide-based nonlinear interferometers and overcame several challenges connected to the use of ultra-broadband light in integrated waveguides, which ultimately allowed us to perform measurements with undetected photons. With this, the work in thesis lays the foundations for future applications of bi-photons from integrated waveguides in the field of ultra-fast spectroscopy. We have identified some of the next steps and believe that there are many other useful applications of the developed sources and setups, which will bring quantum sensors with integrated waveguides to real-world applications.

A Appendix

A.1 Time-bandwidth product of common pulse shapes

In the Fundamentals in chapter 2, we have discussed that the temporal and spectral envelopes $\mathcal{E}(t)$ and $\tilde{\mathcal{E}}(\omega)$ of ultra-short electromagnetic pulses are linked via Fourier transform. Let us write down these two envelopes for a Gaussian pulse shape in a slightly different way than before as

$$\begin{aligned} \mathcal{E}(t) &= E_0 e^{-2\ln 2 \frac{t^2}{\Delta t^2}} \\ \tilde{\mathcal{E}}(\omega) &= E_0 \Delta t \sqrt{\frac{\pi}{2\ln 2}} e^{-\frac{\Delta t^2}{8\ln 2}\omega^2}, \end{aligned} \tag{A.1}$$

where we now also explicitly wrote down the pre-factors that we obtain from the Fourier transformation based on the amplitude of the electric field in the time domain E_0 [108]. Additionally, Δt is now the FWHM of the temporal intensity.

The TBP is typically given as the product of the FWHM of the temporal intensities and spectral intensities. From the above equations, the FWHM of the spectral intensity is $\Delta\omega = \frac{4\ln 2}{\Delta t}$. Further more, the TBP is more commonly calculated in terms of frequencies ν instead of angular frequencies, such that we end up with

$$\Delta\nu \cdot \Delta t = \frac{4\ln 2}{2\pi\Delta t} \cdot \Delta t = \frac{2\ln 2}{\pi} = 0.441 \tag{A.2}$$

for a Gaussian pulse profile. However, there are many other possible pulse shapes which feature vastly different TBPs. An overview over TBPs for a few common pulse shapes is given in table A.1. Here, we give the expression for the spectral and temporal envelopes of a certain pulse shape and the corresponding TBP. Note that frequency and time form a Fourier pair and can therefore be exchanged in the columns of this table. For example, in this work, we are often dealing with rectangular spectra which then show a sinc^2 shape in the temporal domain and exhibit a TBP of 0.886.

Table A.1: Comparison of TBPs for the most common pulse shapes in the temporal and spectral domain (adapted from [108]).

Shape	$\mathcal{E}(t)$	$\tilde{\mathcal{E}}(\omega)$	$\Delta\nu\Delta t$
Gaussian	$E_0 e^{-2\ln 2\frac{t^2}{\Delta t^2}}$	$E_0\Delta t\sqrt{\frac{\pi}{2\ln 2}}e^{-\frac{\Delta t^2}{8\ln 2}\omega^2}$	0.441
Hyperbolic sechant	$E_0\text{sech}[2\ln(1+\sqrt{2})\frac{t}{\Delta t}]$	$E_0\Delta t\frac{\pi}{4\ln(1+\sqrt{2})}\cdot\text{sech}\left(\frac{\pi\Delta t}{4\ln(1+\sqrt{2})}\omega\right)$	0.315
Rectangular	$E_0,\ t\in[-\Delta t/2,\Delta t/2]$	$E_0\Delta t\,\text{sinc}\left(\frac{\Delta t}{2}\omega\right)$	0.886
Symmetric exponential	$E_0 e^{-ln2\frac{t}{\Delta t}}$	$\frac{E_0\Delta t\ln 2}{\Delta t^2\omega^2+(\ln 2)^2}$	0.142

A.2 Waveguide and poling masks

Below, the waveguide and poling masks for the NIR and MIR PDC sources are shown. The waveguide chip layout for the NIR source with the annotated poling periods is depicted in Fig. A.1. The colored groups of three waveguides each are poled with the same poling period. Each waveguide exhibits a width of 7 µm. The corresponding poling pattern consists of the base elements depicted in Fig. A.2. These base elements are slightly larger than the waveguides onto which they will be patterned. The exhibit a ratio between the with of the pattern w and period of the poling of 0.45, which leads to ideal results after poling with a 50 : 50 duty cycle.

The waveguide chip layout for the MIR source with the annotated poling periods is depicted in Fig. A.3. The colored groups of three waveguides each are poled with the same poling period. Each waveguide exhibits a width of 18, 20 and 22 µm. The corresponding poling pattern consists of the base elements depicted in Fig. A.4. These base elements are slightly larger than the waveguides onto which they will be patterned and adapted to the waveguide widths as they vary within one group. The exhibit a ratio between the with of the pattern w and period of the poling of 0.45, which leads to ideal results after poling with a 50 : 50 duty cycle.

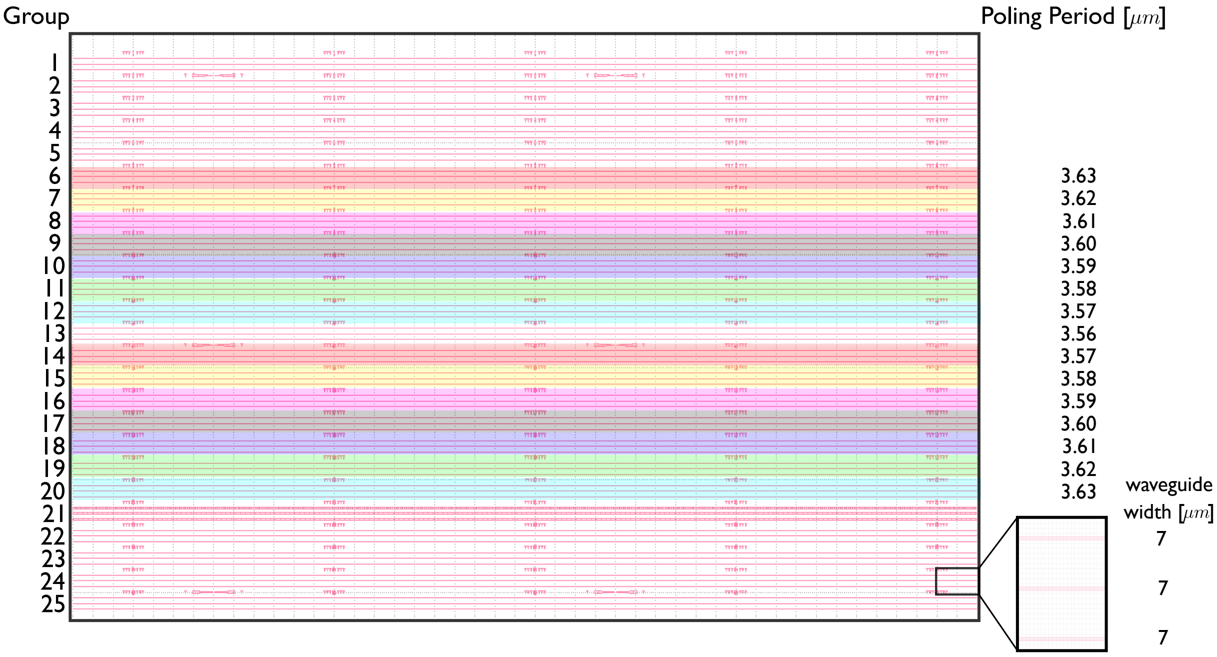

Figure A.1: Layout of the waveguide chip for generation of GVM PDC at 830 nm and 1400 nm. The colored groups of waveguides have been periodically poled with the annotated poling periods.

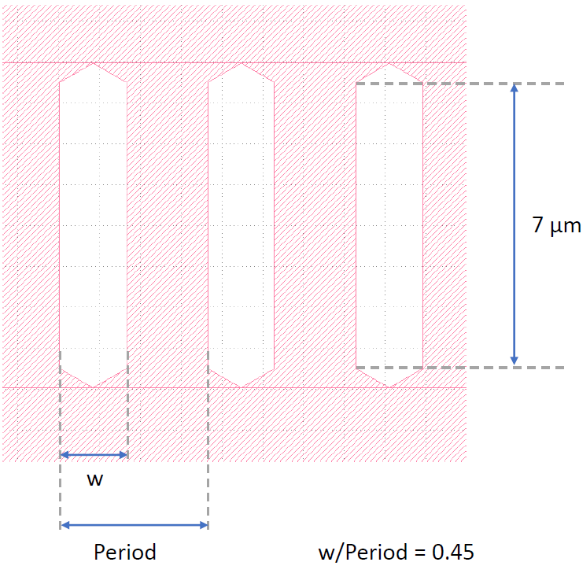

Figure A.2: Layout of the poling patterns on the waveguide chip for generation of GVM PDC at 830 nm and 1400 nm.

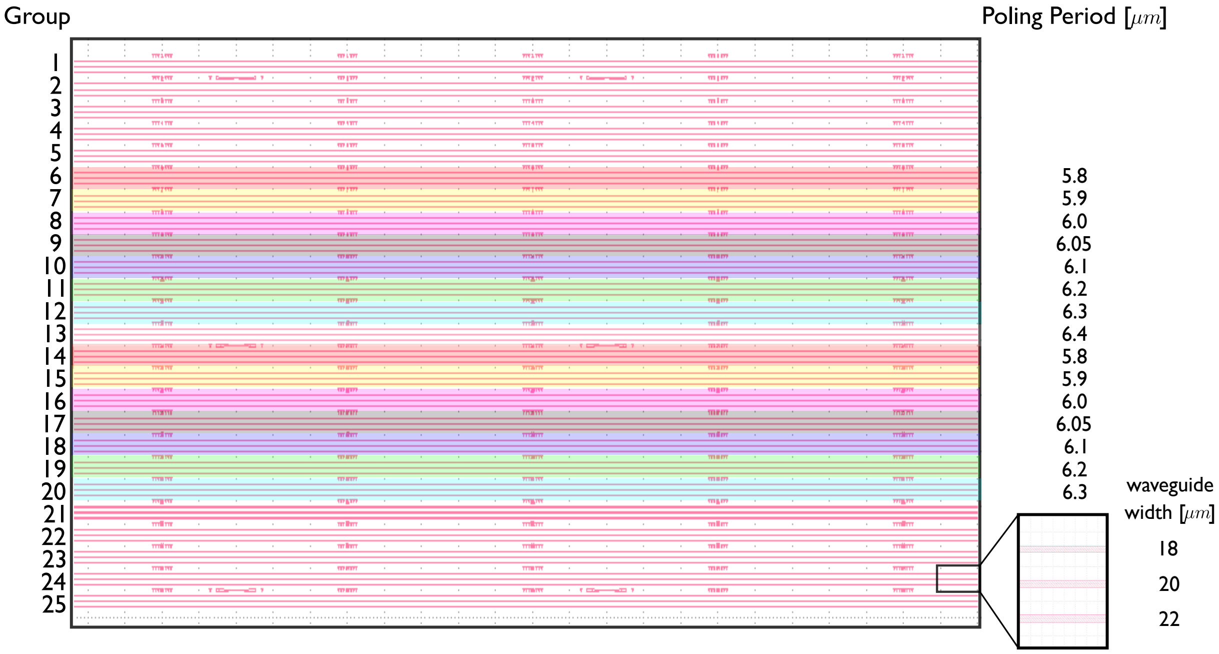

Figure A.3: Layout of the waveguide chip for generation of ultra-broadband PDC via GVM and GVD cancellation at 850 nm and 2800 nm. The colored groups of waveguides have been periodically poled with the annotated poling periods

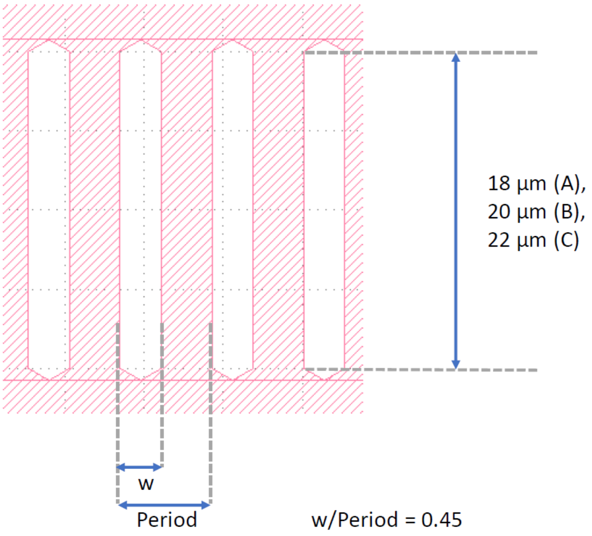

Figure A.4: Layout of the poling patterns on the waveguide chip for generation of ultra-broadband PDC via GVM and GVD cancellation at 850 nm and 2800 nm.

A.3 Pump gain optimization in induced coherence

Here, we derive the visibilities and optimal pump gain ratios for the induced coherence geometry. To this end, we use the same assumptions as in the derivation of the pump optimization in the SU(1,1) geometry in chapter 2. A schematic of this interferometer is depicted in Fig. A.5.

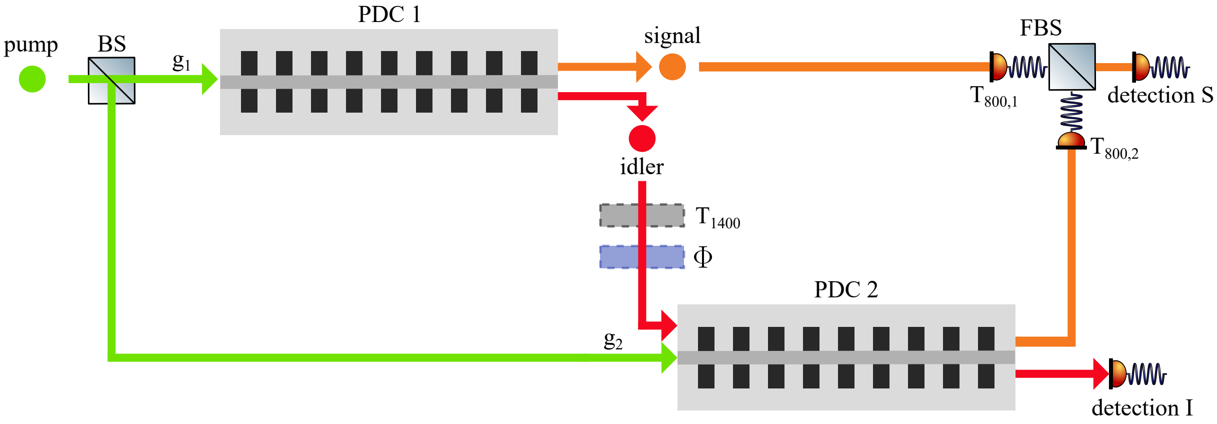

Figure A.5: Scheme of the interferometer in the IC geometry with detection channels of signal and idler as well as the corresponding transmission values $T_{800,1}$, $T_{800,2}$ and T_{1400} as well as the pump gains g_1 and g_2.

The count rates of signal photons after the beamsplitter (S), idler photons (I) and coincidences (coinc) are given by

$$\begin{aligned} C_S &= T_{800,1}g_1^2 + T_{800,2}g_2^2 + 2\sqrt{T_{800,1}T_{800,2}T_{1400}}g_1g_2\cos(\Phi) \\ C_I &= T_{1400}g_1^2 + g_2^2 + 2\sqrt{T_{800,1}T_{800,2}T_{1400}}g_1g_2\cos(\Phi) \\ C_{coinc} &= T_{1400}T_{800,1}g_1^2 + T_{800,2}g_2^2 + 2\sqrt{T_{800,1}T_{800,2}T_{1400}}g_1g_2\cos(\Phi) \end{aligned} \tag{A.3}$$

where Φ is the relative phase between the two processes.

This leads to a spectral interference visibility V_{800} at the signal wavelength around 800 nm, V_{1400} at the signal wavelength around 1400 nm and for the coincidences V_{coinc} of

$$\begin{aligned} V_{800} &= \frac{2\sqrt{T_{800,1}T_{800,2}T_{1400}}g_1g_2}{T_{800,1}g_1^2 + T_{800,2}g_2^2} \\ V_{1400} &= \frac{2\sqrt{T_{800,1}T_{800,2}T_{1400}}g_1g_2}{T_{1400}g_1^2 + g_2^2} \\ V_{coinc} &= \frac{2\sqrt{T_{800,1}T_{800,2}T_{1400}}g_1g_2}{T_{1400}T_{800,1}g_1^2 + T_{800,2}g_2^2}. \end{aligned} \tag{A.4}$$

From this expression, we can see the optimal pump gain ratio for the maximum visibility in measurements with undetected photons where the sample is placed in the idler arm around 1400 nm and the signal photons at 800 nm are detected is given by

$$\frac{g_1^2}{g_2^2}_S = \frac{T_{800,2}}{T_{800,1}} \tag{A.5}$$

and thus is independent of any loss introduced by the sample. Meanwhile, the value of the maximally achievable visibility at this optimal pump gain ratio is given by this transmission of the idler arm T_{1400}. For the two other cases of detection at the idler wavelength or via coincidence counting, which we are less interested in when performing measurements with undetected photons, the optimal pump gain ratios are given by

$$\begin{aligned} \frac{g_1^2}{g_2^2} &= \frac{1}{T_{1400}} \\ \text{and} \quad \frac{g_1^2}{g_2^2} &= \frac{T_{800,2}}{T_{800,1}T_{1400}}. \end{aligned} \tag{A.6}$$

Furthermore, the maximally achievable visibility is given by the product of the signal transmissions $T_{800,1} \cdot T_{800,2}$ in the idler case. Thus, with transmissions on the order of 50% due to fiber couplings, this visibility is very low in the discussed setup. However, mode matching of the optical field to the fiber allows to increase this visibility to reach close to 100%. Meanwhile, for the coincidences, the maximally achievable visibility is independent of the transmissions in the setup and can always reach 100%.

To conclude, we see that the gain optimization in the IC case is very similar to the one performed in the SU(1,1) setup. However, the conceptual and experimental details allow to achieve an advantage in the implementation of measurements with undetected photons, as we discuss in the main text.

A.4 Reference UVFS glass transmission

The transmission data of UVFS glass is given in Fig.A.6 and has been retrieved upon request from Corning. This glass has been used in chapter 5 as a sample for direct absorption spectroscopy and Fourier transform spectroscopy. The transmission shows a prominent absorption feature around 2750 nm, which has been employed to test our absorption measurements with undetected photons.

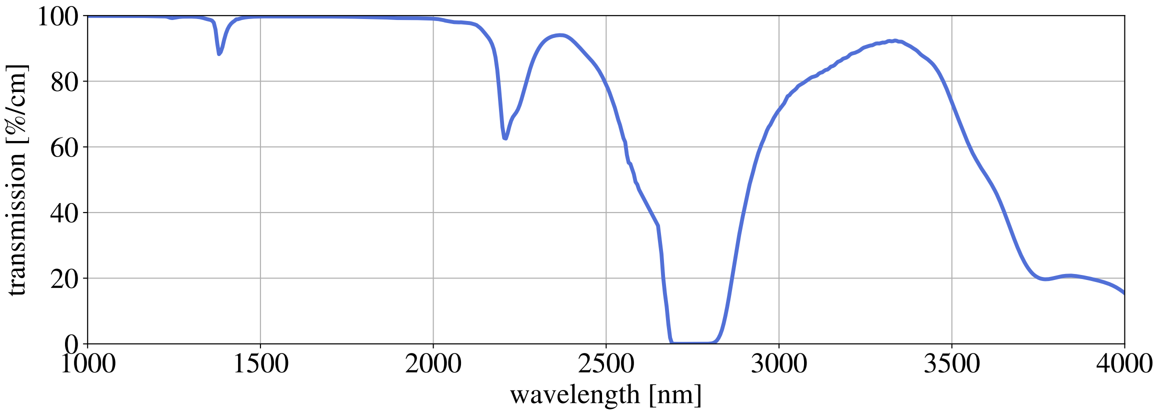

Figure A.6: Transmission data for UVFS glass in the mid-IR.

B

Acknowledgements

During my PhD, I had the great opportunity to become a part of a vibrant and enthusiastic group of scientists in a quickly evolving field of research. It has been this environment that made this thesis possible and my work truly enjoyable.

First, I would like to thank Professor Christine Silberhorn for inviting me to her group and guiding me through my PhD. Thanks to her vision and the provided freedom, I had the opportunity to develop my own ideas and follow my interests on the border between quantum optics and ultra-fast spectroscopy.

A big thanks goes to Dr. Benjamin Brecht for hands-on supervision during my PhD, the coordination of my research in the general framework of the networks subgroup and his guidance towards ideas that are worth pursuing. His useful tips on a daily basis and invaluable support during the writing process of publications and this thesis helped me a lot.

Being a part of the Max Planck School of Photonics allowed me to get in contact with many fellow PhD students and to have insightful discussions with fellows of the school. I am thankful for the co-supervision of Professor Maria Chekhova and the opportunity to visit her research group in Erlangen to broaden my scientific background.

Next in line are the people with whom I worked the closest in the lab: René and Abira. It has been a pleasure working with you and pushing the boundaries of integrated waveguides and spectroscopy altogether, although we met some demons on the way. René followed me for the longest part of this journey and endured me as his neighbour in the lab and the office. I am thankful for Abira's companionship, first as a highly motivated student and ultimately as a great lab mate.

I am beyond grateful for the detailed proof-reading of this thesis by Michael, Silia, Abhinandan, Patrick, Philip and René.

The start of my PhD would have only been half as enjoyable without our little cohort of PhD students who decided to embark on this journey of pursuing a PhD together. Thank you Laura, Dana, Federico and Patrick! Additionally, I am truly thankful for all the support and good times spent inside the lab and at other occasions with Silia, Philip, Patrick and Fabian.

Overall, all current and previous members of the IQO group had their small contributions in this endeavour, maybe only by sharing a coffee or helping out with equipment. I am especially grateful for the collaboration with our heroes in the clean-room who made my ideas of waveguide samples and challenging coatings reality. Thank you Raimund, Viktor, Christof, Olga, Philipp and Sebastian!

Last but definitely not least, a heartfelt thank you goes to my family and my girlfriend Anne for supporting me during my time in Paderborn and always believing in me.

Bibliography

[1] A. G. J. MacFarlane, J. P. Dowling, and G. J. Milburn, “Quantum technology: the second quantum revolution”, *Philosophical Transactions of the Royal Society of London. Series A: Mathematical, Physical and Engineering Sciences* **361**, 1809 (2003).

[2] I. H. Deutsch, “Harnessing the Power of the Second Quantum Revolution”, *PRX Quantum* **1** (2020).

[3] D. Ganapathy et al., “Broadband Quantum Enhancement of the LIGO Detectors with Frequency-Dependent Squeezing”, *Phys. Rev. X* **13** (2023).

[4] C. S. Hamilton et al., “Gaussian Boson Sampling”, *Phys. Rev. Lett.* **119** (2017).

[5] Y.-H. Deng et al., “Solving Graph Problems Using Gaussian Boson Sampling”, *Phys. Rev. Lett.* **130** (2023).

[6] S. Mukamel et al., “Roadmap on quantum light spectroscopy”, *Journal of Physics B: Atomic, Molecular and Optical Physics* **53**, 7 (2020).

[7] B. H. Stuart, *Infrared Spectroscopy: Fundamentals and Applications*, John Wiley and Sons (2004).

[8] M. Vainio and L. Halonen, “Mid-infrared optical parametric oscillators and frequency combs for molecular spectroscopy”, *Phys. Chem. Chem. Phys.* **18** (2016).

[9] R. C. Miller and W. A. Nordland, “Absolute Signs of Second-Harmonic Generation Coefficients of Piezoelectric Crystals”, *Phys. Rev. B* **2** (1970).

[10] R. S. Finn and J. F. Ward, “Nonlinear-Optical Measurement of Dispersion in Gases”, *Appl. Opt.* **11**, 9 (1972).

[11] J. W. Hahn and E. S. Lee, “Measurement of nonresonant third-order susceptibilities of various gases by the nonlinear interferometric technique”, *J. Opt. Soc. Am. B* **12**, 6 (1995).

[12] M. V. Chekhova and Z. Y. Ou, “Nonlinear interferometers in quantum optics”, *Adv. Opt. Photon.* **8** (2016).

[13] G. B. Lemos et al., “Quantum imaging with undetected photons”, *Nature* **512** (2014).

[14] L. J. Wang, X. Y. Zou, and L. Mandel, “Induced coherence without induced emission”, *Phys. Rev. A* **44** (1991).

[15] J. Fuenzalida, E. Giese, and M. Gräfe, “Nonlinear Interferometry: A New Approach for Imaging and Sensing”, *Advanced Quantum Technologies* **7**, 6 (2024).

[16] E. Pearce et al., “Practical quantum imaging with undetected photons”, *Opt. Continuum* **2**, 11 (2023).

[17] H. Defienne et al., “Advances in quantum imaging”, *Nature Photonics* **18** (2024).

[18] A. Paterova et al., “Measurement of infrared optical constants with visible photons”, *New Journal of Physics* **20**, 4 (2018).

[19] C. Lindner et al., “Nonlinear interferometer for Fourier-transform mid-infrared gas spectroscopy using near-infrared detection”, *Opt. Express* **29**, 3 (2021).

[20] P. Kaufmann et al., “Mid-IR spectroscopy with NIR grating spectrometers”, *Opt. Express* **30**, 4 (2022).

[21] A. Vallés et al., “Optical sectioning in induced coherence tomography with frequency-entangled photons”, *Phys. Rev. A* **97** (2018).

[22] A. Rojas-Santana et al., “Analysis of the signal measured in spectral-domain optical coherence tomography based on nonlinear interferometers”, *Phys. Rev. A* **106** (2022).

[23] D. Pohl et al., “An integrated broadband spectrometer on thin-film lithium niobate”, *Nature Photonics* **14**, 1 (2020).

[24] Y. Chen et al., “Review of Integrated Optical Biosensors for Point-Of-Care Applications”, *Biosensors* **10**, 12 (2020).

[25] I. A. Walmsley and C. Dorrer, “Characterization of ultrashort electromagnetic pulses”, *Adv. Opt. Photon.* **1**, 2 (2009).

[26] B. E. A. Saleh and M.C. Teich, *Fundamentals of Photonics*, 2nd ed., John Wiley and Sons Ltd (2007).

[27] A. Monmayrant, S. J. Weber, and B. Chatel, “A newcomer’s guide to ultrashort pulse shaping and characterization”, *Journal of Physics B: Atomic, Molecular and Optical Physics* **43**, 10 (2010).

[28] L. Lepetit, G. Chériaux, and M. Joffre, “Linear techniques of phase measurement by femtosecond spectral interferometry for applications in spectroscopy”, *J. Opt. Soc. Am. B* **12**, 12 (1995).

[29] W. Drexler and J. G. Fujimoto, *Optical Coherence Tomography*, 2nd ed., Springer Cham (2015).

[30] S. Aumann et al., “Optical Coherence Tomography (OCT): Principle and Technical Realization”, In: *High Resolution Imaging in Microscopy and Ophthalmology: New Frontiers in Biomedical Optics*, J. F. Bille, Springer International Publishing (2019).

[31] R. Leitgeb, C. K. Hitzenberger, and A. F. Fercher, “Performance of fourier domain vs. time domain optical coherence tomography”, *Opt. Express* **11**, 8 (2003).

[32] P. Griffiths and J. A. Haseth, *Fourier Transform Infrared Spectrometry*, John Wiley and Sons Ltd (2007).

[33] J. R. Birch, “Dispersive Fourier transform spectroscopy”, *Microchimica Acta* **93**, 1 (1987).

[34] B. Yurke, S. L. McCall, and J. R. Klauder, “SU(2) and SU(1,1) interferometers”, *Phys. Rev. A* **33** (1986).

[35] D. Li et al., “The phase sensitivity of an SU(1,1) interferometer with coherent and squeezed-vacuum light”, *New Journal of Physics* **16**, 7 (2014).

[36] A. Riazi et al., “Alignment-free dispersion measurement with interfering biphotons”, *Opt. Lett.* **44**, 6 (2019).

[37] A. Vanselow et al., “Frequency-domain optical coherence tomography with undetected mid-infrared photons”, *Optica* **7**, 12 (2020).

[38] G. J. Machado et al., “Optical coherence tomography with a nonlinear interferometer in the high parametric gain regime”, *Applied Physics Letters* **117**, 9 (2020).

[39] S. Neves et al., “Open-path detection of organic vapors via quantum infrared spectroscopy”, *APL Photonics* **9**, 9 (2024).

[40] T. Tamir, *Guided-wave optoelectronics*, Springer-Verlag Berlin, Heidelberg (1988).

[41] C. Grossmann, H.-G. Roos, and M. Stynes, *Numerical Treatment of Partial Differential Equations*, 1st ed., Springer Berlin, Heidelberg (2007).

[42] M. Santandrea et al., “Fabrication limits of waveguides in nonlinear crystals and their impact on quantum optics applications”, *New J. Phys.* **21** (2019).

[43] M. Santandrea, *Design of nonlinear integrated devices for quantum optics applications*, PhD thesis, Paderborn University (2019).

[44] J. C. Knight and D. V. Skryabin, “Nonlinear waveguide optics and photonic crystal fibers”, *Opt. Express* **15**, 23 (2007).

[45] R. W. Boyd R. W. Boyd, *Nonlinear Optics*, Third Edition, Academic Press (2008).

[46] R.S. Weis and T.K. Gaylord, “Lithium niobate: Summary of physical properties and crystal structure”, *Appl. Phys. A* **37** (1985).

[47] K. Y. Spasibko et al., “Ring-shaped spectra of parametric downconversion and entangled photons that never meet”, *Opt. Lett.* **41**, 12 (2016).

[48] M. Yamada et al., “First-order quasi-phase matched LiNbO3 waveguide periodically poled by applying an external field for efficient blue second-harmonic generation”, *Applied Physics Letters* **62**, 5 (1993).

[49] M. M. Fejer et al., “Quasi-Phase-Matched Second Harmonic Generation: Tuning and Tolerances”, *IEEE Journal of Quantum Electronics* **28**, 11 (1992).

[50] W. P. Grice and I. A. Walmsley, “Spectral information and distinguishability in type-II down-conversion with a broadband pump”, *Phys. Rev. A* **56** (1997).

[51] A. Christ et al., “Probing multimode squeezing with correlation functions”, *New Journal of Physics* **13**, 3 (2011).

[52] Andreas Christ et al., “Theory of quantum frequency conversion and type-II parametric down-conversion in the high-gain regime”, *New Journal of Physics* **15**, 5 (2013).

[53] Y. Jeronimo-Moreno and A. B. U’Ren, “Control, measurement, and propagation of entanglement in photon pairs generated through type-II parametric down-conversion”, *Phys. Rev. A* **79** (2009).

[54] M. Santandrea et al., “Lossy SU(1,1) interferometers in the single-photon-pair regime”, *Quantum Science and Technology* **8**, 2 (2023).

[55] J. W. MacLean, J. M. Donohue, and K. J. Resch, “Direct Characterization of Ultrafast Energy-Time Entangled Photon Pairs”, *Phys. Rev. Lett.* **120** (2018).

[56] J. D. Franson, “Nonlocal cancellation of dispersion”, *Phys. Rev. A* **45** (1992).

[57] S. Panahiyan et al., “Nonlinear Interferometry for Quantum-Enhanced Measurements of Multiphoton Absorption”, *Phys. Rev. Lett.* **130** (2023).

[58] L. Cui et al., “Quantum state engineering by nonlinear quantum interference”, *Phys. Rev. A* **102** (2020).

[59] H. M. Wiseman and K. Mölmer, “Induced coherence with and without induced emission”, *Physics Letters A* **270**, 5 (2000).

[60] J. Flórez et al., *Enhanced nonlinear interferometry via seeding*, 2022, arXiv: `2209.06749 [quant-ph]`.

[61] N. R. Gemmell et al., “Loss-Compensated and Enhanced Midinfrared Interaction-Free Sensing with Undetected Photons”, *Phys. Rev. Appl.* **19** (2023).

[62] B. J. Smith et al., “Photon pair generation in birefringent optical fibers”, *Opt. Express* **17**, 26 (2009).

[63] E. Y. Zhu et al., “Poled-fiber source of broadband polarization-entangled photon pairs”, *Opt. Lett.* **38**, 21 (2013).

[64] M. A. Smirnov et al., “Bright ultra-broadband fiber-based biphoton source”, *Opt. Lett.* **49**, 14 (2024).

[65] R. Pollmann et al., “Integrated, bright broadband, two-colour parametric down-conversion source”, *Opt. Express* **32**, 14 (2024).

[66] C. Chen et al., “Compensation-free broadband entangled photon pair sources”, *Opt. Express* **25**, 19 (2017).

[67] A. Eckstein, B. Brecht, and C. Silberhorn, “A quantum pulse gate based on spectrally engineered sum frequency generation”, *Opt. Express* **19** (2011).

[68] P. A. Hegarty et al., “Turn all the lights off: Bright- and dark-field second-harmonic microscopy to select contrast mechanisms for ferroelectric domain walls”, *Journal of Applied Physics* **131**, 24 (2022).

[69] K. N. Chopra and K. V. Narasimham, “Thin film coating design and fabrication of broadband dielectric coated laser mirror”, *Journal of Optics* **17**, 2 (1986).

[70] F. Roeder et al., “Ultra-broadband non-degenerate guided-wave bi-photon source in the near and mid-infrared”, *New Journal of Physics* **26**, 12 (2024).

[71] W. Sohler and R. Regener, “Loss in low-finesse Ti:LiNbO3 optical waveguide resonates”, *Appl. Phys. B* **36** (1984).

[72] S. W. Jolly and P. Kockaert, “Coupling to multi-mode waveguides with space-time shaped free-space pulses”, *Journal of Optics* **25**, 5 (2023).

[73] J. Villarroel et al., “Analysis of photorefractive optical damage in lithium niobate: application to planar waveguides”, *Opt. Express* **18**, 20 (2010).

[74] Y. Kong et al., “OH- absorption spectra in doped lithium niobate crystals”, *Physics Letters A* **196**, 1 (1994).

[75] J. Williams et al., “Ultrashort pulse biphoton source in lithium niobate nanophotonics at 2 mum”, *Nanophotonics* **13**, 18 (2024).

[76] N. A. Harper et al., “Highly efficient visible and near-IR photon pair generation with thin-film lithium niobate”, *Optica Quantum* **2**, 2 (2024).

[77] M. Fiorentino et al., “Spontaneous parametric down-conversion in periodically poled KTP waveguides and bulk crystals”, *Opt. Express* **15**, 12 (2007).

[78] N. Montaut et al., “High-Efficiency Plug-and-Play Source of Heralded Single Photons”, *Phys. Rev. Appl.* **8** (2017).

[79] D. Tabakaev et al., “Spatial Properties of Entangled Two-Photon Absorption”, *Phys. Rev. Lett.* **129** (2022).

[80] B. Dayan et al., “Nonlinear Interactions with an Ultrahigh Flux of Broadband Entangled Photons”, *Phys. Rev. Lett.* **94** (2005).

[81] A. Vanselow et al., “Ultra-broadband SPDC for spectrally far separated photon pairs”, *Opt. Lett.* **44** (2019).

[82] M. Manceau et al., “Detection Loss Tolerant Supersensitive Phase Measurement with an SU(1,1) Interferometer”, *Phys. Rev. Lett.* **119** (2017).

[83] D. Kalashnikov, A. Paterova, and S. Kulik, “Infrared spectroscopy with visible light”, *Nature Photon* **10** (2016).

[84] N. R. Gemmell et al., “Coupling undetected sensing modes by quantum erasure”, *APL Quantum* **1**, 3 (2024).

[85] A. Christ et al., “Spatial modes in waveguided parametric down-conversion”, *Phys. Rev. A* **80** (2009).

[86] I. Kviatkovsky et al., “Microscopy with undetected photons in the mid-infrared”, *Science Advances* **6**, 42 (2020).

[87] F. Roeder et al., “Measurement of Ultrashort Biphoton Correlation Times with an Integrated Two-Color Broadband SU(1, 1)-Interferometer”, *PRX Quantum* **5** (2024).

[88] M. Jankowski, J. Mishra, and M. M. Fejer, “Dispersion-engineered $\chi^{(2)}$ nanophotonics: a flexible tool for nonclassical light”, *Journal of Physics: Photonics* **3**, 4 (2021).

[89] D. J. Kane and R. Trebino, “Single-shot measurement of the intensity and phase of an arbitrary ultrashort pulse by using frequency-resolved optical gating”, *Opt. Lett.* **18**, 10 (1993).

[90] C. Iaconis and I. A. Walmsley, “Spectral phase interferometry for direct electric-field reconstruction of ultrashort optical pulses”, *Opt. Lett.* **23**, 10 (1998).

[91] C. K. Hong, Z. Y. Ou, and L. Mandel, “Measurement of subpicosecond time intervals between two photons by interference”, *Phys. Rev. Lett.* **59** (1987).

[92] S.-Y. Baek, O. Kwon, and Y.-H. Kim, “Nonlocal dispersion control of a single-photon waveform”, *Phys. Rev. A* **78** (2008).

[93] S.-Y. Baek, O. Kwon, and Y.-H. Kim, “Temporal shaping of a heralded single-photon wave packet”, *Phys. Rev. A* **77** (2008).

[94] A. Valencia et al., “Entangled Two-Photon Wave Packet in a Dispersive Medium”, *Phys. Rev. Lett.* **88** (2002).

[95] S. E. Harris, “Chirp and Compress: Toward Single-Cycle Biphotons”, *Phys. Rev. Lett.* **98** (2007).

[96] Y. Shaked et al., “Observing the nonclassical nature of ultra-broadband bi-photons at ultrafast speed”, *New J. Phys.* **16** (2014).

[97] Y. Shaked et al., “Ocatve-spanning spectral phase control for single-cycle biphotons”, *New J. Phys.* **17** (2015).

[98] A. B. U’Ren et al., “Generation of Pure-State Single-Photon Wavepackets by Conditional Preparation Based on Spontaneous Parametric Downconversion”, *Las. Phys.* **15** (2005).

[99] K.-H. Luo et al., “Quantum optical coherence: From linear to nonlinear interferometers”, *Phys. Rev. A* **104**, 043707 (2021).

[100] M. Wojtkowski et al., “Ultrahigh-resolution, high-speed, Fourier domain optical coherence tomography and methods for dispersion compensation”, *Opt. Express* **12**, 11 (2004).

[101] F. Roeder et al., “Towards integrated sensor for optimized OCT with undetected photons”, *in preparation* (2025).

[102] C. Lindner, *Nonlinear interferometers based on spontaneous parametric downconversion for Fourier transform mid-infrared spectroscopy*, PhD thesis, University of Freiburg (2022).

[103] P. R. Sharapova et al., “Toolbox for the design of LiNbO3-based passive and active integrated quantum circuits”, *New Journal of Physics* **19**, 12 (2017).

[104] G. Finco et al., “Monolithic thin-film lithium niobate broadband spectrometer with one nanometre resolution”, *Nat. Commun.* **15**, 2330 (2024).

[105] A. Y. Hwang et al., “Mid-infrared spectroscopy with a broadly tunable thin-film lithium niobate optical parametric oscillator”, *Optica* **10**, 11 (2023).

[106] J. Kaur et al., “Spectral domain nonlinear quantum interferometry with pulsed laser excitation”, *Phys. Rev. A* **108** (2023).

[107] J. Kaur et al., “High-spectral-resolution quantum Fourier-transform infrared spectroscopy with pulsed laser excitation”, *Phys. Rev. Appl.* **22** (2024).

[108] F. Traeger, *Springer Handbook of Lasers and Optics*, 2nd ed., Springer Berlin, Heidelberg (2012).